Modelling and validation of neutral particle flow by means of stochastic algorithms using the example of a fusion divertor

Zur Erlangung des akademischen Grades eines

Doktors der Ingenieurwissenschaften (Dr.-Ing.)

von der KIT-Fakultät für Maschinenbau des

Karlsruher Instituts für Technologie (KIT)

genehmigte

DISSERTATION

von

M. Sc. Cristian Gleason González

geboren in Naucalpan de Juárez, Mexiko

Tag der mündlichen Prüfung: 29.09.2022

Hauptreferent: Prof. Dr.-Ing. Robert Stieglitz

Karlsruher Institut für Technologie

Korreferent: Prof. Dr. Mathias Groth

Aalto University

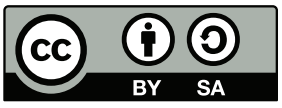

Kurzfassung

Die Partikelabfuhr ist ein Schlüsselprozess, der die Plasmakerndichte und das Abpumpen der Heliumasche, die aus den Kernreaktionen resultiert, steuert. In Fusionsanlagen wie dem Tokamak in seiner Divertorkonfiguration, steht die Partikelströmung im Divertor und in der Subdivertor-Region in Zusammenhang mit dem Druck und dem Gas, welches durch das Toruspumpensystem abgepumpt wird. Deshalb ist die vorausschauende Modellierung der Neutralpartikel-Abfuhr von entscheidender Bedeutung für das Verständnis sowie für die Optimierung des Betriebs von Vakuumsystemen in Fusionsanlagen.

Das Hauptziel der hier vorliegenden Dissertation ist die Entwicklung eines numerischen Tools, das auf der Direct Simulation Monte Carlo Methode basiert ist. Dieses soll die Neutralgasströmung in Fusionsanwendungen beschreiben. Der im Funktionsumfang der Open-Source C++ Toolbox für Computational Fluid Dynamik, OpenFOAM, enthaltene DSMC Solver *dsmcFoam* wird erstmals im Rahmen der Kernfusion zur Modellierung, Simulation und Validierung von Neutralgas-Strömungen im Divertorbereich angewendet.

Ein erforderlicher erster Schritt für die Anwendung des *dsmcFoam* in der Divertorregion ist es, sicherzustellen, dass der Solver die Gasströmungen in einer einfachen Geometrie vorhersagen kann. Hierzu wird *dsmcFoam* mit theoretischen Vorhersagen verifiziert und mit unabhängigen numerischen Berechnungen abgeglichen. Die Sensitivitätsanalyse der Modellierungsparameter zeigt die Auswirkungen auf das Strömungsfeld in Abhängigkeit von Zeitschritt, Zellgrößenabhängigkeit und Anzahl der modellierten Partikel. Im zweiten Schritt werden die Solver-Funktionalitäten weiterentwickelt, um die Gasabsorption an Oberflächen über die Stickingkoeffizient (Haftwahrscheinlichkeit) zu modellieren.

Mit dieser neuen Funktionalität des *dsmcFoam*-Solvers wird die Analyse der Partikelabfuhr im Subdivertor des Tokamaks JT-60SA durchgeführt. Die Analyse umfasst die Studie der Gasströmung mit und ohne Wechselwirkungen von Neutralteilchen. Die Studie bestätigt, dass die Berücksichtigung von Kollisionen zwischen Teilchen eine wesentliche Rolle in der Beschreibung des Neutralgastransports und der Gasströmungsentwicklung in Tokamak-Subdivertoren spielt. Dies zeigt sich in den Druckwerten des DSMC-Kollisionsmodells, welche im Vergleich zu den Druckwerten vom kollisionslosen DSMC-Modell um etwa 25% bzw. 40% ansteigen. Dieser Vergleich ist der erste seiner Art im Anwendungskontext der Kernfusion.

Die zweite Anwendung des *dsmcFoam* besteht in der Analyse der Gasströmung in einem Divertor-Hochdruckszenario im Tokamak ITER. Die Neutralgasströmung wird für einen 10 Pa Divertordruck in der ITER-2009-Designgeometrie untersucht. Dabei wird gezeigt, dass die Gaszirkulations-Effekte durch den Divertor in direkter Abhängigkeit

zum Druck am Pumpenauslass stehen. Der Zusammenhang zwischen dem Gas, das zur Plasmahauptkammer strömt und dem Druck am Pumpenauslass, wird festgestellt. Die Simulationen haben ergeben, dass der Druckanstieg am Pumpenauslass die Gasströmung auf der Niederfeldseite (LFS) verstärkt, während auf der Hochfeldseite (HFS) kein Effekt zu beobachten ist. Die Studie zeigt, dass sich die Erhöhung der Gasströmung auf der Niederfeldseite durch eine Rückströmung am Pumpenausfluss ergibt.

Durch die Kombination von Experimentaldaten mit DSMC-Modellierung wird die Berechnung der Gasströmung im gesamten Subdivertor des Tokamaks ASDEX Upgrade (AUG) ermöglicht. Mit dem installierten Divertor III in AUG wurden Experimente, die mit Fokus auf die Partikelabfuhr im Betrieb des Tokamaks bei voller Leistung der kryogenen Pumpen durchgeführt wurden, mit DSMC modelliert. Die Modellierung zeigt, dass die Partikelflüsse unterhalb der Divertordome-Region und am LFS mit den experimentellen Messungen vergleichbar sind. Zwischen den kalkulierten Gasströmungen in der Modellierung und den Messungen an den HFS-Manometern wurde hinter den Divertortarget eine Diskrepanz festgestellt. Die Sensitivitäten zur AUG-Modellierung haben die Abhängigkeiten zwischen den Subdivertor-Parametern aufgezeigt, die für den Divertorbetrieb von Bedeutung sind.

Summary

Particle exhaust is a key process that controls the plasma core density and the pumping of the helium ash resulting from the nuclear reactions. In fusion machines such as the tokamak in its divertor configuration, the particle flow in the divertor and sub-divertor region is related to the pressure and the gas being pumped by the torus pumping system. This is why predictive modelling of the neutral particle exhaust is crucial for understanding and optimizing the operation of vacuum systems in fusion devices.

The main objective of this dissertation is to develop a numerical tool based on the Direct Simulation Monte Carlo (DSMC) Method that describes the neutral gas flow in fusion applications. Within the framework of the open-source C++ toolbox for computational fluid dynamics OpenFOAM, the in-built DSMC solver *dsmcFoam* is employed for modelling, simulation and validation of the neutral gas flows in the divertor region for the first time in a context of nuclear fusion. A necessary step to apply *dsmcFoam* in the divertor region is to first assure that the solver can predict gas flows in a simple geometry. Therefore, *dsmcFoam* is verified against theoretical predictions and benchmarked against independent numerical calculations. The sensitivity analysis on the modelling parameters shows the effect on the flow field as a function of time step, cell size dependence and number of modelled particles. As second step, the solver capabilities are further developed in order to model gas absorption at surfaces via the sticking probability.

With this new capability of the *dsmcFoam* solver, the analysis of the particle exhaust in the sub-divertor of the JT-60SA tokamak is performed. The analysis has been carried out by studying the gas flow with and without neutral particle interactions. The study confirms that the inclusion of collisions between particles plays a significant role in the description of the neutral gas transport and the gas flow development in tokamak sub-divertors. This is reflected in the pressure values of the DSMC collisional model, which increase by around 25% and 40% when comparing them with the pressure values obtained with the DSMC-collisionless model. The comparison is the first of its type in the application context of nuclear fusion.

The second application of *dsmcFoam* consists of the analysis of the gas flow of a high-divertor pressure scenario in ITER tokamak. For a 10 Pa divertor pressure, the neutral gas flow in the ITER 2009-design geometry is studied. Here the gas recirculation effects through the divertor are shown to have a direct dependency with the pressure at the pumping port. The relation between the gas flowing towards the plasma main chamber and the pressure at the pumping port is obtained. The simulations have shown that the pressure increase at the pumping port enhances the gas flow at the low-field side (LFS), whereas at the high-field-side (HFS) no effect is observed. The study shows that flow reversal near the pumping port occurs, leading to an increase of the particle flow at the LFS.

The combination of experimental data and DSMC modelling allows the calculation of neutral gas flow in the entire sub-divertor of ASDEX Upgrade (AUG) tokamak. With the installed Divertor III in AUG, dedicated experiments focusing in the particle exhaust by operating the tokamak with full cryogenic pumping is modelled with DSMC. The modelling shows that particle fluxes below the divertor dome region and at the LFS are comparable to the experimental measurements. A mismatch is found between the calculated gas fluxes in the modelling and the measurements at the HFS manometers, behind the divertor target. The sensitivities on the AUG modelling have shed light onto dependencies among sub-divertor parameters, which are of relevance in divertor operation.

Acknowledgements

This dissertation has taken its final form as a result not only of my own work and efforts but as a result of fruitful collaborations with many people. Without their support and time invested, this project will not have succeeded at all.

First of all, I will like to thank to my academic supervisor Professor Robert Stieglitz for allowing me to start my research project in nuclear fusion technology at KIT and for providing regularly valuable suggestions on the structure and directions of this work. I am indebted to my daily supervisors Dr. Christian Day and Dr. Stylianos Varoutis for the numerous helpful and inspiring discussions throughout my time in the Institute of Technical Physics at KIT. To both of them I wish to extend also my gratitude not only for the in-depth introduction to the fascinating world of neutral gas dynamics through DSMC and its applications, but also for your patience, constant advice and support. Additionally, I would like to thank my friends and colleagues for all the support and for the technical discussions, great, funny and at sometimes even musical moments along the years at ITEP: Santiago, Matthieu, Aurelien, Sebastian, Ulli and Vishnu.

To Professor Mathias Groth, I would also like to thank him for accepting being the Co-referent (external professor) of my dissertation and for giving me the opportunity to participate in modelling activities at JET. Also, I would like to thank him the opportunity to show us Helsinki and Aalto University. Furthermore, I would like to thank also the JT-60 SA colleagues for the collaboration focusing on the neutral dynamics modelling which enriched my understanding of vacuum physics and exhaust conditions in future fusion devices. The experiences with Mathias and his group, JET colleagues and JT-60SA show that international collaboration is a way to go for nuclear fusion.

I would like to thank the task force leaders of MST and Max Planck Institute of Plasma Physics for the opportunity to execute the experimental campaign conducted at ASDEX Upgrade. Special thanks go to Prof. Arne Kallenbach, Dr. Andreas Scarabosio, Dr. Thomas Eich, Dr. Albrecht Herrmann, Dr. Volker Rohde, Dr. Marco Wischmeier, Dr. Steffen Potzel, the whole experimental team and everyone involved in the post-processing. Chronologically, I would like to thank Albrecht and Volker for the opportunity of getting involved in the machine understanding by visiting AUG, during the divertor III installation, and for the further insights of the vacuum operation in AUG. The support of Thomas Eich was with no doubt necessary at the beginning and during the campaign. I am in great gratitude to Arne for the experimental planning and for being the discharge operator for the plasma shots with the non-standard operational conditions of the cryopump. To Andreas, I would like to thank the time spent in explaining neutral physics and calibration procedures of the neutral gauges at AUG. Stefen, many thanks for the

time spent on retrieving the spectroscopy data and the helpful insights regarding the SBD measurements. For the whole experience involving physics, soccer and grills, many thanks to the AUG Team and the MST1!

To my family I would like to dedicate this dissertation. Thanks to all of you for being there, for supporting me and for being part of my daily inspiration. Particularly to Karla and Fernando many thanks for your support during the writing process of the dissertation. To Carlo I would like to also thank you for the unvaluable support during the last period of the thesis. Of course, I would like to thank, *mein Schatz* Andrea: thanks for being there, sharing all moments and for supporting me at anytime. You were the main pillar during this time.

Table of contents

List of symbols

Latin letters [unit]	Description
a_Q [-]	Accommodation coefficient of a particle property Q
A [-]	Macroscopic variable (fluctuating in time)
A_{pump} [m^2]	Pump area
A_{tot} [m^2]	Pump area (total, effective)
$b = b(\chi)$ [m^2]	Projection surface in a ring (collision theory)
B [T]	Magnetic field
$\mathbf{B_p}$ [T]	Poloidal magnetic field
$\mathbf{B_t}$ [T]	Toroidal magnetic field
c_j [J/K]	Heat capacity at constant volume ($j = V$) and heat capacity at constant pressure ($j = p$)
C_p [J/kgK]	Specific heat capacity at constant pressure
d [m]	Diameter of a particle of radius r
d_i [m]	Distance between the center of a cell and one of its sides
dS [m^2]	Surface element
E_{rel} [J]	Relative energy
E_r [J]	Translational relative velocity
$E_A = \frac{\sigma_A}{\lvert A \rvert}$	Error bar of a sampled macroscopic variable A
$f(\mathbf{r}, \mathbf{v}, t)$	Distribution function (Boltzmann equation)
f	Degrees of freedom (overall temperature)
f_0 [-]	Equilibrium distribution function
f_{coll} [s^{-1}]	Collision frequency (see also ν_{pq})

$\mathbf{F}(r)$ [N]	Force with only a radial dependence (inverse power model)
$\mathbf{F}_L$ [N]	Lorentz force
F_N [-]	Conversion factor in DSMC
I_p [MA]	Plasma current (in tokamaks)
k_B [1.38x10^{-23} J/K]	Boltzmann constant
$\hat{k}$ [-]	Direction of momentum transfer in the k-direction (z-direction)
Kn [-]	Knudsen number
L [m]	Characteristic length of the physical system
m [kg]	Mass of a particle
m_j [kg]	Mass of particle "j"
m_r [kg]	Reduced mass of a system
M [-]	Number of samples (DSMC averaging)
Ma	Mach number
n [m^{-3}]	Number density
n_e [m^{-3}]	Electron number density
n_i [m^{-3}]	Ion number density
$\hat{n}$ [-]	Unit normal vector to a surface
$\hat{n}_{\parallel}$ [-]	Tangential unit vector
$\hat{n}_{\perp}$ [-]	Normal unit vector
N	Number of particles
N_{physical}	Number of physical particles
N_{DSMC}	Number of simulated particles in DSMC
N_{cand} [-]	Number of particles that are candidates to collide (DSMC algorithm)
$\langle N_{coll} \rangle$ [-]	Mean number of collisions
$\langle N_{DSMC} \rangle_{cell} = nV_{cell}/F_N$ [-]	Mean number of simulated particles in a cell
p [Pa]	Pressure

P [kg m/s]	Momentum of a particle
Pr	Prandtl number
$P_R(v_r)$	Reaction probability between two particles
q [C]	Elementary charge
r [m]	Vector position in real space **r** = (x, y, z)
r [m]	Distance between particles (Potential energy)
$\mathbf{r_0}$ [m]	Initial vector position of particle in space
R [$m^{-3}s^{-1}$]	Rate per unit volume
R, R' [m]	Major radius (plasma in tokamaks)
$\Re_u$ [-]	Random number between 0 and 1
$\Re_U$ [-]	Random number from a uniform distribution function U
$s = V\beta$ [-]	Speed ratio
S [m^3/s]	Pumping speed
t_{res} [s]	Residence time of a particle in a computational cell
T [K]	Temperature
$T_j(\mathbf{r}, t)$ [K / m^3]	Temperature per volume cell, j = translational, rotational or vibrational
$T_{overall}, T_{ov}$ [K]	Overall temperature
T_k [K]	Temperature of k = wall, reference, translational modes, rotational modes
$U(r)$ [J]	Potential energy as a function of radius (conservative central forces)
$U_{[0,\,1]}$ [-]	Uniform probability distribution function
v [m/s]	Velocity of a particle = (v_x, v_y, v_z)
v_{mp} [m/s]	Most probable thermal speed
v_{mean} [m/s]	Average or mean molecular speed
v_{rms} [m/s]	RMS molecular speed
$\mathbf{v_k}$ [m/s]	Pre-collision velocity of particle "k"

$\mathbf{v}^*_{\boldsymbol{k}}$ [m/s]	Post-collision velocity of particle "k"
v' [m/s]	Thermal or random velocity of a particle
v [m/s]	Speed (magnitude of velocity)
v_r [m/s]	Relative velocity between two particles
$\mathbf{v}_{\mathrm{CM}}$ [m/s]	Velocity of the center of mass
V [m/s]	Macroscopic stream velocity (bulk velocity)
V_{cell}, V_c [m^3]	Volume of a cell where a collision takes place (DSMC)
W [-]	Reduced mass flow rate
W^j	Transmission probability at an open boundary "*j*"
W_o	Function of the reduced mass, relative translational velocity and the two constants α, η appearing in the definition of **F**(r)
Z_i	Charge number

Greek letters

α	Particle of type α
α [–]	Fraction of incident particles that are reflected diffusively at a surface
β [1/m/s]	Inverse of particle speed
$\gamma = C_p / C_V$	Ratio of specific heats
$\Gamma(n)$ [-]	Gamma function
Γ_k [part/m^2s]	Particle flux, where *k* can take the values of *i* (incident) and *r* (reflected)

Γ_{FX} [part/m^{2}s]	Particle flux measured in the barometer number FX, where X is a dummy variable taking the values of 1 until 12
δ [-]	Rarefaction parameter (gas dynamics)
δA [-]	Small perturbation of variable *A*
Δt [s]	Time step (computational)
Δx [m]	Cell size (grid of a computational domain)
$\langle(\Delta A)^2\rangle$	Variance of macroscopic variable
ε [°, rad]	Azimuthal angle (post-collsion velocities)
η, α [-]	Positive constants employed in the definition of the force with radial dependence (inverse power model)
θ [rad]	Poloidal direction (coordinate system)
κ [W/(m K)]	Thermal conductivity
κ_j [1/Pa]	Compressibility at j = *T* (isothermal), *p* (isobaric)
λ [m]	Mean free path
μ [Pa s]	Viscosity
μ_{VHS} [Pa s]	Viscosity resulting from the VHS binary collision model (the index VHS can be also substituted by HS or Maxwell)
ν_{pq} [1/s]	Collision frequency between species *p* and *q*
ν_{VHS} [1/s]	Collision frequency calculated with the VHS binary collison model (the index VHS can be also substituted by HS or Maxwell)
ξ	Sticking probability of a surface
ξ [-]	Power or value of exponent in the expression of the ratio between total cross

	section and reference cross section (VHS collision model)
π [3.1415...]	Pi number
ρ [kg/m^3]	Mass density
$\sigma_A \propto \sqrt{\langle(\Delta A)^2\rangle}$	Std. deviation of macroscopic variable
σ_{fus} [barn = 10^{-28} m^2]	Fusion cross section
σ_{tot} [barn = 10^{-28} m^2]	Total collision cross section
σ_{μ} [barn = 10^{-28} m^2]	Viscosity cross section
σ_{tot}^{HS} [barn = 10^{-28} m^2]	Total cross section of the Hard Sphere model (HS)
σ_{tot}^{VHS} [barn = 10^{-28} m^2]	Total cross section of the Variable Hard Sphere model (VHS)
$\langle\sigma v\rangle$ [m^{3}s^{-1}]	Reaction rate (fusion reactions and collisions)
$(\sigma v_r)_{max}$ [m^3/s]	Maximum value of the collision rate in a cell (DSMC)
τ_{coll} [s]	Mean collision time (physical)
τ_{rel} [s]	Relaxation time (BGK operator)
φ[rad]	Toroidal direction (coordinate system)
$\hat{\varphi}$ [any combination of MKS units]	Macroscopic parameter
χ [rad]	Deflection angle of the relative velocity (collision theory)
ω [-]	Viscosity index
$d\Omega$ [rad]	Differential element of solid angle

Operators

$\left(\frac{\partial f}{\partial t}\right)_{\text{coll}}$	Collision operator (Boltzmann Equation)
$F_x(x)$ [-]	Cumulative distribution function (probability)

$\langle A \rangle$ [-]	Expectation value, mean value of A
$n!$	Factorial operation of a number n
$\nabla_{\mathbf{r}}$	Gradient operator $\nabla_{\mathbf{r}} = \left(\frac{\partial}{\partial x}, \frac{\partial}{\partial y}, \frac{\partial}{\partial z} \right)$
$\nabla_{\mathbf{v}}$	Gradient operator $\nabla_{\mathbf{v}} = \left(\frac{\partial}{\partial v_x}, \frac{\partial}{\partial v_y}, \frac{\partial}{\partial v_z} \right)$
$\int_{\Re^3} []$	Integral operation over the real space (x-, y- and z-directions)
$\int_{S^2} []$	Integral operation over the sphere S^2
$\|\mathbf{v}\| = \sqrt{\sum_{i=1} v_i^2}$	Magnitude of a vector $\mathbf{v}$
O( )	Order of magnitude
$\partial/\partial t = (\dot{}\,)$ [-]	Partial derivative of time
$P_{coll}(i,j)$ [-]	Collision probability between particle “i” and particle “j”
$P_{\perp}(v_{\perp})$ [-]	Probability distribution function of a particle to have a normal velocity (speed) $v_{\perp}$
$P_{\parallel}(v_{\parallel})$ [-]	Probability distribution function of a particle to have a parallel velocity (speed) $v_{\parallel}$
$P_w(\mathbf{v}' \rightarrow \mathbf{v};\mathbf{r})$	Probability that a particle which strikes a wall at a position $\mathbf{r}$ with a velocity $\mathbf{v}'$ will be reflected at $\mathbf{r}$ with velocity $\mathbf{v}$

List of most used acronyms

AUG = ASDEX-Upgrade = Axially Symmetric Divertor Experiment Upgrade

BC(s) = boundary condition(s)

DSMC = Direct Simulation Monte Carlo

HFS = high-field side (in a tokamak)

ITER = International Thermonuclear Experimental Reactor

JET = Joint European Torus

JT-60SA = Japan Torus 60 Super Advance

Kn = Kundsen number

LFS = low-field side (in a tokamak)

MC = Monte Carlo

MCF = magnetic confinement fusion

NTC = no-time counter (scheme)

PFR = plasma flux region

SOL = scrape-off layer

SOLPS = Scrape-Off Layer Plasma Simulation

Tokamak = toroidal chamber with magnetic coils

1 Introduction

1.1 Nuclear fusion, MCF and neutral particle interactions in fusion devices

Nuclear fusion occurs when two light nuclei form a heavier element. To trigger a fusion reaction, two nuclei have to move at sufficient relative velocity, so that the inter-particle Coulomb barrier can be overcome with a non-zero probability via quantum tunneling [1]. The fusion cross section σ_{fus} gives the probability for a fusion reaction to occur between the nuclei. Typically, the expression of the cross section includes a geometrical factor which is inversely proportional to the relative energy between particles E_{rel} [2] and also terms involving the Coulomb barrier that is direct proportional to an exponential factor of the form $\exp\left(-E_{\mathrm{rel}}^{-1/2}\right)$ [3].

From the reactions involving the two hydrogen isotopes deuterium (D) and tritium (T), the one with a 50%-50% mixture of D-T is the most promising for fusion reactor assessments, because its highest fusion cross section at the lowest energy [4] (65 keV in the center-of-mass, which corresponds to approximately to 700 Mio °C). The reaction reads

$$\mathrm{D} + \mathrm{T} \longrightarrow {}^{4}\mathrm{He}\,(3.5\,\mathrm{MeV}) + \mathrm{n}\,(14.1\,\mathrm{MeV}). \tag{1.1}$$

Helium, also known as $\alpha-$particle, is then a fusion product that will remain in the system and it will provide its energy to maintain the fusion reaction. Once its energy is deposited, the helium ash needs to be removed in order to avoid a dilution process. This point will be recalled later on. However, from a fusion reactor perspective it is the number of fusion reactions per unit volume and unit time that is relevant to the energy production. Thus, the rate per unit volume *R* involving nuclei 1 and 2 is given by [5]

$$R = n_1 n_2 \left\langle \sigma_{\mathrm{fus}} \cdot v_{\mathrm{rel}} \right\rangle, \tag{1.2}$$

where the average of $\sigma_{fus} v_{\mathrm{rel}}$ is taken over the velocity space $v_{\mathrm{rel}} \propto \sqrt{E_{\mathrm{rel}}}$ at a given temperature *T*.

For a reactor system with temperature in the range of 10-100 keV, nuclear fusion is feasible. Thus, for the nuclear fusion to succeed one needs (i) to heat the fuel (D, T) at temperatures to the order of 10^6 K and (ii) the fuel should be enclosed in a vessel that can

sustain high-temperature conditions. At such temperatures the electrons are striped from their parental atoms in the fuel such that $n_e \approx Z_i n_i$ (quasi-neutrality condition), forming a state of matter called plasma [6]. Plasmas are characterized for being globally neutral and by its collective behavior provided electromagnetic forces that couples charged particles. Thus, a way to confine the plasma for future fusion power generation is by means of magnetic fields under high-vacuum conditions. This leads us to the magnetic confinement fusion (MCF) concept.

The main idea behind MCF is that charged particles q are confined by magnetic fields $\mathbf{B}$ due to the Lorentz force $\mathbf{F_L} = q\mathbf{v} \times \mathbf{B}$ acting on charge carriers moving with velocity $\mathbf{v}$. The Lorentz force $\mathbf{F}_\mathrm{L}$ forces the charge carriers to have circular and perpendicular path to the magnetic field lines. The resulting helical motion of the charged particles *attaches* the particles along the magnetic field lines, where the particles gyrate in a counter- and clockwise manner for positively and negatively charged particles, respectively.

However, magnetic field lines with open ends will not confine the particles at all. Therefore, one needs to close the field lines in order to keep the particles inside the system. This idea is employed in MCF and thus a common feature of the different confinement concepts is the toroidal topology that characterizes the plasmas (i.e. a donut-shaped vacuum vessel encloses the plasma). Two confinement concepts have been widely developed in MCF and plasma physics research, namely the tokamak and the stellarator. The concepts differ on the principles behind their operation. For instance, the tokamak relies on the induction of a current to confine the plasma whereas the stellarator does not. The subject of the thesis is mainly concerned with the applications in tokamaks and therefore these are described here.

The word tokamak is taken from the russian acronym of *тороидальная камера с магнитными катушками,* which stands for “toroidal chamber with magnetic coils” [7]. The tokamak operation is based on the transformer principle, thus once the gas is ionized inside the vessel, an electric current (plasma current I_p) is induced in the toroidal direction φ by a central solenoid or primary transformer coil, as a consequence of the Faraday’s law of induction, see Figure 1.1. A magnetic field in the toroidal direction B_t is generated by the toroidal field coils which restrict their motion to the field lines.

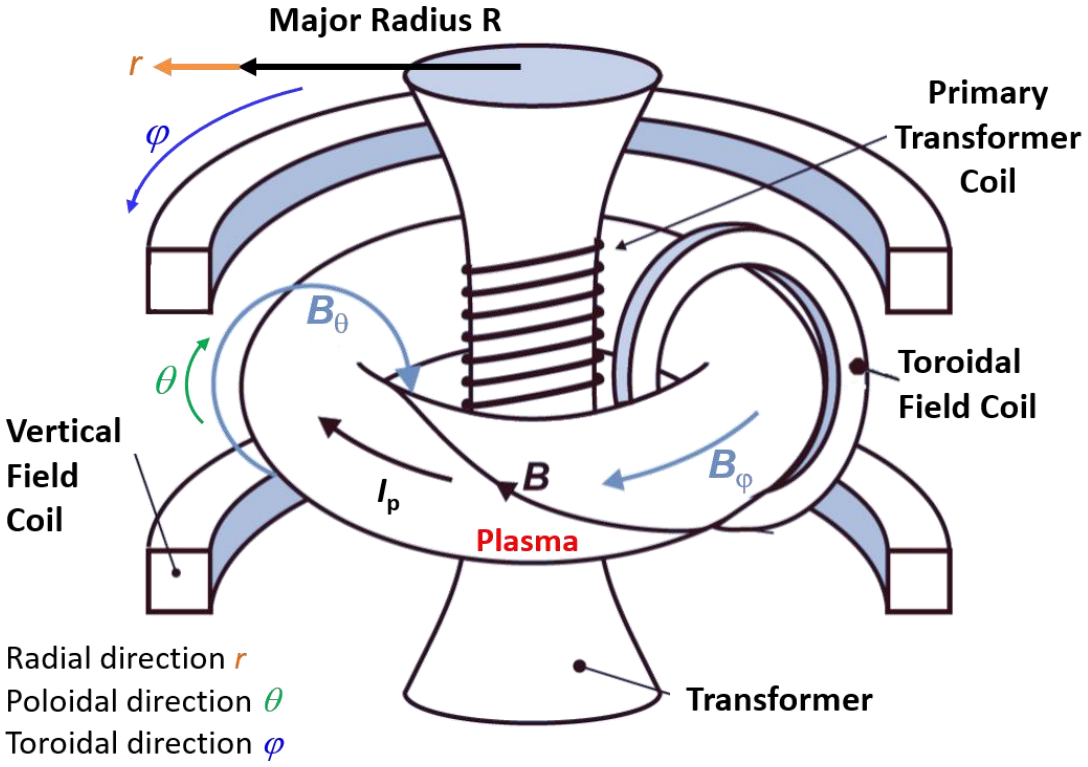

Figure 1.1 Schematic view and relevant component of a simplified Tokamak device. Figure adapted from [6].

Apart from the ions and electrons which are confined in the vessel, the neutral particles constitute an important component in the dynamics of the core and the periphery of a tokamak. Located at the plasma periphery, the neutral particles can either refuel the plasma by re-entering the core region and thereafter being ionized by collisions with the plasma particles or leaving the plasma chamber. This process provides momentum and energy to the plasma, altering the global power and particle balance [8], [9].

To achieve the particle balance and plasma density in tokamaks usually one combines particle fueling and exhaust. The former requires external sources such as gas puffing, pellet and neutral beam injection; whereas the latter involves the torus exhaust system. Both are interlinked by the overall gas throughput [10], [11] that can be handled by the exhaust system. Thus, the torus exhaust system has a considerable impact in the overall performance of tokamaks due to its inter-connections with additional systems in a reactor. The particle exhaust can be performed via a pumped divertor which bridges the tokamak throughput with further stages in the fuel cycle in fusion reactors for tritium recovery and isotope separation [12]. At the divertor region in a tokamak, the magnetic field lines are diverted to a location far from the plasma by shaping the magnetic field. The divertor is therefore a key component in tokamaks since not only serves as first stage

for the particle removal but also allows impurity control (plasma contamination), extraction of heat and helium ash produced by the fusion reaction.

The main focus of this thesis is the study of neutral particle flows in tokamak divertors and therefore, the domain of interest is hereby introduced. In the tokamak configuration, particles leaving the plasma core, ions and electrons, cross the magnetic surface named separtrix and enter a region called scrape-off layer (SOL). There, the particles follow the magnetic field lines that direct them to the divertor region, where the particle pumping occurs. The divertor geometry can have a “w”-form and its structure typically consists of 4 main parts, see Figure 1.2:

- cassette body,
- dome,
- vertical targets (inner and outer),
- reflector plates.

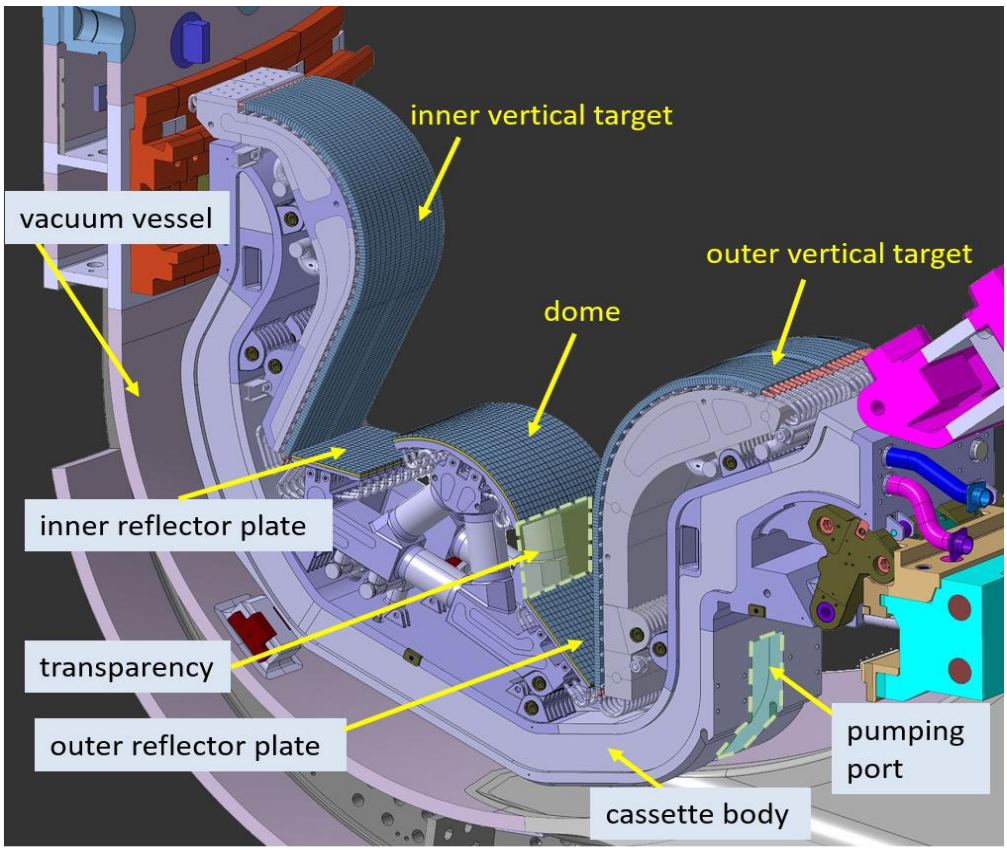

Figure 1.2 Example of the divertor geometry and its different components (ITER tokamak): cassette body, dome, inner and outer vertical targets and both reflector plates: inner and outer [13].

The sub-divertor domain is defined as the volume below the dome together with the ducts behind the vertical targets up the pumping port. In some existing sub-divertors, the region also includes the pump (in most cases a cryopump or a turbo-molecular pump). Since the plasma particles are already neutralized in this region, the magnetic field does

not affect their motion at all. However, the pressure distribution between the ducts behind the targets, pumping port and region below the dome can establish the neutral gas flow across the sub-divertor domain.

During tokamak operation, the sub-divertor and the divertor regions are coupled by the transparency apertures located between the dome and the reflector plates, see area with dashed line in Figure 1.2. The transparency allows the particles to move from the strike points to the sub-divertor due to the pressure gradients or to move between inner and outer reflectors. The neutral gas flows between the main chamber and the sub-divertor are also interlinked by the small gaps or apertures located at the end of the ducts behind both vertical targets.

The sub-divertor region is the main domain of interest in all the analyses in this doctoral thesis. The understanding and description of neutral gas dynamics in the sub-divertor demands the use of sophisticated models that can treat the transport of mass, momentum and energy of neutral flows. In this dissertation, a step in this direction is done by modelling the neutral gas flow in high- and mid-sized tokamak sub-divertors: JT-60SA, ITER and ASDEX Upgrade.

From the modelling perspective, one option is to employ analytical models based on first principles analysis or based on the solution of the Boltzmann equation, which dictates the dynamics of the particle distribution function in neutral transport studies. However, due to the complexity of the collision integral, which is a 7-dimensional integral, the integro-differential equation is not always solvable for practical applications. Alternatively, one can greatly profit by the introduction of particle-based models for the simulation of gas dynamics that either numerically solves the Boltzmann equation or directly simulates the motion of the particles in the gas. The description of neutral gas flow is the main subject of chapter 2. As next step, the tokamak parameters and the periphery of the plasma and its relation to the neutral gas flow in the divertor are introduced.

1.2 Tokamak parameters, SOL plasma flows and divertor neutrals

The tokamak in its divertor configuration is shown in Figure 1.3. Regarding its geometry, the tokamak device is characterized by two parameters. The first is the major radius R, defined as the distance measured from the toroidal axis of symmetry. The second parameter is the minor radius r, the distance from the geometric or magnetic axis to the poloidal plane. In praxis, the major radius R is employed as geometric coordinate and as a figure of merit of each specific tokamak. The Z- and φ-directions complete the coordinate system of the tokamak. The midplane is taken as the surface defined at $Z = 0$, which is employed for the boundary conditions between the core and plasma edge.

For the plasma on the other hand, its topology is determined by the magnetic field geometry. The magnetic field in the system results from the superposition of the toroidal and the poloidal magnetic fields $\mathbf{B} = B_\varphi \hat{\mathbf{e}}_\varphi + B_\theta \hat{\mathbf{e}}_\theta$, where $\hat{\mathbf{e}}_\varphi$ and $\hat{\mathbf{e}}_\theta$ are the normal unit vectors in the toroidal and poloidal directions respectively. The toroidal field, generated by the toroidal field coils, is inversely proportional to the major radius $B_\varphi \propto R^{-1}$, obtained by Ampère's law, see [14] Chapter 3, whereas the poloidal magnetic field is directly proportional to the plasma current $B_\theta \propto I_p$. The sum of both magnetic field forms helicoidal field lines centered at the magnetic axis.

By means of external coils placed below the divertor (not shown), a poloidal magnetic field is generated such that at the so-called *x-point* inside the vessel the poloidal magnetic field B_θ, generated by the plasma, vanishes. Therefore, the poloidal magnetic field inside the vessel is said to be *diverted* and hence, the name divertor configuration.

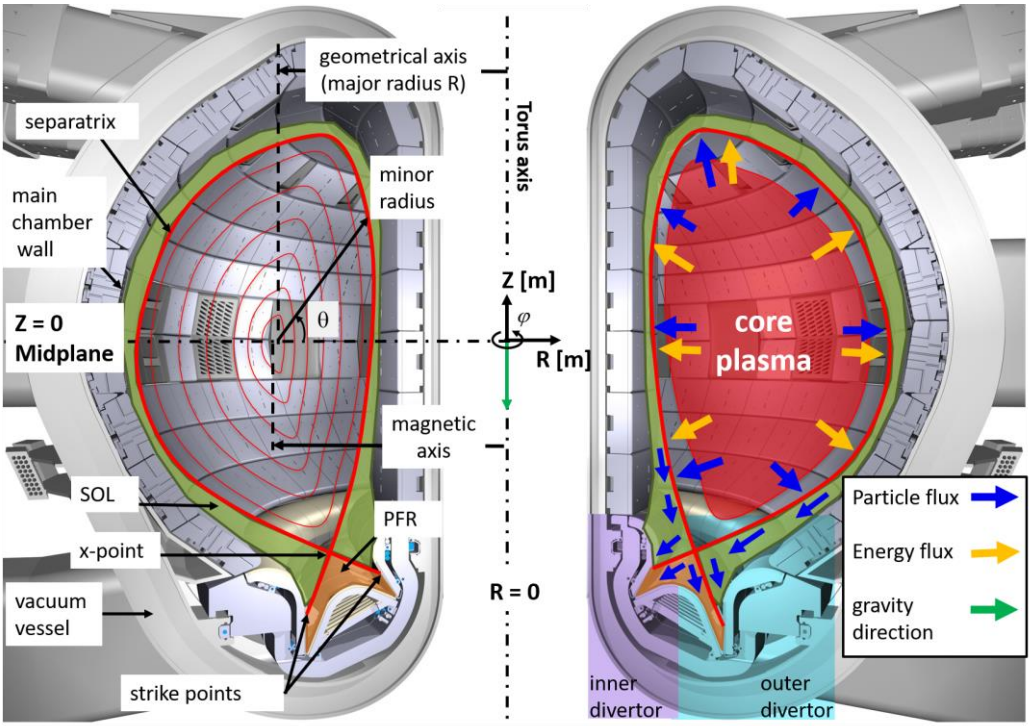

Figure 1.3 Poloidal cross section of a modern tokamak plasma configuration incorporating a lower divertor and relevant dimensional quantitites and its figures of merit. Particles and heat fluxes, blue and yellow arrows respectively, diffuse from the plasma core towards the exterior of the plasma crossing the separatrix and interacting with the divertor targets. Image modified from [15].

The last closed field magnetic surface (LCFS or separatrix), where the x-point is located, defines the boundary between the core and the edge plasma. The plasma edge region is called the scrape-off layer (SOL), shown in green color in Figure 1.3, where open magnetic field lines intersect the divertor vertical targets (outer and inner divertor). The SOL width is typically of the order of few centimeters, which contrasts the size of

the minor radius of medium-sized tokamaks to the order of meters. The region below the x-point is called the private flux region (PFR), depicted in orange in Figure 1.3. Here particle transport from the SOL occurs, which is then directed to the divertor targets.

In addition to the power and particle fluxes in the SOL, a key parameter in fusion devices is the average of the neutral pressures in the divertor region comprising both the divertor and sub-divertor volumes. These two regions are depicted in Figure 1.4, see yellow and red colored regions below the dome. The particle balance building the neutral pressure in the divertor region is strongly dependent in the recycling conditions, i.e. the ionization and recombination of hydrogenic ions and atoms. As presented in [16] pp 35, the neutral particles can also result from the interactions between ions and surfaces (e.g. divertor targets, reflectors). For instance, ions striking the divertor surfaces can be re-scattered back as neutral atoms or the ions are first adsorbed as a neutral by the surface followed by a thermally desorption process with a second neutral atom impinging the surface, re-ejecting both particles as a single molecule. A second mechanism is the Frank Condon process, where a molecule dissociates after colliding with an electron, forming two neutral atoms. Thus, the population of neutrals in the divertor and sub-divertor region is closed related to the ion and electron fluxes at the targets. In order to achieve a desired particle balance in the tokamak, the particle control is performed by pumping out the neutrals in the divertor region.

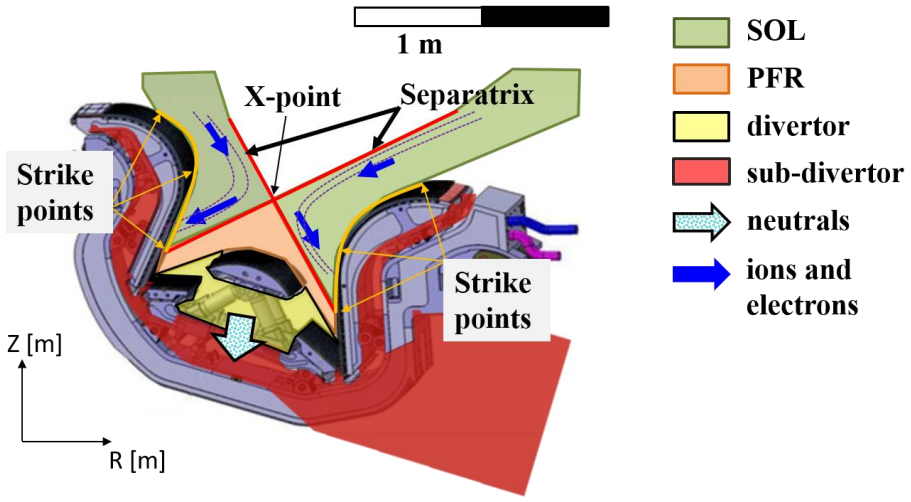

Figure 1.4 Physical domains in the divertor region. As before the SOL is depicted in green, where the plasma particles exit the core plasma and are directed to the targets. The PFR above the divertor dome is also shown (orange region) and both the divertor and the sub-divertor regions, depicted in yellow and red colors, where mainly neutral particles are found.

In current tokamaks, hydrogen isotopes and impurities injected or generated during plasma operations are primarily pumped out and trapped by a cryogenic pump, namely: JET, ASDEX-Upgrade, DIII-D, MAST and JT-60SA (upgrade of JT-60U). In the case of future fusion devices like ITER in its DT operation phase, the corresponding exhaust pumping system will comprise three stages: 1) cryopumps as primary pumps [17] [18];

2) cryogenic roughing pumps [10]; and 3) modified piston pumps [19]. For a DEMO device, alternative approaches to the particle exhaust are preferred due to the due to the limitations of the pumping technologies and substantially enlarged requirements for a DEMO device compared to ITER. Different pumping technologies are currently under discussion, making the subject an active research field, for a complete review on this topic the reader is referred to [19].

Thus, for present and furture fusion devices plasma egde conditions, divertor neutral pressure, impurity concentration, particle fuelling as well as particle removal are intrinsically related. For example, in [20] it is shown that the combination of impurity seeding and high neutral pressure reduces the power loading of the target. Recent experimental observations at JET showed a linear dependence between the sub-divertor pressure and the tokamak particle fuelling [21]. However, geometrical factors of the divertor cassette can also influence the tokamak particle balance at the divertor, especially the particle pumping. In [22] is highlighted the influence of the pumping port location and the existence of the dome on the developed flow field in a DEMO divertor cassette, where a factor of 2-3 of increase in the pumped particle between the studied pumping port locations.

1.3 Objective of work

The main focus of this dissertation is to develop a computational tool based on the Direct Simulation Monte Carlo (DSMC) method to describe the neutral particle flow in tokamak divertors.

The code is first verified against a well-established internal flow problem of a gas flow across a rectangular channel. Based on this verification, a validation process is conducted by analyzing the impact of boundary conditions, simulation parameters and uncertainties. For instance, the DSMC method accuracy depends on the number of particles, cell size and time step, which are taken as the main parameters to be studied. The DSMC modelling is compared against analytical expressions and a code-to-code comparison with an independent code [23] [24] closes the validation and verification chapter.

Once verified and validated, the DSMC tool is applied to three tokamak divertors to demonstrate its capabilities. First, for the JT-60SA divertor the analysis of a collisionless flow in the view of a code-to-code comparison in terms of local quantities is performed. Based solely on the DSMC approach, as next step the impact of the gas flow collisionality is assessed for a typical operational condition in terms of the Knudsen number and macroscopic variables.

The second application focuses on the analysis of the gas flow in the ITER divertor. Different pressure boundary conditions at the pumping port are applied. This is done in order to quantify the effect on the macroscopic field variables of the particle flow at the

divertor outlets and thus identifying the sensitivity of the assumed operation configurations.

The gas flow in ASDEX Upgrade divertor is the main subject of the third application. The essential difference with ITER is the type of boundary condition applied as pumping surface, which is based on the concept of sticking probability. Different models for describing the particle flow in the sub-divertor are employed for comparision purposes against experimental data. This allows to identify the fundamental contributions to the gas flow in terms of pump and pressure conditions at the divertor boundaries.

1.4 Structure of work

Based on the objective of the thesis, the dissertation is structured as follows:

In Chapter 1, the concept of magnetic confinement fusion is introduced. This allows the reader to focus on the physical domain of interest: the divertor structure. The most important aspects related to the neutral gas in the divertor are introduced.

Chapter 2 copes with the concepts that describe the neutral gas transport by means of the deterministic and statistical methods. By doing this, the introduction of the DSMC method can be done and the reader can put in context the DSMC method as an statistical approach. The chapter provides a summary of the current modelling of neutral gas flow in tokamak divertors.

The physical foundations as well as the numerical methodologies underlying the DSMC method are explained in Chapter 3. An overview of the DSMC algorithm is first introduced, which allows the reader to familiarize with the steps involved in the DSMC calculations. With this overview, it is possible to follow the rest of the chapter, which describes in detail the DSMC algorithm steps.

Chapter 4 introduces the general statement of the problem of the gas flow through two parallel plates. The solution of the problem is presented for different collisionality regimes in terms of the flow rates and the pressure distribution. The comparison with closed-formed expressions and external codes is presented. Additionally, the dependence of the solution with the cell size, time step and number of simulated particles is given. This explicitly shows the relation of the parameter choice and calculated macroscopic variables in DSMC.

The description of the neutral gas flows in tokamak divertors with the DSMC code is the main focus of Chapter 5. The chapter is divided in three subchapters devoted to the divertors: JT-60SA, ITER and ASDEX Upgrade (AUG), respectively. In this chapter, many aspects of the DSMC code capabilities such as the modelling of collisionless and collisional flows as well as the application of new developed boundary conditions are presented.

First, the gas flow in JT-60SA modelled with DSMC is benchmarked against a Monte Carlo code, for collisionless flow conditions. Next, the neutral-neutral intreractions are turn on in order to model the collisional flow with DSMC. In the ITER calculations, the characterization of the neutral gas flows in ITER sub-divertor in relevant operation scenarios is presented. Effects of gas recirculation and pressure rise at the pumping port on the overall behavior of the gas flow are addressed. As third application of the DSMC code, the neutral gas flow of experiments through the sub-divertor are modelled on the Divertor III in AUG. The analysis of the corresponding macroscopic quantities of the pumped working gas is performed in terms of pressure, particle fluxes and flow patterns. The results of the DSMC modelling provide further insights on the interpretation of the gas signals measured in AUG experiments.

In Chapter 6 are given the concluding remarks and summary of the work followed by the outlook for possible next steps in this field of research. The structure of the work is summarized in Figure 1.5.

Chapter 1 and chapter 2
Introduction and particle transport overview

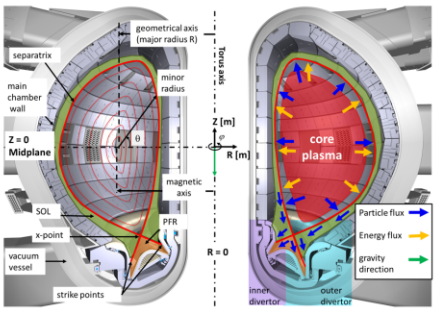

- Nuclear fusion and magnetic confinement concepts are introduced.
- The need of a description of neutral gas flows is posed and the introduction of the Kn number is presented.
- Particle transport description: deterministic and stochastic methods are described.

Chapter 3
DSMC modelling

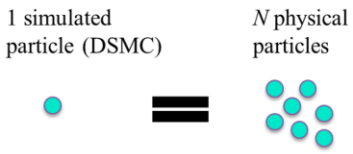

- The 4-step DSMC algorithm is described in terms of the collision models, interactions between particle-surface as well as the definition of the time step and computational domain.
- The most relevant physical aspects of the DSMC method are described.

Chapter 4
Verification and benchmark

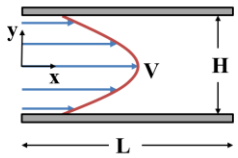

- Functionality of code in well-established internal flow problem for low- and intermediate collisionality
- Sensitivity of parameters on the flow fields in terms of
  - time step
  - mesh size
  - number of simulated particles

Chapter 5
Application of the DSMC method to neutral gas flows in tokamak divertors

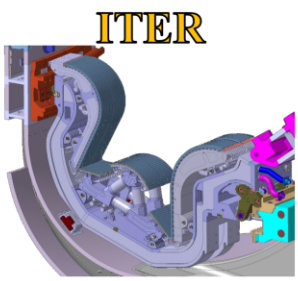

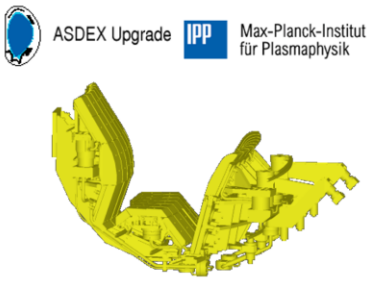

- Code-code comparison with Monte Carlo codes.
- Demonstration of DSMC capabilities to describe collisionless and collisional flows.
- Effect of the pressure boundaries on the neutral gas flow.
- Extension of code features to describe the particle pumping.

Figure 1.5 Structure of present work.

2 Neutral particle transport in divertor tokamaks

The purpose of this chapter is to cover the neutral particle transport ideas and concepts which the author has found useful in dealing with gas dynamics in the sub-divertor of a tokamak. First, the concept of rarefied gases, the degree of rarefaction of a gas flow via the Knudsen number and the classification of the flow regimes are introduced. This leads to a natural introduction of the particle-based modelling, where both deterministic and stochastic models are presented. The chapter ends with the description of the proposed approach which combines a particle-based method with input of a plasma solver or experimental data of a tokamak device.

2.1 Knudsen number and flow regimes

In dealing with the physics of gas modelling, one is faced with the situation to choose between the continuum model and the molecular-based description. In the former, the macroscopic variables are the dependent variables whereas the spatial coordinates and time are the independent ones. The molecular models on the other hand consider the fluid as a set of discrete particles, which can be molecules, atoms and electrons. To decide which approach suits better to a particular problem, depends on the local fluid properties, fluid microscopic structure and thermodynamic equilibrium.

One way to introduce the degree of rarefaction (flow regimes) is to define the Knudsen number (Kn), which relates the traveled distance by the particles between collisions, i.e. the mean free path λ, to the characteristic length scale of the physical system (L) which reads to

$$Kn = \frac{\lambda}{L}. \tag{2.1}$$

Equation (2.1) serves as a criterion to characterize the flow regime which is beneficial in the case of simple geometries, e.g. pipes, slits, orifices, capillaries or channels, since only the mean free path, the inner diameter of pipe or the distance between channels are required as input.

A more general criterion that indicates the degree of rarefaction can be defined in terms of local flow properties. The criterion is quantified by the mean free path λ and a length scale based on the local variation of a macroscopic parameter $\hat{\varphi}$, such as density or temperature. Thus, a measure of distance L can be written as

$$L = \frac{\hat{\varphi}}{|\nabla \hat{\varphi}|}. \tag{2.2}$$

In this way, a local Knudsen number Kn_{loc} can be defined as follows

$$Kn_{\mathrm{loc}} = \frac{\lambda}{\hat{\varphi}/|\nabla \hat{\varphi}|}. \tag{2.3}$$

If not otherwise stated, in this work the relations (2.1) and (2.3) are employed in the characterization of the flow regime. The flow regimes can also be defined by the dimensionless rarefaction parameter δ describing the degree of gas rarefaction as the reciprocal of the Knudsen number

$$\delta \sim \frac{1}{Kn}. \tag{2.4}$$

Depending on the range in which the value of δ lies, one may have free molecular ($\delta \to 0$), transitional ($\delta \sim 1$) and continuum ($\delta \gg 1$) regime.

Thus, one can describe the flow regime either by means of the Knudsen number or by the rarefaction parameter. In Figure 2.1 the flow regimes together with their corresponding physical model and local Knudsen number are shown:

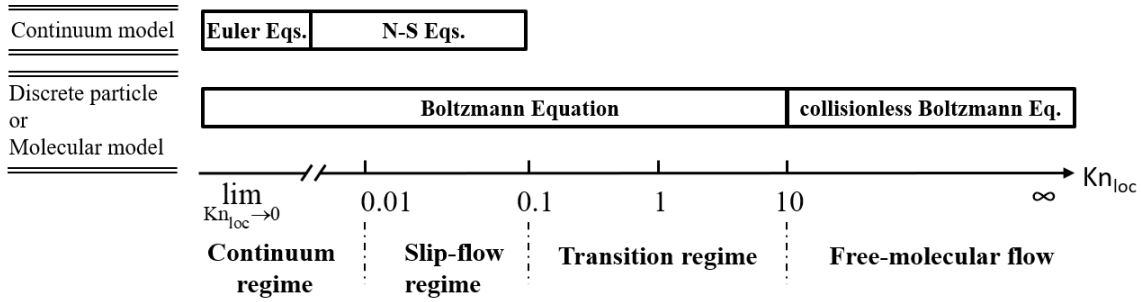

Figure 2.1 Knudsen number and the flow regimes. The continuum and particle model describe the flow in different flow regimes. Adapted from [25].

According to [25] pp. 3 and [26], the flow regimes are classified as:

Continuum regime ($0 \leq Kn < 0.001$). Euler equations, which describe how the flow velocity **u**, pressure p and density ρ of a moving fluid relate to each other. These equations are derived from a more general relations, the Navier-Stokes (N-S) equations. The Euler equations are defined in the limit of the *zero Knudsen* number.

Continuum slip- flow regime ($0.001 \leq Kn < 0.1$). Here the N-S equations with slip boundary conditions govern the flow. In a layer of the order of a mean free path, also known as a Knudsen layer, viscous effects are dominant between the bulk fluid and the wall surface. Here, the no-slip boundary conditions (BCs) in the N-S equations seemed to fail, making

the N-S approach not suitable anymore and the introduction of a slip length or setting the velocity at the wall is necessary.

Transition regime ($0.1 \leq Kn < 10$). Rarefactions effects become more important as the Knudsen number increases and the relationships that define the stress tensor and the heat flux vector break down [27]. Higher-order corrections in these relations results in the Burnett or Woods equations [28]. The Boltzmann equation can be utilized at the microscopic level in order to describe the flow and via the Chapman-Enskog expansion, the Burnett equations can be also derived. However, in cases of practical interest the Boltzmann equation cannot be solved easily unless the so-called nonlinear collision integral is simplified. This gives us the chance to introduce alternative methods of solution, which will be covered in the next section.

Free-molecular regime ($Kn \geq 10$). Typically for high-Knudsen numbers $\lambda/L \gg 1$, the probability of interaction between particles and physical walls, for internal flows, is greater than the corresponding interaction between particles. Collisionless flows are associated with high values of the mean free path, which are encountered at very low densities, such as the phenomena occurring in high-altitude aerodynamics, or small characteristic dimensions. The flow in this regime can be described by the collisionless Boltzmann equation (collision operator is zero).

2.2 Current state of research of particle-based modelling of neutral gas flows

In contrast to the continuum modelling of a fluid, embodied in the analytical or numerical solution of the hydrodynamic equations, the particle-based approaches compute the trajectories and velocities of the particles that model the atoms (or molecules) of the fluid or gas. Typically, in a particle-based approach the description can be grouped in two types of methods: deterministic and statistical. Specific properties of both methods are here highlighted and no attempt is made to have a rigoruous mathematical proof of every single concept of each method. However, the text should permit the reader to easily identify the key concepts in order to find additional information in theory textbooks if required.

Deterministic methods: Molecular Dynamics (MD) [29][30][31], which belongs to the set of deterministic approaches, is a very popular numerical approach for molecular simulations to study fluids. First, a set of N particles (atoms/molecules) located in a region of space are assigned with a random velocity corresponding to a Boltzmann distribution at the temperature of interest. The particles are allowed to interact in a pairwise sense in terms of a two-body potential and the time evolution of the particle positions is determined by integrating Newton's equation of motion. To pick an appropriate potential and to validate the simulation results with experiments or with available analytical/computational results is part of the art of the MD approach. Typically, the potential between two particles is the generalized Lennard–Jones potential, where an attractive and a repulsive term constitute the interaction between particles separated by a distance r.

The Lattice Boltzmann methods (LBM) are also used regularly in the simulation of fluids. In LBM a fluid is assumed to be composed of virtual fluid particles, which move and collide with other fluid particles in a simulation region conserving mass and momentum. A simulation area is regarded as a lattice system, and fluid particles move from site to site; that is, they do not move freely in a region. The most significant difference of this method in relation to the MD method is that the lattice Boltzmann method treats the particle distribution function of velocities rather than the positions and the velocities of the fluid particles.

The most serious limitation of molecular dynamics simulations is the number of molecules N that can realistically be modelled. Because the computation of an element of trajectory for any particular molecule requires consideration of all other molecules as potential collision partners, the number of operations required by the MD method is proportional to N^2. By imposing a cut-off in the potential, i.e. the potential has a finite radius of influence, only the nearest-neighbor particles are treated as potential collision partners reducing the amount of operations to $O(N)$ or even $O(N \ln N)$.

An alternative to the MD and LBM models is to compute the probability of finding a molecule at a particular position and state by solving the kinetic equation. Relevant quantities such as the particle number, momentum or energy of the molecules within an element of volume can be computed from the probability distribution f. Ludwig Boltzmann [32] deduced the kinetic equation, which determines the evolution of the distribution function f at any point in phase-space and in time, it reads to:

$$\frac{\partial f_\alpha}{\partial t} + \mathbf{v}\cdot\nabla f_\alpha + \left(\frac{1}{m_\alpha}\sum \mathbf{F}\right)\cdot\nabla_{\mathbf{v}} f_\alpha = \left(\frac{\partial f_\alpha}{\partial t}\right)_{coll} \tag{2.5}$$

$$= \iiint_{v_i'}\iiint_{v'}\iiint_{v_i}\left[f_\alpha' f_i' - f_\alpha f_i\right]\times \left|\mathbf{v}_{rel}\right|\sigma'\left(\mathbf{v},\mathbf{v}_i \to \mathbf{v}', \mathbf{v}_i'\right) d^3v_i d^3v' d^3v_i'.$$

The equation describes the evolution over time of the distribution function f of a particle of type α with mass m_α and velocity $\mathbf{v}$ subjected to external forces $\mathbf{F}$. The following notation is also employed for the spatial derivative $\nabla = (\partial/\partial x, \partial/\partial y, \partial/\partial z)$, which acts in real space (x, y, z), whereas the velocity derivate $\nabla_{\mathbf{v}} = \left(\partial/\partial \mathbf{v}_x, \partial/\partial \mathbf{v}_y, \partial/\partial \mathbf{v}_z\right)$ operates in velocity space $(\mathrm{v}_x, \mathrm{v}_y, \mathrm{v}_z)$. The collisions with other particles of type i are included in the collisional operator (right-hand side of Eq. (2.5)). The variables without tilde are pre-collision quantites, whereas the variables with tilde are post-collision quantities and the sub-index i describes a quantity of a particle of type i. Also important is the term σ' which describes the probability for a collision to occur between particles of type α and i. In the absence of collisions, the term at the right-hand side of Eq. (2.5) is zero.

All the information of the physical state of a single particle is described by the distribution function. For example, the number of particles of type α at $\mathbf{r} + d\mathbf{r}$ with velocities $\mathbf{v} + d\mathbf{v}$ in a particular time t is given by:

$$f_\alpha(\mathbf{r},\mathbf{v},t)\,d^3r d^3v = \text{number of particles in } d^3r d^3v \text{ at time } t \tag{2.6}$$

On the other hand, integration of the distribution function f over the velocity variable leads to:

$$n_\alpha(\mathbf{r},t) \equiv \iiint_v f_\alpha(\mathbf{r},\mathbf{v},t)\,d^3v, \tag{2.7}$$

which is the number of particles of type α per unit volume (particle or number density). Moreover, the mean velocity $\mathbf{V}$ of a particle at position $\mathbf{r}$ and time t is calculated as:

$$\mathbf{V}(\mathbf{r},t) \equiv \langle \mathbf{v}(\mathbf{r},t) \rangle = \frac{1}{n_\alpha(\mathbf{r},t)} \iiint_v \mathbf{v}\, f_\alpha(\mathbf{r},\mathbf{v},t)\,d^3v, \tag{2.8}$$

which is just the macroscopic velocity of the fluid, described by the equations of hydrodynamics. For a gas in equilibrium, the distribution function has the following form:

$$f_{eq}(v) = 4\pi \left(\frac{m}{2\pi k_B T} \right)^{3/2} v^2 e^{-mv^2/2k_B T}. \tag{2.9}$$

The above expression is called the Maxwell-Boltzmann distribution function. This distribution allows us to calculate three relevant quantities in a gas in equilibrium conditions:

1. Average speed

$$\langle v \rangle = \frac{\int_0^\infty v f_{eq}(v) dv}{\int_0^\infty f_{eq}(v) dv} = \sqrt{\frac{8k_B T}{\pi m}}. \tag{2.10}$$

2. Most probable speed (where the maximum value of the Maxwell-Boltzmann distribution is found)

$$\frac{d}{dv} f_{eq}(v) = 0 \tag{2.11}$$

$$\Rightarrow v_{mp} = \sqrt{\frac{2k_B T}{m}}.$$

3. Root-mean square speed or rms speed

$$v_{rms} = \sqrt{\langle v^2 \rangle} = \sqrt{\frac{\int_0^\infty v^2 f_{eq}(v) dv}{\int_0^\infty f_{eq}(v) dv}} = \sqrt{\frac{3k_B T}{m}} \,. \tag{2.12}$$

In all the expressions above, m is the particle's mass, T its temperature and k_B the Boltzmann constant.

The major concern when solving the Boltzmann equation is the treatment of the nonlinear collision term in Eq. (2.5). However, some approximations are possible in order to linearize this term. In the following, it is assumed that a function f_0 exists and satisfies the Boltzmann equation (2.5) in both equilibrium and steady state.

Let f_0 be a known equilibrium distribution of our system, the solution f can be expressed as f_0 and small perturbation δf:

$$f = f_0 (1 + \delta f), \tag{2.13}$$

If the perturbation δf is small enough, the term $O(\delta f^2)$ can be neglected and the equation is linear with respect to the new unknown δf. By far one of the most used approaches to numerically solve the Boltzmann equation is to replace the collision operator by a much simpler function

$$\left(\frac{\partial f}{\partial t} \right)_{\text{coll}} = \frac{f_0(\mathbf{v}) - f(\mathbf{v})}{\tau_{rel}}, \tag{2.14}$$

as before f_0 is the equilibrium solution of the Boltzmann equation, Eq. (2.5), and τ_{rel} is the relaxation time which is inverse proportional to the density and governs the rate of change of $f(\mathbf{v})$. Introducing Eq. (2.14) into the right-hand side of Eq. (2.5), the resultant equation is referred as the BGK equation, named after those who first proposed it, Bhatnager, Gross and Krook [33].

The introduction of the BGK operator notably reduces the original complexity of the Boltzmann equation, however the equation to be solved is still a non-linear integro-differential equation. Typically, a numerical solution of the BGK equation makes life easier, making the problem more tractable than a similar assault on the Boltzmann equation, due to the absence of the exuberant number of integrals. From its definition in Eq. (2.14), one can see that the BGK approximation possesses only a single parameter, namely the relaxation time (or its reciprocal: collision frequency).

This parameter can be tweaked to provide the correct gas viscosity, μ, or the correct thermal conductivity, κ, but both cannot be correct simultaneously. Hadjiconstantinou [34] highlighted this issue by noting that a direct analysis of the BGK equation provides a Prandtl number

$$\mathrm{Pr} = \frac{C_p \mu}{\kappa}, \tag{2.15}$$

equal to 1 for a monatomic gas, rather than the correct value of Pr = 2/3. In the above equation, C_p is the specific heat at constant pressure, μ is the viscosity and κ the thermal conductivity of the gas. A generalization of the BGK model, known as the *Ellipsoid Statistical* (ES) *Model* [35] overcomes some of the issues of the BGK approximation by introducing a rather complex expression of the local velocity distribution function $f(\mathbf{v})$. However, in the process some of the properties which make the BGK approximation useful, namely its simplicity, are lost. Thus, essentially, by correctly recovering the Pr number, the collision frequency (through viscosity and conductivity) of the process is properly modelled.

An application of the BGK approach in tokamak divertors has been done with the EIRENE [36] code. EIRENE is a 3D Monte Carlo code simultaneously solving a system of time dependent or stationary linear kinetic transport equations. EIRENE has been coupled to SOL fluid plasma equations (B2 code [37]), resulting in a coupled code named B2-EIRENE, which has been employed for the description of considerable number of fusion experiments, see [38] and the references therein. The main drawback of EIRENE is that the Pr number is not recovered for monoatomic gases, resulting in inexact collision frequency based upon the viscosity of the gas.

The SOLPS code (versions 4.x), based on B2-EIRENE, has been chosen to be the main tool to describe the ITER divertor modelling [39]–[42], [43]. As described in [43], major efforts have been made in order to include *non-linear* neutral models (e.g. elliptic BGK model) for ITER calculations. However, this upgrade is not always available for older versions of B2-EIRENE, thus adding an interrogative whether the non-linear treatment of neutrals influences previous calculations that served as comparison with experimental data. Nevertheless, despite the non-linear treatment of neutrals in the *old* or *new* EIRENE codes, the fact that it includes a vast physics makes EIRENE a very valuable approach to describe neutrals in fusion devices.

Semi-empirical deterministic approaches have been also developed for the description of neutral flows and conductance studies in vacuum and divertor systems in tokamaks. ITERVAC, developed at Karlsruhe Institute of Technology, models complex vacuum systems as a network of channels with a predefined constant shape and length. The network construction fulfills the conservation of mass and the gas flow properties are based on known expressions and correlations of ducts and pipes with different cross-sections. Main parameters for the simulations are gas type, temperature, inlet and pump pressures and pumping speeds of the pumps. To simulate the vacuum system of a tokamak, ITERVAC needs a background plasma (gas sources), previously calculated by SOL plasma fluid codes like SOLPS. In [44] the ITER torus vacuum system is analyzed and identification of pumping optimization addressed. The standard three-dimensional nature

of ITERVAC allows the study of divertor gaps affecting the divertor operation and pumping scenarios [45]. Despite ITERVAC versatility of 3D and 2D calculations, the main concern is the geometry approximation used in describing the divertor flows and the validity of the employed expressions of the particle flow. This poses the problem of selecting the proper channel geometry, which represents the complex geometries such as a divertor or sub-divertor of a tokamak and thus affecting the resulting gas flow through the system.

Statistical methods: As an alternative to the aforementioned models that numerically solve the Boltzmann equation, numerical schemes based on Monte Carlo methods offer a powerful and robust techniques for solving rarefied gas flows.

The MC technique is based on sequences of random numbers to obtain sample variables of the macroscopic properties of the problem. This technique is widely used in in particle transport applications, such as neutron and radiation physics. In collisionless gas flows in the free-molecular flow regime, the Test Particle Monte Carlo (TPMC) approach includes such MC techniques. In the TPMC mehod, the particles are defined by its position $\mathbf{r}$, its direction of travel Ω, and its energy E at time t. The domain of interest is divided into a grid, where the particles inside the system can move in straight lines. During the complete simulation, the particles inside the system are tracked and their interactions with the solid surfaces applied, such as reflection and absorption. As a particle moves along its trajectory, several results (called tallies) are updated so that, after many histories, some desired property of the flow field can be estimated.

Developed by JAEA (Japan Atomic Energy Agency), NEUT2D is a TPMC code for neutral particles [46]. In NEUT2D, the particles in the system only interact with the surfaces of the main chamber, divertor and sub-divertor structures. In the past, characterization of divertor particle pumping has been simulated for experimental conditions in JT-60U tokamak [47], where potential design parameters optimization, such as pumping speed under gas saturated wall conditions, is addressed as an outcome of the numerical study. However, since the neutral–neutral collisions are not included in NEUT2D, the effects of collisionality in the divertor due to neutrals remains unanswered.

The DEGAS2 is also a 3D Monte-Carlo neutral transport code [48] based on the TPMC method. Transient calculations can be run being aware that the minimum time step should depend by a typical transit time for a neutral particle across a so called "zone". In [49] a “zone” might be used to represent the vacuum region around the plasma which is comprised of several (possibly disconnected) polygons. Or, a plasma flux surface on which density and temperature are constant might be a single zone. Benchmark studies between EIRENE and DEGAS2 have been performed with identical input yielding different outcomes, mainly due to the different primary source terms that are employed in the transport equation [36]. However, the main drawback of this approach is that in high-

collisional and transitional flows, the TPMC is not appropriate to describe such flow conditions.

The DSMC method, developed between 1960 and 1980 mainly by G.A. Bird [25], has become one of the most effective numerical techniques to tackle gas flows in rarefied conditions. Particularly, the DSMC method has been preferred by the gas dynamics community as the numerical approach to study gas flows in the transition regime. DSMC remains valid, though extremely expensive to use, for much lower values of *Kn*. In the DSMC method, each model particle represents an effective number of real atoms (and/or molecules) in the physical system. The model particles are sorted into cells and the particles' time evolution is done in time steps of duration Δt in which their free motion and collisions between them are uncoupled, see Figure 2.2.

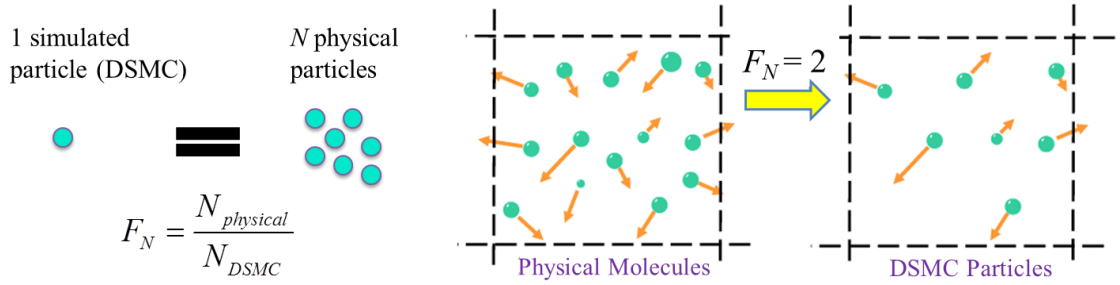

Figure 2.2 The concept of DSMC particles: each simulated particle in a DSMC simulation represents a finite number of physical particles of the gas. In the figure of the right side is depicted the case when 14 physical particles are simulated with 7 DSMC particles, i.e. $F_N = 2$.

However, the DSMC method does not deal with the analytical or numerical solution of the Boltzmann equation directly. Instead, the DSMC approach treats the movement of individual particles in a similar fashion as the MD calculations. The DSMC generates collisions stochastically with scattering rates and post-collision velocity distributions determined from the kinetic theory of dilute gases, which contrasts the MD calculations where the collisions are exactly calculated.

The versatility of the DSMC method for defining different collisions models, particle-wall interactions as well as its applicability in all flow regimes, have made the DSMC method the selected approach to analyze the gas flows during the dissertation. On the other hand, the simplicity of the DSMC algorithm allows for straightforward incorporation of additional physical models and for its application to complex geometries such as the tokamak divertors. For the conditions of interest in this dissertation, the current DSMC code is not able to describe particle pumping at surfaces and therefore, a boundary condition has been specially developed and added to the DSMC code library.

2.3 Neutral gas flow modelling with a background plasma and experimental data as inputs

By applying the DSMC approach to a background plasma calculation at defined interfaces between the divertor and sub-divertor domains, the neutral gas flow in the divertor is modelled in this dissertation, see Figure 2.3. The approach allows to simulate the gas flow which corresponds to relevant operational scenarios using the reference divertor geometry of a tokamak device.

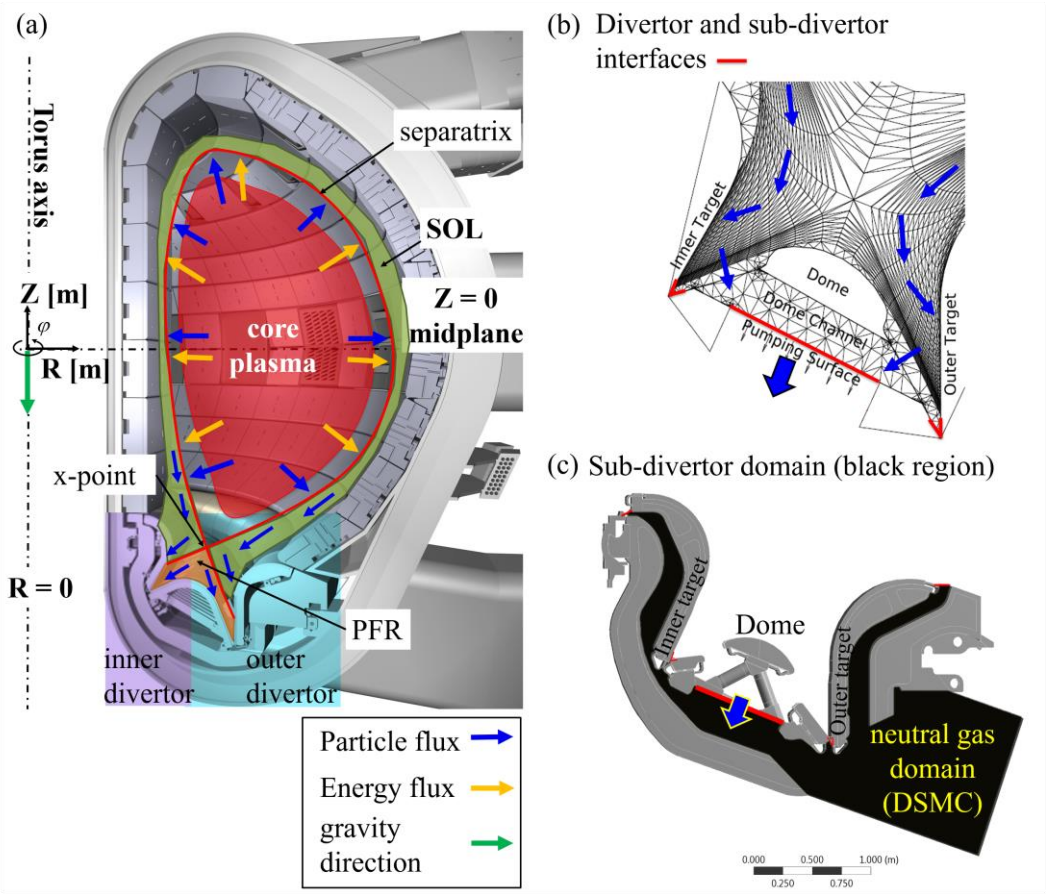

Figure 2.3 (a) Cross-section of a tokamak showing the plasma core, separatrix and SOL. (b) Grid of the background plasma calculation: the plasma code, e.g. SOLPS, calculates the particle and energy fluxes at the plasma edge including at the divertor region (surfaces and below the dome). The resulting macroscopic variables of the neutrals are applied as BCs for DSMC solver at the interfaces between the divertor and sub-divertor (red lines). (c) The neutral gas flow domain of the DSMC solver is shown (black region).

Typically, two grids are employed in plasma edge analysis, namely: the grid for the plasma edge and a second grid for the neutrals. The latter surrounds the plasma up to the main chamber wall as shown in Figure 2.3(b). Therefore, overlapping grids are necessary in order to transfer information between the edge of SOL/PFR and the following regions: the vacuum, main chamber wall, divertor structures as well as apertures (e.g. transparencies and reflectors introduced in chapter 1).

Strategy to describe the neutral gas flow in sub-divertors with DSMC

First, based on the plasma solution at each computational cell of the SOL and PFR the physical state of the plasma particles, i.e. position, velocity, temperature and pressure, is transferred to the grid of neutral domain in order to calculate the macroscopic states of the neutrals. In a second step, the neutral sources for the plasma edge flows are updated and transferred back to the plasma (fluid) grid. An iterative process between the plasma (fluid equations) and the kinetic approaches is usually performed in order to obtain a final global solution. Once obtained the macroscopic state of the neutrals at the divertor region with the background plasma, the analysis with the DSMC solver can be started since all the information at the inlets and outlets are known at this point, see Figure 2.3(c). At the end of the next chapter, a detailed description of additional parameters needed for the neutral gas flow simulation with a DSMC solver is introduced.

In addition to the proposed use of a background plasma or neutral calculation as input of the DSMC solver, in this dissertation experimental data is also employed as inlet boundary conditions to the divertor gas modelling at the corresponding interface surface. By doing this, the same input between modelling and experiment is set, which together with information of the experimental setup or plasma discharge, the DSMC approach can provide further insights in the interpretation of the experimental measurements.

While many challenges in the field of neutral gas flow modelling have already been addressed regarding both plasma-neutral and particle-surface interactions with traditional plasma codes, some important questions remain unanswered. The systematic study of collisionality in the tokamak divertor for a given plasma scenario needs to be evaluated in order to provide insight of the influence of neutral-neutral collisions in the divertor flows. This open question is addressed in this dissertation by means of the modular capabilities of the DSMC code by switching *on* and *off* the collision kernel of the DSMC algorithm. A second aspect treated in this work is to improve the understanding in the governing dynamics in the divertor gas flow in order to aid the interpretation of current experiments in tokamaks. By focusing in the aforementioned it is possible to address the level of neutral gas flow modelling sophistication for present and future fusion devices.

3 The DSMC modelling

3.1 Overview of the DSMC method

The DSMC method is based on the physical concept of rarefied gases and on the physical assumptions that form the basis for the derivation of the Boltzmann equation, i.e. molecular chaos and restrictions related to dilute gases. The former dictates that the collision operator can be written solely in terms of a one-particle distribution function whereas in the latter the mean molecular diameter is much smaller than the mean molecular space in the gas.

Before starting the description of the DSMC algorithm, let us recall that the idea of the DSMC method is to model the movement and collisions of a group of particles. In the DSMC method each simulated particle represents a group of physical particles. Denoted by F_N, the conversion factor is defined as the physical-to-simulated-particle ratio $F_N = N_{physical}/N_{DSMC}$. With $F_N = 1$, a simulated particle represents a single physical particle and thus the assumption of the MD approach is recovered (in the sense that single particles are simulated).

As in most numerical models, in DSMC a physical domain of interest needs to be defined first. Then, a computational grid representing the physical space is generated for the method to be executed. The selection of the cell size involves certain requirements derived from physical quantities of the problem under consideration. The properties of the cell size are described in sub-chapter Chapter 3.2. The cells of the grid are used as a control volume in order to sample the macroscopic states of the gas flow.

At time $t = 0$ in a DSMC simulation the computational grid is filled with N simulated particles, randomly distributed with uniform density throughout the domain. Thereafter, the DSMC algorithm can be regarded as a 4-step process. At each time step Δt: first, the particles in the domain are moved ballistically from their initial position $\mathbf{r}_o$ with their assigned velocity $\mathbf{v}$ according to the equation

$$\mathbf{r} = \mathbf{r}_o + \mathbf{v}\Delta t \,. \tag{3.1}$$

Thus, the particles follow straight line trajectories as if they do not interact with each other. This step is here referred as the free-flight step.

Secondly, the boundary conditions are executed once the particles are moved, namely: the particle inflow at open boundaries and the particle-wall interactions are performed. As the third step, the calculation of the intermolecular collisions takes place in a cell-wise strategy: collisions are performed among particles sorted in the same cell. Finally, in the fourth step, the macroscopic variables of interest, such as velocity of the flow, temperature and pressure are sampled in the computational domain. Here, a DSMC

algorithm based on a 4-step process is described for clarity purposes, however, in the literature the *boundary-condition-* and the *macroscopic-variable-sampling*-steps are often omitted when describing the DSMC algorithm. This is done in order to stress that in the DSMC method the particle movement (advection or free-stream stage) and collisions are decoupled.

In summary, the 4-step process in the DSMC method reads to:

1. Movement of the DSMC particles via the equation of motion $\mathbf{r} = \mathbf{r}_o + \mathbf{v}\,\Delta t$.

2. Application of boundary conditions such as inserting particles at inlets or deleting them at outlets is performed. In this step also the interaction between particles with wall boundaries is executed.

3. Once the particles are *moved*, the particles are sorted in the computational grid and the collision step between DSMC particles is performed. A criterion is defined for a collision to take place between two DSMC particles.

4. In this step the macroscopic variables as pressure, temperature and bulk velocity are calculated. Then, the DSMC algorithm repeats from the step number one.

The overview of the DSMC algorithm is illustrated in Figure 3.1. Three key parameters define the DSMC simulation, the time step, the number of particles in the system and the cell size. The time parameter Δt in a DSMC simulation is identical with the physical time of the real flow. Therefore, the decoupling between the free-flight step and the collision process is assured if the chosen time step Δt is small compared to the average time between collisions, or local mean collision time τ_{coll} [25] [50]. The physical reason behind this constraint is that if $\Delta t > \tau_{coll}$ is selected, more than one collision can occur during a time step and thus the decoupling assumption breaks.

Additional to the selection of the time step, the number of simulated particles *N* and the cell size Δx of the employed grid also affect the simulation of the neutral gas flow. Details on the selection criterion of these three parameters will be specially discussed in the following sub-chapter. By *convergence* of the DSMC method one needs to differentiate from the same term used in the context of the discretization of differential equations (such as the hydrodynamic ones), where the so-called *Courant stability criterion* imposes strong restrictions on the time step: Δt should be less than a relevant time scale of the process to be simulated [51]. In this sense, any DSMC simulation will always converge or in other words, it will not *crash* due to Δt-dependent numerical instabilities.

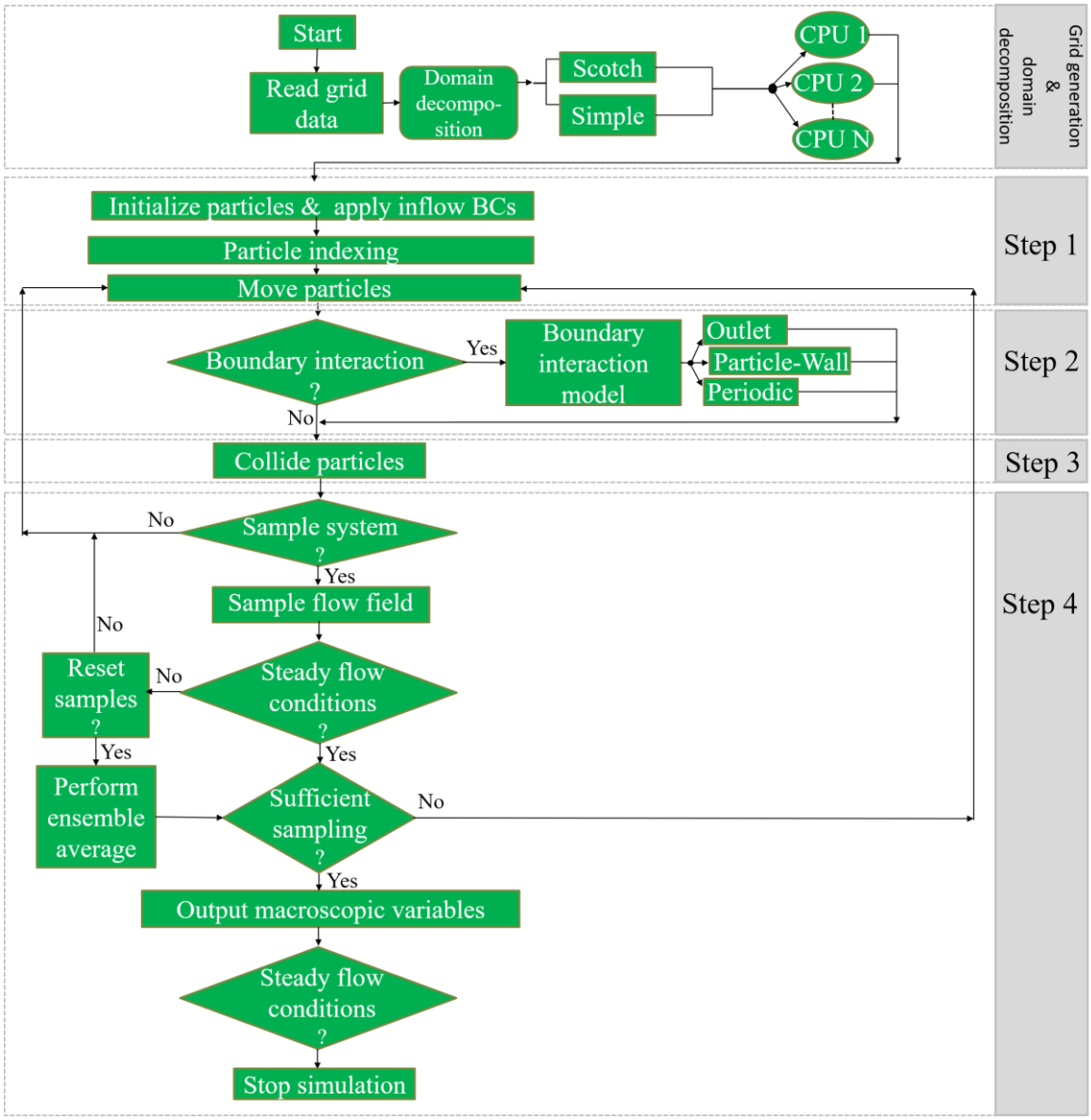

Figure 3.1 A general DSMC method flow chart.

3.2 Neutral particle collision dynamics

For the collisions to take place, a computational grid representing the physical domain is used as reference for the collision and sampling process in DSMC. The cell size Δx should be smaller than the mean free path λ [25]. Thus, in DSMC simulations it is required that

$$\Delta x < \lambda . \tag{3.2}$$

Situations where the criterion has not been fulfilled [52] have led to the appearance of unphysical behavior of the flow as pointed out in [53]. More recently, studies [54] of the dependency of transport coefficients, such as viscosity or thermal conductivity, on the

cell size have confirmed the empirical findings and it has been addressed that significant errors occurred when the criterion is violated. This suggests that an *a priori* analysis of the flow is required in order to define an optimum cell size if the flow gradients and the mean free path are not well known. If there is available experimental data, it is possible to estimate the change on λ in the domain of interest by means of pressure and temperature values, since for the majority of the collision models employed in DSMC the mean free path is a function of the temperature and pressure $\lambda = \lambda(T, p)$.

The appropriate time step is deduced from the above relation Eq. (3.2). Dividing both side of this equation by the most probable thermal speed $\mathrm{v}_{mp} = \sqrt{2k_B T/m}$, introduced in chapter 2, it is obtained:

$$\begin{aligned} &\frac{\Delta x}{\mathrm{v}_{mp}} < \frac{\lambda}{\mathrm{v}_{mp}} \\ &\Rightarrow \Delta t < \tau_{coll}\ , \end{aligned} \tag{3.3}$$

where τ_{coll} and λ are the mean collision time and mean free path introduced in previous chapter. Here k_B is the Boltzmann constant, T is the temperature and m is the particle's mass. The condition (3.3) means that the simulation time step is selected such that only a single collision between a particle A with some particle B inside the cell of size Δx within a time step is possible. With the simulation time step chosen, the first step of the DSMC that involves the solution of the linear equation (3.1) can be performed. Additionally, once the cell size is fixed, it can happen that during the complete time step Δt, a DSMC particle might not leave the cell, called here *residence time* in a cell (time required to travel the whole cell). Therefore, the residence time can also be treated as an additional parameter. Then, by selecting a time step that satisfies: $\Delta t < min\{\Delta t_\tau, \Delta t_{res}\}$, both criteria are met.

The molecular interactions are typically based on the type of forces $\mathbf{F}(r) = -dU/dr$ between particles populating the system, in which $U(r)$ is their corresponding potential. In DSMC short-ranged, repulsive potentials are implicitly employed, where the potential U is a function of r only, i.e. it is restricted to the use of conservative central forces. This type of force can be exemplified with the inverse power law model according to:

$$\mathbf{F}(r) = \frac{\alpha}{r^{\eta}} \hat{\mathbf{e}}_r\,, \tag{3.4}$$

where r is the distance between particles, α and η are positive constants. Furthermore, the positive sign of the equation indicates that force is directed in the radial unit vector $\hat{\mathbf{e}}_r$, outwards the center of force. Classically, for impenetrable particles under the action of a central potential, the differential collision cross-section σ is determined by the distance of the closest approach, or impact parameter, $b(\chi)$ and the projection of the differential area of the ring $bdbd\varepsilon$ along the solid angle $d\Omega$ after collision, as shown in Figure 3.2(a)

and (b). Thus, the total collision cross-section σ_{tot} can be obtained from the differential one if the contribution of the entire solid angle is taken into account, namely:

$$\sigma_{tot} = \iint_{d\Omega} \sigma d\Omega = 2\pi \int_{0}^{\pi} \sigma \sin(\chi)\, d\chi = 2\pi \int_{\chi=0}^{\chi=\pi} b(\chi)\, db. \tag{3.5}$$

This relation is useful only when the relation between the deflection angle χ and the impact parameter b is known, so that the terms inside the integral sign can be expressed in terms of χ. In addition to the total cross-section and relevant to the transport properties of the gas, the so-called viscosity and diffusion cross sections play an important role in the treatment of practical problems of molecular motion. Thus, by means of the Chapman Enskog theory [55] the viscosity cross-section reads to:

$$\sigma_{\mu} = \iint_{d\Omega} \sin^2(\chi)\, \sigma d\Omega = 2\pi \int_{\chi=0}^{\chi=\pi} \sin^2(\chi)\, b(\chi)\, db. \tag{3.6}$$

In the framework of the Chapman-Enskog theory [27],[55] the importance of the viscosity cross-section is that it appears in the first approximation of the viscosity coefficient, which for a pure substance (single gas with molecular mass m) at a temperature T is given by:

$$\mu = \frac{(5/8)\sqrt{\pi m k_B T}}{\left[m/(4k_B T)\right]^4 \int_0^{\infty} v_r^7 \sigma_{\mu} \exp\left[-m v_r^2/(4k_B T)\right] dv_r}. \tag{3.7}$$

In equation (3.7) v_r is the magnitude of the relative velocity, sometimes also denoted as $\|\mathbf{v}_r\|$. In this equation k_B is the the Boltzmann constant as before and σ_μ the viscosity cross-section. Thus, different expressions for the coefficient of viscosity will appear since the evaluation of the Eq. (3.7) relies on the quantities inside the integral in the denominator, which in turn depends on the molecular model under consideration as presented later on this chapter.

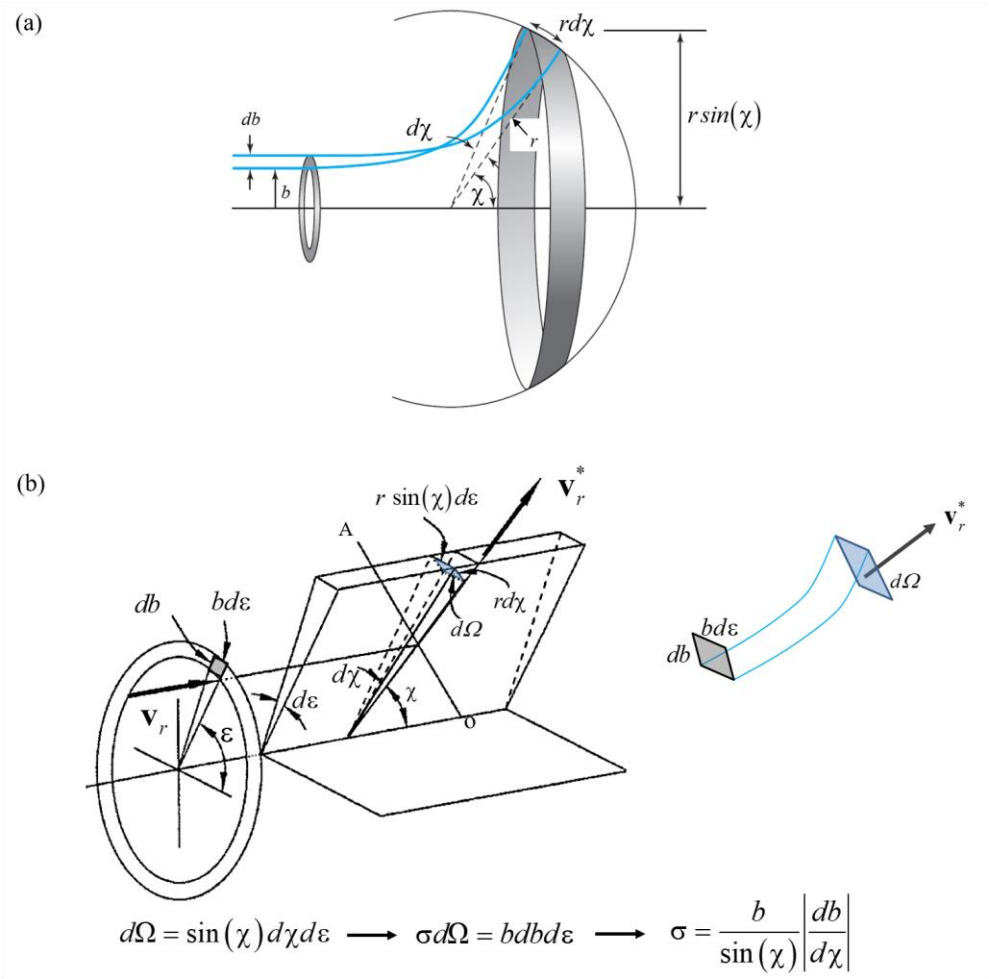

Figure 3.2 Calculation of the differential cross-section for the scattering process of particle 1 relative to particle 2 (being the center force source). (a) Impact parameter *b*, the differential *db* and the arc-length along the zenith angle χ. (b) The differential cross-section contributions in all directions. Adapted from [30], [56] and [57].

In terms of the inverse power law model of Eq. (3.4), the associated potential $U(r) = \alpha/[(\eta - 1)r^{\eta-1}]$ and by a transformation from the laboratory to the Center of Mass frame of reference, the differential cross-section can be written in terms of the relative translational energy $E_r = 1/2\, m_r v_r^2$ as [58]:

$$\sigma d\Omega = W_0 \left(\frac{1}{2} \frac{\alpha}{1/2\, m_r v_r^2} \right)^{\frac{2}{\eta-1}} dW_0 d\varepsilon , \tag{3.8}$$

where $W_0 = b\left(\frac{m_r v_r^2}{\alpha}\right)^{\frac{1}{\eta-1}}$. While the total collision cross-section reads to:

$$\sigma_{tot} = \pi W_{0,m}^2 \left(\frac{1}{2}\frac{\alpha}{1/2\, m_r v_r^2}\right)^{\frac{2}{\eta-1}}. \tag{3.9}$$

Here $W_{0,m}$, α and η are constants whereas the reduced mass of the two colliding particles is given by $m_r = m_1 m_2 / m_1 + m_2$. $W_{0,m}$ is chosen to be an arbitrary constant in order to stipulate a truncation value of χ. This assures the convergence of the differential cross-section integral of Eq. (3.8).

The **Maxwell model** is a special case of Eq. (3.4) with $\eta = 5$. One characteristic is that its collision cross-section is inversely proportional to the relative velocity, this makes the collision frequency for this model f_{coll} independent of the relative velocity since $f_{coll} \propto \sigma v_r$. For analytical studies this independence simplifies the analytical methods for the collision integrals. Nevertheless, the Maxwell model yields an unrealistic dependence of the viscosity coefficient with the temperature, where a linear behavior is found: $\mu_{\text{Maxwell}} \propto T$, leading to some limitations in practical applications.

The **Hard Sphere** (HS) **model** is one of the simplest molecular models available in DSMC. According to Eq. (3.4) the model is the limiting case for $\eta \to \infty$. Then, the model considers a particle as an impenetrable sphere of radius *r* with mass *m* and the collisions are completely elastic. Consider a binary collision as in Figure 3.3, where particle 1 traveling from the left hits particle 2 (regarded as fixed). The deflection angle χ of the relative velocity is given by $\chi = \pi - 2\theta_A$. In the HS model the collision cross section does not depend on the relative velocity since as seen in Figure 3.3, the deflection angle is given by:

$$\cos\left(\frac{\chi}{2}\right) = \frac{b}{r_1 + r_2}, \tag{3.10}$$

with a differential and total cross section given by,

$$\sigma^{HS} = \frac{d^2}{4}, \tag{3.11}$$

and,

$$\sigma_{tot}^{HS} = \pi d^2 . \tag{3.12}$$

In the last two equations it is assumed that identical particles are involved in the collision, i.e. $m = m_1 = m_2$ and $d = 2r = r_1 + r_2$. By introducing Eq. (3.12) into the first equality of the viscosity cross-section of Eq. (3.6), the following is obtained

$$\sigma_\mu = \frac{2}{3}\sigma_{tot}^{HS} . \tag{3.13}$$

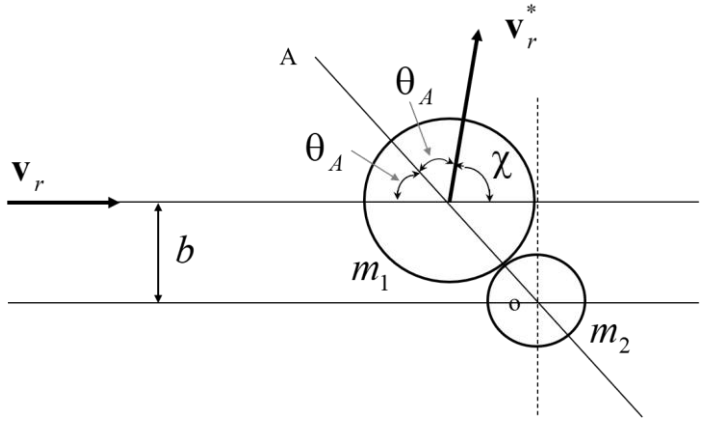

Figure 3.3 Scattering process between two particles with mass m_1 and m_2. The particle 2 is considered as fixed and thus the particle 1 moves towards 2.

The above result is also achieved if Eq. (3.10) is used in the second equality of Eq. (3.6) or by means of Eq. (3.8) by taking the limit $\eta \to \infty$ and then integrating over the solid angle. The viscosity coefficient in the HS model is obtained by introducing the above Eq. (3.13) into the first approx. of the viscosity coefficient, Eq. (3.7):

$$\mu_{\mathrm{HS}} = \frac{5}{16}\frac{\left(\pi m k_B T\right)^{1/2}}{\sigma_{tot}^{HS}} = \frac{5}{16}\left(\frac{m k_B}{\pi}\right)\frac{T^{1/2}}{d^2} . \tag{3.14}$$

In the HS model the post-collision velocities are calculated with ease, since $v_r^* = v_r$ and the scattering is independent of the angle of incidence as seen in Eq. (3.11). However, the fact that the power of ½ in T differs from the real gases, where typically a power in the range 0.73-0.77 is found (O_2, N_2, air) [25][59][58], makes the HS model in some cases not suitable to use. The reason behind the mismatch of the exponent of T of is that the total cross-section depends on the relative velocity.

In the **Variable Hard Sphere** (VHS) **model** the particles possess scattering that is angle independent as the HS model as in Eq. (3.11). However, the total cross-section is a function of the relative velocity, in a similar fashion as in the inverse power law model. The angle independent scattering is chosen since the generation of the post-collision velocities can be performed in a very simple manner and the dependence of the relative

velocity of the cross-section is chosen in order to appropriate model the viscosity coefficient.

The VHS model is constructed by the following relations:

$$\frac{\sigma_{tot}}{\sigma_{tot,Ref}} = \left(\frac{d}{d_{Ref}}\right)^2 = \left(\frac{v_r}{v_{r,Ref}}\right)^{-2\xi} = \left(\frac{E_r}{E_{r,Ref}}\right)^{-\xi}. \tag{3.15}$$

For the total cross-section, molecular diameter, relative velocity and relative translational energy a reference value is introduced. The reference values $\sigma_{tot,Ref}$ $\sigma_{tot,Ref}$ and d_{Ref} are defined in terms of $v_{r,Ref}$ in order to have an unambiguous relation between them. The inflection angle in the VHS model is the same as the HS model reading to:

$$b = d\cos\left(\frac{\chi}{2}\right), \tag{3.16}$$

assuming identical particles. By introducing $\sigma_{tot} = \sigma_{tot,Ref}\left(v_r / v_{r,Ref}\right)^{-2\xi}$ in the first approximation of the viscosity coefficient in Eq. (3.7), the VHS-viscosity can be written as:

$$\mu_{VHS} = \frac{15}{8}\frac{\sqrt{\pi m k_B}\left(4k_B/m\right)^{\xi}}{\Gamma\left(4-\xi\right)\sigma_{tot,Ref}v_{r,Ref}^{2\xi}}T^{\frac{1}{2}+\xi}. \tag{3.17}$$

Thus, if the particular power dependence of the viscosity with the temperature of the gas is known, the value of ξ can be adjusted in such a manner as to model the viscosity coefficient appropriately. In practice, it is usual to refer to the parameter ω, or viscosity index, as a function of ξ as:

$$\omega \equiv \frac{1}{2} + \xi, \tag{3.18}$$

such that one has $\mu_{VHS} \propto T^{\omega}$ and therefore, Eq. (3.17) can be the rewritten for practical applications as follows,

$$\mu_{VHS} = \left(\frac{15}{2}\frac{1}{d^2_{\mathrm{Ref}}\left(7-2\omega\right)\left(5-2\omega\right)}\sqrt{\frac{mk_BT_{\mathrm{Ref}}}{\pi}}\right)\left(\frac{T}{T_{\mathrm{Ref}}}\right)^{\omega}. \tag{3.19}$$

Finally, a list of relations between ω, ξ with the power η of the inverse power law Eq. (3.4) can be set. A comparison between the third equality in Eq. (3.15) $\sigma_{tot} \propto v_r^{-2\xi}$ and the total cross-section of the inverse power law Eq. (3.9) $\sigma_{tot} \propto v_r^{-4/\eta-1}$ leads to:

$$\xi = \frac{2}{\eta - 1}. \tag{3.20}$$

Adding ½ in both sides in the above relation and using Eq. (3.18), it can be seen that

$$\omega = \frac{1}{2}\frac{\eta + 3}{\eta - 1}. \tag{3.21}$$

With the above definitions, the previously discussed models can be recovered:

i. The Maxwell model requires $\eta = 5$, giving the values of $\omega = 1$ and $\xi = 1/2$.
ii. The Hard Sphere (HS) model is obtained in the limit $\eta \to \infty$, which yields $\omega = 1/2$ and $\xi = 0$.
iii. Some common exponents in the VHS model can be found in Bird's book [59] which span the range of $[\omega_1,\ \omega_2] = [0.6, 0.9]$. The corresponding range of ξ and η reads $0.1 \leq \xi \leq 0.4$ and $6 \leq \eta \leq 21$.

The assumptions of the above models allow us to naturally introduce the way collisions are implemented in DSMC. As shown in Figure 3.4, after all particles in the computational domain have been moved and the application of the BCs performed, at each cell a given number of particles are randomly selected for collisions as discussed below.

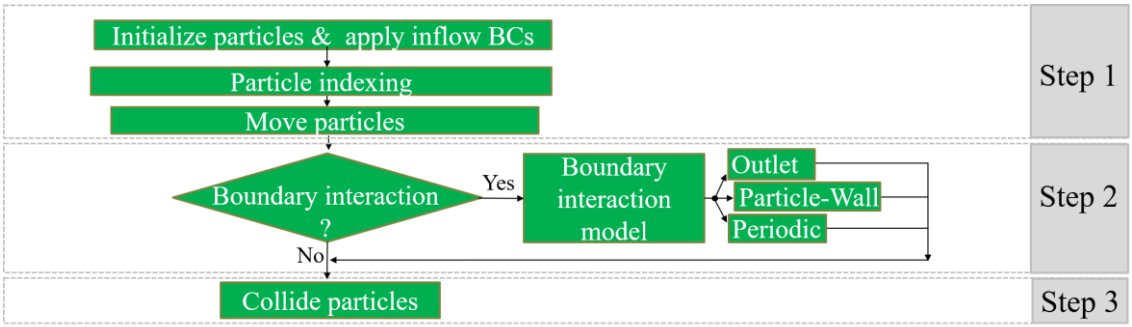

Figure 3.4 Part of the DSMC algorithm. Here the *move*, *BC application* (interaction of the gas with open boundaries and surfaces) and *collision* stages are shown.

First, in Figure 3.5 are depicted N particles contained in a cell volume V, such that $n = N \cdot V^{-1}$. For binary collisions, the reaction between two particles with relative velocity $\mathbf{v}_r$ takes place, if and only if, during the time interval Δt both particles are located in the same volume element $A \cdot L = \pi d^2 \cdot L = \sigma \cdot (v_r \Delta t)$ with base area σ (collision cross-section). In the last equality Eq. (3.12) has been employed. The reaction probability $P_R(v_r)$ between the two particles can be written as the ratio of the volumes

$$P_R(v_r) = \frac{\sigma(v_r) \cdot v_r \cdot \Delta t}{V}. \tag{3.22}$$

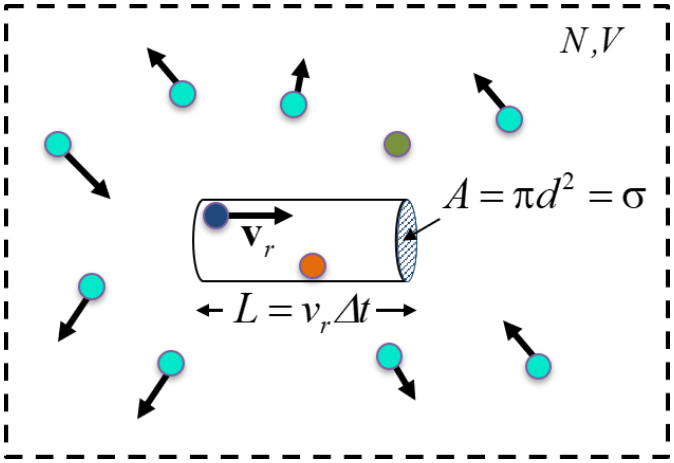

Figure 3.5 Frame reference at rest for both the orange and the green particles, which have the same relative velocity v_r to the dark blue particle. During the time interval Δt, the *collisional volume*, cylinder of volume $A\,L = \sigma v_r \Delta t$, encloses only the blue and the orange particles, making a collision between them possible. Since the green particle is located outside this collision volume, it is not taken into account for possible collision partners.

The total collision probability, which is the expectation value of the total number of collisions $\langle N_{coll} \rangle$, is the sum of all individual probabilities. Therefore, the mean number of collisions for one single particle $\langle N_{coll} \rangle_s$ and using $N-1 \approx N$ for large $N >> 1$ is,

$$\begin{aligned} \langle N_{coll} \rangle_s &= \sum_{k=2}^{N} P_R\left(v_r(1,k)\right) = \left(\sum_{k=2}^{N} 1\right) \frac{\Delta t}{V} \cdot \langle \sigma v_r \rangle = \frac{N-1}{V} \Delta t \cdot \langle \sigma v_r \rangle_s , \\ &\approx n \Delta t \cdot \langle \sigma v_r \rangle_s , \end{aligned} \tag{3.23}$$

and altogether the mean number of collisions is:

$$\begin{aligned} \langle N_{coll} \rangle &= \sum_{i=1}^{N-1} \sum_{k=i+1}^{N} P_R^{i,k} = \left(\sum_{i=1}^{N-1} \sum_{k=i+1}^{N} 1\right) \langle P_R\left(v_r(i,k)\right) \rangle \\ &= \frac{N(N-1)}{2V} \Delta t \cdot \langle \sigma v_r \rangle \approx \frac{1}{2} N \cdot n \cdot \Delta t \cdot \langle \sigma v_r \rangle \end{aligned} . \tag{3.24}$$

Here, $\langle \sigma v_r \rangle$ is the average of all products $\sigma^{(i,k)} v_r^{(i,k)}$ of particles i and k.

In DSMC the collisions are treated in a stochastic manner. A pair of potential collision partners in a cell, say particles i and j, are chosen randomly from the total number of particles N_{cell} within the cell. The probability of a collision to occur between particles i and j, or $P_{coll}(i,j)$, depends only on the rate $\sigma v_r(i,j)$. This means that for the aforementioned VHS model, the product σv_r is a again function of v_r, making the magnitude of the relative velocity v_r the only parameter used in the determination of the collision

probability of particles *i* and *j*, even if the particles are moving away from each other. This yields a collision probability which can be expressed by

$$P_{coll}(i,j) = \frac{\sigma v_r(i,j)}{\sum_{m=1}^{N_{cell}} \sum_{n=1}^{m-1} \sigma v_r(m,n)}, \tag{3.25}$$

for a pair of particles *i* and *j*. The job of the denominator is to normalize the discrete probability distribution. Thus, in each time step a product of σ and $v_r(i,j)$ is calculated and the single collision rate is weighted to the total collision rate in a cell.

However, if at each time step the double summation of $\sigma^{(m,n)} v_r^{(m,n)}$ needs to be performed for all possible collision pairs, the process gets computationally expensive as the calculation time scales with $(N_{cell})^2$ in this case. Instead, Bird [25] proposed a scheme where the collision probability follows the relation,

$$P_{coll}(i,j) = \frac{\sigma v_r(i,j)}{(\sigma v_r)_{max}}, \tag{3.26}$$

where the largest value of the rate in a cell $(\sigma v_r)_{max}$ is introduced. By an acceptance-rejection procedure, the collision is accepted if $\sigma v_r(i,j)/(\sigma v_r)_{max} > \Re_u$, where $\Re_u$ is a random number between 0 and 1, generated from a uniform distribution. If the pair is accepted, the collision takes place, the velocities of the particles are reset and the post-collision velocities generated as discussed below. The process starts all over again (selection of a pair within the cell) until the required number of candidate pairs are fulfilled.

To calculate the required number of candidates is equivalent to knowing the total number of collisions, given by Eq. (3.24). Thus, the average number of real particles in the cell is nV_{cell}, which can be written in terms of the average number of simulated particles as $\langle N_{DSMC} \rangle_{cell} = nV_{cell}/F_N$ by using the definition of the conversion factor F_N. By taking the maximum value of the rate $(\sigma v_r)_{max}$ in Eq. (3.24), the number of collisions in a cell during a time step is:

$$P_{coll}(i,j) = \frac{\sigma v_r(i,j)}{(\sigma v_r)_{max}}. \tag{3.27}$$

It can be seen that for each cell in the domain the local-cell rate $(\sigma v_r)_{max}$ needs to be stored and updated at each time step Δt. Thus, a value of $(\sigma v_r)_{max}$ is set initially for a given cell and as the simulation advances, this value is corrected such that in Eq. (3.26) one reaches

$\langle \sigma v_r \rangle_{max}$. The above equation can be also obtained if one looks the ratio of total accepted to the total candidates ratio

$$\frac{N_{coll}}{N_{cand}} = \frac{\sigma v_r}{(\sigma v_r)_{max}}, \tag{3.28}$$

where the equality holds since the probability of accepting a pair is proportional to their rate σv_r according to the acceptance-rejection procedure. Thus, solving the above equation for N_{cand} and using the relation of F_{N}, one obtains Eq. (3.26). The above procedure: pair selection and total number of collisions in a cell is called the NTC scheme, developed by Bird [60] and widely described [25]. Alternative schemes employed in DSMC are the Time Counter (TC) [25], Null Collision [61], [62] and Generalized Scheme [63], which differ from the NTC scheme in the way it is calculated the number of collisions and the computational efficiency. The reader is referred to [56] for a review of further insights in several collision procedures in DSMC. Bird later updated the above version of the NTC scheme, where instead of $N_{DSMC}\langle N_{DSMC}\rangle$, it is used $N_{DSMC}(N_{DSMC}-1)$ as in the third equality of Eq. (3.23). By doing this, a microscopic collision does not depend in a macroscopic variable such as the number density n via $N_{DSMC}F_N/V_{cell}$ and the value of the number of collisions does not depend on an average value of $\langle N_{DSMC}\rangle$, which takes some time to be established. Here, the updated version of the NTC scheme has been employed in this work.

The final step in the DSMC collision procedure is to derive the post-collision velocities of the pair of particles. This is done via the conservation of linear momentum applied to the velocity of the Center of Mass (CM) of the 2 particles where the velocity remains unchanged by the collision i.e.

$$\mathbf{v}_{\text{CM}} = \mathbf{v}^{*}_{\text{CM}}. \tag{3.29}$$

According to the conservation of energy, the magnitude of the relative velocity suffers no modification by the collision:

$$\left\|\mathbf{v}_{\text{CM}}\right\| = \left\|\mathbf{v}^{*}_{\text{CM}}\right\|. \tag{3.30}$$

Eqs. (3.29) and (3.30) provide 4 constraints for the 6 unknowns. The two remaining unknown variables are set by the angles χ and ε of the relative velocity as shown in Figure 3.6.

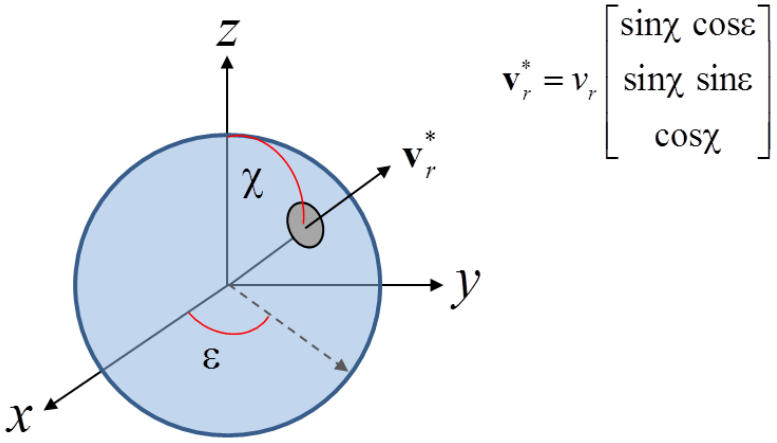

Figure 3.6 Post-collision velocity in the CM frame of reference.

For the HS and VHS collision model a random scattering angle is applied. To do this, the angles are randomly distributed along the unit sphere and the sampling techniques introduced in previous chapters can be used. For instance, the azimuthal angle ε is uniformly distributed between 0 and 2π and thus, the angle can be generated as $\varepsilon = 2\pi\Re_u$.

The polar angle χ is distributed according to the probability $P(\chi)d\chi = 1/2\sin(\chi)\,d\chi$ and by changing variable to $x = \cos(\chi)$, the distribution is now uniformly distributed in [-1,1]. By doing this change of variable, there is no necessity to calculate the angle directly but the values of $\sin(\chi)$ and $\cos(\chi)$ in terms of a random number $\Re_u$ as,

$$x = \cos\chi = 2\Re_u - 1, \tag{3.31}$$

and,

$$\sin\chi = \sqrt{1-x^2}\,. \tag{3.32}$$

Once the post-collisions velocities in the CM frame of reference are calculated, the velocities of particles *i* and *j* are transformed to the laboratory frame of reference via:

$$\mathbf{v}_i^* = \mathbf{v}_{\mathrm{CM}}^* + \left(\frac{m_j}{m_i + m_j}\right)\mathbf{v}_{\mathrm{r}}^*\,, \tag{3.33}$$

$$\mathbf{v}_j^* = \mathbf{v}_{\mathrm{CM}}^* + \left(\frac{m_i}{m_i + m_j}\right)\mathbf{v}_{\mathrm{r}}^*\,. \tag{3.34}$$

3.3 Boundary conditions: particle generation at open boundaries

Once the computational grid is defined, the DSMC simulation starts at time $t = 0$ s when a finite number of particles N are randomly distributed in the computational domain. According to the DSMC flow chart of the previous chapter, the particles are then moved ballistically as if they do not interact with each other and the boundary conditions (BCs) are executed. In DSMC there are two main BCs: particle inflow/outflow and the particle-wall interaction. The former involves the generation of particles at open boundaries entering the domain with a certain velocity while particles reaching an exit are removed from the domain. The particle-wall interaction is performed accordingly to the defined reflection mechanism.

The use of some results of kinetic theory (see Appendix B) and some basic considerations are needed for the introduction of the inflow BCs. First, consider particles of mass m whose velocity relative to the macroscopic stream velocity is given by $\mathbf{v} - \mathbf{V}$. This difference, sometimes called thermal or random velocity, is denoted by $\mathbf{v}'$. Second, the reciprocal of the most probable molecular thermal speed v_{mp}, denoted as β, is:

$$\beta = \sqrt{\frac{m}{2k_B T}}. \tag{3.35}$$

Finally, it is useful to define a dimensionless quantity, the ratio of the magnitude of the stream velocity to most probable molecular thermal speed as:

$$s = \frac{V}{v_{mp}} = V\beta. \tag{3.36}$$

With the above to definition, the particle flux (inflow) in the positive x-direction across a surface element dS in an equilibrium gas is given by:

$$\left(\frac{dN}{dSdt}\right)_{in} = \Gamma_{in} = \frac{1}{2\sqrt{\pi}}\frac{n_{in}}{\beta_{in}}\left[\exp\left(-s^2\cos^2\theta\right) + \sqrt{\pi}s\cos\theta\left(1 + \operatorname{erf}\left(s\cos\theta\right)\right)\right], \tag{3.37}$$

where $\beta_{in} = \sqrt{\frac{m}{2k_B T_{in}}}$ and $s = V_{in}\beta_{in}$. The flow quantities at the surface element, entering the domain are denoted with the subscript "in", see Figure 3.7.

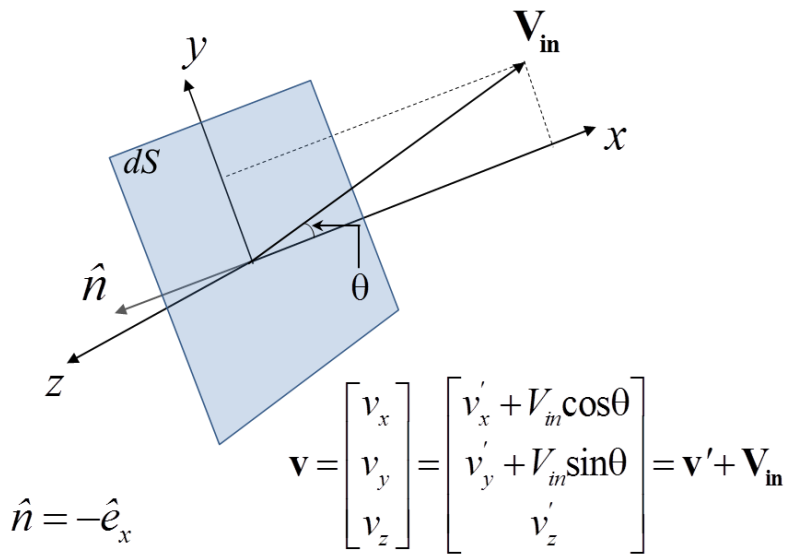

Figure 3.7 Particle flux crossing a surface element *dS* part of the boundary *S*. In the present construction, the coordinate system is such that the unit normal vector to the surface element $\hat{n} = -\hat{e}_x$ is anti-parallel to the positive *x*-direction. The macroscopic stream velocity V_{in} lies on the *xy*-plane and the surface element *dS* on the *yz*-plane.

The Eq. (3.37) is one of the central equations in DSMC and it is employed for calculating the prescribed inflow BCs. It is worth noting that for stationary gas conditions $\mathbf{V}_{in} = 0$ and $s = 0$ thus Eq. (3.37) now reads to:

$$\Gamma_{in} = \frac{1}{4} n_{in} \langle v \rangle . \tag{3.38}$$

Here, $\langle v \rangle$ is the average molecular speed given by the expression:

$$\langle v \rangle = \sqrt{\frac{8 k_B T_{in}}{\pi m}} . \tag{3.39}$$

Thus, the fundamental result of stationary gas conditions is recovered.

In the DSMC method, the particle occurence itself at a given inflow cross-section is a completely randomly chosen distribution which follows a univariate probability function, while the particle velocity is a property following a Boltzmann-distribution. Thus, the generation of particles at the inflow BC requires a uniform distribution (Poisson process) to avoid non-physical non-equilibrium effects [64]. Typically, Poisson processes are employed to model the number of events that occur independently of each other at a constant average rate in a fixed time interval or spatial area, in this case the generation of particles at random positions (*x*, *y*, *z*) at the inflow surface.

Regarding the inflow BCs, the velocity generation at open boundaries follows a Maxwellian distribution[1],

$$f_0(v') = \left(\frac{m}{2\pi k_B T} \right)^{3/2} \exp\left(-\frac{m v'^2}{2 k_B T} \right), \tag{3.40}$$

where *v'* is the magnitude of the thermal velocity. For certain models of particle-wall reflection, such as the *Diffuse-Wall*, the particles are thermalized after impinging with the wall. Therefore, a velocity generation is required, typically following a Maxwell-Boltzmann distribution centered at the temperature T of the wall. Moreover, in the collision process one also needs to define the post-collision angles in terms of an appropriate random sampling.

In practice, sampling the above distributions: uniform, Gaussian or Poisson (also known as probability density functions PDF) has its own strategies and involves the calculation of invertible functions. Thus, for a given PDF $f(x)$ and knowing that its cumulative distribution $F(x)$ is given by,

$$F_x(x) = \int_{-\infty}^{x} f(\xi) d\xi, \tag{3.41}$$

the problem reduces to finding the target variable x (position, particle speed, post-collision angles).

One way to proceed is by first equating $F_x(x)$ to a random number between 0 and 1, followed by solving the integral and then, an inversion of the equation is executed. This will allow us to have x in terms of the inverted function f^{-1}, known as the inverse-cumulative method [65].

An application of this method is found in DSMC for the generation of particles uniformly and randomly distributed across the domain at the beginning of a simulation, see flowchart in Figure 3.1. However, there are cases in which the inversion fails because one encounters non-invertible distributions or it is not suitable for certain distributions. Then, methods such as the Acceptance-Rejection [66] are widely employed.

The procedure for the acceptance-rejection method reads: first, let the variable of interest x be defined in an interval $[a, b]$, say a particle velocity that lies between $v + dv$, and its corresponding PDF $f \in [f_a, f_b]$. Since for continuous functions in a closed and

[1] This equation is the solution of the steady-state and force-free Boltzmann equation of Eq. (2.5), introduced earlier. The equation has been used as f_0 in the description of the approximations for the solution of the Boltzmann equation in Chapter 2. The constant appearing before the exponential function is the result of normalization and the exponent 3/2 reflects the fact that 3 degrees of freedom are considered.

bounded interval, the maximum and minimum values of f are attained at least once in that interval, a maximum of the distribution $f_{\max}$ can be defined. Then, a random number $x_{trial} \in [a,b]$ is generated and the ratio f_{trial} / f_{max} is equated to a second random number $R \in [0,1]$. If one has $f_{trial} < f_{max} R$, the value of x (velocity, angles) is accepted and is rejected otherwise. In other words, a pair of random variables (x_{trial}, f_{trial}) is generated and accepted if the pair lies within the shaded region below the PDF $f(x)$ envelope, otherwise the pair is rejected and the process of pair generation is repeated until a value is accepted, see Figure 3.8. In this way it is possible to sample the particle velocity components, say v_x, with its corresponding Maxwell-Boltzmann distribution.

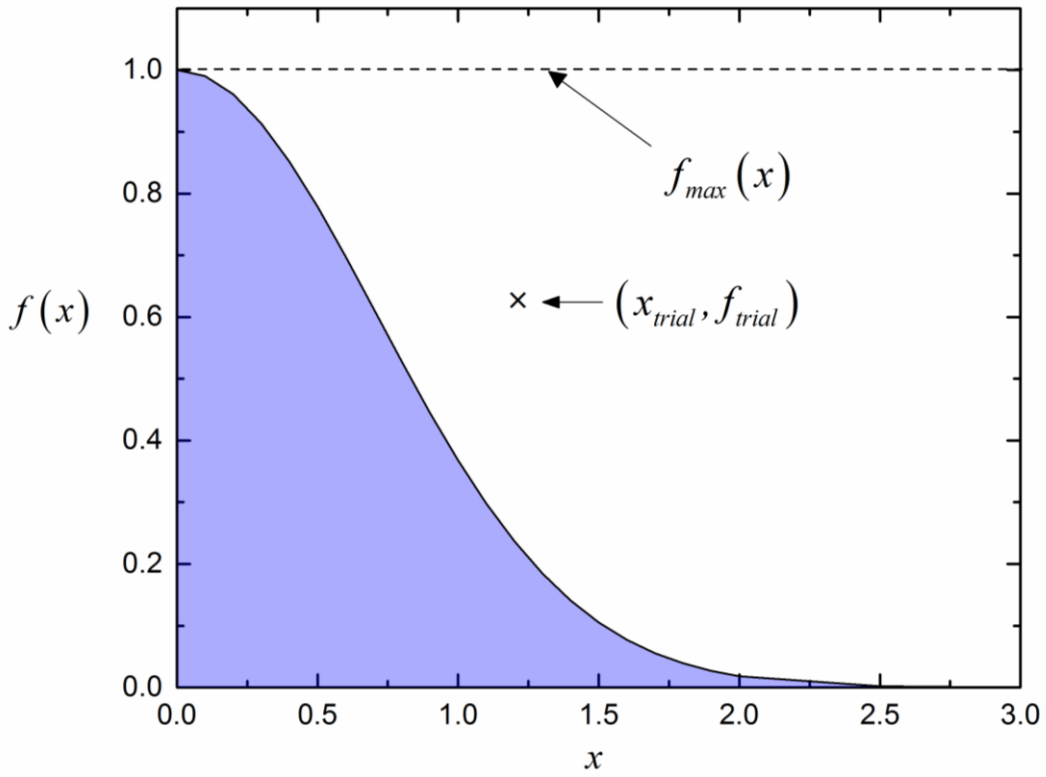

Figure 3.8 The procedure of the acceptance-rejection method. By knowing both the image of the distribution $f(x)$ and its maximum value in the domain of interest, the generated random variable x (speed, post-collision angles) and its corresponding $f(x)$ are accepted if the pair (x_{trial}, f_{trial}) lies within the shaded region.

3.4 Boundary conditions: particle-surface interaction

During their motion, the DSMC particles can strike surfaces, obstacles or interfaces within the domain. Therefore, various gas-surface interaction models are employed in

DSMC, namely: specular surfaces, periodic boundary conditions, thermal walls and more complex models based on accommodation coefficients.

For instance, when a particle strikes a specular surface, the model considers that the particle rebounds elastically as if hitting a flat surface. Thus, the model assumes that both the gas and solid molecules are rigid elastic spheres and the collision results in an inversion of the particle's velocity component normal to the surface. The velocity component parallel to the surface remains unchanged. Because in real applications the specular reflection conditions are not always met, one might employ the diffuse wall BC.

The diffuse wall BC assumes that the particles leaving the surface scatter with an equilibrium Maxwell-Boltzmann distribution centered at the temperature of the surface T_w. Hence, the velocity components of the particle are *reset* after colliding with the surface with the velocity component normal to the wall distributed as

$$P_{\perp}\left(v_{\perp}\right)=\frac{m}{k_B T_w} v_{\perp} \exp\left(-\frac{m v_{\perp}^{2}}{2 k_B T_w}\right), \tag{3.42}$$

whereas the parallel velocity component is distributed as

$$P_{||}\left(v_{||}\right)=\sqrt{\frac{m}{2\pi k_B T_w}} \exp\left(-\frac{m v_{||}^{2}}{2 k_B T_w}\right). \tag{3.43}$$

The generation of these velocity distributions is computed by means of the two procedures for the perpendicular velocity, the Acceptance-Rejection method is used while the inversion-cumulative is employed for the generation of values of the parallel component of the velocity. DSMC calculations with diffuse wall BC have shown good agreement with experimental data of rarefied gases in hypersonic conditions [67]. One can consider this BC as if the reflected particles are the flux of a fictitious equilibrium gas on the opposite side of the surface.

Real surfaces however are neither completely specular nor fully diffusive. Maxwell formulated the problem in the following manner [68], first let $P_w(\mathbf{v'}\rightarrow\mathbf{v};\ \mathbf{r})$ be a function describing the probability that a particle, which strikes a wall at a position $\mathbf{r}$ with a velocity $\mathbf{v}'$,will be reflected at $\mathbf{r}$ with velocity $\mathbf{v}$. It is also assumed that no particle absorption at the wall takes place and that an instant emission of the particles from the surface happens after these have impinged on it. In the Maxwell model, two types of particle-surface interaction were identified. In the first place Maxwell considered particles that strike a surface can be specularly reflected, so that their velocity after impinging the wall is given by $\mathbf{v}=\mathbf{v}'-2\hat{n}(\hat{n}\cdot\mathbf{v}')$ for $\hat{n}\cdot\mathbf{v}'<0$, see Figure 3.9. This means that the horizontal component of the velocity does not change and only the component normal to the wall has changed direction but not magnitude. The second type of interaction distinguished by Maxwell considers that after impinging with the wall, a particle is re-emitted back to the

system in its ground state with a velocity sampled from a Maxwellian distribution centered at the wall temperature T_{wall}. The velocities are then sampled from equations (3.42) and (3.43) introduced previously. Thus, the diffuse reflection can be interpreted as a type of interaction where a complete loss of memory by the reflected particle occurs. One can generalize the Maxwell model by considering that a fraction α of the incident particles are reflected diffusively (diffuse wall BC) and the remaining incident particles $(1-\alpha)$ are assumed to reflect specularly as:

$$P_w(\mathbf{v}' \to \mathbf{v};\mathbf{r}) = \alpha \ |\mathbf{v}\cdot\hat{n}| \ f_w(\mathbf{v}) + (1-\alpha)\delta\left[\mathbf{v} - \mathbf{v}' + 2\hat{n}(\hat{n}\cdot\mathbf{v}')\right], \tag{3.44}$$

where $f_w(\mathbf{v})$ is given by equation $f_w(v) = m/2\pi(kT_w)^2 \exp\left(-mv^2/2kT_w\right)$. Thus, two contributions in the Maxwell Model are included, as shown in Figure 3.9(a):

- Specular reflection, where the change of momentum occurs only for the component of velocity normal to the surface.

- Diffuse reflection, after striking the wall the particles are reflected equally in all directions. The velocity of the particles after reflection is randomly assigned according to a half-range Maxwellian distribution determined by the surface temperature.

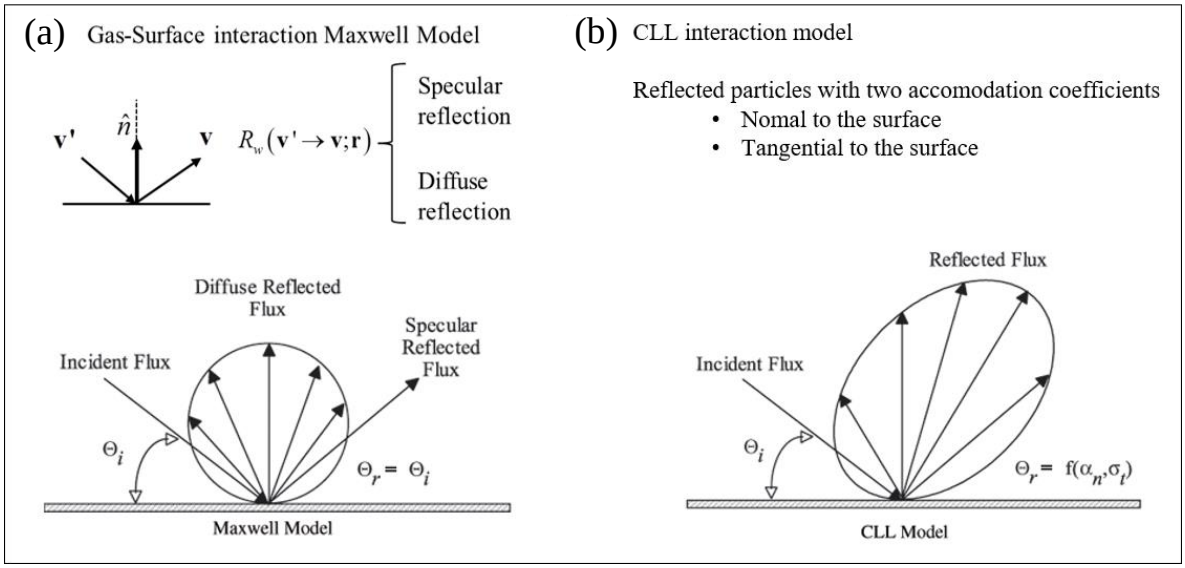

Figure 3.9 Gas-surface interaction model. (a) The Maxwell model considers two types of boundary conditions where incident particles can be reflected diffusely and a second interaction is defined as specular reflection with the surface. (b) The CLL model considers the normal and tangential accommodation coefficients for the sampling of the Maxwellian distribution of the velocities after reflection. Figure adapted from [69].

However, the predicted angular distributions of the Maxwell model do not agree with the observed scattering distributions in beam experiments [70][71], which turn out

to be petal-shaped. This behavior leads to the development of further models and among all of them, the Cercignani-Lampis (CL) model [72] and its implementation in DSMC by Lord [73] (CLL-model) have produced the best numerical agreement with both hypersonic [69] and beam experiments [74]. The CLL model is based in the so-called accommodation coefficients and it is depicted in Figure 3.9(b). In general, an accommodation coefficient of a particle property Q is defined in terms of incident and reflected fluxes as follows:

$$a_Q = \frac{\Gamma_i - \Gamma_r}{\Gamma_i - \Gamma_w}, \tag{3.45}$$

where Γ_i and Γ_r are the incident and reflected fluxes of Q and Γ_w is the reflected flux related to the diffuse wall BC. The fluxes are calculated by equations (3.37) and (3.38). The property Q can be for instance, the particle momentum **P** or the particle energy E. If one takes $Q = \mathbf{P}$, then for each velocity component two accommodation coefficients are calculated: a normal one related to the velocity components perpendicular to the surface and the tangential ones related to the velocity component parallel to the surface. This is the heart of the CLL model. If now one takes $Q = E$ and $a_E = 1$, both the reflected and the wall energy fluxes are the same $\Gamma_r = \Gamma_w$, thus the diffuse wall BC is recovered and the velocities sampling can be done via Eqs. (3.42) and (3.43).

Typically, in cryogenic surface applications this particular accommodation coefficient is referred as the thermal accommodation coefficient and its value ranges $a_E \in [0,1]$. A physical situation often encountered in gas dynamics applications and particularly in vacuum systems is the physical adsorption of particles on a surface or sorbent. With a defined probability $p \in [0,1]$ that the particles impinging on the surface are absorbed called as sticking probability BC. Here, the sticking probability BC is numerically implemented due to its important role as a pumping process. In Table 3.1 the outline of the algorithm is presented.

As the particle hits the surface, a random number is generated between 0 and 1 representing the probability of being absorbed at the moment of the impact. If this probability lies below the defined sticking probability p, the particle will be absorbed by the surface. Otherwise, the particle is reflected with a Maxwell-Boltzmann distribution according to the wall surface temperature, just as in the diffuse wall BC. For the sampling of distributions in the sticking probability BC, namely the uniform and normal (Maxwell-Boltzmann) distributions, the numerical strategies shown in the last section are employed.

Table 3.1 Implementation of the sticking probability BC for the particle wall collisions

User-defined sticking probability p is read.

When particles impinge a surface (at temperature T_w) a random number is first generated: $\Re_u$, which lies between 0 and unity

- If $\Re_u \le p$

  Delete the particle from domain, i.e. the particle is absorbed by the surface

- If $\Re_u > p$

  Store the mass, velocity and energy of the particle in the variables m, $\mathbf{v}$ and E

  Generate a vector normal to the wall $\hat{n}_\perp$ and compute the normal velocity magnitude $\|\mathbf{v}\cdot\hat{n}_\perp\|$

  By doing this, it can be computed the normal component of the Maxwellian distribution (Eq. (3.42))

  Next, compute the wall tangential velocity $\mathbf{v}_\parallel = \mathbf{v} - \mathbf{v}\cdot\hat{n}_\perp$

  While the $\|\mathbf{v}_\parallel\| \approx \varepsilon$ with $\varepsilon << 1$, add a perturbation δ to the incoming velocity $\mathbf{v}$ and compute again the normal and tangential velocities

  Compute a tangential unit vector $\hat{n}_\parallel = \mathbf{v}_\parallel / \|\mathbf{v}_\parallel\|$

  Calculate the velocity based on Eqs. (3.42) and (3.43) with $T=T_w$, via the procedures described in this chapter then return the reflected velocity $\mathbf{v}_r$

3.5 Macroscopic states in DSMC

Once all the particles have been moved and collided, the macroscopic states are calculated in DSMC. Most of the physical quantities are computed as averages as

$$\begin{Bmatrix} n(\mathbf{r},t) \\ \mathbf{P}(\mathbf{r},t) \\ \mathbf{V}(\mathbf{r},t) \\ T_{tr}(\mathbf{r},t) \\ p(\mathbf{r},t) \end{Bmatrix} = \frac{1}{V_c}\sum_{i=1}^{N} \begin{Bmatrix} N_i \\ m\mathbf{v}_i \\ \mathbf{v}_i / N_i \\ \frac{2}{3k_B}\left(\frac{1}{2}\left\langle m_i \|\mathbf{v}\|_i^2 \right\rangle - \frac{1}{2}\langle m_i \rangle \|\mathbf{V}\|^2\right) \\ N_i k_B T_{tr} \end{Bmatrix}. \tag{3.46}$$

Here, a cell of volume V_c located at $\mathbf{r}$ contains N_{DSMC}-particles, thus the density n, linear momentum, flow velocity $\mathbf{V}$ of the bulk and translational temperature T_{tr} are estimated by counting all the particle contributions in that cell. Thus, the DSMC method uses a cell

system for sampling the macroscopic variables. As an inherent stochastic process, the macroscopic variables are fluctuating until steady state conditions are locally established, and thus statistics can be performed on the variables. The temperature T_{tr} is estimated from the equipartition theorem, where 3 degrees of freedom are considered in the above equation. The local pressure $p(\mathbf{r},t)$ is evaluated via the ideal gas law using the translational temperature. If rotational and vibrational modes (here referred as internal modes) are involved, like in polyatomic molecules, the overall temperature T_{ov} has to be invoked:

$$T_{ov} = \frac{3T_{tr} + fT_{int}}{3+f} \quad , \tag{3.47}$$

where *f* denotes the degrees of freedom of the internal modes. For example, for atoms the rotational degrees of freedom are zero whereas for diatomic molecules a value of 2 is assigned. Other physical quantities such as mean free path and mean collision time are also sampled in each cell during the DSMC calculation. The calculation of the macroscopic variables in Eq. (3.46) is based on the number of DSMC particles at each cell, thus the physical value of each quantity is recovered by introducing the conversion factor F_N.

As in any study that involves the calculation of averaged physical quantities, the appearance of statistical fluctuations is of natural consequence. Typically, in a DSMC simulation the fluctuations in a cell are inversely proportional to the square root of the number of particles located on it [75] and for the case of steady flows, the fluctuations are also dependent of the number of independent samples employed [75], [76]. As a result, it is necessary to determine the optimum number of particles in each cell; enough to promote statistical accuracy while maintaining a non-prohibitive computational time. At least 20 particles per cell have been traditionally employed in DSMC studies [25], [59], but as indicated in [77] a factor of 5 greater could be favorable not only to decrease the error but also to increase the efficiency of the calculation. It is clear that upon available computational resources, one may choose the former or the latter option. Thus, one needs to find a compromise of the cell dimensions because the smaller the cell size gets, the less DSMC-particles will be contained on it and thus achieving poor cell statistics. This leads us to define a criterion on DSMC that establishes a certain convergence and accuracy level during the simulations.

3.6 Convergence criterion of DSMC simulations

For each DSMC analysis a convergence criterion is needed in order to decide whether the DSMC simulation has *converged* to a statistical stationary state everywhere throughout the domain. The criterion employes the total number of particles in the system and it takes the form at the time step *k*:

$$\left| N_{tot}\left(t = t_k\right) - \left\langle N \right\rangle_{tot} \right| < \varepsilon \,. \tag{3.48}$$

In a typical DSMC simulation, at the simulation start $t = 0$ N particles are already set inside the domain. As mentioned before in this chapter, once the particles are moved at each time step, the appropriate number of particles enters the domain at the inlet whereas at the outlet the particles are deleted. This process has the effect that the total amount of particles in the system changes in time. The temporal evolution of the total number of particles has three possibilities

$$\begin{aligned} &\text{Case 1: } N_{tot}\left(t = t_k\right) = N_{tot}\left(t = 0\right) - \left|\delta N\right| < N_{tot}\left(t = 0\right) \\ &\text{Case 2: } N_{tot}\left(t = t_k\right) = N_{tot}\left(t = 0\right) \pm \left|\delta N\right| \sim N_{tot}\left(t = 0\right). \\ &\text{Case 3: } N_{tot}\left(t = t_k\right) = N_{tot}\left(t = 0\right) + \left|\delta N\right| > N_{tot}\left(t = 0\right) \end{aligned} \tag{3.49}$$

For instance, if the total number of particles in the system is initially underestimated, then its temporal evolution monotonically increases until a final value (Case 3), rea-ching a plateau, see Figure 3.10.

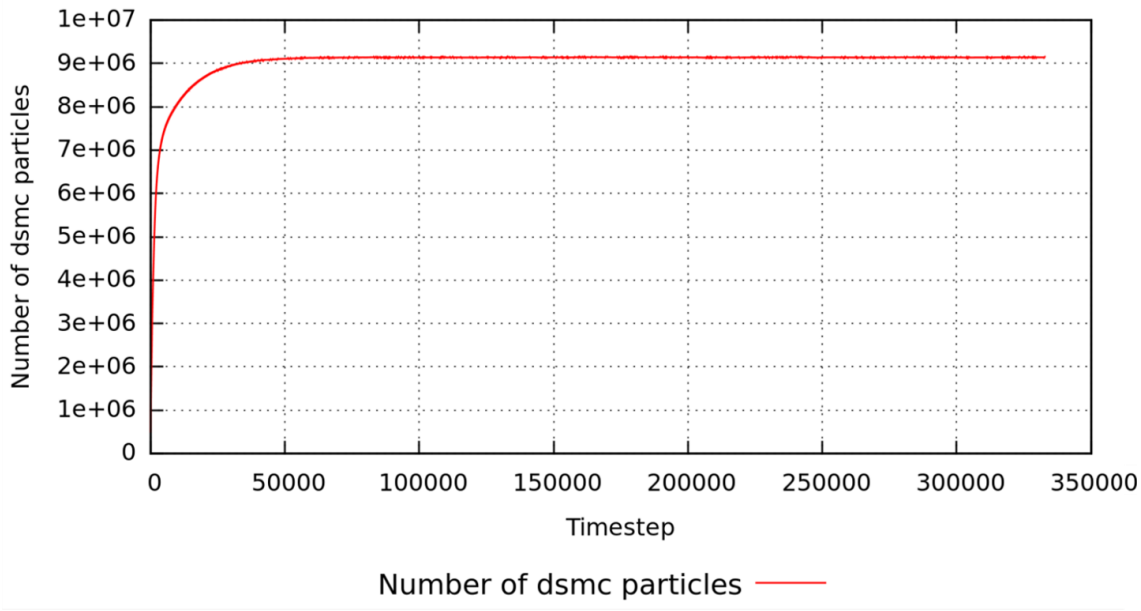

Figure 3.10. Example of the temporal evolution of the total number of DSMC particles in a simulation as a function of the time steps (Case 3).

The *convergence* of the DSMC simulation is hereby referred to a simulation which the maximium variation of the total number of particles is less than 2% after reaching the plateau region, as described above. A simulation that has converged in this sense, if stopped and restarted again, the time variation of the number of particles typically has temporal evolution as shown in Figure 3.11, resembling case 2 of Eq. (3.49). Subsequently, the statistics are then accumulated over substantial period of time in order to

reduced the local variation of the macroscopic variables, which leads us to the statistical error in DSMC macroscopic variables.

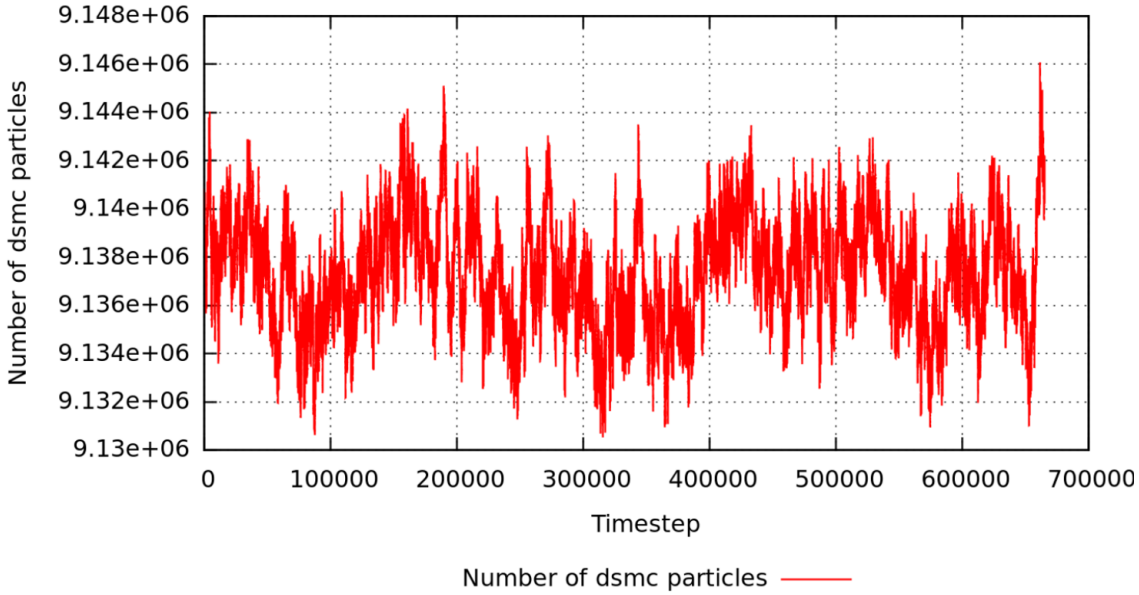

Figure 3.11 Stationary conditions with respect to the total number of particles in a DSMC simulation: the value of the number of particles in the system fluctuates around a mean value. At this point the convergence criterion is applied.

3.7 Statistical error analysis in DSMC

The errors can be determined via confidence intervals and the calculation of the standard deviation. However, it is possible to determine the deviations from the mean value by applying equilibrium statistical mechanics [57], [78] as in [79], [80] where a framework for the application of the fluctuations was employed and verified by molecular simulations. In the following paragraphs the key concepts are presented to describe the fluctuation relations based on the derivation of [57].

In equilibrium statistical mechanics, the statistical error in DSMC of a macroscopic variable A is taken as the ratio of its standard deviation σ_A to the value of the macroscopic variable $|A|$. Hence, the main idea in the deduction of the fluctuations is to estimate the variance of a macroscopic variable $\langle(\Delta A)^2\rangle$via the Maxwell-Boltzmann statistics, where $\sigma_A \propto \sqrt{\langle(\Delta A)^2\rangle}$. In DSMC the average values are estimated over M independent samples and in steady state scenarios, and these sequential realizations are taken in different times t. The standard deviation for a macroscopic variable A is given by [57]:

$$\sigma_A = \frac{\sqrt{\left\langle (\Delta A)^2 \right\rangle}}{\sqrt{M}}, \tag{3.50}$$

and the error in the estimate of the macroscopic variable A is taken as,

$$E_A = \frac{\sigma_A}{|A|}. \tag{3.51}$$

Equation (3.51) provides a way to define expressions for the statistical error in the macroscopic variables in DSMC. These expressions are summarized in the following table.

Table 3.2 Statistical error of macroscopic variables A employed in the present DSMC simulations, as derived in [75]

A (variable)	$E_A = \frac{\sigma_A}{\lvert A\rvert} = \frac{\sqrt{\left\langle (\Delta A)^2 \right\rangle}}{\sqrt{M}\cdot\lvert A\rvert}$
$\mathbf{V}\cdot\hat{\mathbf{e}}_i$	$\frac{1}{\sqrt{M}}\frac{\sqrt{k_B T_0}}{\sqrt{mN_0}\cdot\lvert\mathbf{V}\cdot\hat{\mathbf{e}}_i\rvert}$
N (or ρ)	$\frac{1}{\sqrt{M}}\frac{\sqrt{\kappa_T/\kappa^i{}_T}}{\sqrt{N_0}}$
T	$\frac{1}{\sqrt{MN_0}}\frac{\sqrt{k_B}}{\sqrt{c_V}}$
P	$\frac{1}{\sqrt{MN_0}}\frac{p_0^i}{p_0}Ac\sqrt{\gamma}$

Here $\mathbf{V}\cdot\hat{\mathbf{e}}_i$ means the i-th component of the flow velocity with $i=\{x,y,z\}$. In the above expressions $\kappa_T = -V^{-1}(\partial V/\partial p)_T$ has been introduced, the isothermal compressibility at constant temperature and $\kappa^i{}_T$ is the compressibility of the reference dilute gas at same density and temperature. Also, the heat capacity per particle at constant volume is defined as $c_V = C_V/N_0$ and Ac is the ratio of the fluids's speed of sound to the speed of sound of a reference ideal gas at the same temperature. Finally, the quantity p_0^i is the pressure of an ideal gas under the same conditions and $\gamma = c_p/c_V$ is the adiabatic exponent.

In addition to the described statistical errors, deterministic errors due to finite values of the chosen parameters in DSMC, namely: Δt, Δx and F_N do play a role for the accuracy of the macroscopic states of the flow. Assuming that in a DSMC simulation the three key parameters are carefully chosen employing the criteria given in Chapter 3.1, it can be assured that the estimated macroscopic variable of the flow A has already minimized their influence and the sampling as well as the employed physical models (intermolecular collisions and particle-wall interaction) are the leading contributions to the uncertainty. For instance, it has been shown [54] that the employed intermolecular collision model may alter the transport coefficients of the flow by some factors, but the functional dependence with the cell size remains the same.

3.8 The DSMC code

The numerical code employed in the analysis of sub-divertor gas flows is implemented within the framework of an open-source C++ toolbox for computational fluid dynamics: OpenFOAM [81], freely available for download under the GNU general public license [82]. The corresponding DSMC solver: *dsmcFoam*, which is based on Bird's algorithm described in this chapter, is capable to execute simulations for steady and transient conditions as well as gas flows in arbitrary geometries.

For the geometry and mesh generation, in OpenFoam two in-built grid generators are available: *snappyHexMesh* and *blockMesh*. However, in these mesh utilities, the user introduces manually each vertex and line of the computational domain of interest. Due to the complexity of the divertor geometry, it is rather cumbersome to define each node and lines forming the divertor cassette contour. Therefore, the compatibility of OpenFOAM with additional grid generators software is used. Mesh utilities such as GMSH [83], the grid generator included in SALOME [84] or the in-built generators in ANSYS [85], eases the inclusion of complex geometries and grids in *dsmcFoam*. In the present work, GMSH has been employed as grid generator for the analysis of sub-divertor gas flows. For simple geometries such as a rectangular channel, *blockMesh* is preferred.

The workflow of a simulation is illustrated in Figure 3.12. First, the geometry representing the physical domain of the flow is analyzed. Complex geometries as fusion divertors require access to engineering files to define the flow domain. To do this, one needs to identify and define first the interfaces between the main chamber and the neutral region of the sub-divertor. Thus, the physical domain is carefully analyzed in order to define a computational domain which is then meshed. The meshing or the grid generation is then applied to the chosen computational domain. As final stage of the workflow, the boundary conditions and DSMC parameters are again verified in order to start the simulation.

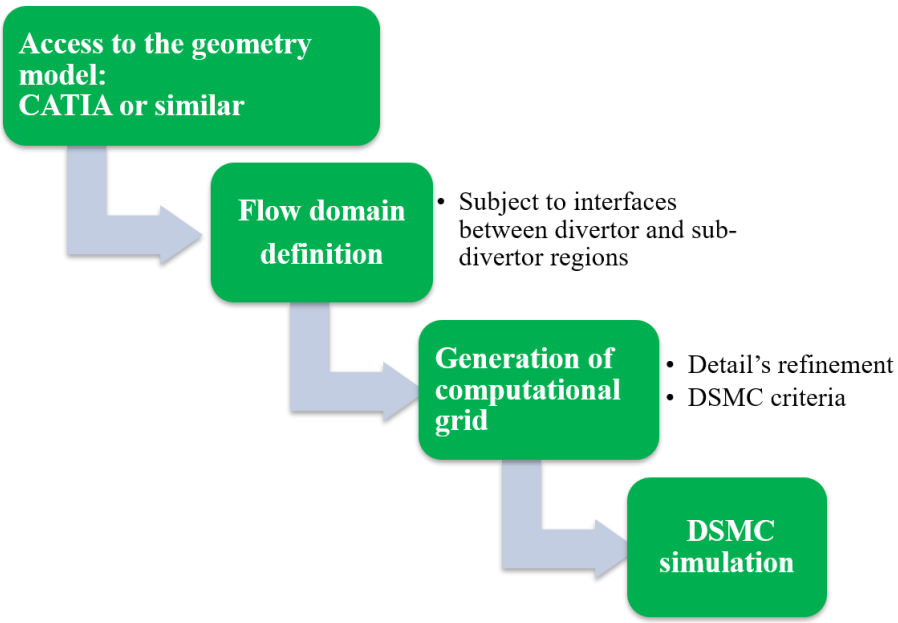

Figure 3.12 Workflow employed in the present thesis for the study of neutral gas flows in simple and complex geometries.

In the present work, the neutral gas flow in the sub-divertor is modelled employing an updated version of *dsmcFoam*, where the capabilities of its original release have been extended [86]. One of the new features that is employed in this thesis is the pressure boundary condition. This boundary condition is quite important for the work of this thesis because in some cases, as in the gas flow studies in the rectangular channel and ASDEX Upgrade, there is no available information of the velocity profile of the neutral particles at the inlets or outlets of the sub-divertor.

In applying the boundary conditions for the gas-surface interactions, in this thesis the specular reflection and the diffuse wall boundary conditions available in the *dsmcFoam* solver. In order to model the effect of particle absorption in surfaces, the sticking probability boundary condition is developed and employed in this dissertation. In the DSMC code it is possible to include atoms and molecules as type of gas particles, which includes their properties as mass, diameter and degrees of freedom (translational, rotational). The collisional kernel in the DSMC code include the hard sphere model, which assumes a dependency with the distance between the pair particles involved in the collision. The VHS model included in the code calculate the collision cross section with the dependency with the relative velocity between particle pairs. The temperature dependence of the viscosity as a power law is included in the DSMC code, which results in a solely input parameter i.e. the exponent or also called the viscosity index ω.

Thus, the DSMC simulations need many parameters, which can be condensed in three main types: boundary type, DSMC properties (time step, conversion factor) and

particle attributes. Throughout the dissertation for each modelled problem of gas flows, a table summarizing all the parameters is given in the following format:

Table 3.3 Template of table for input of DSMC simulations (the column "Value" is left in blank on purpose)

	Type / Parameter	Value	Unit
Boundary name			
Inlet, outlet, wall, pump	Pressure type (inlet)		
	Pressure		Pa
	Temperature		K
	Pressure type (outlet)		
	Pressure		Pa
	Velocity type (inlet)		
	Velocity		m/s
	Temperature (transl., rot., vib.)		K
	Number density		m^{-3}
	Wall		
	Velocity		m/s
	Temperature		K
	Pump		
	Sticking probability		-
	Velocity		m/s
	Temperature		K
DSMC properties			
Time step	Δt		s
Conversion factor	F_N		-
Particle-wall interaction	Specular, diffuse reflection		
Binary collision model	VHS		
	Reference temperature		K
Particle attributes			
Particle name	(Argon, Deuterium, …)		
mass	m		kg
diameter	d		m
rotational DoF	Rotational DoF		-
viscosity index	ω		-

4 Verification and benchmark: flow in channel

4.1 Rarefied gas flow in a rectangular channel

The first objective of the thesis is to verify and benchmark the computational tool (*dsmcFoam*) by applying the DSMC code to rarefied gas flows in simple geometries. A well-known problem in rarefied gas dynamics community is the gas flow through a rectangular channel [87]. The system consists of a monoatomic gas Argon (Ar) flowing through a channel of height H and length L, connecting two semi-infinite reservoirs. If the width of the channel in z-direction is much greater than its height, the influence of the lateral wall located at $z = \pm z_0$ is negligible, and thus the problem can be considered two dimensional as shown in Figure 4.1.

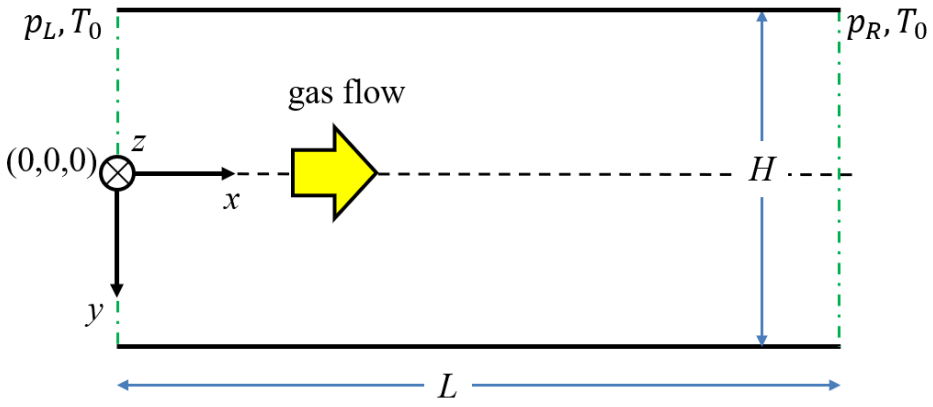

Figure 4.1 Scheme of the flow, coordinates and regions: inlet (pressure value of p_L) and outlet (pressure value of p_R).

The same gas is contained in side the channel (inlet and outlet), where the constant pressures p_L and p_R are defined, respectively. For the computation $p_L > p_R$ is assumed and the temperature T_0 is set at the inlet, outlet and wall surface. The solution of the problem is determined by the dimensionless rarefaction parameter describing the degree of gas rarefaction $\delta = p_L H / \mu v_{mp}$, where μ is the dynamic viscosity of the gas. Moreover, the solution is also dictated by the ratio length-to-height L/H and the reservoirs pressure ratio p_R/p_L. The aim of the simulation is to calculate the macroscopic variables along the channel including the reduced mass flow rate W which is defined as

$$W = \frac{\dot{M}}{\dot{M}_0}. \tag{4.1}$$

where $\dot{M}$ is the mass flow rate through the channel at any value of L/H, p_R/p_L and δ, whereas

$$\dot{M}_0 = \frac{Hp_L}{\sqrt{\pi}v_0} = \frac{\mu_0}{\sqrt{\pi}}\delta, \tag{4.2}$$

is the mass flow rate through a slit ($L/H = 0$) with an expansion into vacuum $p_R = 0$ Pa in the free-molecular limit. In the case of the parallel plates for the two-dimensional problem, the mass flow is calculated as the intergral across the height of the channel at one position x.

The performed simulations have been conducted for different rarefaction parameters. 10^{-3}, 1 and 10. The ratio length-to-height L/H is set to 5 and a value of the pressure ratio p_R/p_L of 0.1 is chosen. The selection of the pressure ratio is justified based on findings in Ref. [87] that reveal large statistical scattering for pressure ratios close to unity. Moreover, in [24] suggest that for a pressure ratio range between 0.5 and 1 a numerical solution of the Boltzmann equation is more appropriate to describe this system.

In order to define the cell dimensions in x- and y-direction, first the mean free path with the highest-pressure value is calculated (left-hand side of the channel, p_L). This sets the minimum cell size in the DSMC calculation ($\Delta x = \lambda/3$, Chapter 3.4). By employing the thermal or random component of the flow velocity $v_{th} = V_\infty + v_{mp}$ and the cell size Δx, the residence time of a particle in a cell is calculated as $t_{res} = \Delta x/v_{th}$. From Chapter 3, the value of the time step does not exceed the mean collision time $\tau_{coll} = \lambda/v_{mp}$. This latter condition is assured by calculating the collision time at the inlet and relative to this value a time step is defined. This procedure is applied to each DSMC simulation for the different rarefaction parameters. The diffuse reflection boundary condition presented in Chapter 3.3 is employed as gas-surface interaction in the simulations, whereas the VHS collision model has been employed in all stuy cases. In the following, the DSMC simulation refers to the results of the *dsmcFoam* solver unless otherwise stated.

Table 4.1 The summary of the model parameters for $\delta = 1$ is presented in the following table

	Type / Parameter	Value	Unit
Boundary name			
Inlet	Pressure type (inlet)		
	Pressure	8×10^{-2}	Pa
	Temperature	300	K
Outlet	Pressure type (outlet)		
	Pressure	8×10^{-3}	Pa
Wall	Wall		
	Velocity	0	m/s
	Temperature	300	K
DSMC properties			
Time step	Δt	1×10^{-5}	s
Conversion factor	F_N	5×10^{10}	-
Particle-wall interaction	Diffuse reflection		
	Temperature	300	K
Binary collision model	Variable Hard Sphere model		
	Reference temperature	300	K
Particle attributes			
Particle name	Argon (Ar)		
mass	m	66.3×10^{-27}	kg
diameter	d	4.17×10^{-10}	m
rotational DoF	Rotational DoF	0	-
viscosity index	ω	0.81	-

In the present analysis the rarefaction parameter ranges from the free molecular to the near-continuum gas flow regime and thus, expressions for the pressure profile and mass flow rate through the channel are needed in order to compare with theoretical expressions. The gas flow can be analyzed from the perspective of a continuum-fluid framework in terms of the Navier-Stokes equations for Kn < 0.1, as mentioned in Chapter 2.1, where generally, the average gas velocity at the wall is different from that of the surface due to the interactions between the gas and wall molecules, and thus a velocity slip occurs. The Navier-Stokes equations in one dimension with the slip condition at the wall for a gas flow through parallel plates read

$$\frac{\partial^2 u_x}{\partial y^2} = \frac{1}{\mu}\frac{dp}{dx}, \qquad u_x\big|_{y=y_{wall}} = \pm A_1 \lambda \left.\frac{\partial u_x}{\partial y}\right|_{y=y_{wall}} - A_2 \lambda^2 \left.\frac{\partial^2 u_x}{\partial y^2}\right|_{y=y_{wall}}. \tag{4.3}$$

Where the y is the cartesian coordinate along the channel height and the x-direction along the flow direction, i.e. the channel length. The coefficients A are dependent on the velocity

slip coefficients and the molecular interaction model. Gallis *et al.* [88] employs approximate close-formed expressions based on the Navier-Stokes equations to describe the steady flow of an ideal gas through tubes and channels which agree with the experimental measurements of [89]. In [88] the expression of the pressure profile along the channel is a function of the mean Knudsen number Kn_m, the accommodation coefficient (a value of unity for full accommodation i.e. diffuse reflection) and three dimensionless coefficients which are related to the flow behaviour in the different flow regimes. The expression of the pressure profile along the channel length reads

$$\frac{x}{L}=\frac{\left(p_L^2-p^2\right)+2\left(6\mathrm{Kn}_m\right)\left(\frac{2-\alpha}{\alpha}\right)p_m\left(p_L-p\right)\left\{\left(1+b_1\alpha\right)-\left(1+b_1\alpha-b_0\right)\left(\frac{b_2\mathrm{Kn}_m p_m}{p_L-p}\right)\ln\left[\frac{p_L+b_2\mathrm{Kn}_m p_m}{p+b_2\mathrm{Kn}_m p_m}\right]\right\}}{\left(p_L^2-p_R^2\right)+2\left(6\mathrm{Kn}_m\right)\left(\frac{2-\alpha}{\alpha}\right)p_m\left(p_L-p_R\right)\left\{\left(1+b_1\alpha\right)-\left(1+b_1\alpha-b_0\right)\left(\frac{b_2\mathrm{Kn}_m p_m}{p_L-p_R}\right)\ln\left[\frac{p_L+b_2\mathrm{Kn}_m p_m}{p_R+b_2\mathrm{Kn}_m p_m}\right]\right\}}, \quad (4.4)$$

where p_L and p_R are the pressure at the left (inlet) and right (outlet) reservoir and the rest of the variables is defined as

$$\begin{Bmatrix} p_m \\ \\ \mathrm{Kn}_m \end{Bmatrix}=\begin{Bmatrix} \frac{p_L+p_R}{2} \\ \\ \frac{\lambda_m}{H} \end{Bmatrix} \text{ and } \alpha=\begin{cases} 0 & \text{specular reflection} \\ 1 & \text{diffuse reflection} \end{cases}, \quad (4.5)$$

where the Knudsen number Kn_m is calculated as the ratio of the average mean free path to the channel height at the inlet. Depending on the flow regime of the problem to solve, the expression of $\{...\}$ in Eq. (4.4) has the following limits in the continuum and the free molecular regimes:

$$\begin{aligned} &\lim_{Kn_m\to 0}\left\{\left(1+b_1\alpha\right)-\left(1+b_1\alpha-b_0\right)\left(\frac{b_2\mathrm{Kn}_m p_m}{p_1-p_x}\right)\ln\left[\frac{p_L+b_2\mathrm{Kn}_m p_m}{p_x+b_2\mathrm{Kn}_m p_m}\right]\right\}=1+b_1\alpha\ \left(\delta\to\infty\right), \\ &\lim_{Kn_m\to\infty}\left\{\left(1+b_1\alpha\right)-\left(1+b_1\alpha-b_0\right)\left(\frac{b_2\mathrm{Kn}_m p_m}{p_1-p_x}\right)\ln\left[\frac{p_L+b_2\mathrm{Kn}_m p_m}{p_x+b_2\mathrm{Kn}_m p_m}\right]\right\}=b_0\ \left(\delta\to 0\right), \end{aligned} \quad (4.6)$$

where p_x can take the value of p in the expression of $\{...\}$ in the numerator of Eq.(4.4) whereas it takes the value of p_R (outlet) in the corresponding expression of $\{...\}$ in the denominator of Eq. (4.4). Therefore, the coefficient b_1 is related to the near continuum regime, b_0 to the free molecular and the coefficient b_2 controls the transition between the continuum and the free molecular flow regime. These coefficients are selected such that the mass flow rate proposed in [88]

$$\frac{\dot{M}}{\dot{M}_C}=1+\left(6\mathrm{Kn}_m\right)\left(\frac{2-\alpha}{\alpha}\right)\left\{\left(1+b_1\alpha\right)-\left(1+b_1\alpha-b_0\right)\left(\frac{b_2\mathrm{Kn}_m p_m}{p_L-p_R}\right)\ln\left[\frac{p_L+b_2\mathrm{Kn}_m p_m}{p_R+b_2\mathrm{Kn}_m p_m}\right]\right\}, \quad (4.7)$$

matches the flow rate calculated with the DSMC method. These values read: $b_0 = 6.5 \times 10^{-4}$, $b_1 = 0.5$ and $b_2 = 0.01$. In Eq. (4.7) the quantity $\dot{M}_C$ represents the mass flow rate defined in the continuum regime whereas the expression in $\{...\}$ is defined by Eq. (4.6).

The different inlet pressure at each rarefaction parameter dictates the necessary time step to be employed. The time step does satisfy the DSMC requirements that it be less than the mean collision time for all test cases. For the highest collisionality case with $\delta = 10$ a ratio of $\Delta t/\tau_{coll} = 3.57\times 10^{-2}$ is employed. As shown in Table 4.1 for the analysis with the rarefaction parameter $\delta = 1$ a ratio of $\Delta t/\tau_{coll} = 5.29 \times 10^{-2}$ is found. Finally, for the case $\delta = 10^{-3}$ a ratio of $\Delta t/\tau_{coll} = 5.29 \times 10^{-6}$ is used.

The averaging process at each cell in the system starts once the stationary conditions in the simulation are reached. This condition is reached approximately after N-time steps: 150,000 ($\delta = 10^{-3}$), 20,000 ($\delta = 1$) and aprox. 100,000 ($\delta = 10$). In the low collisional case $\delta = 10^{-3}$ the total number of particles reaches a minimum after 50,000 time steps and its value remains approximately constant after 150, 000 time steps, as shown in Figure 4.2. In Figure 4.3 is shown the variation in time of the total number of the DSMC particles for the anaysis with δ= 1 and δ= 10. In Figure 4.3(b) is shown the aforementioned plateau appearing in the behaviour of a DSMC simulation.

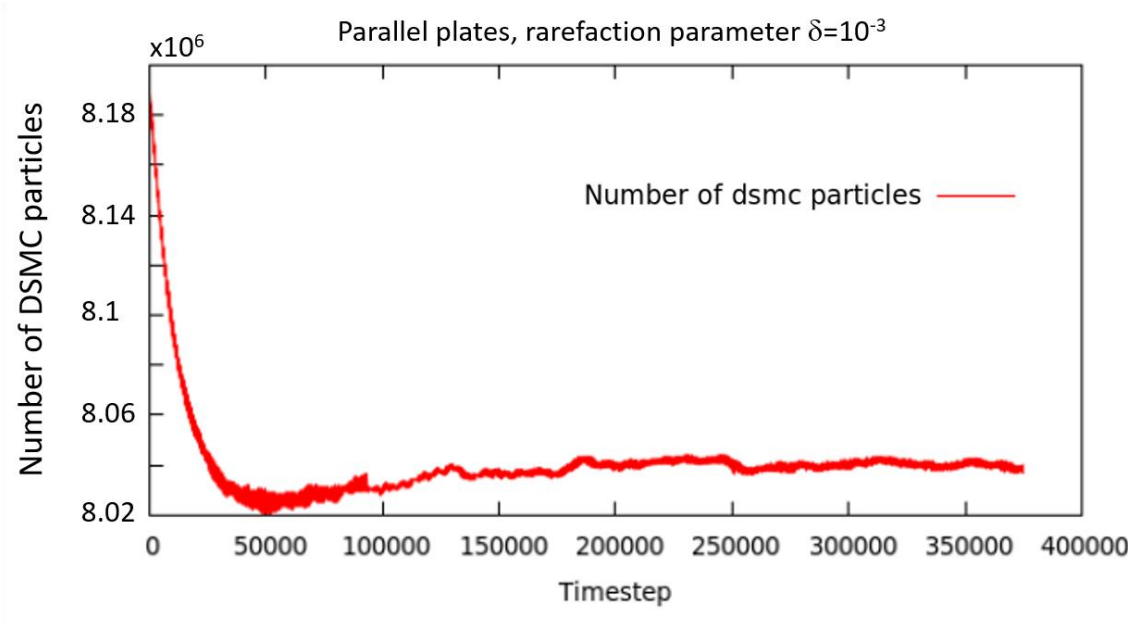

Figure 4.2 Number of DSMC particles in the system for the rarefaction parameter $\delta = 10^{-3}$, for the parallel plates studies of Argon gas, VHS collision model, gas temperature of 300 K, *L/H*=5, outlet/inlet pressure ratio of 0.1.

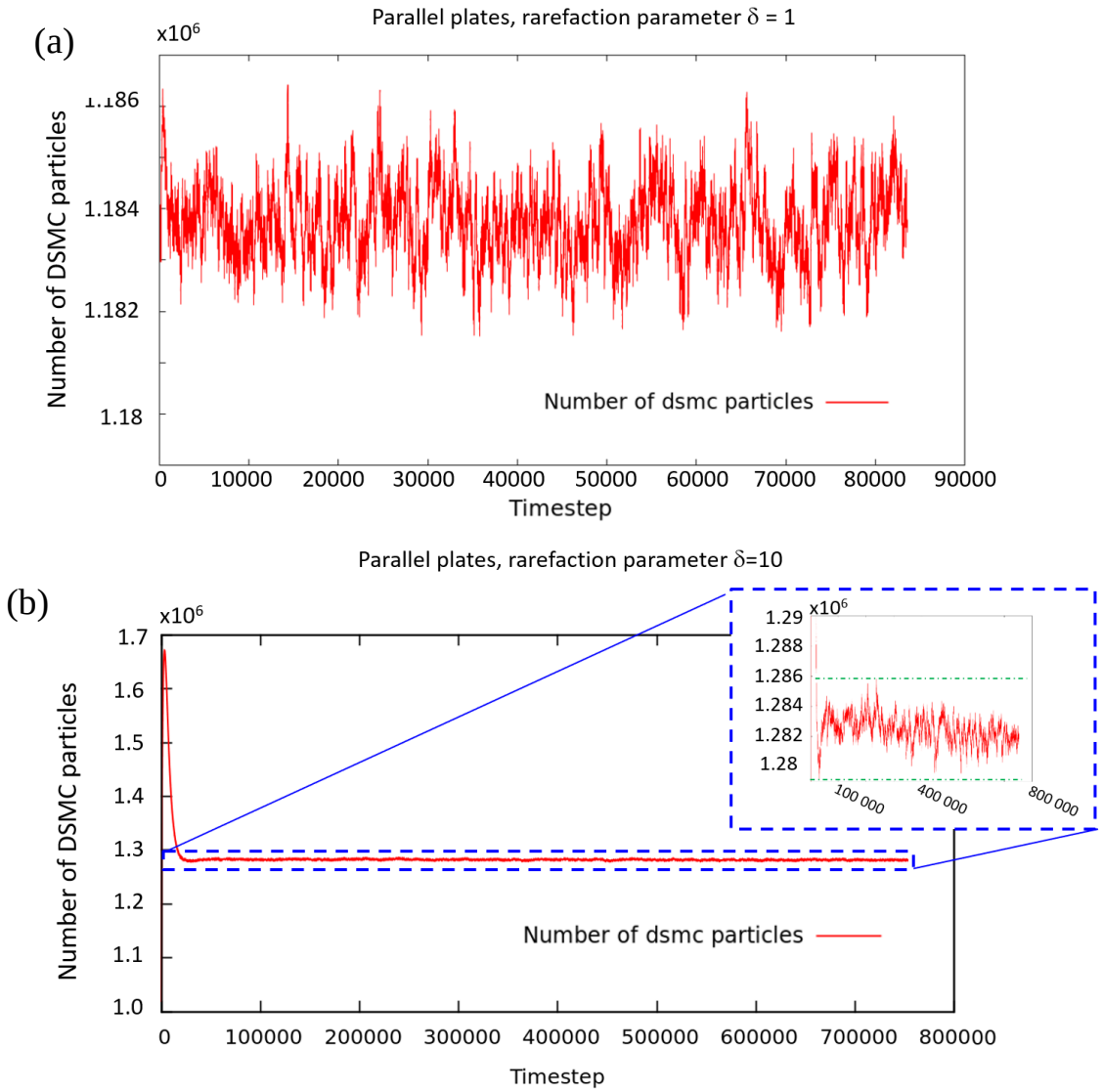

Figure 4.3 Number of DSMC particles in the system for the rarefaction parameter (a) δ = 1 and (b) δ = 10, for the parallel plates studies of Argon gas, VHS collision model, gas temperature of 300 K, *L/H*=5, outlet/inlet pressure ratio of 0.1.

The numerical calculation of the pressure along the channel length (at $y = 0$) with *dsmcFoam* and the closed expression developed by Gallis *et al*. are shown in Figure 4.4. For the comparison 100 points equally distributed along the x-axis in the DSMC calculation have been sampled and plotted.

The analysis showed that along the majority of the channel length a relative difference of 5% between DSMC and the expression of Eq. (4.4) is found, representing 66% of the total sampled points for the studies with δ = 10. In the case of δ = 1 is observed that 82% of the sampled points have a relative difference of 6%. At the channel entrance the values of DSMC and the closed expression have the maximum deviation in all the study cases

and around the value 0.2 of *x/L*, the difference between both values is considerably reduced, as an example of this observation in Figure 4.5 is shown the percentage difference distribution between the *dsmcFoam* solver and Eq. (4.4) for the case mid- and high-collisionality. As reported in [88], by increasing the pressure the concavity of the profile varies, which is exactly what is here observed. This gives the author the confidence that the DSMC solver captures the main characteristics of the gas flow in the channel for different flow regimes.

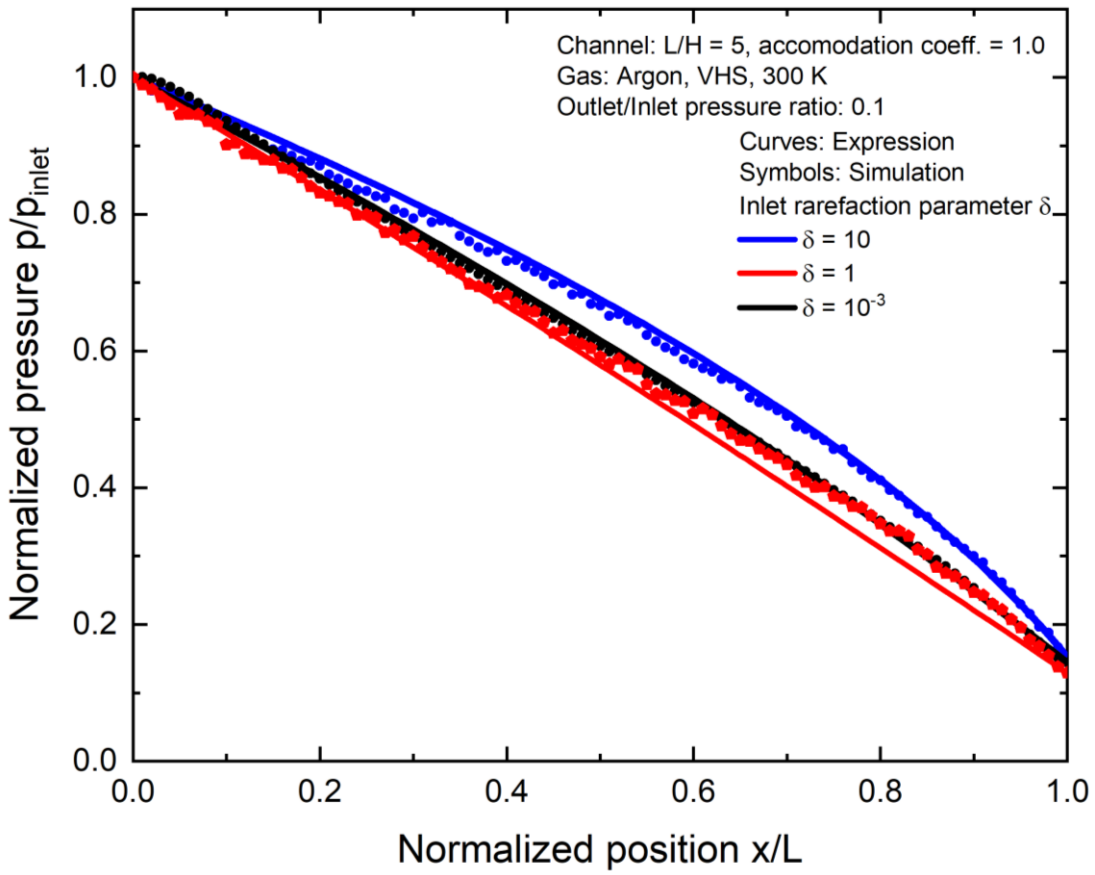

Figure 4.4 Normalized pressure as a function of the normalized position along the *x*-axis (channel length): gas Argon, VHS collision model, full accommodation coefficient at the wall (diffuse scattering), temperature of 300 K, *L/H*=5, outlet/inlet pressure ratio of 0.1, rarefaction parameters of 10^{-3}, 1 and 10.

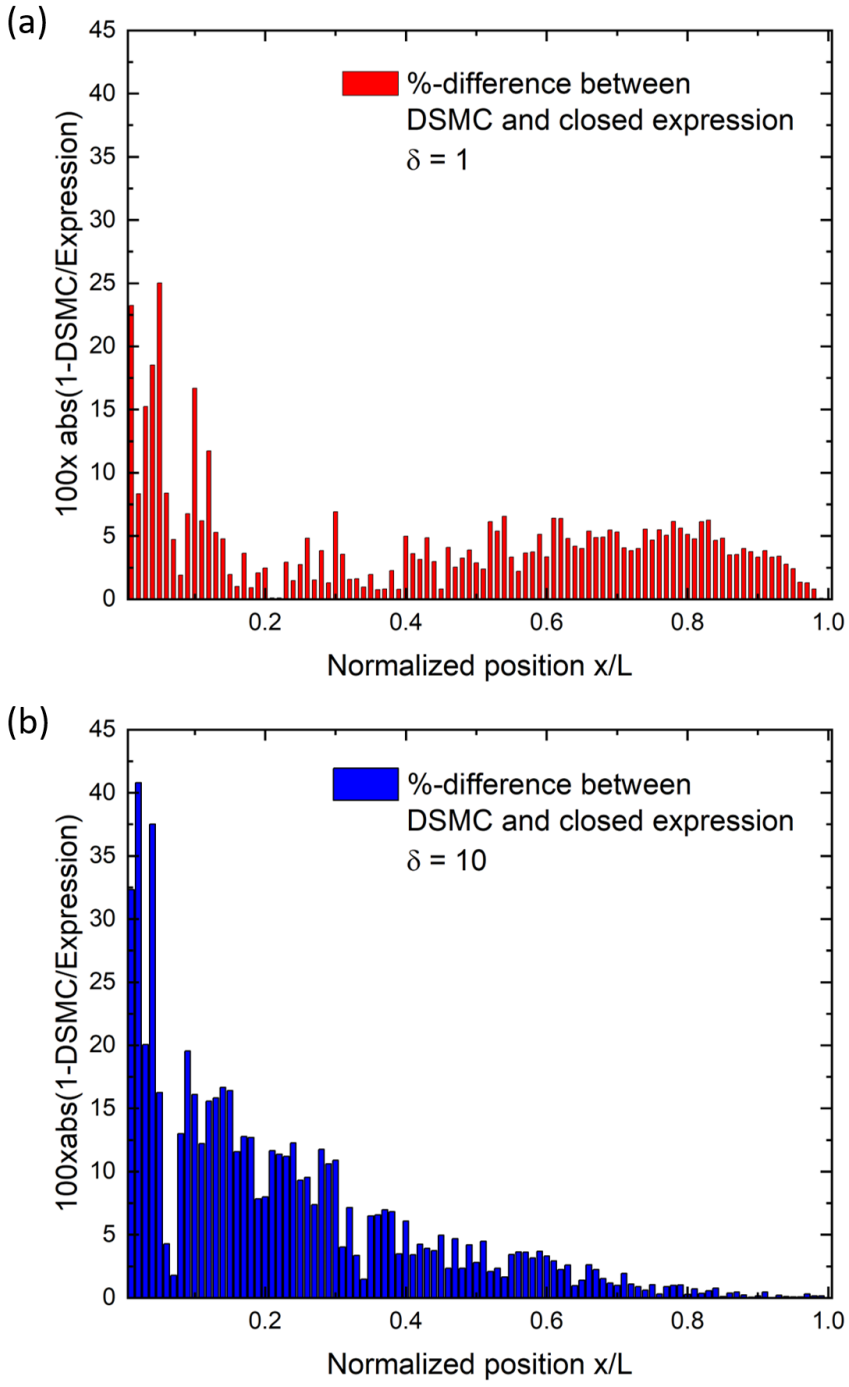

Figure 4.5 Percentage difference between DSMC and Eq. (4.4) for the values of the pressure along the channel axis (y = 0) for the DSMC analysis for rarefaction parameter (a) and (b) δ = 10. The plot is generated by sampling the pressure values along the the x-axis: The DSMC simulations employs Argon as working gas, VHS collision model, full accommodation coefficient at the wall (diffuse scattering), temperature of 300 K, L/H=5 and outlet/inlet pressure ratio of 0.1.

As next step, the DSMC solution obtained with *dsmcFoam* is benchmarked with numerical analysis obtained in [24] studying the same geometry. The numerical studies in [24] focuses on the numerical simulation of the gas flow through parallel plates with DSMC for a wide range of conditions which includes the ratios p_R/p_L and L/H here studied. The present comparison focuses on the ratio length-to-height L/H of 5 and a value of the pressure ratio p_R/p_L of 0.1.

In Figure 4.6 are shown the pressure profiles predicted by the *dsmcFoam* and the values reported in [24] along the channel length and at the channel axis ($y = 0$). The plots shown in Figure 4.6 are normalized to the pressure values found at the channel inlet. The pressure evolution is well-captured by the DSMC code, where the values for $\delta = 10$ lie above the ones of the case $\delta = 1$ across the whole channel length. The axial profile of pressure increases its curvature with the increase of the rarefaction parameter, as seen in [24] and in [90].

The results for the reduced flow rate W in terms of rarefaction parameter δ are shown in Figure 4.7. As expected, the reduced mass flow in the present work tends to its value at free molecular conditions as δ goes to zero. However, the present *dsmcFoam* solver predicts higher values of the reduced mass flow rate by 20% to 30%. Since the model in [24] employs a different mesh strategy, three-level grid, for the same flow conditions, as a second step a finer grid for the the flow in the *dsmcFoam* solver is employed. The refinement is applied to the study case $\delta = 10^{-3}$. The same geometry boundary conditions i.e. $L/H = 5$, $p_R/p_L = 0.1$ for the "finer mesh" case for $\delta = 10^{-3}$ are employed. The temperature is taken as 300 K as before. For this case, the structured mesh consisted only of 700 divisions in the horizontal and 120 in the vertical direction are employed. A comparison of the computed reduced flow rates with those in [24] is given in Table 4.2. Results show that the calculated values of the reduced mass flow rate W are in numerical agreement within 10% for the coarse mesh. By employing the grid refinement, the relative different between the reduced mass flow rates is 2%.

(a)

(b)

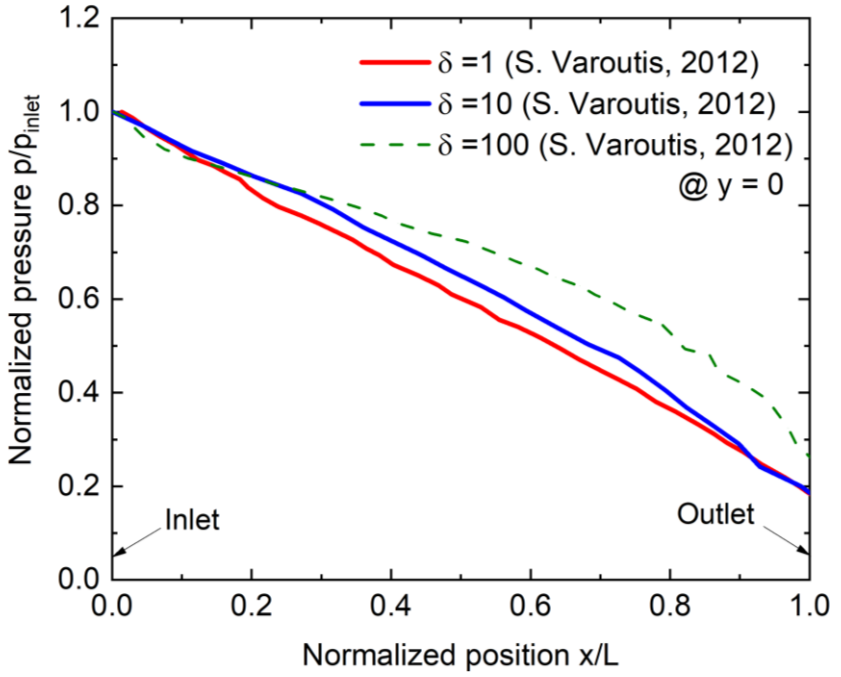

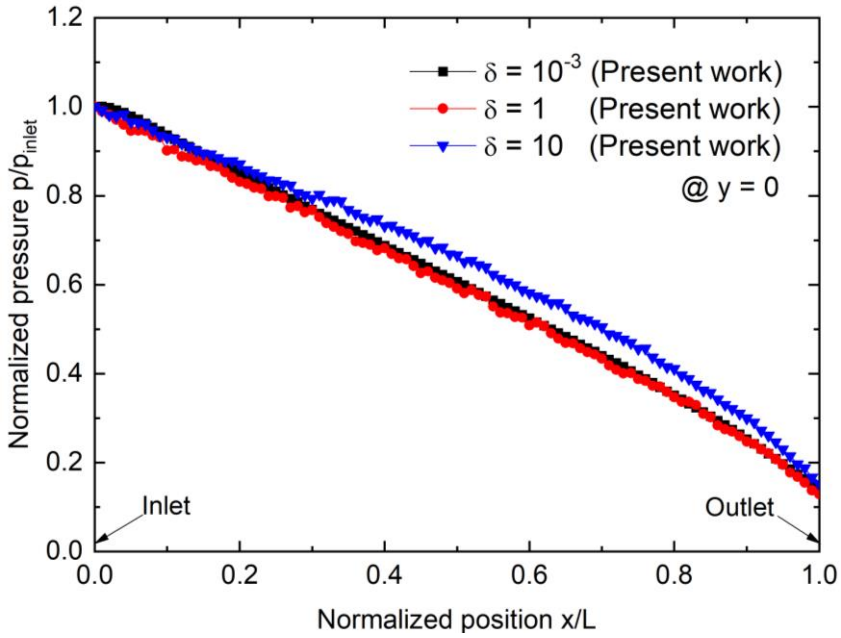

Figure 4.6 (a) Pressure evolution along the channel at the channel axis (y = 0) calculated with the *dsmcFoam* code for the cases $\delta = 10^{-3}, 1, 10$ for the pressure ratio $p_R/p_L = 0.1$ and L/H = 5. (b) The reference values in [24] are sampled at the axis of the channel L/H = 5 and $p_R/p_L = 0.1$.

Table 4.2 Reduced flow rate W as function of δ, $p_R/p_L = 0.1$ aspect ratio $L/H = 5$

δ	W			$\frac{\lvert\Delta W\rvert_{(a)}}{W}$ (%)	$\frac{\lvert\Delta W\rvert_{(b)}}{W}$ (%)
	(a) Coarse Mesh	(b) Fine Mesh	Ref. [24]		
10^{-3}	0.3531	0.3145	0.321	9.1	2.02

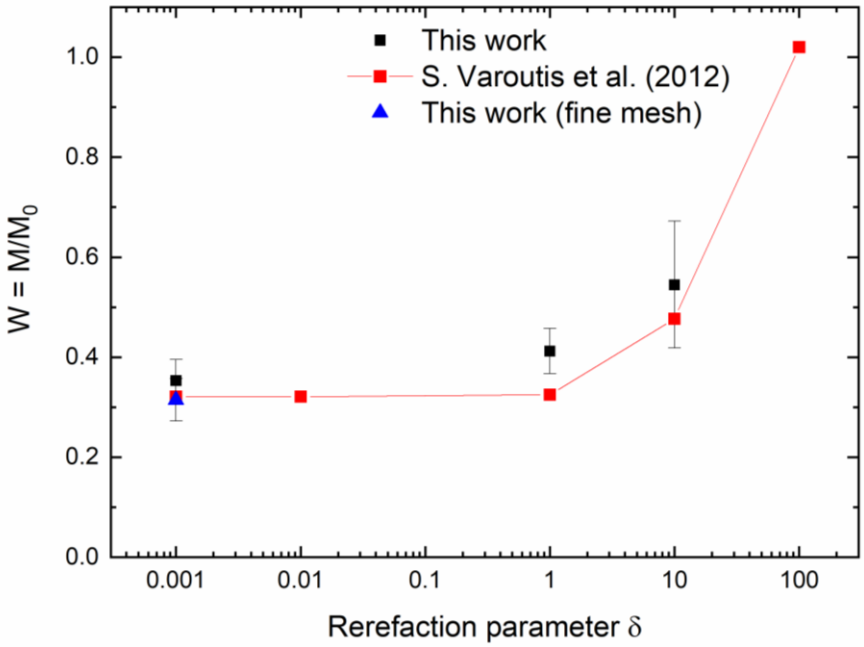

Figure 4.7 Reduced flow rate W as a function of the rarefaction parameter δ for p_R/p_L = 0.1 and L/H = 5.

It is concluded that the reduced mass flow rate of this system is very sensible to the employed computational grid. A gain of 8% relative to the target value of Ref. [24] is achieved when a denser grid is employed (factor of 1.4 in Δx and 1.2 Δy). The founding is crucial, since at the beginning of the chapter, the sensitivity of the cell size suggests that a 500x100 grid yields the minimum variation of the macroscopic variables. As suggested in [24], a multi-level grid is suitable for axy-symmetric flows in order to capture the gradients near the wall.

By following the strategy of a single-level grid in a flow with preferential direction, a reduction of 30% on the cell size translates in a reduction of 12% in the mass flow rate. This means that for this type of flow configuration, a necessary condition for the DSMC method to provide an accurate solution (lower bound) is given by $\Delta x/\lambda < 0.01$, which is less than unity, as stated in chapter 3. For the time step it is here suggested, once the cell size is selected, to choose a simulation time step such that $\Delta t < \tau_{coll}$, which ensures that only one collision can occur during a simulation time step and the decoupling

assumption of DSMC between movement and collision steps is fulfilled. The collision time is dependent on the mean free path which is related to the cell size of the mesh. In our case, 1/10 τ_{coll} is more than sufficient to fulfill the DSMC condition. Additional to the timestep, care must be taken by selecting the cell size and the number of particles in the cell, because by maintaining the number of particles constant in the system and by increasing the number of computational cells, the fluctuations are expected to increase since $\Delta \propto 1/\sqrt{N}$ and thus the statistical noise of the flow field variables increases too. Therefore, the effects of the deterministic errors on the macroscopic flow variables A_i, i.e. A_i are analyzed as a second step. The deterministic errors are based on the analysis of a system by modifying the DSMC parameters and therefore the rest of the chapter will treat the deterministic erros in the following order:

1. Real-to-DSMC particle ratio F_N.
2. Cell size Δx .
3. Time step Δt .

For the analyses, the working gas is Argon, the ratio of out-to-in pressure is 0.1, the ratio *L/H* is 5 as before. The temperature at inlet, outlet and wall is set to 300 K. The rarefaction parameter at inlet is defined as $\delta_{in} = 10^{-3}$ such that the Knudsen number is much greater than 10, in order to have free-molecular flow conditions (Kn ~ 886). In such rarefied flow conditions, the mean collision time τ_{coll} of 1.89 s.

4.2 Particle number effects

The reduction of number of particles in the system has been done by modifying the real-to-simulated particle rate F_N. Thus, in order to address the effect of the number of DSMC particles in the system, two study cases are compared against the reference simulation, where the F_N is a factor of 10 and 100 the reference simulation.

The sampling procedure has been performed in all cases, once achieved the steady state conditions, where the number of iterations of the simulation $N\Delta t$ of the order of 10^4 have been conducted. The importance of the number of particles N_0 is directly related to the statistical errors shown in Table 3.2 in Chapter 3.7,where a functional dependence of $E_{Statistical} \sim 1/\sqrt{N_0}$ is found. Figure 4.8 illustrates the effect of the total number of DSMC particles on the magnitude of the flow velocity at the channel center where the profile has a parabolic-shape. In all the simulations the time step and the cell size are kept constant and equal to the reference case. A maximum variation of 7% in the flow speed profile as a function of the transverse coordinate-*y* between the reference simulation and the two simulations with 10 and 100 times the real-to-simulated ratio is observed. For the latter simulations, the profiles scatter around the reference solution and the relative differences are enhanced in the interval $y = [-0.2, 0.4]$.

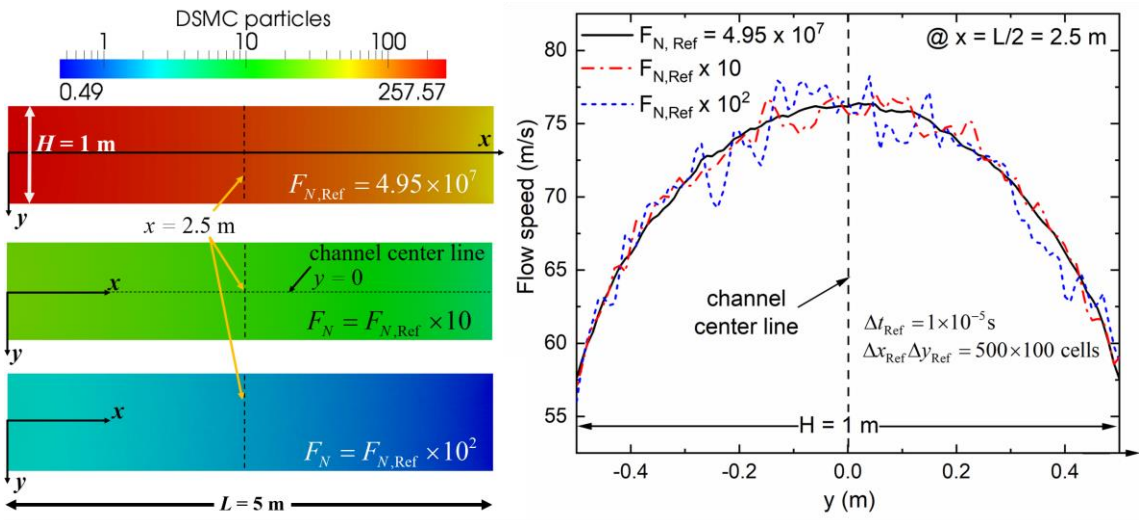

Figure 4.8 Influence of the total number of particles employed in DSMC simulations for Poiseuille flow. Left: DSMC particles across the domain for three simulations, each with different F_N. Right: The flow speed profile at the middle of the channel for the different F_N case studies.

Moreover, the suggested 30-40 DSMC particles per cell for a *good* DSMC practice has been accomplished for the reference case (average ~ 160 DSMC particles) and the DSMC simulation with $F_N = F_{N,Ref} \times 10$ (16 DSMC particles). For the case of the real-to-simulated particle ratio $F_N = F_{N,Ref} \times 100$, cells with less than 2 particles have been detected in the area near the outlet (low pressure side of the channel) and barely 3 particles per cell have been identified near the inlet. In Figure 4.9 the evolution of the number of DSMC particles along the channel axis (center line, y = 0) is shown for stationary conditions. In the reference study case, by summing the number of collisions over all the cells an average of 20 collisions in the whole system is obtained. For the case $F_N = F_{N,Ref} \times 10$, a total of 3 collisions across the whole channel are calculated, reflecting the reduction of total number of particles available for defining a collision partner (pairs). This underlines the importance of setting the minimum particles per cell. For the present flow conditions, the reference case fulfills the condition of more than 20 DSMC particles at each cell in the domain, see in Figure 4.9 the shadowed region in green.

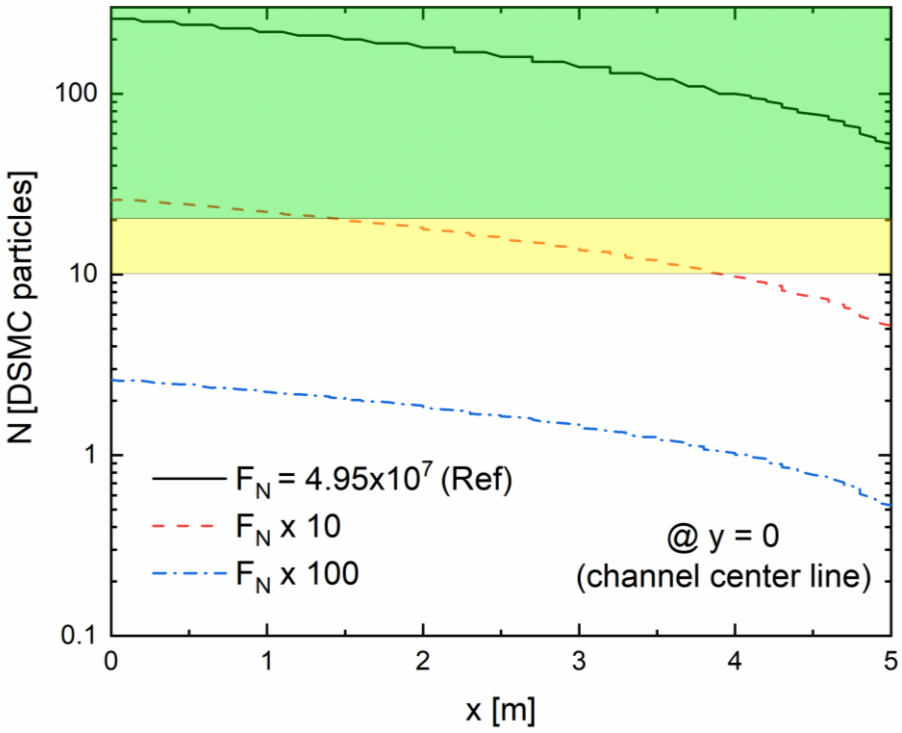

Figure 4.9 Number of DSMC particles along the center line of the channel (y = 0) plotted from inlet to outlet. The green shadowed region depicts the range where the number of particles is greater than 20, whereas the yellow region encloses the range where the number of particles ranges between 10 and 20.

Along the x-axis variations between the temperature and velocity profiles are presented in Figure 4.10 and Figure 4.11, respectively. The evolution along the x-axis of the temperature T, normalized to the inlet temperature in the reference simulation, is shown in Figure 4.10. No significant variations are found in the temperature profiles (~ 1% relative difference between the three cases). Same dependence for the temperature is found along the axis in [24], i.e. in all studies a decrease of the temperature is observed, as expected for a gas subject to an expansion (gas flowing from a higher to a lower pressure region, $p_R < p_L$).

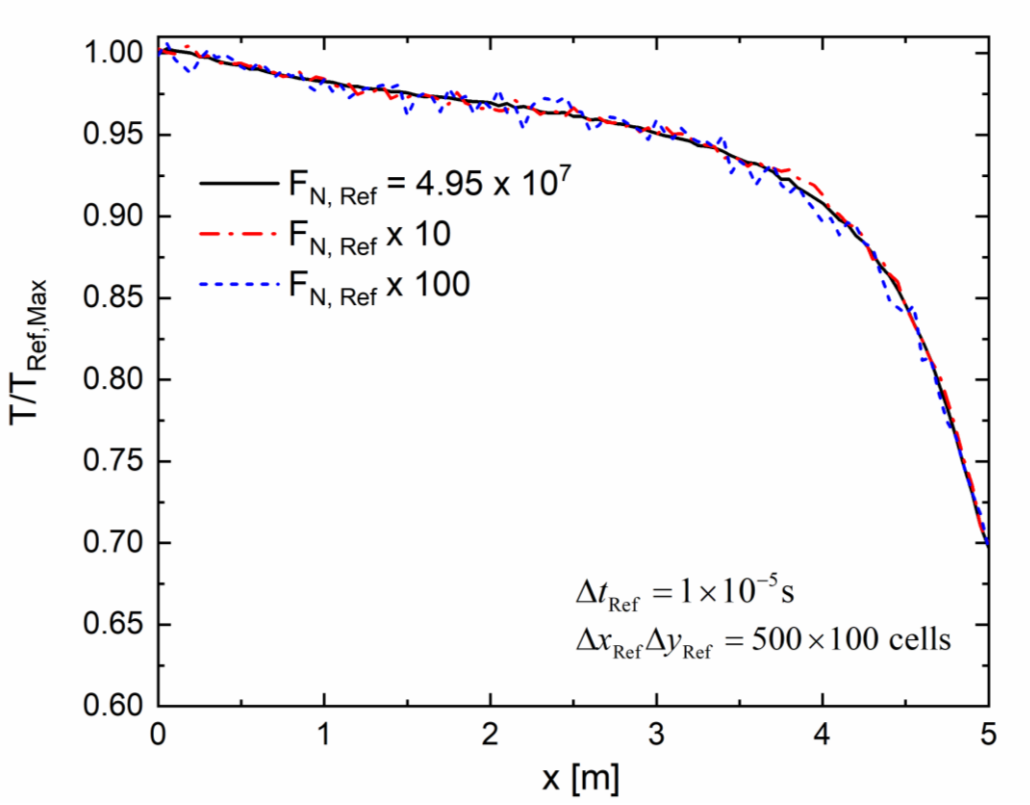

Figure 4.10 Variation of total number of DSMC particles for a Poiseuille flow and its effects on the macroscopic variables along the channel. The temperature normalized to the maximum temperature at inlet of reference case is plotted along the x-axis at $y = 0$ (axis of channel).

The axial velocity (x-direction) is shown in Figure 4.11(a). According to the decrease on the temperature values shown in Figure 4.10 due to the expansion, the flow speed increases by a factor of 5.5 relative to the inlet speed (initial speed at the channel entrance $x = 0$), see Figure 4.11(a) and (b). Fluctuating values around the reference solution are observed and enhanced in the beginning and the mid-part of the channel length, as shown in Figure 4.11(b).

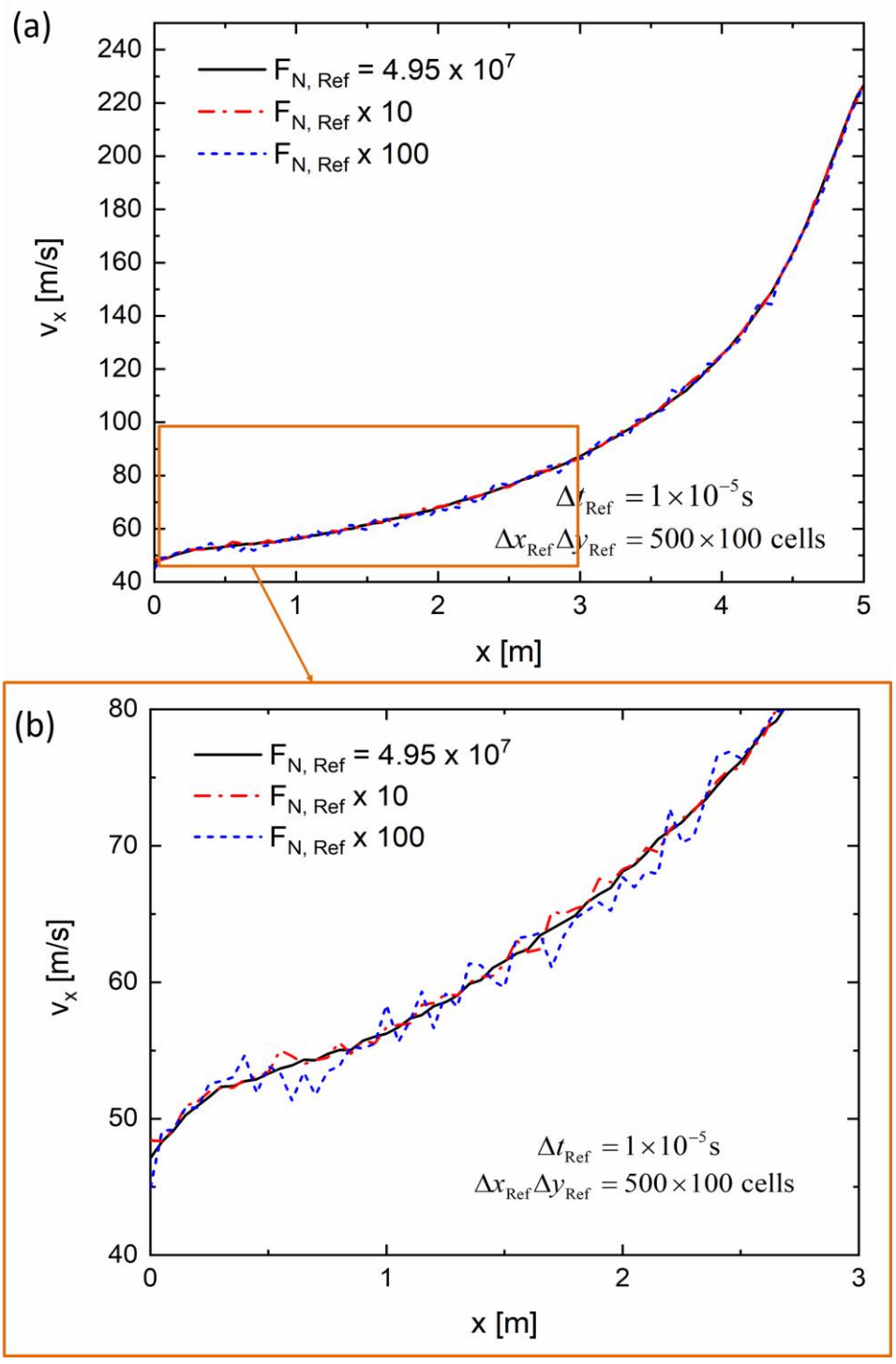

Figure 4.11 Variation of total number of DSMC particles for a Poiseuille flow and its effects on the macroscopic variables along the channel: (a) Flow velocity magnitude in the *x*-direction and (b) an enhanced view of the velocity in the *x*-direction (first half of the channel).

4.3 Cell size Δx effects

The macroscopic variables in the DSMC method are obtained as mean values of quantites over the cell volume in the computational domain. Thus, deviations can be found if the cell dimensions are comparable or larger than a mean free path. Here, the reference simulation is compared with two coarser meshes: one with the number of elements reduced by a factor of 4 (250x50 cells, coarse mesh) and one by a factor of 16 (125x25 cells, maximum coarse mesh). For all the cases, the time step and real-to-simulated particle ratio were constant and equal to the reference simulation, namely $\Delta t_{\mathrm{Ref}} = 1 \times 10^{-5}$ s and $F_{N,\mathrm{Ref}} = 4.95 \times 10^{7}$ respectively. Figure 4.12 presents the behavior of the flow speed ploted along the *y*-axis at the center of the channel (x = 2.5 m) as a function of the cell size. In examining the relative differences of the flow speed profiles obtained in the three cases, two main observations are found:

1) First, although no significant differences are observed in the flow speed profiles, see Figure 4.12(a), the relative values of the flow speed between neighboring cells increase as the cell size decreases as shown in Figure 4.12(b) and (c). At first sight this could be misleading since it is expected a converged behavior of a macroscopic variable A if one has in the limits $\Delta t \to 0$, $\Delta x \to 0$ and $F_N \to \infty$. However, the total number of DSMC particles is constant for three simulation and thus, at the same geometrical point, increasing the cell size translates in a reduction of the statistical scattering, because more DSMC particles contribute to the average of the macroscopic variable than the reference simulation. This suggests, that for the present rarefied gas conditions a coarser mesh can contribute to the reduction of the variation of macroscopic variables across the computational domain, see Figure 4.12(b)-(c).

2) The second observation has to do with the offset between velocity profiles. The velocity in the x-direction along the channel length (midplane y = 0, channel axis) is shown in Figure 4.13. The profiles show no anomalous behavior following a parabolic form and all the profiles of coarser meshes lie above the reference solution as seen in Figure 4.12. The requirement for the mean free path ($\Delta x < \lambda$) in all the three study cases is accomplished.

(a)

(b)

(c)

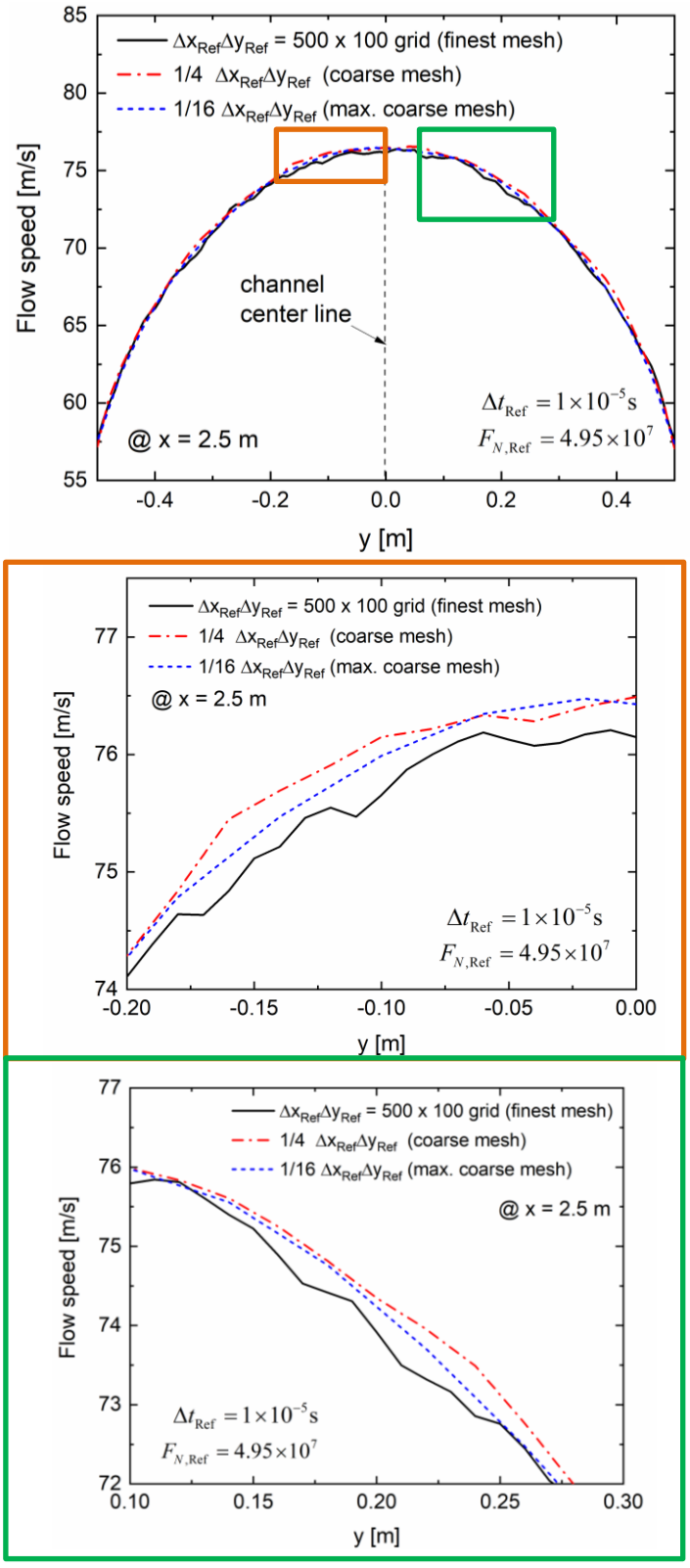

Figure 4.12 Calculated streamwise velocity of a Poiseuille flow as a function of the spanwise coordinate y in the plane x = 2.5 m for different spanwise resolutions for $\Delta t = 1 \times 10^{-5}$ s, $F_N = 4.95 \times 10^7$. b) close-up of a) in the same x-plane for -0.2 m < y < 0 m. c) close-up of a) in the same x-plane 0.1 m < y < 0.3 m.

In all cases the rate of change of the speed is positive and only the two cases with coarser meshes differ on the value of the initial velocity with the reference simulation by 11%. This difference remains constant around the point x = 3 m and from this location the relative difference between cases is reduced to < 5 %. The figures suggest an overestimation of the flow speed with coarser grids.

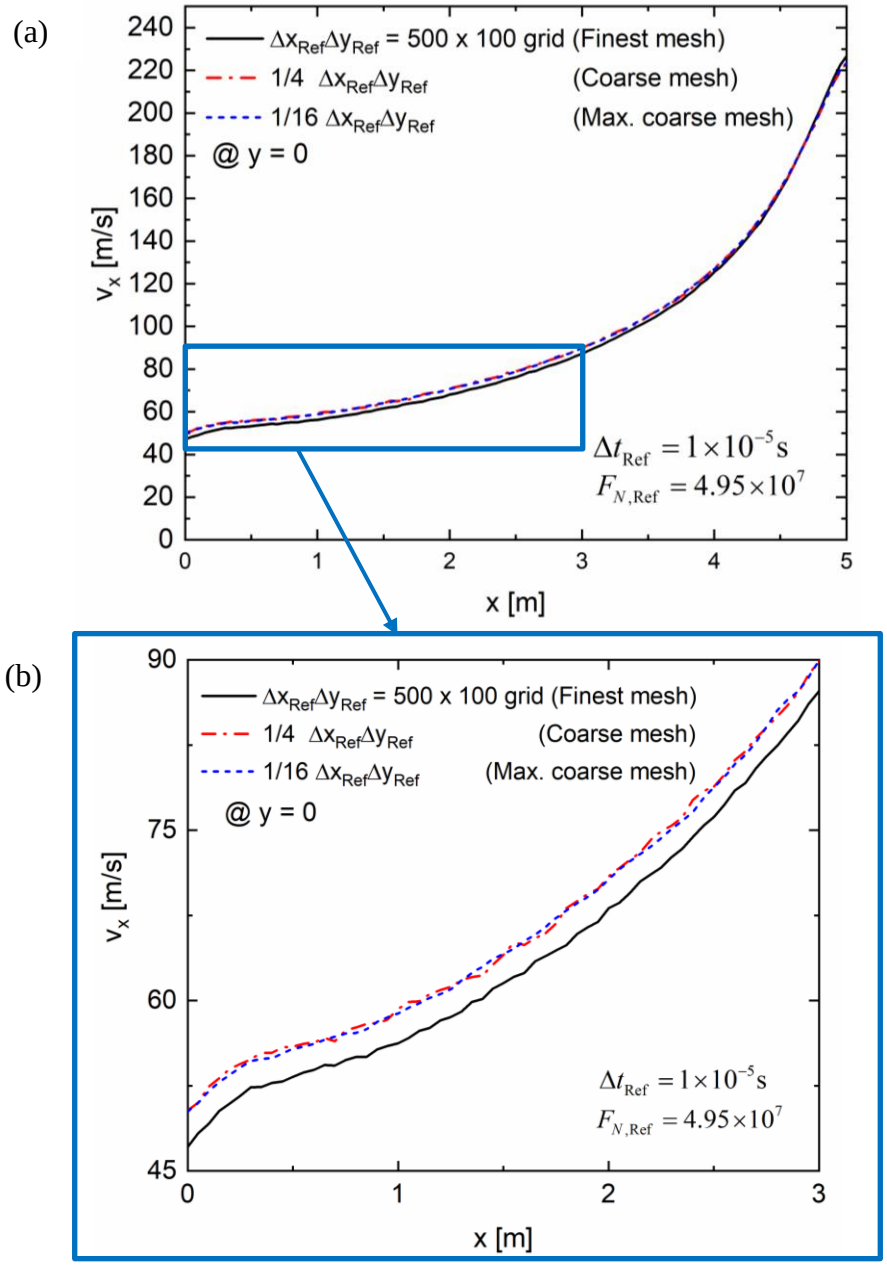

Figure 4.13 Streamwise velocity (a) of a Poiseuille flow as a function of x in the midplane y = 0 for $\Delta t = 1 \times 10^{-5}$ s, $F_N = 4.95 \times 10^7$ and different spanwise resolutions. (b) Enhanced view of the velocity at the first half of the channel.

In Figure 4.14 the calculated pressure along the channel midplane (y = 0) for different spanwise resolutions is shown. A maximum deviation of 1.7 % relative to the reference value is found between the case studies. The observed weak dependence of the pressure with the cell size is reported in [54]. Such independence follows from the fact that in the DSMC method the positions of the colliding particles are uncorrelated with the change in their velocities, as expected for ideal gases, where the particles do not interact with one another [57] pp 352. For flows at high vacuum conditions, where the collisions between particles do not play a predominant role, the selection of the cell size can be more flexible. In any case, the DSMC criterion for the cell size and the mean free path $\Delta x < \lambda$ should always be met.

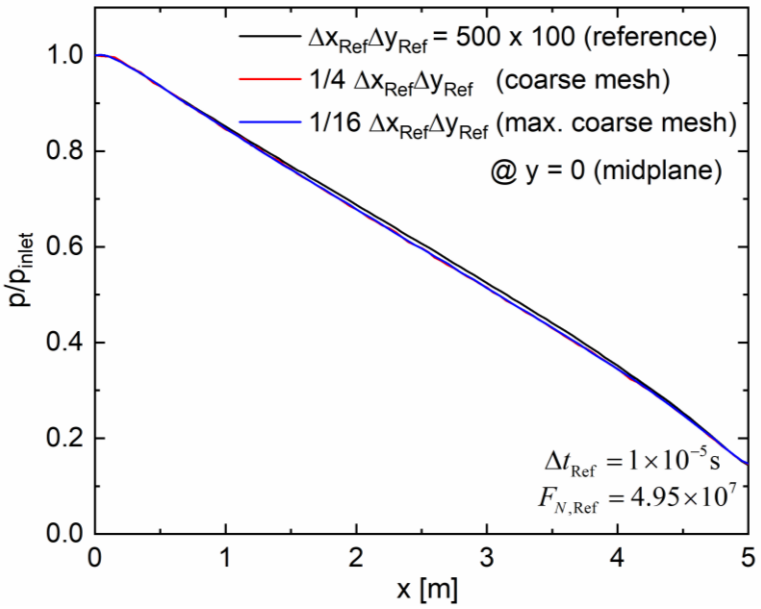

Figure 4.14 Pressure profiles for a Poiseuille flow at the midplane y = 0 for $\Delta t = 1 \times 10^{-5}$ s, $F_N = 4.95 \times 10^7$ and different spanwise resolutions.

4.4 Time step Δt effects

The time-step Δt plays a key role in decoupling the movement and collisions steps in the DSMC method. Regarding the reference simulation, the time step fulfilled the DSMC criterion of having $\Delta t < \tau_{coll} = \lambda / v_{mp}$ at the physical domain. For comparison purposes, three additional simulations have been executed using time steps of $5 \times \Delta t_{Ref}$, $10 \times \Delta t_{Ref}$ and $100 \times \Delta t_{Ref}$, respectively. In these additional simulations, the employed computational mesh and the real-to-simulated particle ratio remained the same as the reference case.

The effect of the time step on the macroscopic flow variables is shown in Figure 4.15 and Figure 4.16. The flow speed at the channel center (x = 2.5 m) as a function of the y-

coordinate for the three case studies is plotted in Figure 4.15(a). A parabolic profile is observed in all the cases, with a maximum flow speed value at $y = 0$, the mean relative errors of 24.6 and 29.8% between the reference study and the cases with $\Delta t = 10 \times \Delta t_{\mathrm{Ref}}$ and $5 \times \Delta t_{Ref}$ are found, respectively. Between the reference scenario and the highest value chosen for the time step, i.e. $\Delta t = 100 \times \Delta t_{Ref}$, a percentage difference of 19.6 % (mean) is observed (see Figure 4.15(b), black line).

The comparison between velocity profiles along the x-axis is plotted in Figure 4.16(a) in the midplane $y = 0$. For the reference case and the studies with $\Delta t = 5 \times \Delta t_{Ref}$ and $\Delta t = 10 \times \Delta t_{Ref}$it is observed that the axial velocity increases with the similar rate and at $x = 4.5$ m the curves of the reference and the case with $\Delta t = 10 \times \Delta t_{Ref}$ intersect. This is in contrast with the results of the study with $\Delta t = 100 \times \Delta t_{Ref}$, where the axial velocity at the inlet is 3.5 times the value found in the reference scenario. Moreover, its corresponding axial profile does not show the monotonic behavior as the reference scenario, since the slope of the axial velocity changes sign at a distance $x \approx 2.5\, m$ (blue dashed line in Figure 4.16(a)).

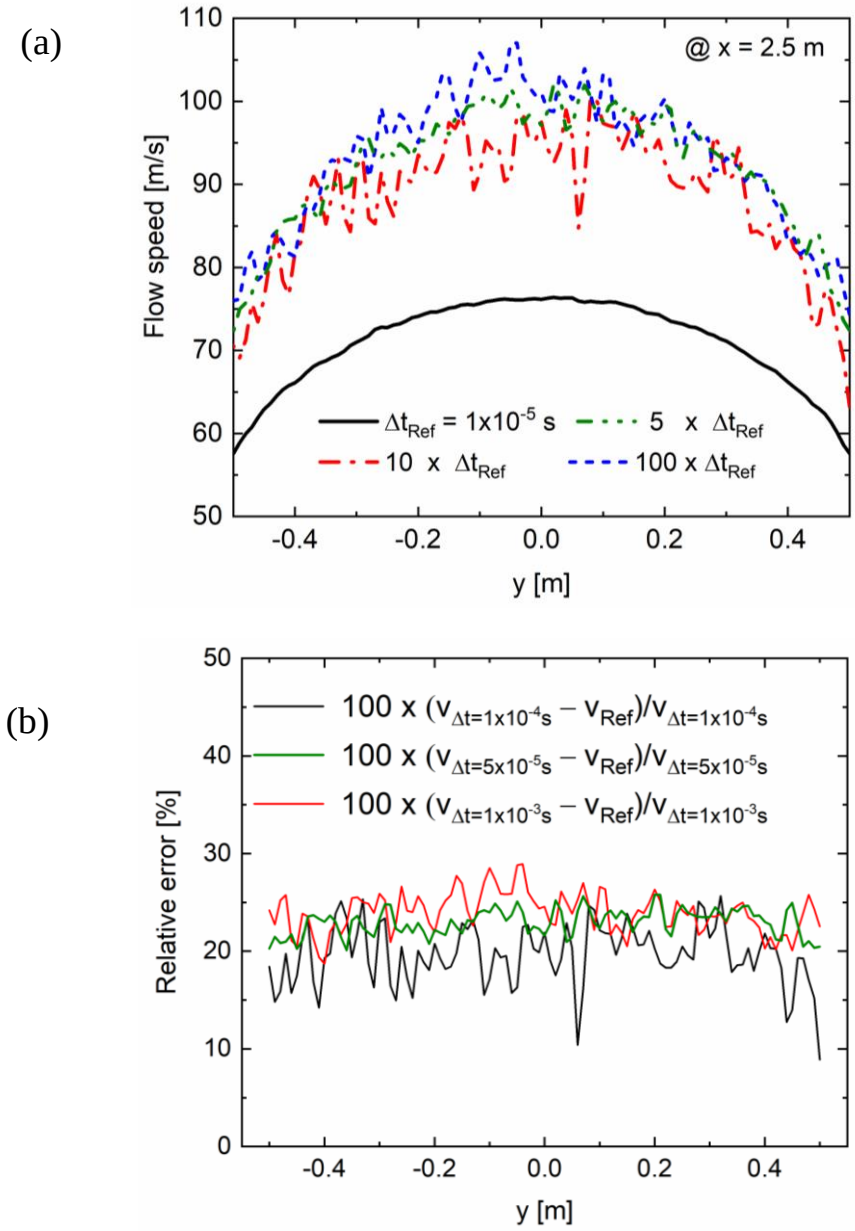

Figure 4.15 (a) Calculated streamwise velocity distribution of a Poiseuille flow as a function of y in the plane x = 2.5 m for four different temporal resolutions. (b) Calculated relative spanwise distribution of the statistical error of the stramwise velocity corresponding to figure (a).

The calculated temperature profiles in the channel mid plane $y = 0$ as a function of the axial coordinate x are shown in Figure 4.16(b). The results of the study cases with $\Delta t = 5 \times \Delta t_{\mathrm{Ref}}$ as well as $\Delta t = 10 \times \Delta t_{\mathrm{Ref}}$ show good agreement with the reference case. The values of $T_{5\times\Delta t_{\mathrm{Ref}}}$ and $T_{10\times\Delta t_{\mathrm{Ref}}}$ oscillate around the reference temperature solution. The difference exhibits an overstimation at the channel outlet of 8.2% (value of $T_{10\times\Delta t_{\mathrm{Ref}}}$ relative to T_{Ref}) and 4.9% ($T_{5\times\Delta t_{\mathrm{Ref}}}$ relative to T_{Ref}). Additionally, the value of $T_{100\times\Delta t_{\mathrm{Ref}}}$ at the inlet is also affected by the unexpected velocity behavior previously described, since

the temperature value is directly related with the particle velocity, i.e. $T \propto v'^2$ (see Chapter 3.5). Thus, an increase of the velocity at the inlet will be reflected in higher temperature at the entrance of the channel, which is captured by the DSMC code. The temperature profiles showed similar dependence with the x-coordinate, a plateau region follow by an enhanced temperature drop at the outlet.

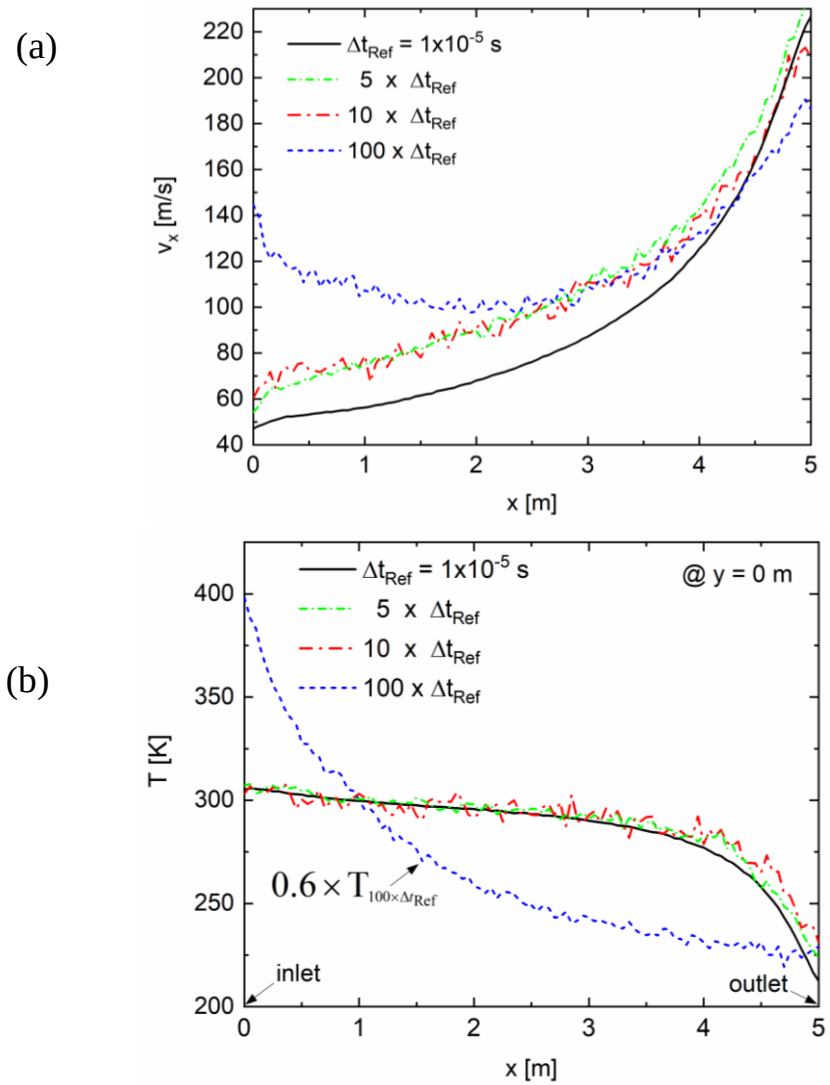

Figure 4.16 (a) The dependence of the axial velocity along the channel for a Poiseuille flow for different time steps. (b) Temperature profiles for three DSMC simulations with different time steps: $\Delta t_{5\times\Delta t(\mathrm{Ref})}$, $\Delta t_{10\times\Delta t(\mathrm{Ref})}$ and Δt_{Ref}.

However, the calculated temperature $T_{100\times\Delta t_{\mathrm{Ref}}}$ yields an exponential drop along the channel depicted in Figure 4.16(b), which contrasts $T_{5\times\Delta t_{\mathrm{Ref}}}$, $T_{10\times\Delta t_{\mathrm{Ref}}}$ and T_{Ref}. This unexpected behavior can be explained by the fact that by employing higher time step values, more than a single collision can occur during Δt which means that the DSMC criterion

regarding the collision time is not met and the separation between movement and collision cannot be treated as a two-step process, as discussed in the previous chapter.

Since the mean free path reflects the collisionality of the gas flow, it is important that the DSMC code predicts the correct interaction beween the particles in the system. In Figure 4.17 the evolution of the mean free path along the channel axis is plotted as function of x for the DSMC simulations with different time steps. All the simulations, except the one with $\Delta t = 100 \times \Delta t_{\mathrm{Ref}}$, showed the expected monotonic increase of λ_{VHS} along the channel axis, due to the fact that the pressure at the inlet is ten times higher as the outlet. Thus, the expected profile of the mean free path is captured by DSMC simulation with time steps $\Delta t < 10 \times \Delta t_{\mathrm{Ref}}$. On the contrary, the simulation with the highest value of time step shows a rather non-physical behavior. The values of the mean free path at the inlet and outlet are almost identical, this means that the pressure at inlet and outlet is equal. This cannot occur, since a pressure difference is needed for a pressure driven flow.

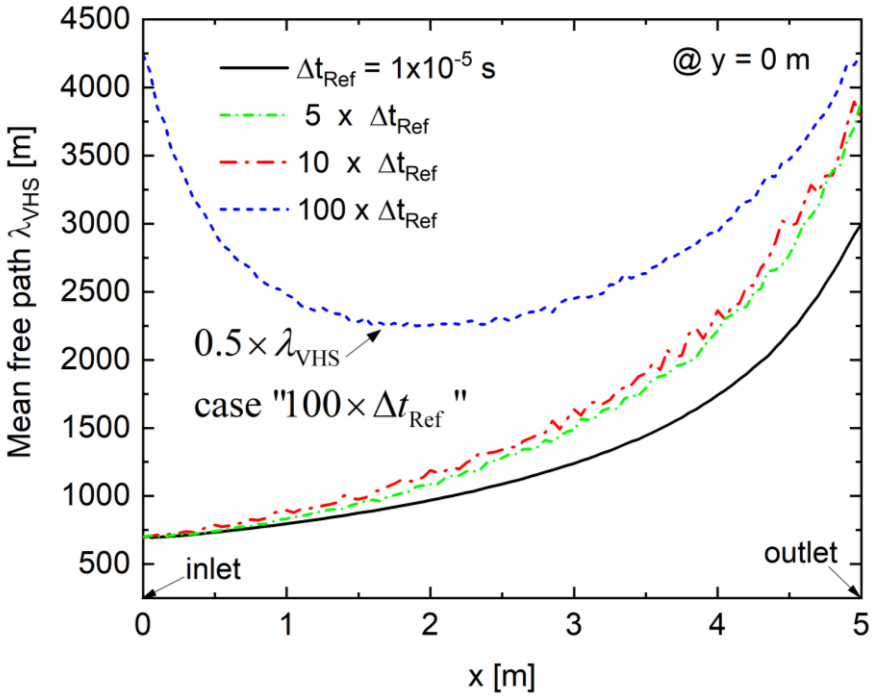

Figure 4.17 Mean free path evolution along the channel length (x direction) for different study cases at the channel axis (y = 0).

The time step variation has the most drastical effect on the macroscopic flow variables among the studied parameters (F_N and Δx). For comparison purposes, three additional simulations have been executed using time steps of $5 \times \Delta t_{Ref}$, $10 \times \Delta t_{Ref}$ and $100 \times \Delta t_{Ref}$, respectively. The flow speed at the channel center as a function of the y-coordinate for the three case studies has a parabolic profile. The maximum flow speed as expected is found at y = 0, the mean relative errors of 24.6 and 29.8% between the

reference study and the cases with $\Delta t = 10 \times \Delta t_{Ref}$ and $\Delta t = 5 \times \Delta t_{Ref}$ are found, respectively. Between the reference scenario and the highest value chosen for the time step, i.e. $\Delta t = 100 \times \Delta t_{Ref}$, a percentage difference of 19.6 % (mean) is calculated. For the reference case and the studies with $\Delta t = 5 \times \Delta t_{Ref}$ and $\Delta t = 10 \times \Delta t_{Ref}$it is observed that the axial velocity increases with the similar rate and at the end of the channel (x = 4.5 m) the curves of the reference and the case with $\Delta t = 10 \times \Delta t_{Ref}$ intersect. This is in contrast with the results of the study with $\Delta t = 100 \times \Delta t_{Ref}$, where the axial velocity at the inlet profile does not show the monotonic increasing behavior as the reference scenario, since the slope of the axial velocity changes sign at the middle of the channel, which lacks of physical sense, since this implies that the fluid is at rest in the middle of the channel. Thus, this means that the net forces at the particles are zero which translates globally in a *no-net* pressure difference between inlet and outlet.

5 Application of the DSMC method to JT-60SA, ITER and ASDEX-Upgrade tokamaks

5.1 Particle flows in JT-60SA: comparison between DSMC and NEUT2D codes and the effects of particle collisions

This sub-chapter focuses on testing the solver capabilities of *dsmcFoam* in its first application on a tokamak divertor:

1. The flow field of a collisionless flow is calculated in the sub-divertor of JT-60SA by NEUT2D and DSMC solvers. The former is a test particle Monte Carlo code for neutrals employed in JT-60SA studies, introduced in Chapter 2.2, whereas the latter, *dsmcFoam,* is set to its *collisionless setup*. The rationale behind this comparison is to show that the capability of the DSMC solver to be set as a *pure* test particle Monte Carlo code, i.e. with no intermolecular collisions. This can be done by switching off the DSMC collision kernel in the solver (see the DSMC flow chart, Chapter 3). As a consequence, the particles will not interact with each other, moving along straight lines and colliding only with the sub-divertor solid walls. In this framework, a direct comparison between both codes is performed.

2. For a high-density operation scenario in JT-60SA, the sub-divertor gas flow is modelled solely by means of the DSMC method. The aim of the analysis is to quantify the effect of the intermolecular collisions in the flow variables in the whole sub-divertor domain. The analysis is first-of-its-kind, since the neutral-neutral interaction has not been yet addressed in JT-60SA by the time the present analyses have been peformed. The versatility of the DSMC code makes possible to address the relative difference between both collisionless and collisional flows. The analysis serves also as basis to understand the physics of the sub-divertor flows in realistic scenarios and to quantify the collisionality regime by means of the Knudsen number, which is relevant to the vacuum system of JT-60SA.

The *dsmcFoam* solver in its original form does not include a boundary condition for particle-surface interaction that models the effect of “absorption” of the particle. Therefore, as part of this dissertation the solver capabilities have been extended by developing the *sticking probability* boundary condition. The main idea of the algorithm is to give a probability to a particle to be absorbed. At each collision of a particle with a pump surface, a random number between 0 and 1 is generated, if the number if lower than the sticking

probability the particle is absorbed, otherwise reflected back to the domain. The detailed description of the boundary condition is found in Chapter 3.4. To guarantee that the boundary condition is working properly, it is necessary to check the particle absorption at the pumping surface in the DSMC code. This is done via a parametric analysis in the sticking probability value. The rationale of the numerical experiments is that a fixed number of particles impinges the pump and with a given probability they are be removed from the domain. By monitoring the particle flux at the pump relative to the incoming flux, a comparison with the initially defined sticking probability can be performed.

5.1.1 Geometry and boundary conditions

The JT-60SA divertor cassette is depicted in Figure 5.1(a). The plasma facing components include the baffles and targets (inner and outer) and dome. The neutral particle flow, represented by yellow arrows, coming from the main chamber enters to the sub-divertor region via the transparencies and moves towards the cryogenic pump located at the bottom of the vacuum vessel.

The benchmark study examines the D_2 gas flow inside the geometry of the JT-60SA sub-divertor, where a simplified 2D-representation has been adopted as indicated in Figure 5.1(b). The sub-divertor includes two inlets and a single outlet. The inlet at the inner divertor target is here referred as Gate 2 (high field side), whereas the inlet near the outer target Gate 1 (low field side). The outlet surface is here referred as pump surface.

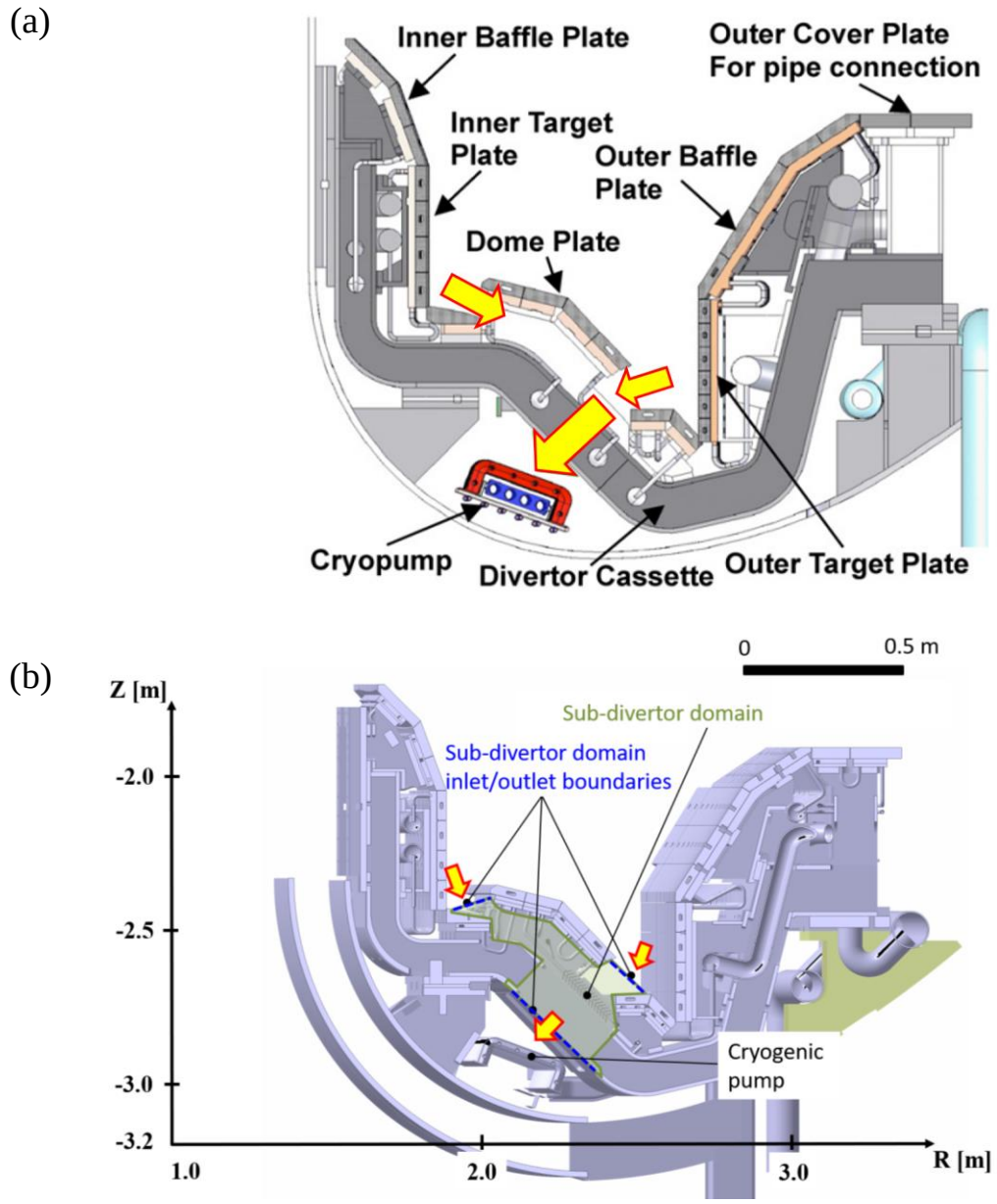

Figure 5.1 (a) The JT-60SA divertor geometry and pumping system: individual components. The yellow arrows represent the gas inflow and outflow in the sub-divertor. (b) The sub-divertor domain is denoted in light green color. The boundaries at the inlet and the outlet are shown with blue dashed lines. The yellow arrows represent the particle flow.

Figure 5.2(a) depicts the physical domain of the sub-divertor and its discretization into cells, the vertices between cells are denoted by the black nodes and the black perimeter in bold line represents the physical boundary of the sub-divertor. In NEUT2D, the macroscopic variables are calculated in the sub-divertor region at the location of the black nodes. The node locations are then employed in DSMC, in order to evaluate the flow variables at the same coordinate. For the benchmark, the chevron baffle located below Gate 1 is not included in the sub-divertor geometry. The reason is to keep the geometry

as simple as possible, since further geometrical elements in the system introduce unnecessary complexity in the analysis.

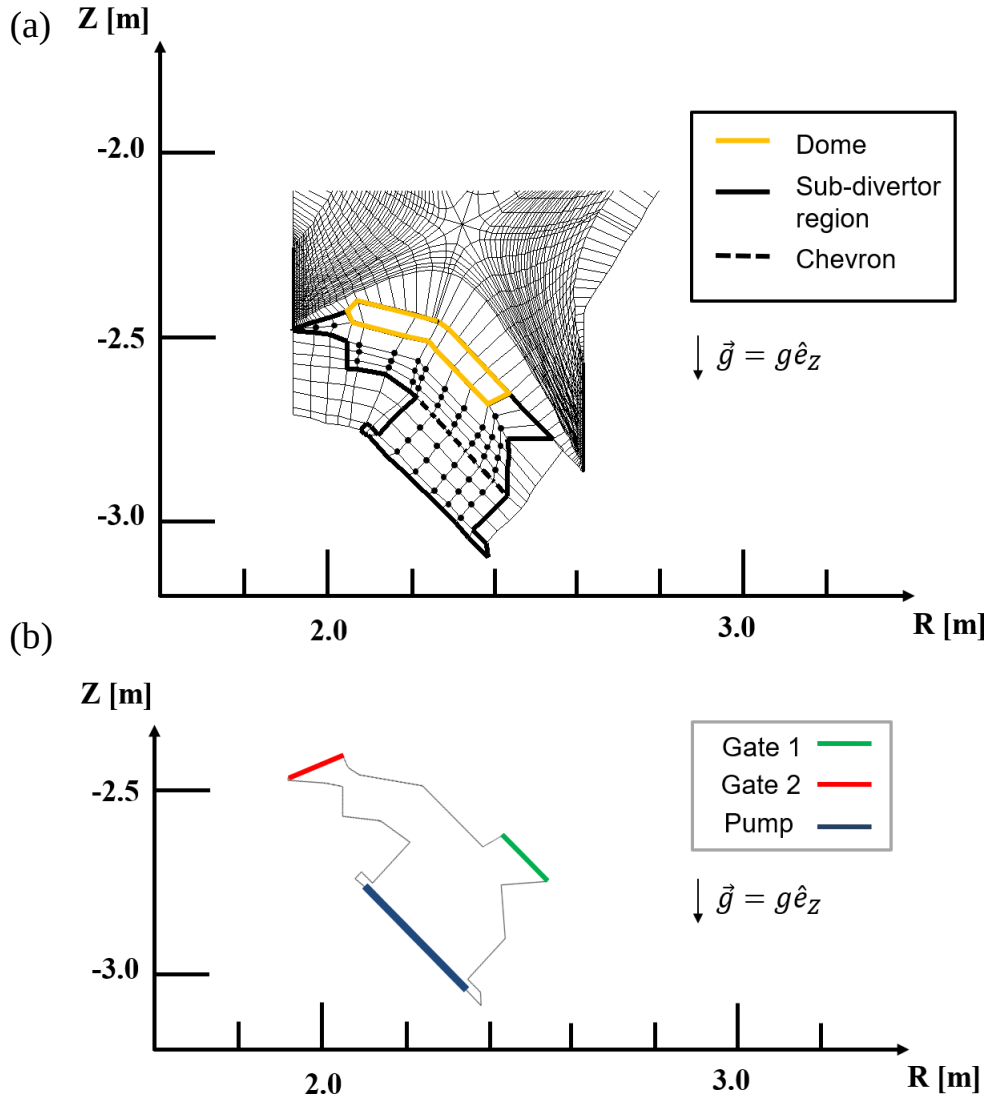

Figure 5.2 (a) The JT-60SA grid: plasma, divertor und sub-divertor region. Sub-divertor region is marked in bold line. At the black nodes (grid vertices) NEUT2D evaluates the flow variables. The same locations are employed in DSMC for the benchmark. (b) Simplified geometry of the sub-divertor domain and the location of the imposed boundary conditions for DSMC and NEUT2D. The direction of the gravity is also shown.

For the second part of the analysis, the collisional effects in deuterium gas flow, a major challenge is the definition of the interfaces (divertor/sub-divertor) as well as the boundary conditions between the sub-divertor and the neutral particles influx from the vessel. This means that the presence of the neutrals coming from the private region and divertor targets towards the sub-divertor has to be introduced by a proper choice of boundary conditions, as explained in Chapter 1.2. Thus, at Gate 1 and Gate 2, i.e. interfaces between plasma main chamber and sub-divertor, the values of the flow field

variables from NEUT2D are set as boundary conditions for DSMC. In the comparision analysis between DSMC with and without collisions, the simplified structure representing the chevron is included in the model. The pumping surface (Pump) located at the bottom part of the physical domain absorbs the particles with a certain probability, yielding a desired ratio of absorbed-to-incoming-particles at the pump.

As mentioned before, the *dsmcFoam* solver in its original release does not include such boundary condition for particle-surface interactions. Therefore, the developed *sticking probability* boundary condition needs to work properly, and therefore it is necessary to check the particle absorption at the pumping surface in the DSMC code. To do this a parametric analysis of the sticking probability values is performed. By monitoring the particle flux reflected back from the pump relative to the incoming flux, an statement can be given regarding the amount of particles absorbed at the pumping surface.

The DSMC solver has the capability to monitor *on-the-fly* the particle fluxes at particular surfaces. The use of structured meshes as shown in Figure 5.3 facilitates the placement of the virtual surfaces at specific locations in the sub-divertor domain, where the *monitoring* takes place. Three virtual surfaces are placed across the domain: the two virtual surfaces near Gates 1 and 2 and a third surface is placed close to the pumping surface as shown in Figure 5.3.

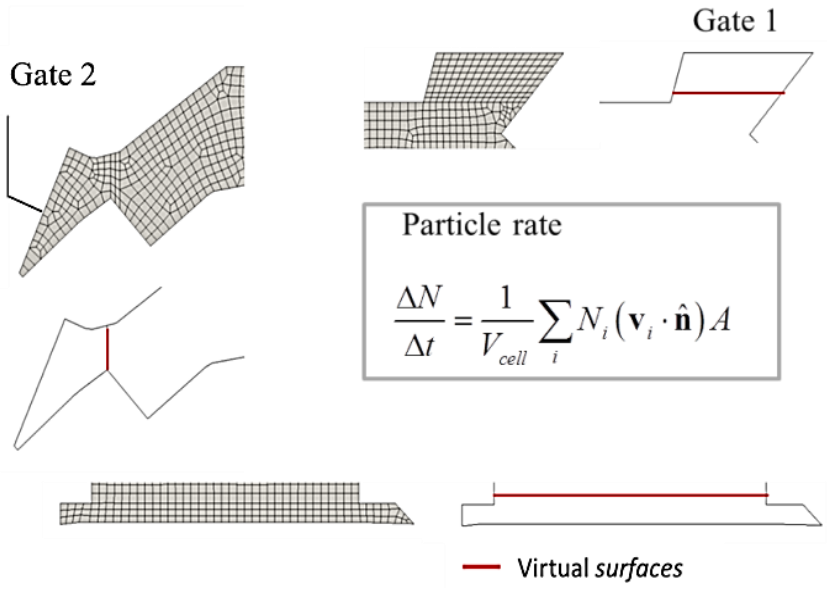

Figure 5.3 An example of a 2D rectangular mesh employed. The red lines are virtual *surfaces* placed on top of the rectangular cells at that location, which monitor the particle rate at any time during the DSMC simulation.

The results of the sticking probability variation are shown in Figure 5.4. The sticking probability is varied from unity (all particles are absorbed by the pump, trivial case) to the minimum value of 0, where all the particles arriving to the pump are reflected back

to the sub-divertor. A total of twelve simulations, all with a constant particle rate of 1.485×10^{18} part/s flowing towards the pump, are conducted. In Figure 5.4 the linear relation between expected sticking probability and the DSMC modelling suggests that the boundary condition simulates the desired number of pumped particles. For values of the sticking probability lower than 0.02, it was found that the relative difference between DSMC and the expected value ranges between 9% and 15%. The simulations involving sticking values between 0.03 and 0.1 yield a difference from the expected sticking probabilities between 1.8% and 4.2%. The rest of the simulated the sticking probabilities has a maximum difference of 10% and a minimum of 3%.

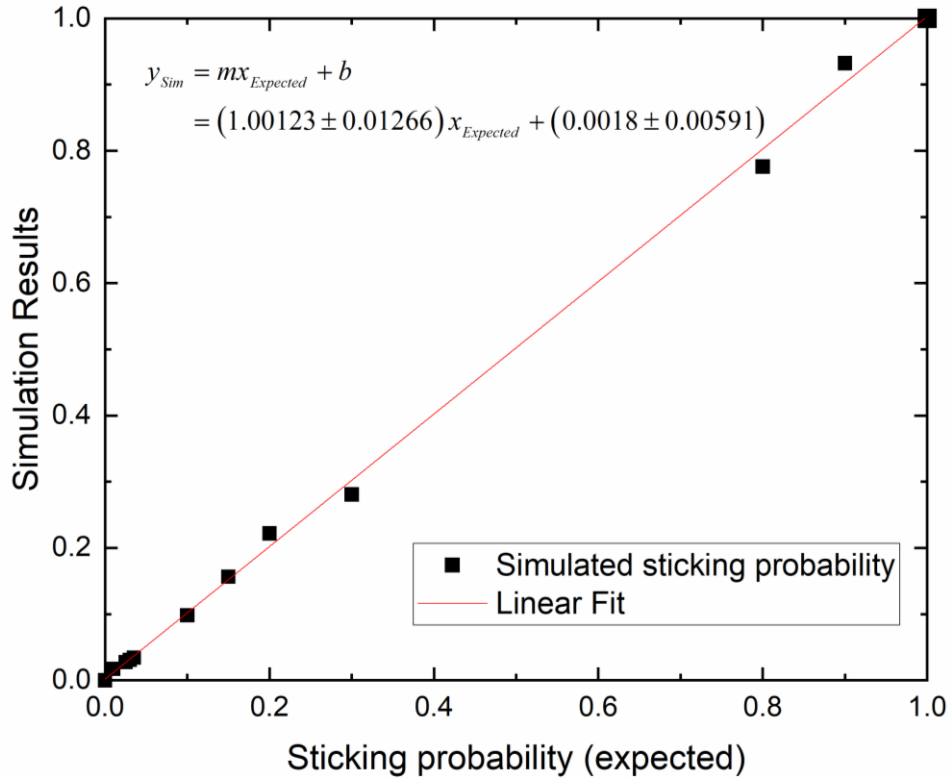

Figure 5.4 Sticking probability modelled at the pump surface: DSMC results (ratio pumped-to-input particles) as a function of the sticking probability (expected).

In this collisionless framework, further analysis is carried out by comparing the macroscopic variables stored at each cell in the sub-divertor domain in both NEUT2D and DSMC as follows: an alternative coordinate system (*R'*, Z') is defined by rotating clockwise 45° the *R*- and *Z*-coordinates, as depicted in Figure 5.5(a). The *R'*-axis lies along the pump boundary and the *Z'*-axis is oriented towards Gate 1.

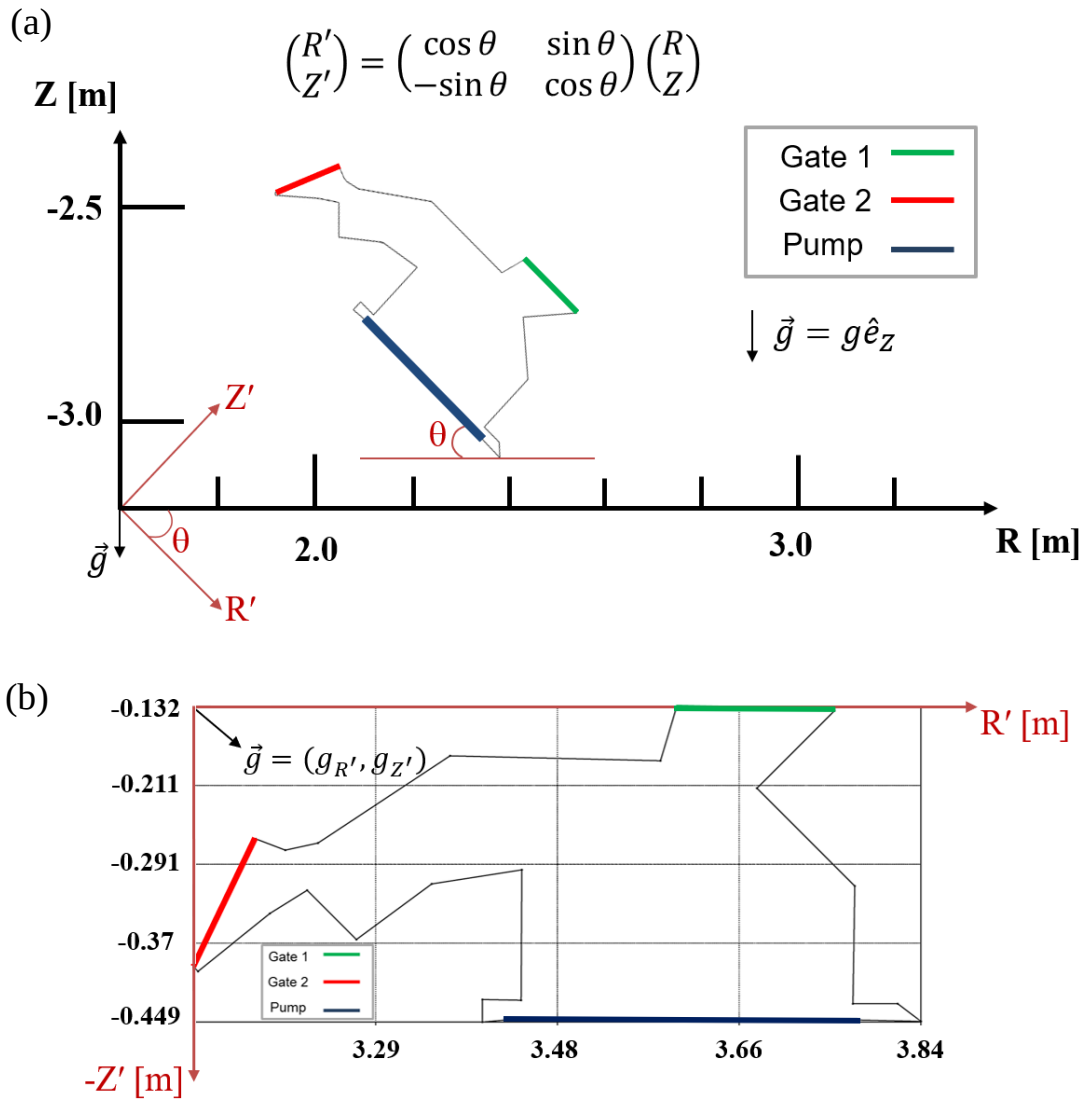

Figure 5.5 (a) The *R*- and *Z*-coordinates are rotated clockwise through an angle of 45°, defining a second coordinate system (*R'*, *Z'*). The domain inlet and outlet boundaries are denoted as Gate1, Gate 2 and Pump. The direction of the gravity is also shown. (b) Rotated system, where the pump surface as well the inlet boundary Gate 1 are parallel to the *R'*-coordinate.

5.1.2 Macroscopic variables NEUT2D and DSMC

For the benchmark, the particle influx (D_2) is generated only at Gate 2 and has a Maxwellian velocity distribution centered at an average temperature of T = 1122.16 K. Both gates are set as open surfaces with a sticking probability of 1.0, this means that the particles impinging these surfaces are absorbed instantly and thus, they are deleted from the domain. The sticking probability at the pumping surface is set to 3% of the total incoming flux. The rest 97% is reflected back to the sub-divertor domain with a cosine distribution at a temperature of 293.16 K. As particle-wall interaction model, in NEUT2D and DSMC the D_2 molecules are diffusely reflected from the sub-divertor walls at a temperature of T_w = 293.16 K. The summary of the DSMC parameters is found in Table 5.1.

Table 5.1 The summary of the DSMC model parameters for the comparison between *dsmcFoam* and NEUT2D for deuterium gas in its molecular form

	Type / Parameter	Value	Unit
Boundary name			
Gate 2	Pressure type (inlet)		
	Pressure	1.24	Pa
	Temperature	1122.61	K
Gate 1	Pressure type (outlet)		
	Sticking probability	1.0	-
Wall	Wall		
	Temperature	293.16	K
Pump	Pump		
	Sticking probability	0.03	-
	Temperature (reflection)	293.16	K
DSMC properties			
Time step	Δt	5×10^{-7}	s
Conversion factor	F_N	1×10^{11}	-
Particle-wall interaction	Diffuse refl. (walls)		
	Temperature	293.16	K
	Accomodation coefficient	1.0	-
Binary collision model	No binary collisions		
Particle attributes			
Particle name	Deuterium (D_2)		
mass	m	6.69×10^{-27}	kg
diameter	d	2.92×10^{-10}	m
rotational degrees of freedom (DoF)	rotational DoF	2	-
viscosity index	ω	0.73	-

To facilitate the understanding of the flow development, the sub-divertor is further divided in 4 different sub-domains as shown in Figure 5.6. At the shown nodes both DSMC and NEUT2D codes sample the values of the flow macroscopic variables A_i, which are compared at a later stage. An enhancement of specific part of each region is shown inside colored boxes. At its first stage, once introduced in the domain, the particles move across a large duct (region I) and flow to region II (transit region) and continue their movement towards region III (outlet region), where the particles exit the sub-divertor domain. The region IV can be regarded as a two-dimensional short vertical channel. The neutral particles impinge the pump region, where a sticking coefficient is set, thus certain particles are reflected back to the sub-divertor and the rest deleted from the system.

At each region, the nodes are given a sub-indexing for post-processing reasons. For example, in region I the flow variables receive the sub-indexing (*i*, *j*), regions II (*k*, *l*),

region III (q, r) and region IV (k l). In region I, where the *sampling* nodes are described by the sub-index (i, j), the i-index *runs* along the R'-axis and the j-index along Z'-axis. In the case of region 2, where the nodes are specified with indices k and l, their values increase with R- and Z-axis, respectively.

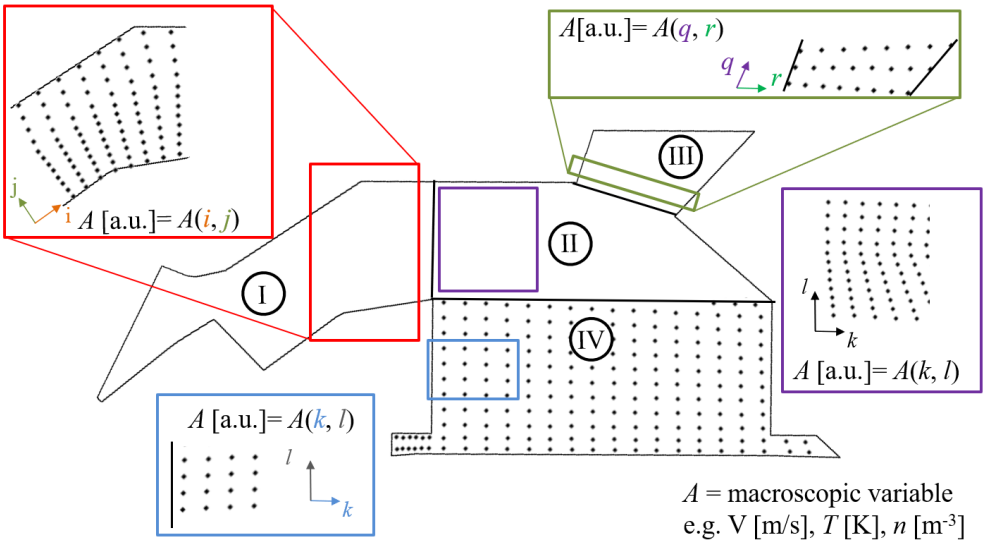

Figure 5.6 The JT-60SA sub-divertor is divided in 4 regions (I-IV). DSMC and NEUT2D values of the macroscopic variables A_i are compared at the same node location.

To illustrate the behaviour of the gas across the entrance and transit regions (Region I and II), the flow velocity is sampled, see the profiles along the selected nodes shown in Figure 5.7. The figure shows the Z'-variations of the flow speed at different R' positions. The particles enter the domain at Gate 2, some of the particles are directed towards the sub-divertor wall and reflected back to the Gate 2, being deleted from the domain. Other particles will ultimately leave the entrance region I, crossing the surface A shown in Figure 5.7(a). The flow speed along region I shows a parabolic-like profile with a maximum around Z'= -0.30 m right after the surface A. As the particles approach region II, the profile broadens due to the non-zero flow velocity contributions of the particles moving parallel to the sub-divertor walls. In Region I, the magnitude of the velocity in DSMC is systematically greater than the values of NEUT2D for $Z' < -0.26$ m as seen in Figure 5.7(b). A maximum and minimum difference between the approaches of 19% and 2%, respectively. In Appendix 8-C, additional plots in region I depicts this observation. Once the gas particles have crossed region I, the gas flow moves towards pump, Gate 1 or continues its trajectory in straight line. Towards the pump in region IV, the flow velocity at each cell has two main contributions: particles moving downwards (negative Z'-direction) coming from the region I and a second contribution from the particles reflected back at the pump surface moving in the $+Z$' direction towards region II. Since the particle velocity is sampled at the pump with a Maxwellian distribution centered at 293.16 K, the gas has zero-flow velocity as any gas in equilibirum, as depicted in Figure 5.7(a).

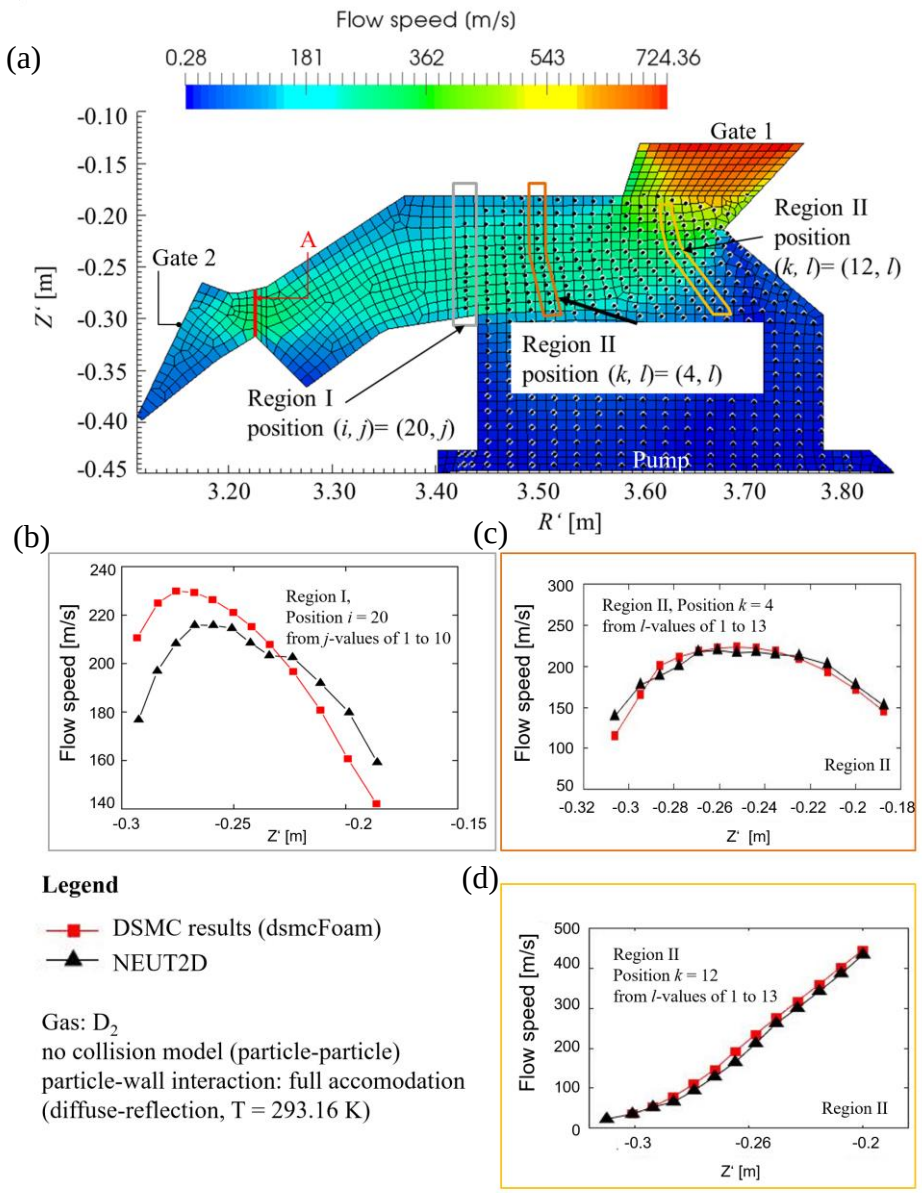

Figure 5.7 (a) Flow speed distribution across JT-60SA, deuterium flow enters the domain at Gate 2 (far-most left inlet), Gate 1 has a sticking coefficient of unity and at the pump 97% of the total of the incoming particles are reflected back. Here both grids are superposed, the structured grid of DSMC and the cell center of NEUT2D grid. (b)-(d): the DSMC and NEUT2D values of the flow speed are sampled at the same computational locations defined by the mid-point of NEUT2D. The node locations, black dots in (a) are associated to a specific sub-indexing (see main text for further details). JT-60SA sub-divertor flow speed profiles in locations across Regions I and II as a function of Z'-coordinate, see (b), (c) and (d).

In Region II, the flow speed profile flattens out within its parabolic shape, see Figure 5.7(c) and (d). The calculated relative difference node-wise between both approaches is less than 5 %, the profiles along selected nodes are found in Appendix 8-C. In a similar fashion to the region II, at the exit near gate 1 in region III, the flow velocity calculated with both codes has relative differences below 10%. Additional profiles are compared

and presented in Appendix 8-C. By analyzing the region IV from its beginning until the position of the pumping surface, it was found that the profiles show qualitatively the same shape, see Figure 5.8**.** Near the pumping surface, the magnitude of the velocity decreases considerably in both codes (factor of 10). In region IV, the particles are being thermalized either by the walls or by the pump. The particle flux being diffusely reflected by the pump (97% of incident flux) have a thermal speed of ~ $1x10^3$ m/s and moves in $+Z'$-direction, which is the opposite direction of the incident particle flux coming from region II, resulting in a reduced net flow velocity calculated at each computational cell. The results show that the profiles in region IV near region II have a better agreement at least qualitatively. In this case, NEUT2D profiles show a maximum around R'= 3.52 m and minimum at R' = 3.7 m as the DSMC outcome.

The *dsmcFoam* solver determines the translational temperature at each cell as the average kinetic energy associated with the thermal motion of the particles. Rewriting the expression Eq. (3.46) introduced in Chapter 3.5 in terms of the peculiar or thermal velocity $\mathrm{v}'$of the particle as:

$$T_{\mathrm{tr}} = \frac{\left\langle m\mathrm{v}'^2 \right\rangle^{\text{per cell}}}{3k_B} = \frac{1}{3k_B}\frac{\sum_{k=1}^{N} m_k \mathrm{v}_k'^2}{N}. \tag{5.1}$$

The thermal velocity v' is related to the particle velocity v and the bulk velocity V by $\mathrm{v}' = \mathrm{v} - \mathrm{V}$. NEUT2D on the other hand expresses the kinetic energy of the particles in eV units, which can be converted to temperature by $E[eV]11608\ K/eV$. Once this is done, the temperature fields are compared between both approaches and shown in Figure 5.9. Simulations show that higher temperatures of DSMC are obtained compared to those of NEUT2D, particularly at Gate 2 (inlet), where a factor of 3 between both codes is found. At the entrance of region II, a difference of 10% between T_{DSMC} and T_{NEUT2D} is found and in region IV an homogenization of the temperature is observed. In both approaches a value about T ~ 293 K is obtained as a consequence of a thermalization with the subdivertor walls and the pump region. A maximum difference of 2% between DSMC and NEUT2D is obtained in region IV. In both approaches in region III (outlet) a particular temperature distribution can be seen in Figure 5.9(a) and (b), which is depicted in more detailed in Figure 5.10 for DSMC. Three zones are identified, one at the exit of the region I, where a minimum of the temperature in DSMC is found with a value of T ~ 210 K. A second zone with constant temperature of T ~ 272 K is found which separates with an isoterms the region III with the third zone, where a temperature range of $T \in [300, 334]$ K is obtained.

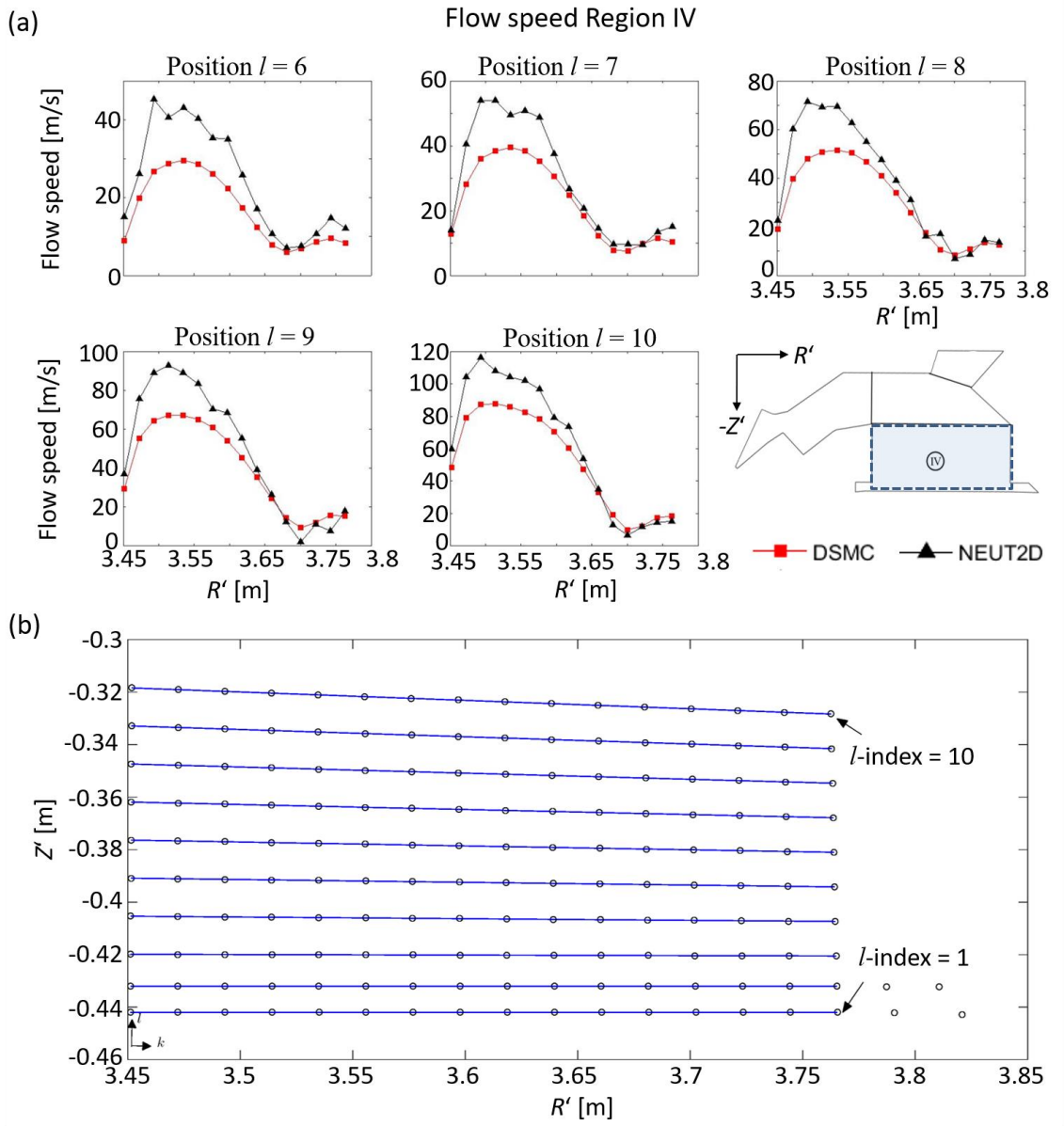

Figure 5.8 Results of the comparison between flow speeds calculated with NEUT2D and DSMC (without collisions). (a) Flow speed profile evaluated at each node (k, l) at constant l-value in region IV. (b) Region IV of the sub-divertor JT-60SA. Here the nodes are given a sub-indexing (k, l). The sub-index k can take values from 1 to 16, whereas the l-index takes the values between 1 and 10. Note: the range of the l-values differs from the ones in region II.

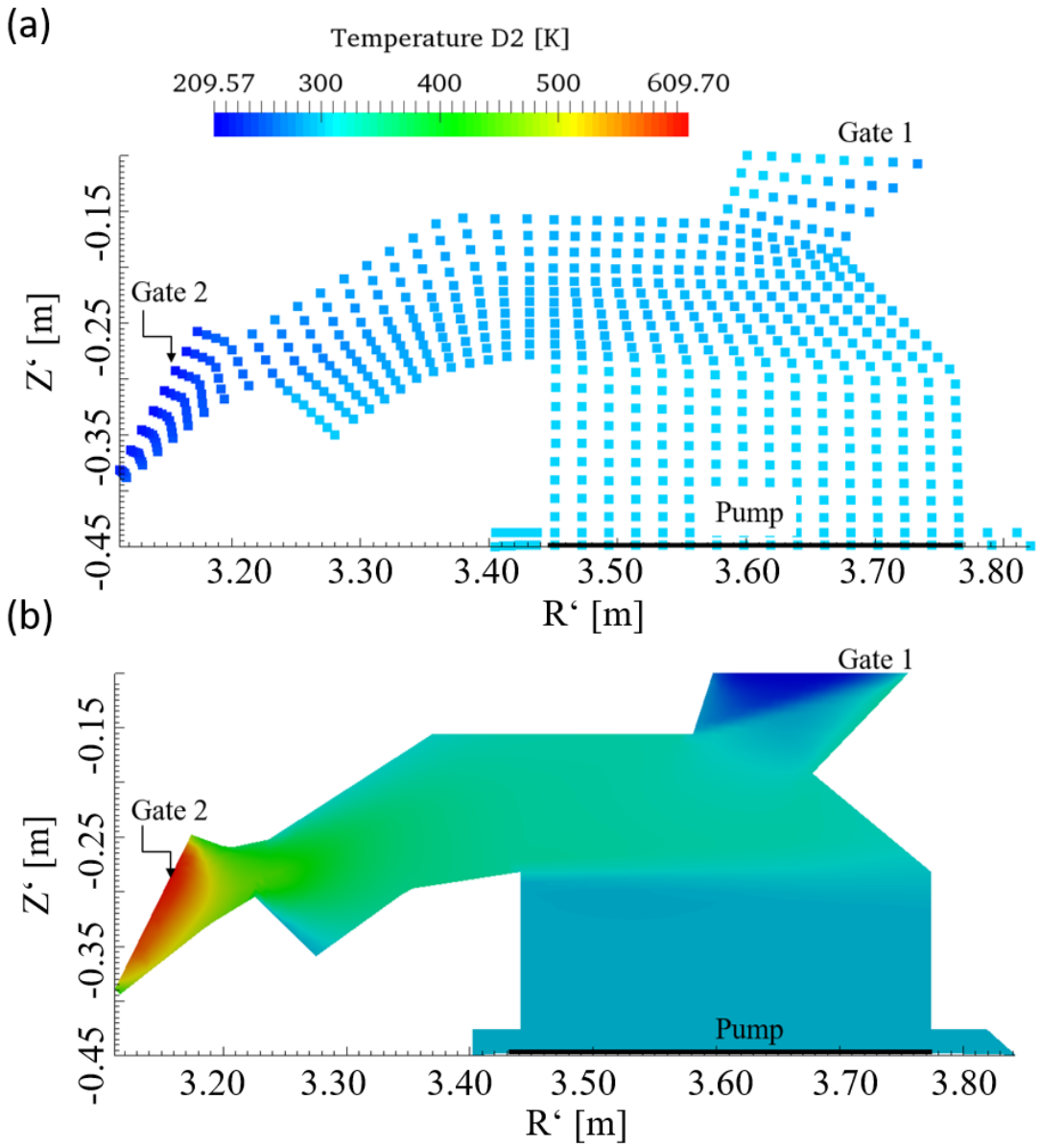

Figure 5.9 Temperature field in JT-60SA domain calculated with a) NEUT2D and b) DSMC method.

Figure 5.10(a) shows the nodes in region III where the flow field is sampled in NEUT2D. At these points the DSMC results are also evaluated. Between the approaches the difference in the temperature increases for values near to the exit of the sub-divertor (outlet), yielding up to 35% relative difference. This is explicitly shown in the temperature profile in Figure 5.11(a) and (b). At the entrance of region III, the difference in the temperature values shows up to 11% between DSMC and NEUT2D, see Figure 5.11(c) and (d).

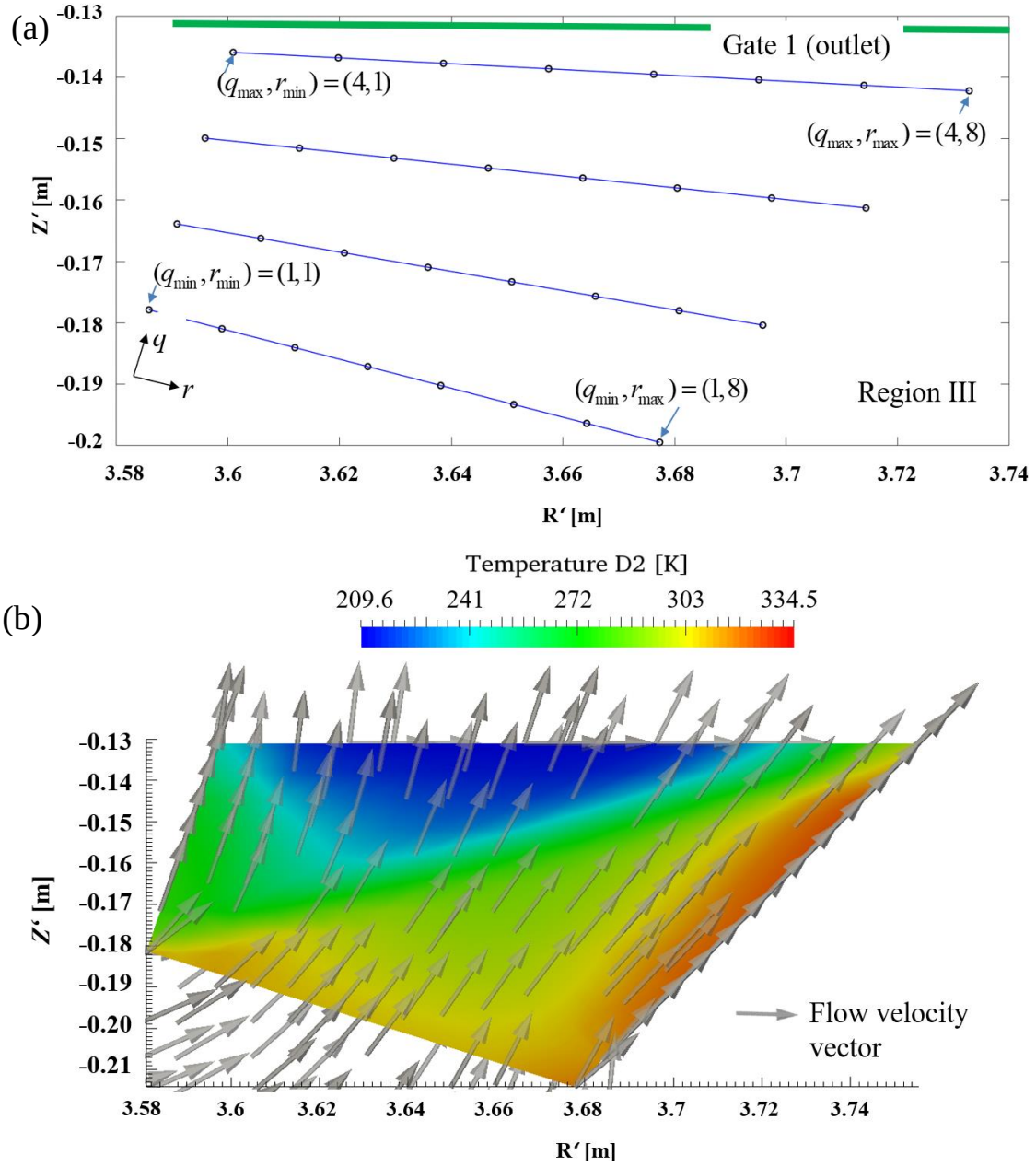

Figure 5.10 JT-60SA sub-divertor region III (near Gate 1, outlet). (a) At the nodes the macroscopic variables between both codes are evaluated. (b) DSMC temperature profile across the region III. The arrows indicate the flow velocity vector of the gas.

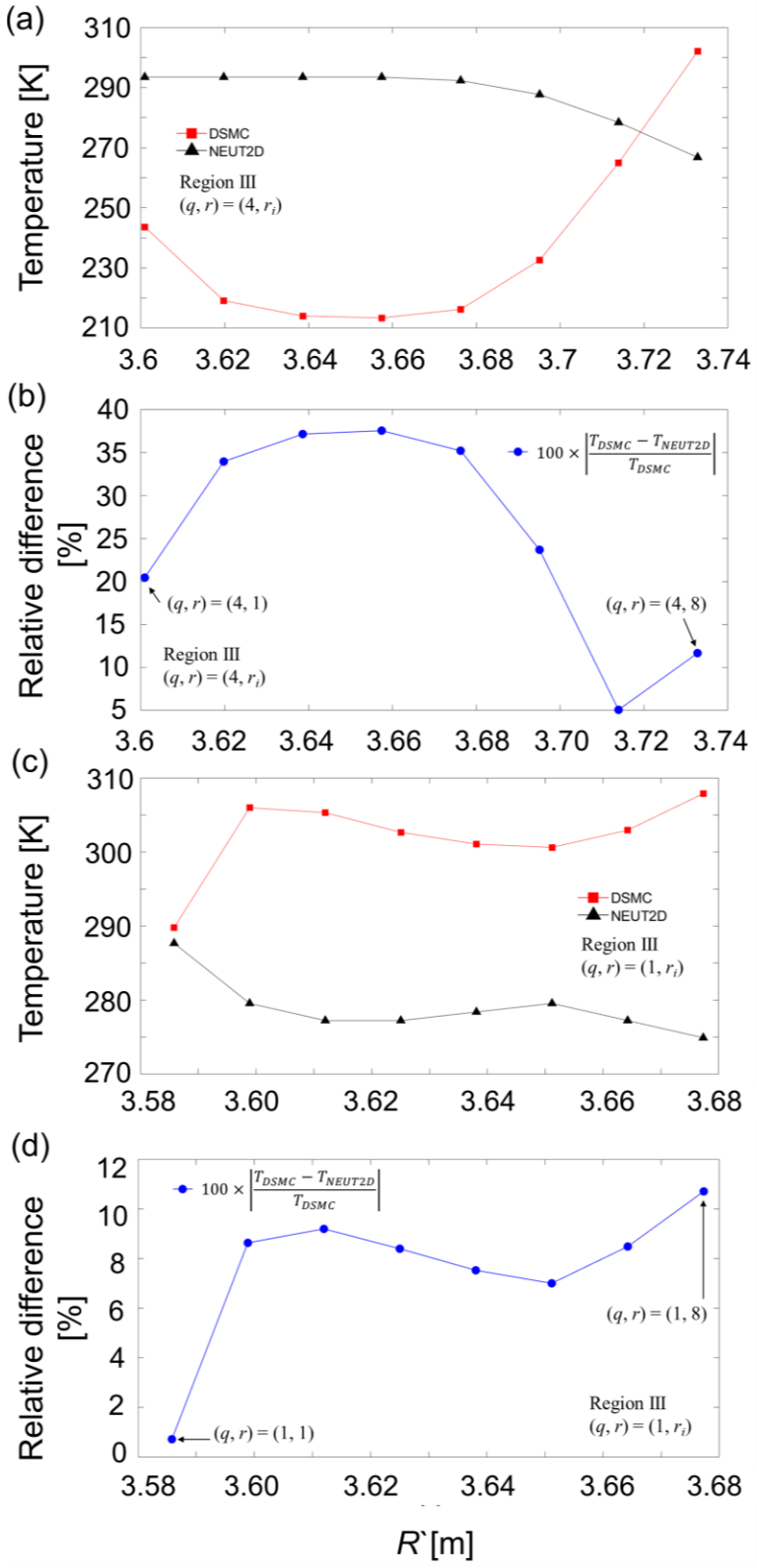

Figure 5.11 Temperature profile of NEUT2D (black) and DSMC (red) in region III: (a) near Gate 1 (outlet) and (c) entrance of region III. Relative difference between both approaches sampled at NEUT2D node locations. The node locations are referred to Figure 5.10.

In Figure 5.12(a) the number density is plotted along a line placed between Gate 2 and Gate 1 and a second line between the pump region and Gate 1. Thus, the arc length spans the regions I, II and III of the sub-divertor domain. Reasonably agreement is found: both codes predict the decrease rate of the density for the position values greater than 0.15 m of the arc length ($R' > 3.29$ m), with a relative difference less than 30%.

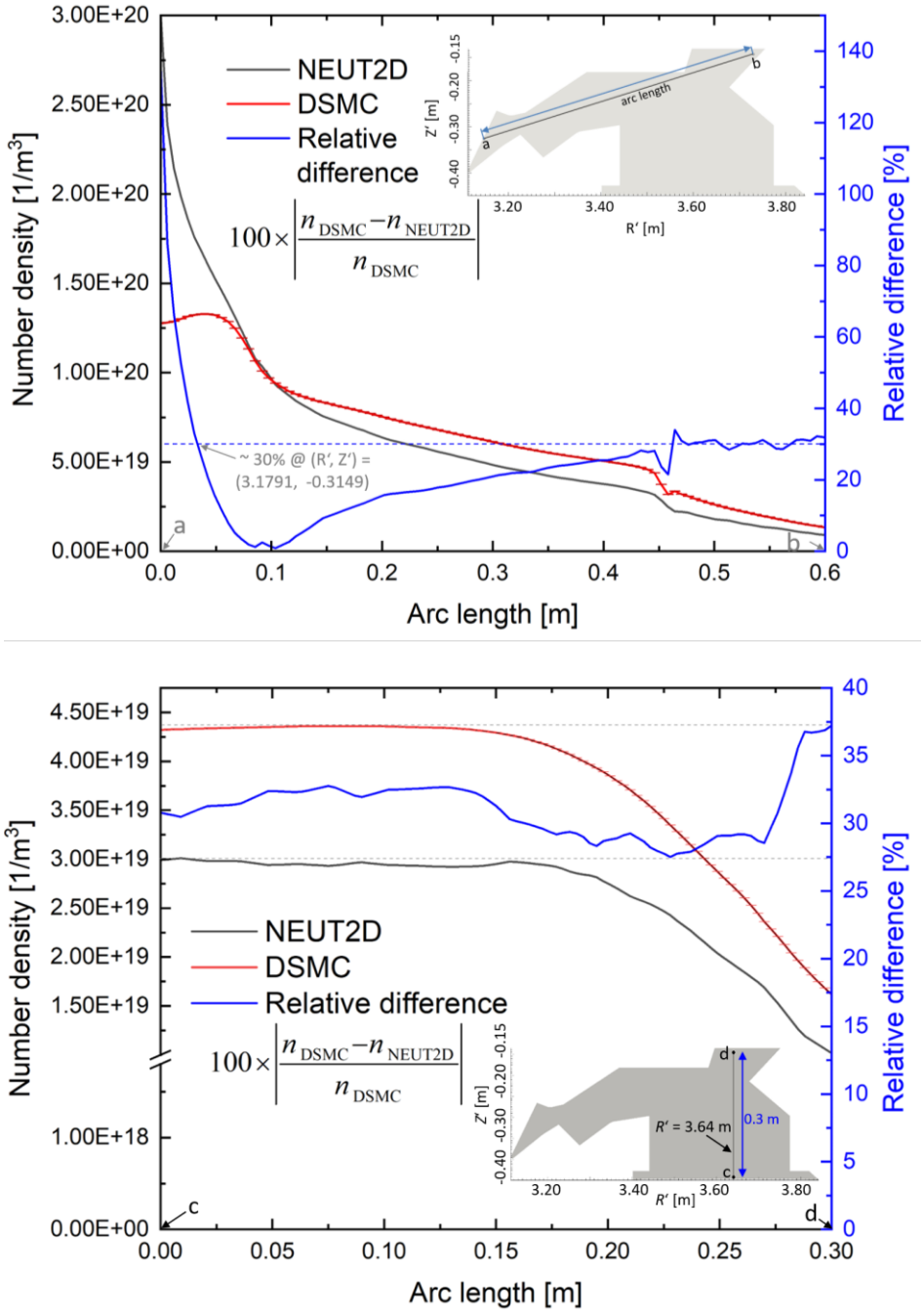

Figure 5.12 Number density calculated with NEUT2D and DSMC. The density is sampled along. Top figure: arc length between Gate 2 and Gate 1. Bottom figure: vertical line located at a position R' = 3.64 m, which spans the pump region and outlet (Gate 1).

Also shown in Figure 5.12(a) for both codes, the change in the density occurs at the value of the arc length of 0.45 m ($R´$ = 3.58 m), which is exactly at the boundary between region II and region III. The level of scatter appears similar in both results, however a ratio about 3 between codes at the Gate 2 is found. Once the pressure and temperature are defined at the boundary in DSMC, the density follows the ideal law of gases in order to maintain the inflow boundary conditions, whereas in NEUT2D the number of particles per second is fixed defining the number density at the inlet. It follows that at the inlet region NEUT2D calculates higher number density -relative to DSMC- and lower temperatures of about a factor of ~ 3 relative to DSMC, see Figure 5.9. This results on the desired target pressure of about 1 Pa (boundary condition). Similar observations are obtained by anaysing the arc length shown in Figure 5.12(b). The arc length spans the pump region (IV), passing throught region II and ending in region III (near to Gate 1). Qualitatively agreement is found between codes, a constant value of the number density across region IV is calculated with a relative difference 30-33% followed by a drop towards the outlet in region III.

5.1.3 Effect of collisions in JT-60SA sub-divertor gas flows

Having benchmarked the DSMC code in the previous section in collisionless conditions, the introduction of neutral-neutral interactions in the JT-60SA sub-divertor is studied for two cases by activating the collision kernel in *dsmcFoam*.

- Case I: By means of a sensitivity analysis on the pressure values at Gate 2, the effect of the collisions on the sub-divertor flow is first analyzed. Here, it is focused on the capability of *dsmcFoam* to calculate collisions rates, which are then compared to analytical expressions. A second aspect is also studied by comparing binary collision models and the effects on the flow field.

- Case II: The simulation is based on the JT-60SA Scenario #2, see [91] and [92], where a dedicated SONIC calculation has been performed for this task in order to properly set the boundary conditions at the sub-divertor interfaces. A comparison between the collisional and collisionless DSMC solutions is perfomed.

Table 5.2 Case I: summary of the DSMC model parameters for a gas flow in JT-60SA for the sensitivity analysis of pressure at Gate 2 to address collisional effects

	Type / Parameter	Value	Unit
Boundary name			
Gate 2	Pressure type (inlet)		
	Pressure	Case I.a = 1.2 Case I.b = 0.8 Case I.c = 0.6 Case I.d = 0.55 Case I.e = 0.5 Case I.f = 0.2	Pa
	Temperature	1122.61	K
Gate 1	Pressure type (outlet)		
	Sticking probability	1.0	-
Wall	Wall		
	Temperature	293.16	K
Pump	Pressure type (outlet)		
	Pressure	0.12	Pa
DSMC properties			
Time step	Δt	4×10^{-7} (I.a) 1×10^{-5}(I.b-c) 1×10^{-4}(I.e, I.f)	s s s
Conversion factor	F_N	9×10^{12} (I. a,e,f) 1×10^{13} (I. b,c,d)	- -
Particle-wall interaction	Diffuse reflection (wall)		
	Temperature	293.16	K
Binary collision model	Variable Hard Sphere	I. a-f	
	Hard Sphere Model	I.a (variant 1)	
	Maxwell Model	I.a (variant 2)	
	No binary collision	I.a (variant 3)	
	Reference temperature	273	K
Particle attributes			
Particle name	Deuterium (D_2)		
mass	m	6.69×10^{-27}	kg
diameter	d	2.92×10^{-10}	m
rotational DoF	Rotational DoF	2	-
viscosity index	ω	0.73 (I.a-f) 0.5 (I.a variant 1) 1.0 (I.a variant 2)	-

Table 5.3 Case II: summary of the model parameters for JT-60SA for the collisional effects by employing the operational conditions of Scenario #2

	Type / Parameter	Value	Unit
Boundary name			
Gate 2	Pressure type (inlet)		
	Pressure	4.44	Pa
	Temperature	2002.515	K
Gate 1	Pressure type (inlet)		
	Pressure	1.2	Pa
	Temperature	1118.57	K
Wall	Wall and chevron		
	Temperature	293.16	K
Pump			
	Sticking probability	0.03	-
	Temperature (reflection)	293.16	K
DSMC properties			
Time step	Δt	5×10^{-7}	s
Conversion factor	F_N	1×10^{11}	-
Particle-wall interaction	Diffuse refl. (walls & chevron)		
	Temperature	293.16	K
Binary collision model	Variable Hard Sphere model		
	Reference temperature	273	K
Particle attributes			
Particle name	Deuterium (D_2)		
mass	m	6.69×10^{-27}	kg
diameter	d	2.92×10^{-10}	m
rotational DoF	Rotational DoF	2	-
viscosity index	ω	0.73	-

Case I: Sensitivity analysis of pressure at Gate 2 and model parameters

The objective of this analysis is two-fold. First, the collision frequency of the DSMC simulations is compared to the analytical expression found in literature. Second, the intention is to assess the influence of input parameters on the flow, such as pressure at inlet boundary and binary collision model (via the viscosity index ω).

The flow to be modelled is the expansion of deuterium gas entering from Gate 2 and exiting at the pumping surface and Gate 1 in the JT-60SA sub-divertor. The Maxwellian gas centered at 1122.61 K enters the domain at Gate 2 whereas at the outlet at Gate 1 the particles going out of the sub-divertor are removed from the domain. Six different pressure values at Gate 2 are tested and identified with the following nomenclature:

- Case I.a: 1.2 Pa (Gate 2),
- Case I.b: 0.8 Pa (Gate 2),

- Case I.c: 0.6 Pa (Gate 2),
- Case I.d: 0.55 Pa (Gate 2),
- Case I.e: 0.5 Pa (Gate 2) and
- Case I.f: 0.2 Pa (Gate 2).

The VHS collision model has been employed as binary collision model. In the VHS model the total collision cross-section depends on the viscosity index ω which has been calculated from the deuterium data of [93] as before. Dedicated simulations of Case I.a are also performed by considering the hard sphere and Maxwellian binary collision models, which is discussed in the second part of the present analysis. Particles are reflected diffusely from the sub-divertor wall based on a Maxwellian velocity distribution centered at a temperature of 293.16 K. In the DSMC calculations stationary conditions of the flowfield are detected by means of the number of simulated particles present in the computational domain. Once the number of particles has reached stationary conditions, the sampling of the flow properties is begun, see Figure 5.13 for the case I.a.

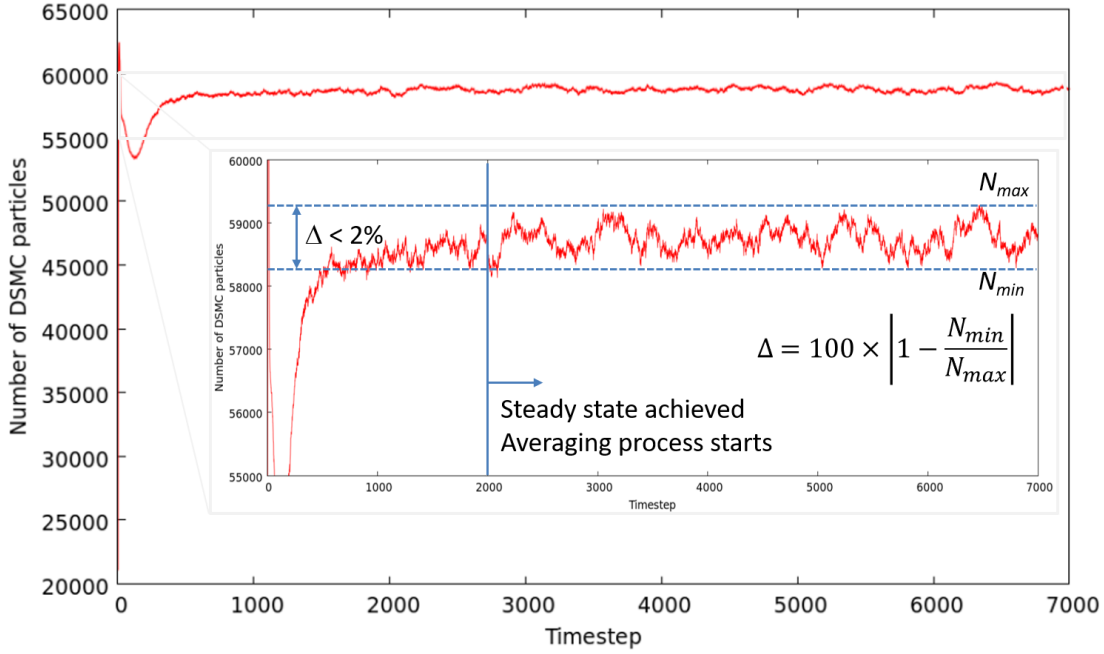

Figure 5.13 Exemplary evolution of the total number of DSMC particles in the system as function of the time steps for the case I.a with a pressure of 1.2 Pa at Gate 2.

The sub-divertor domain is divided into hexahedral cells for all the study cases. In Figure 5.14 is shown the distribution of DSMC particles in the domain where the size of the cell is such that on average at least 20 or more DSMC particles are contained at each cell in most of the domain where high-pressure values are expected (regions I, II and IV). In the cells located in region III near Gate 1 an average of 8.7 and 7.6 DSMC particles per cell are found for the simulation I.a. and I.f respectively.

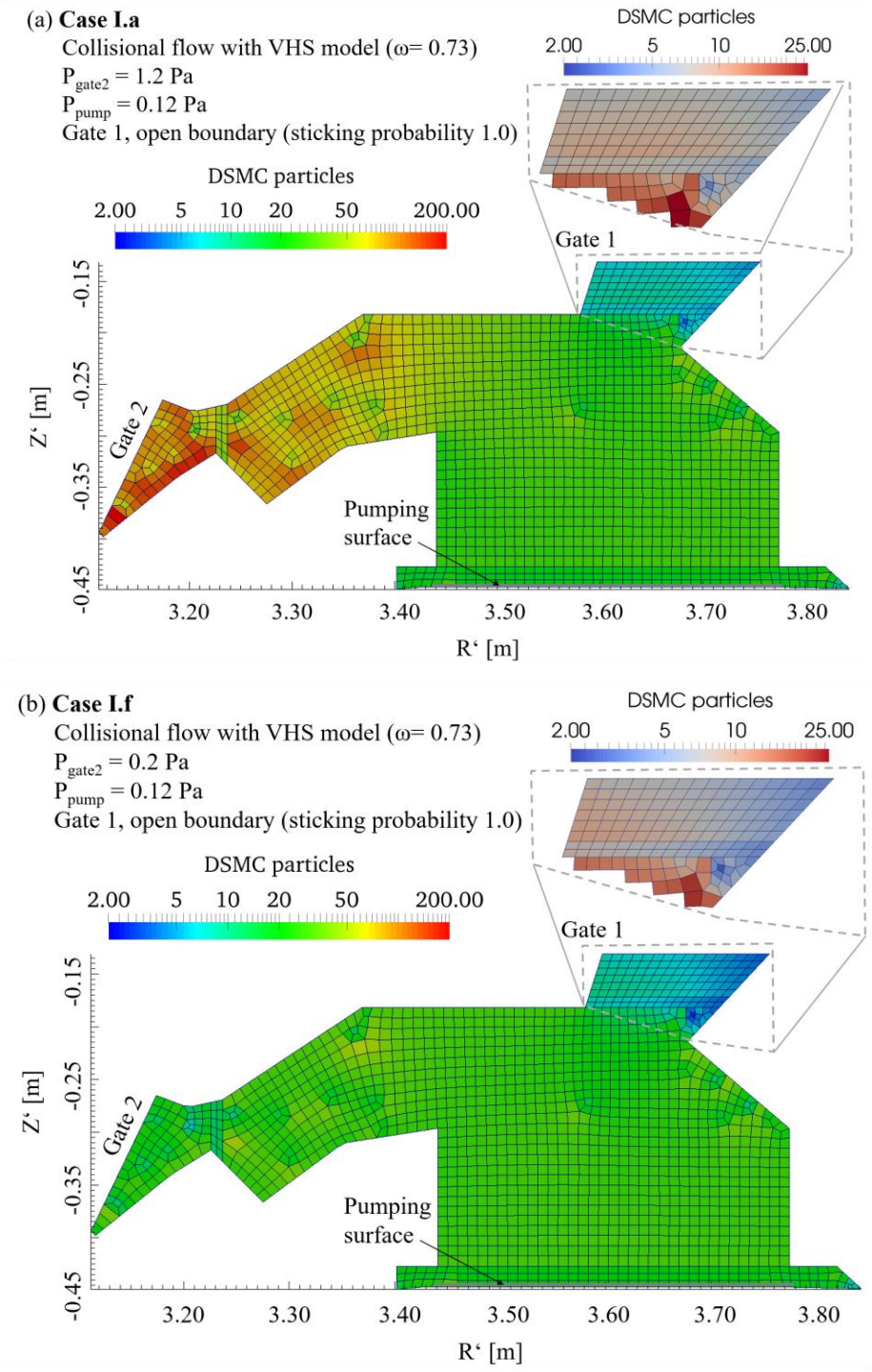

Figure 5.14 Number of DSMC particles in the computational domain for collisional flows in JT-60SA: Top figure: Case I.a with 1.2 Pa at Gate 2. Bottom figure: Case I.f with 0.2 Pa at Gate 2. In both plots on the top right: an enhancement of region III shows the number of DSMC particles near the Gate 1.

In the present analysis the collision frequency and flow variables are plotted along arc lengths shown in Figure 5.15. The spatial change of temperature, number density and flow velocity along these lines is expected to be significant due to the gas expansion.

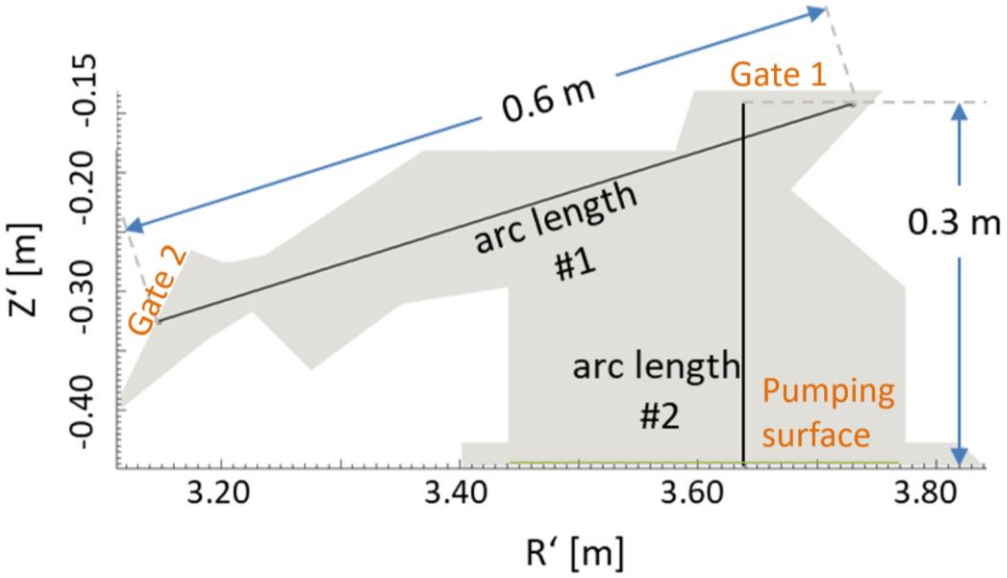

Figure 5.15 Arc length definition across the sub-divertor JT-60SA. The arc length #1 is defined by a line starting at the Gate 2 crossing regions I, II and III ending at the Gate 1. The second arc length spans regions IV, II and III starting at the pumping surface and ending near Gate 1.

In Figure 5.16 the number density is plotted along arc length #1 for the cases I. a-f. It is seen that a maximum value of the number density at R' = 3.2 m is found, with the exception of case I.f with the lowest pressure at Gate 2. Similar to the collisionless flow, around the coordinate R' = 3.6 m the density undergoes a sudden change at the boundary between region II and III, decreasing to a density value at the outlet of 1×10^{19} m^{-3}.

The degree of thermal nonequilibrium in the flow can be observed in the divergence between translational and rotational temperature profiles. Let us recall that both translational and rotational temperatures are related to an overall temperature defined in Chapter (3.5) as

$$T_{\text{overall}} = \frac{3T_{tr} + fT_{rot}}{3+f}.$$

Simulation for the case I.a shows that close to the Gate 1 departure between the translational and rotational modes ocurrs at R' = 3.6 m, which is the boundary between region II and III in the sub-divertor, see Figure 5.16. As shown in Figure 5.17(a) once the gas reaches the outlet, it undergoes an expasion into vacuum and thus, the translational temperature of the gas decreases about 20%, from 300 K to 244 K. The energy associated with the rotational modes does not change during this process, resulting on an overall decrease of the temperature, which is captured by the DSMC solver. Regarding the rest

of the cases I.b-f, the divergence also occurs about the radial coordinate R' = 3.6 m.

In Figure 5.17(b) it is shown the temperature profile along the arc length #2, where a constant value of 300 K in the pumping region is found, which is a trivial finding since only confirms that DSMC correctly set the boundary condition. A temperature divergence between rotational and translational temperature occurs in region III, near Gate 1. In the last third of the arc length, the translational temperature decreased from 300 K to 227 K, which differs by 7% from the value of T_{tr} along arc length #1. This has to do with the position of the arc length relative to the maximum value of the velocity profile, which is discussed later in this chapter. The temperature plots of cases I.b-f are here omitted, since the ratio of translational to overall temperature as well as the ratio rotational to overall temperature are qualitatively similar showing the same order of magnitude as the obtained profile from case I.a.

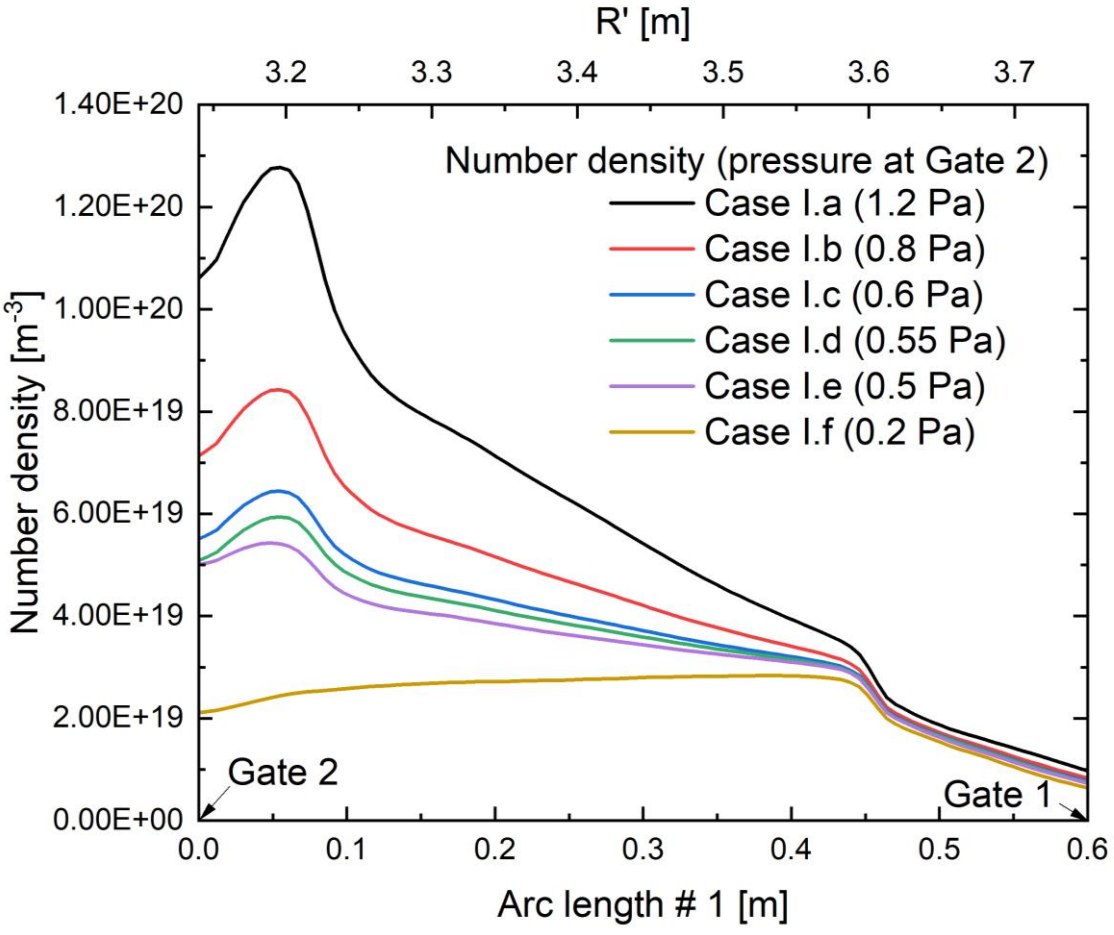

Figure 5.16 Number density of cases I. a-f plotted along the arc length #1 defined between Gate 1 and Gate 2. The DSMC analysis of the deuterium gas flow considers the intermolecular collisions by means the VHS model.

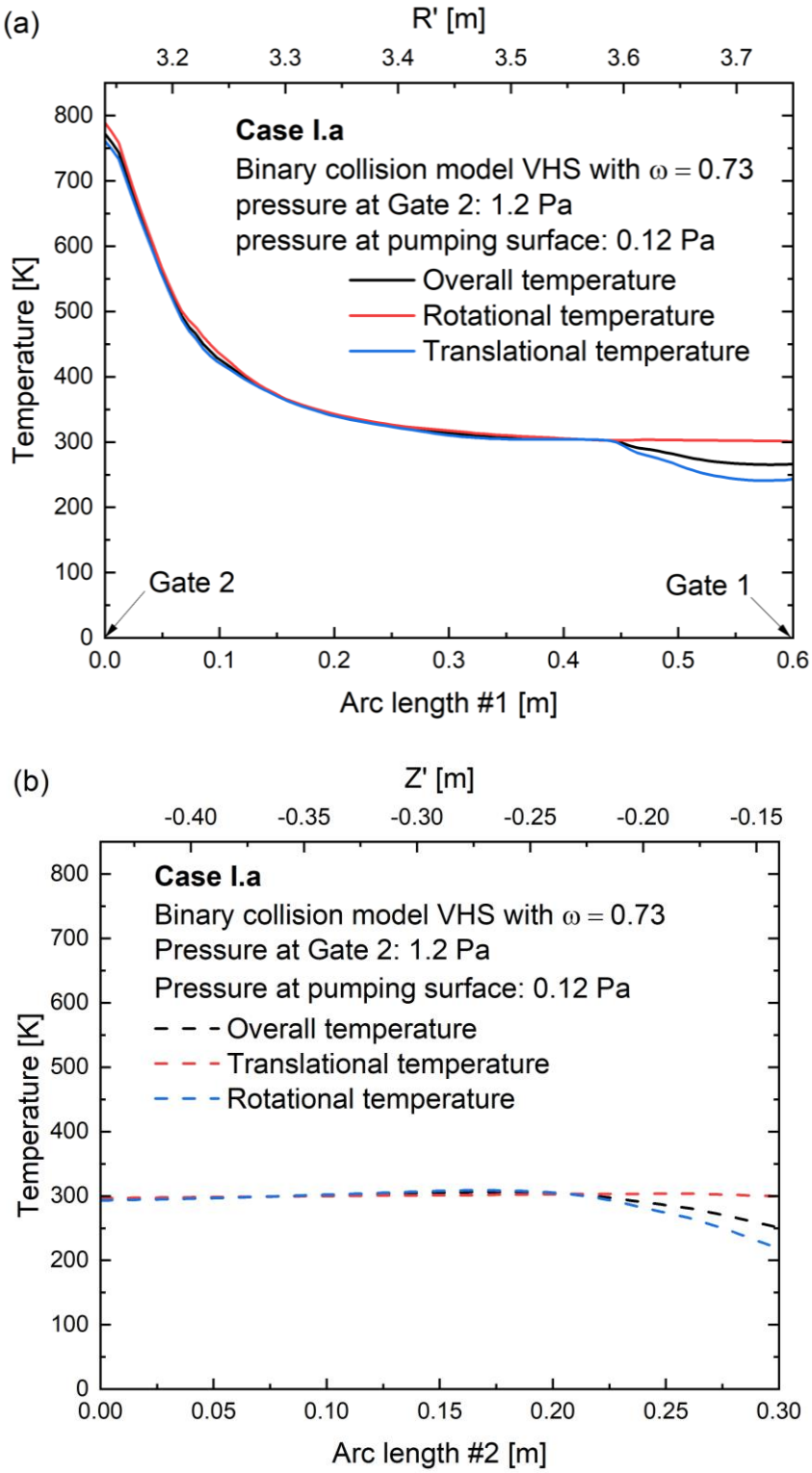

Figure 5.17 (a) Distribution along the arc length #1 for the case I.a for the overall, translational and rotational temperature for the deuterium gas. (b) Overall, translational and rorational temperature distributions along arc length #2. The DSMC analysis of the deuterium gas flow considers the intermolecular collisions by employing the VHS model.

The number of collisions that occur within a DSMC cell during the simulations is directly linked to the local transport properties of the gas. Therefore, for any collisional solver it is essential that the simulated collision frequency recovers the analytical expression from a gas in equilibrium. Here the collision frequency (ν_{pq}) obtained with the *dsmcFoam* solver is compared to the expression given by Eq. (4.74) in Bird's book [25]:

$$\nu_{pq} = 2\sqrt{\pi}\left(d_{ref}\right)_{pq}^{2} n_p \left\{\frac{T}{T_{ref}}\right\}_{pq}^{1-\omega_{pq}} \sqrt{\frac{2k_B T_{ref}}{m_r}}, \tag{5.2}$$

where *p* an *q* represents different gas species, d_{ref}, T_{ref} and ω_{pq} are the parameters of Table 5.2 for reference diameter, temperature and viscosity index, respectively. n_p represents the number density, T the gas temperature, k_B the Boltzmann constant and m_r the reduced mass. The equation (5.2) gives the number of collisions per unit time, which considers the collision between the pairs *pq* and *qp*. In the present work since only deuterium is considered as working gas, a factor of 0.5 needs to be included to obtain the correct frequency.

Comparing the collision frequency of Case I.a calculated with *dsmcFoam* for the VHS model and equation (5.2), reveals that the implementation of the binary collision model correctly predicts the analytical rate since the relative difference between simulation and theory lies below 0.1 %. This is plotted along the arc lengths in Figure 5.18. The profile shape is mainly determined by the product of the radius squared with the density, whereas the amplitude of the expression is dominated by the product inside the square-roots. In the present work the temperature ratio elevated to the power of $1-\omega$ is typically of the order of unity.

The results of study cases b-f (Gate 2 pressure: 0.8 to 0.2 Pa) reveals that the collision frequency decreases by lowering the pressure as one can expect, see Figure 5.19. Near the region of the pumping surface, where all the cases share the same outlet pressure value of 0.12 Pa, the profile derived from Cases I.a and I.f along the arc length #2 relative to the Cases I.b-e d shows a deviation about a mean ($\nu_{I.b-e}$ ~ 6711.83 s^{-1}) of 2.6% and 2.5%, respectively. The prediction of the analytical expression of collision frequency is found to be in good agreement along the two sampled arc lengths for all the study cases. In Figure 5.20, the relative difference between each DSMC simulation and its corresponding expression (5.2) is sampled along the two arc lengths as before. The plot shows that the maximum deviation value occurs in the first 0.15 m of the arc length #1, where the amplitude of the deviation monotonically decreases with the inlet pressure of Gate 2 and a maximum deviation of 0.06% is found. Along the rest of the arc length #1 the relative difference varies around 0.025% for all the runs and systematically it is observed that once the gas reaches the entrance of region III, a pronounced peak in the relative

difference is found. The result sobtained may be regarded as consistent, since the amplitude of this difference is directly correlated to the local flow boundary conditions. For instance, the same pressure value is set at the pumping surface and therefore the collision frequency shall be in the same order of magnitude.

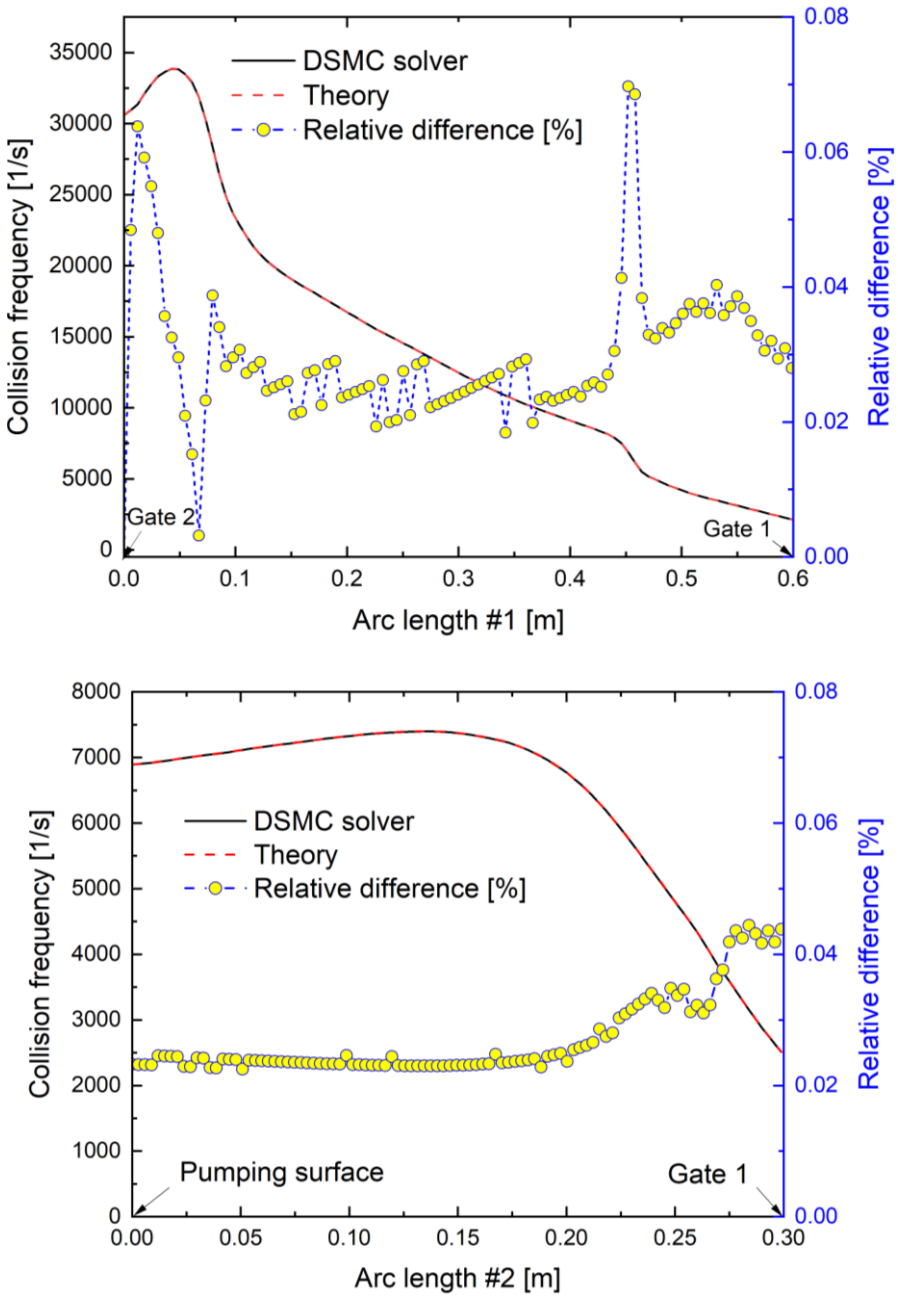

Figure 5.18 Bottom figure: Comparision between DSMC simulations and theoretical expression of the collision frequency sampled along the arc length #1, where 100 points are sampled along this line. The relative difference in percentage between simulation and analytical expression is also shown. The DSMC analysis of the deuterium gas flow considers the intermolecular collisions by employing the VHS model.

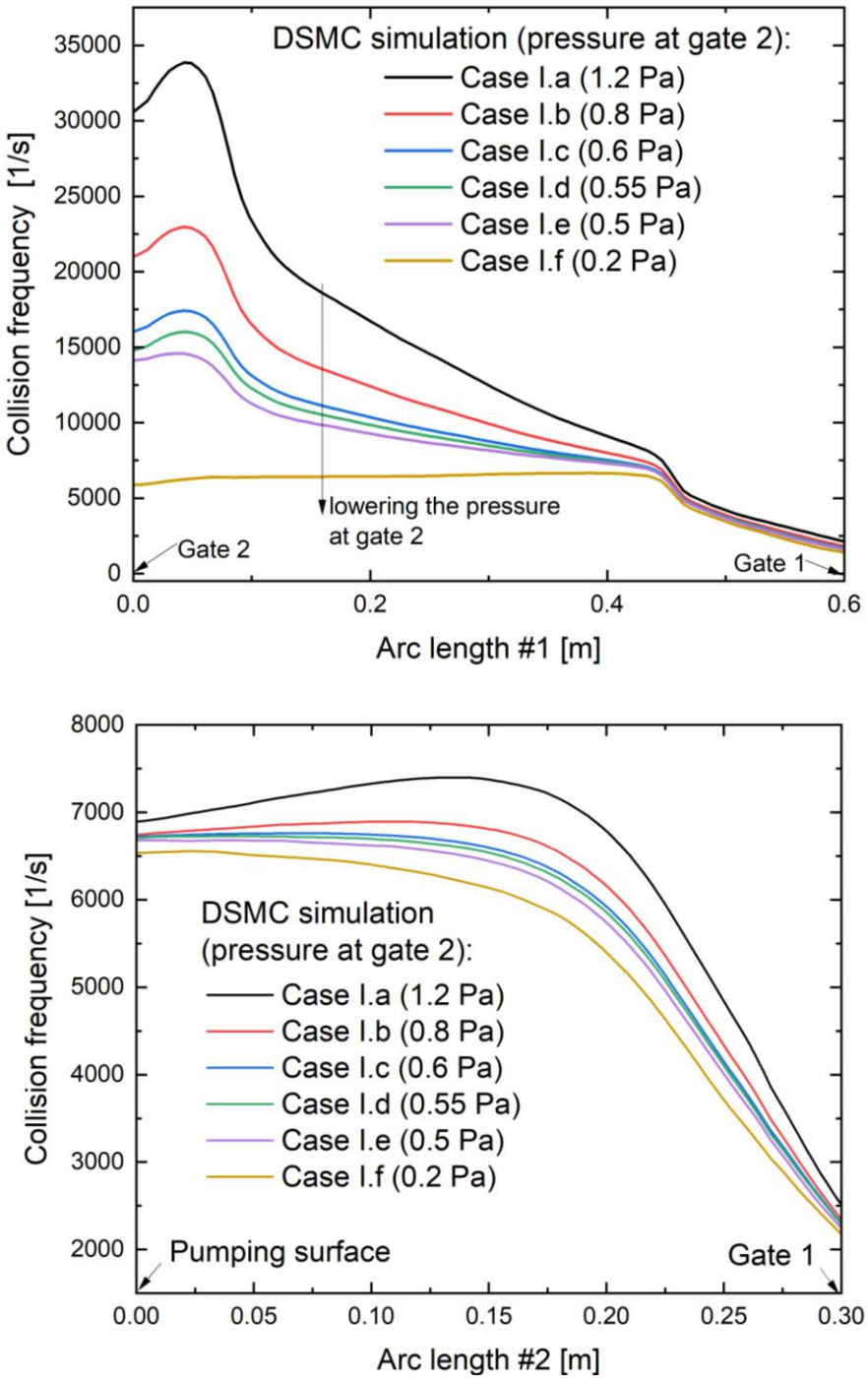

Figure 5.19 Collision rate calculated with *dsmcFoam* for the cases I.a-f along the arc length #1 and #2 (see Figure 5.15). The DSMC analysis of the deuterium gas flow considers the intermolecular collisions by employing the VHS model.

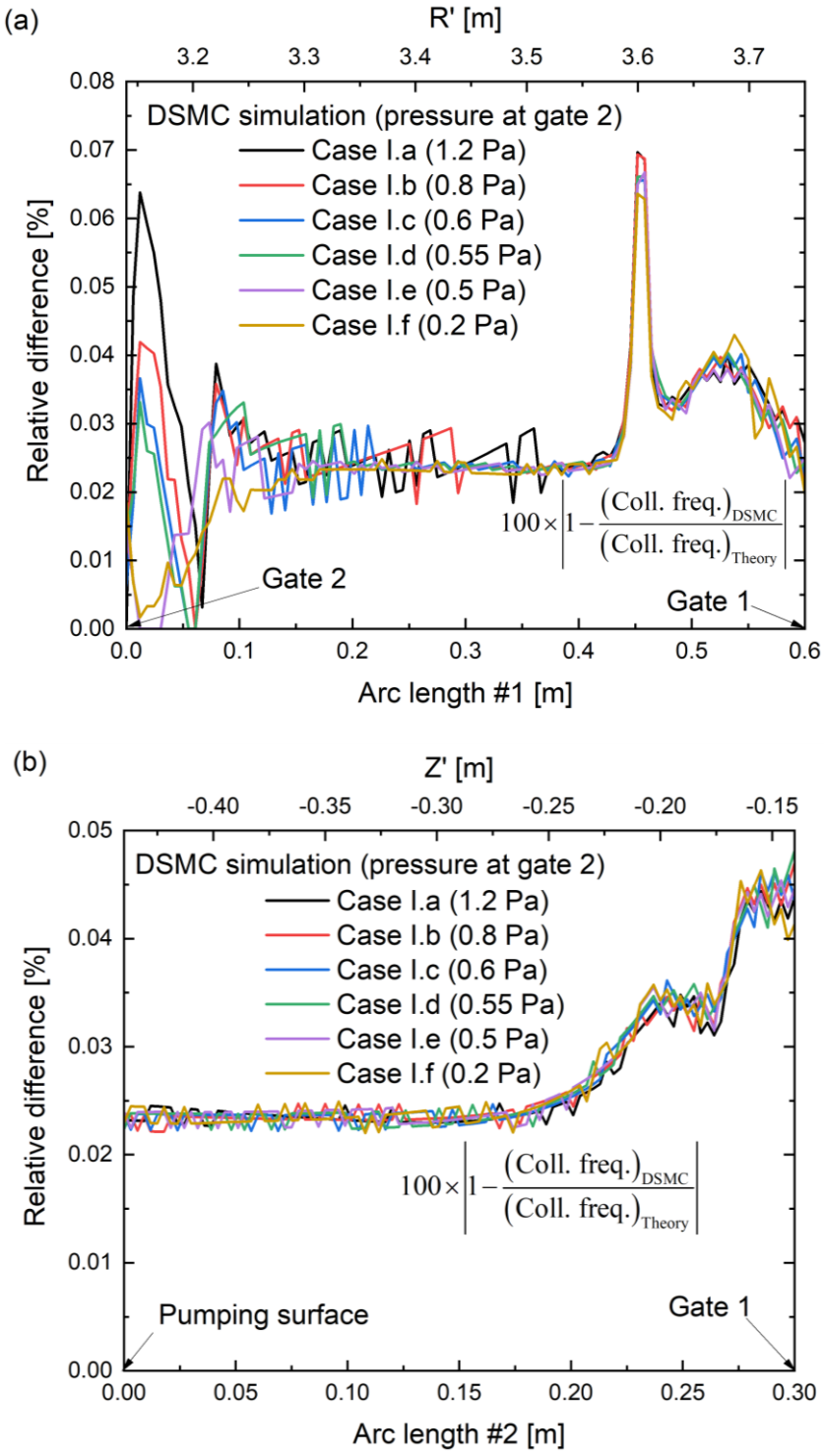

Figure 5.20 Relative difference between DSMC calculations and their corresponding analytical expressions for the collision frequency plotted along two arc lengths: (a) Cases I. a-f along arc length #1 which spans the domain region between Gate 2 and Gate 1. (a) Cases I. a-f along arc length #2 defined at the pumping surface and Gate 1. The DSMC analysis of the deuterium gas flow considers the intermolecular collisions by employing the VHS model.

Having analyzed the number density, temperature and collision frequency, let us turn our attention to the gas behaviour as a function of viscosity index ω, which is associated with the binary collision model employed in the simulation. For the analysis three values of ω have been compared:

i. ω= 1.0 (Maxwell model)
ii. ω= 0.73 (variable hard sphere model, value calculated from viscosity data [93])
iii. ω= 0.5 (hard sphere model)

In all three cases the maximum collision frequency value is found at Gate 2 around 0.5 m of the arc length #1 as before. It was found that the number of collisions for the VHS model is greater than the Maxwell model and lower values than those obtained by the HS model, as shown in Figure 5.21.

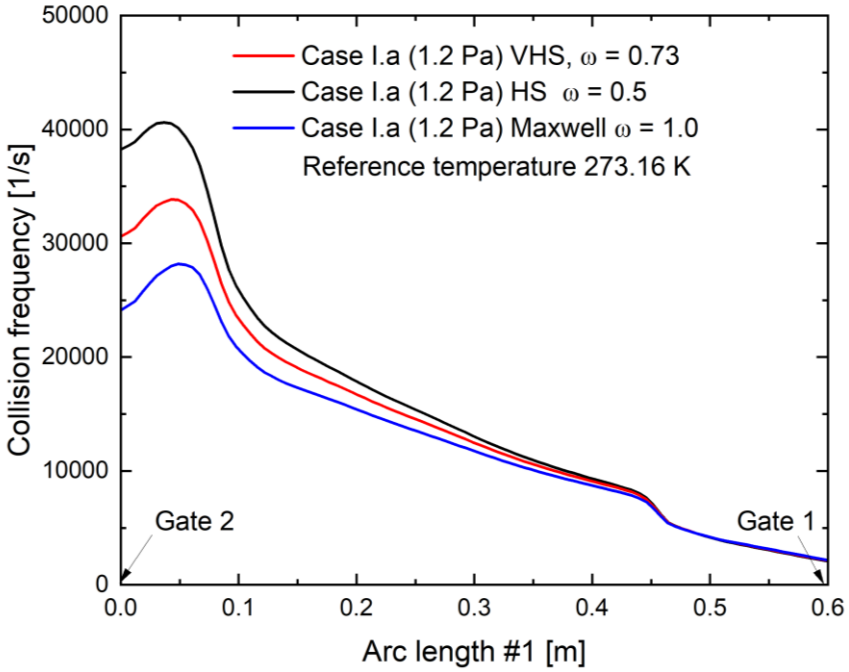

Figure 5.21 Collision frequency calculated with three binary collision models: Maxwell (ω= 1.0, blue line), hard sphere (ω= 0.5, black line) and variable hard sphere (ω= 0.73, red line). The boundaries conditions are set the same at Gate 2 (1.2 Pa), pumping surface (0.3 Pa) and Gate 1 (open boundary, sticking probability of unity). The particle-wall interaction is diffusely with full accommodation with a wall temperature of 293.16 K and T_{ref} of the gas is set to 273.16 K.

The relative difference between models is found in Figure 5.22. The simulation reveals that in regions II, III and IV the difference between models is of the order of +/-2 %. In these regions the temperature is typically of the order of 273 K and therefore the ratio of temperatures in the expression (5.2) is close to unity. This means that in these regions, the collision frequency is mainly driven by the density for the case I.a.

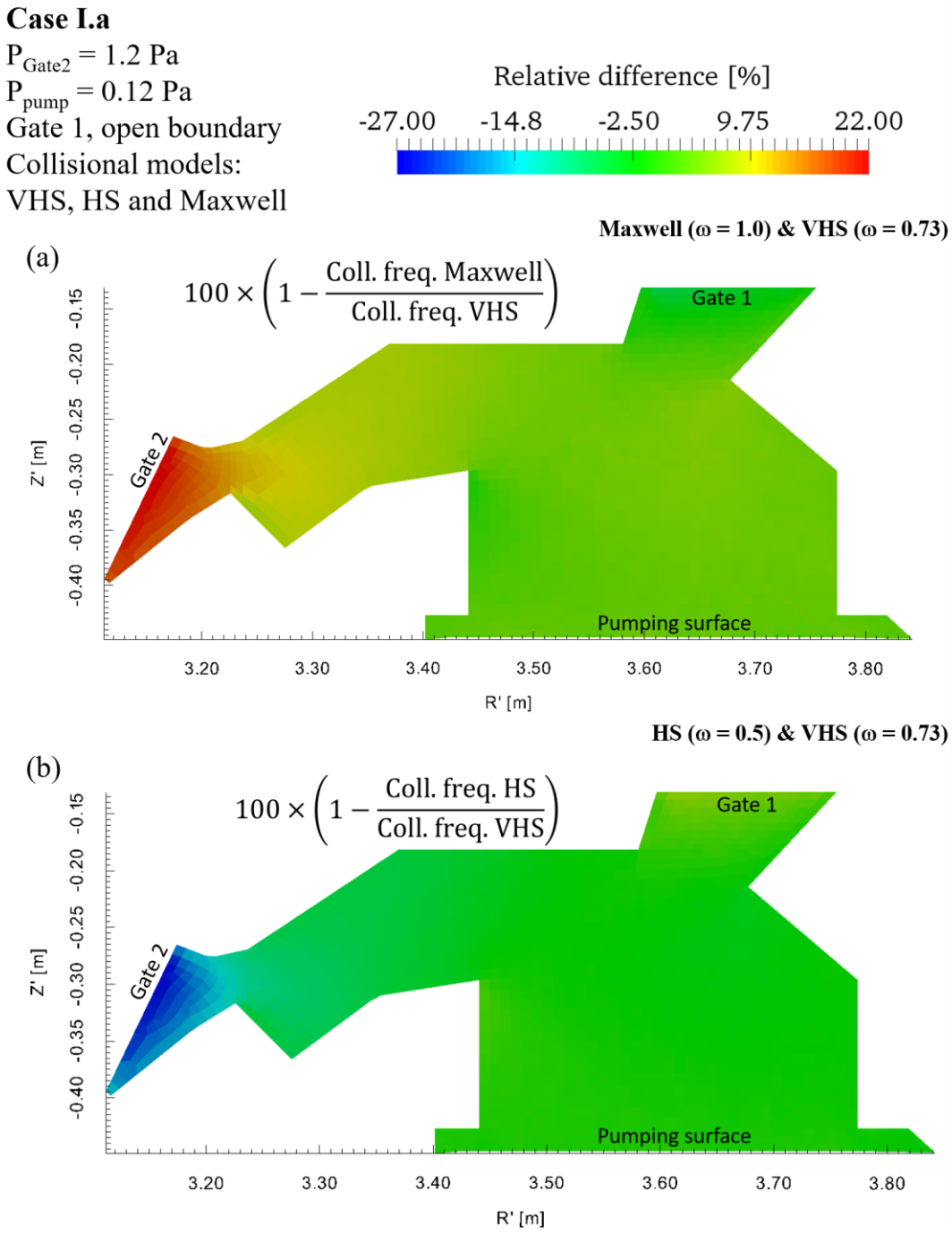

Figure 5.22 Relative difference between collision frequency obtained from Case I.a. employing three binary collision models: Maxwell (ω= 1.0), hard sphere (ω= 0.5) and variable hard sphere (ω= 0.73). The boundaries conditions are set the same at Gate 2 (1.2 Pa), pumping surface (0.3 Pa) and Gate 1 (open boundary, sticking probability of unity). The particle-wall interaction is diffusely with full accommodation with a wall temperature of 293.16 K.

In contrast to regions II-IV, both temperature and density define the number of collisions experienced by the neutrals in region I near Gate 2. This is true particularly for the location in the sub-divertor with *R'*< 3.25 m. Assuming the change of the density is

negligible when different binary collision models are employed, then the ratio T/T_{ref} is the only parameter affecting the value of the collision rate ν. Therefore, it is of parti-cular interest to quantify the introduced *error* in the collision rate ν between binary collision models. Figure 5.23 depicts the percentage difference of both $1 - \nu_{Maxwell}/\nu_{VHS}$ and $1 - \nu_{HS}/\nu_{VHS}$. The following observations for the case I.a. are summarized:

- The range of temperature ratio T/T_{ref} in the flow field restricts the possible deviations of the collision rate between collision models. For the analysis of case I.a., the box in yellow color in Figure 5.23 denotes this range found in most of the sub-divertor domain.

- Although the plot of Figure 5.23 looks quite symmetrical at first sight, actually the curve Maxwell-VHS (red) increases with a lower rate than the decrease rate of the HS-VHS curve (blue) for high temperatures. This means that if the viscosity index of VHS and T_{ref} are maintained constant, at higher temperatures of the gas flow ($T \gg T_{ref}$) the deviations relative to the VHS model of the collision rate are higher for the HS model than those calculated with the Maxwell model.

- In practice, if $T > T_{ref}$ or $T \gg T_{ref}$ occurs, the HS-sphere model overestimates the number of collisions in a high-temperature region, whereas the Maxwell model underestimates the collision rate as shown before. For ratios T/T_{ref} lower than unity, the above observations are opposite (see Figure 5.23 for values $T/T_{ref} < 1$).

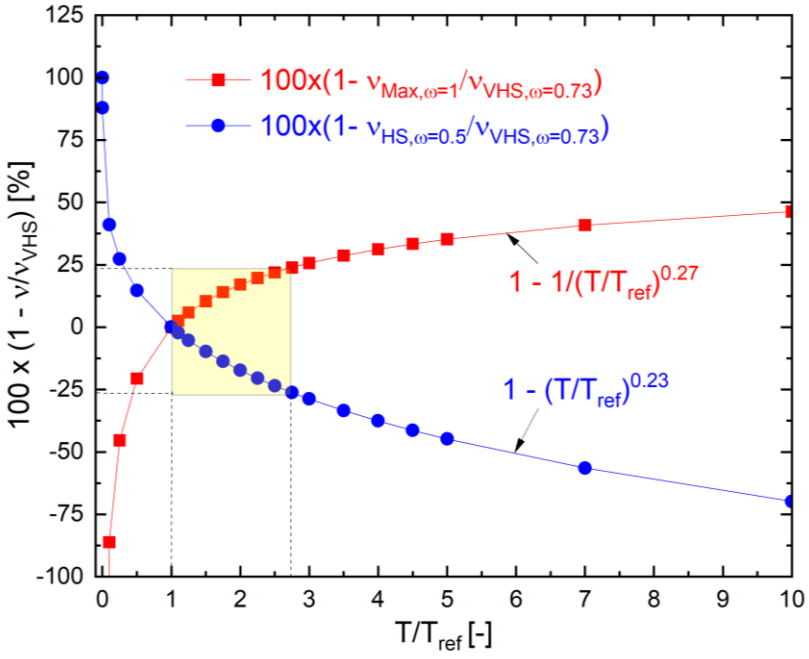

Figure 5.23 Relative difference expressed in % of collision frequency between binary collision models as a function of the temperature ratio T/T_{ref}. The relative difference is taken between the following collision models: Maxwell-VHS and HS-VHS. For the Case I.a. the temperature range of interest at the sub-divertor is depicted in the yellow box.

Case II: Scenario #2 of JT-60SA

The study is performed by switching on the collision module in the DSMC code and comparing the outcome with the collisionless DSMC results. Here, pressure, temperature and the collisionality regime in terms of the *Kn* number are presented.

The simulation is based on the JT-60SA Scenario #2, see [91] and [92], where a dedicated SONIC calculation has been performed for this task in order to properly set the boundary conditions at the sub-divertor interfaces. Deuterium influx in its molecular form is considered in this scenario. By considering single gas species flow, it is possible to isolate the effect of the collisions on D_2.

The influx of deuterium takes place at both gates with a flow speed of 314.3 m/s (Gate 1) and 589 m/s (Gate 2). The temperatures associated to the translational motion of the particles at Gate 1 and 2 are 1118.57 K and 1335.67 K, respectively. At the sub-divertor walls the temperature is set to 293.16 K. Pressure values of 1.24 Pa and 4.4 Pa are imposed at Gate 1 and Gate 2. The diffuse reflection model with full accommodation coefficient is used as before and at the pumping surface, 3% of the particles impinging the boundary are absorbed (deleted from the domain). The rest, 97%, is reflected back to the sub-divertor domain. To model the chevron in JT-60SA sub-divertor, a group of 4-sided structures is now included in front of the pumping duct. The temperature of the chevron structure is set to the value of the wall temperature. Here the collisionality regime is defined as the ratio of the VHS mean free path to the characteristic length of the sub-divertor, i.e. the narrowest distance between the dome sub-divertor wall in region I (0.045 m), see Figure 5.24.

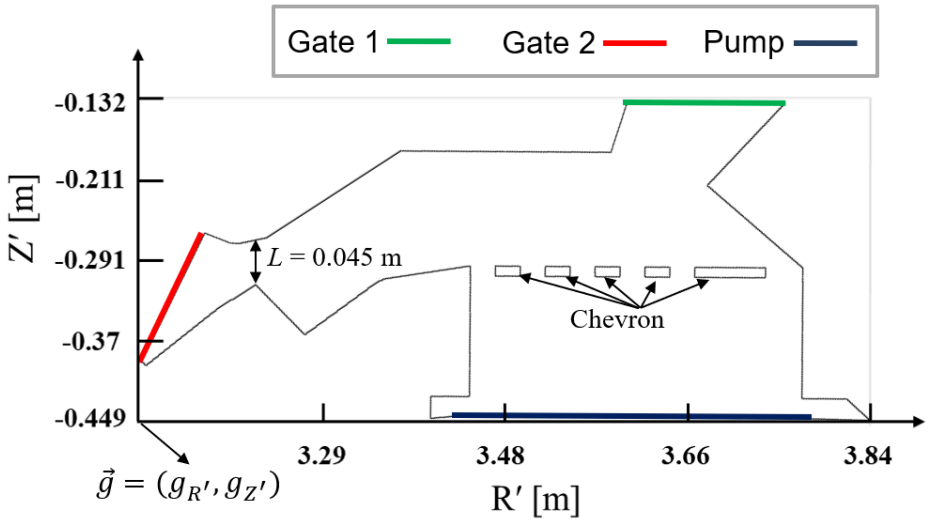

Figure 5.24 JT-60SA simplified sub-divertor domain within the chevron shielding (at same temperature as the walls). The incoming neutral particles from the plasma chamber enter the domain at Gate 1 and Gate 2. The pressure values at Gate 1 and Gate 2 are 1.24 Pa and 4.4 Pa respectively. The pump reflects 97% of the incoming particles as a diffuse boundary condition with a temperature of 293.16 K.

The calculated spatial *Kn* number distribution is plotted in Figure 5.25. The influence of collisions can be neglected for *Kn* > 10, whereas here the *Kn* numbers below 0.5 in the whole sub-divertor domain are observed. This implies the occurrence of a transitional flow, where neither a free collisional nor a continuum approach sufficiently exact describe the flow dynamics. On top of that, by the inclusion of atomic deuterium in the calculations where high-energetic atoms coming from the private flux region will enhance the momentum exchange at both gates, enhancing the collisional effect and modifying the flow field in region II and as consequence region IV.

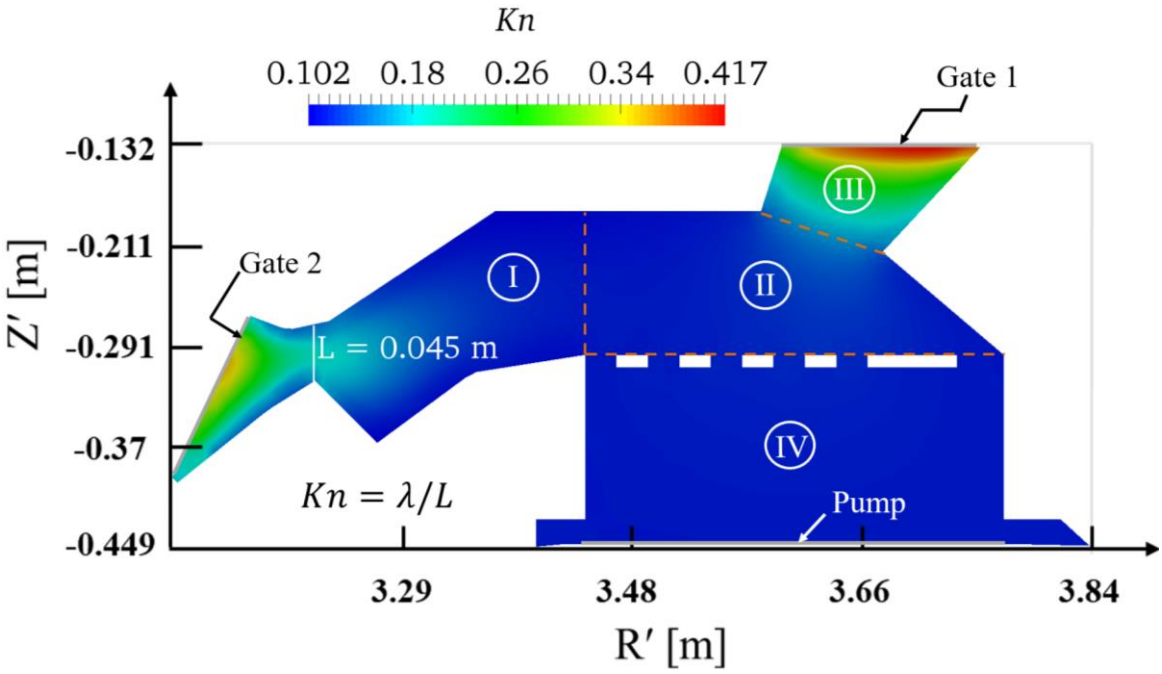

Figure 5.25 The *Kn* number profile along the JT-60SA sub-divertor. The regions I-IV are referred to Figure 5.6.

Figure 5.26 illustrates the contour plots and isobars along the JT-60SA sub-divertor for both study cases. The calculations suggest that the flow conditions in this case are strongly affected by the collisions between the neutrals. Simulations shown that whenever the collisions are taken into account the pressure in the sub-divertor is increased by 20-40% in regions far from the gates, namely in region I (below the dome at around *R'*= 3.49 m and *Z'* = -0.291 m) ~ 30% and II ~ 25% (at around *R'*= 3.66 m and *Z'* =-0.211 m). In region IV, the discrepancy between the collisionless and collisional case is increased furthermore where 40% difference is found.

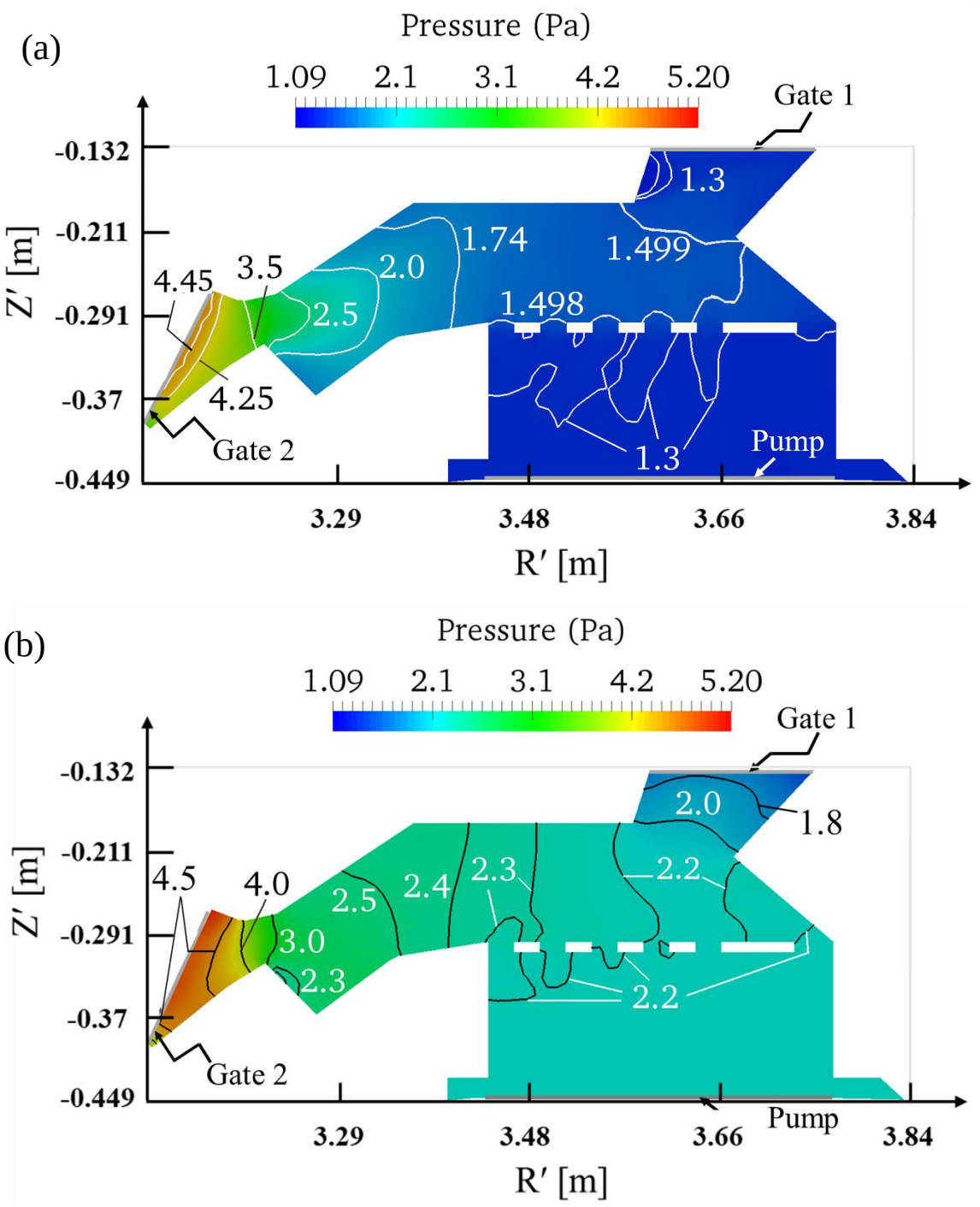

Figure 5.26 (a) Isobars in DSMC simulations (collisions off). (b) Isobars in DSMC (collisions on). For both DSMC analyses the JT-60SA scenario #2 boundary conditions is considered, where neutral particles enter the domain at Gate 1 and Gate 2 and the pump absorbs 97% of particles impinging this boundary. The temperature of the wall and structures (chevron) is set to 293.16 K.

The effect of collisions can also be seen in the temperature distribution of the flow. For this, the ratio of temperatures across the domain is sampled in order to calculate the

relative difference between collisionless and collisional approaches. In Figure 5.27 it is shown that near both gates, the difference between temperatures reaches its maximum. It is worth noting that in this region the highest value of pressure is found. For the simulation without collisions, the overall temperature in the sub-divertor is at least a factor of 0.5 and 0.8 lower than the collisional simulation near Gate 1 and 2, respectively. In region II, the relative difference between DSMC analyses ranges between ~ 3% and ~ 30% where the highest difference is found above the chevron that lies directly below Gate 2, see Figure 5.28. Almost constant temperature ratio is found in region IV, since in this region the gas is thermalized within the chevron and the pumping surface.

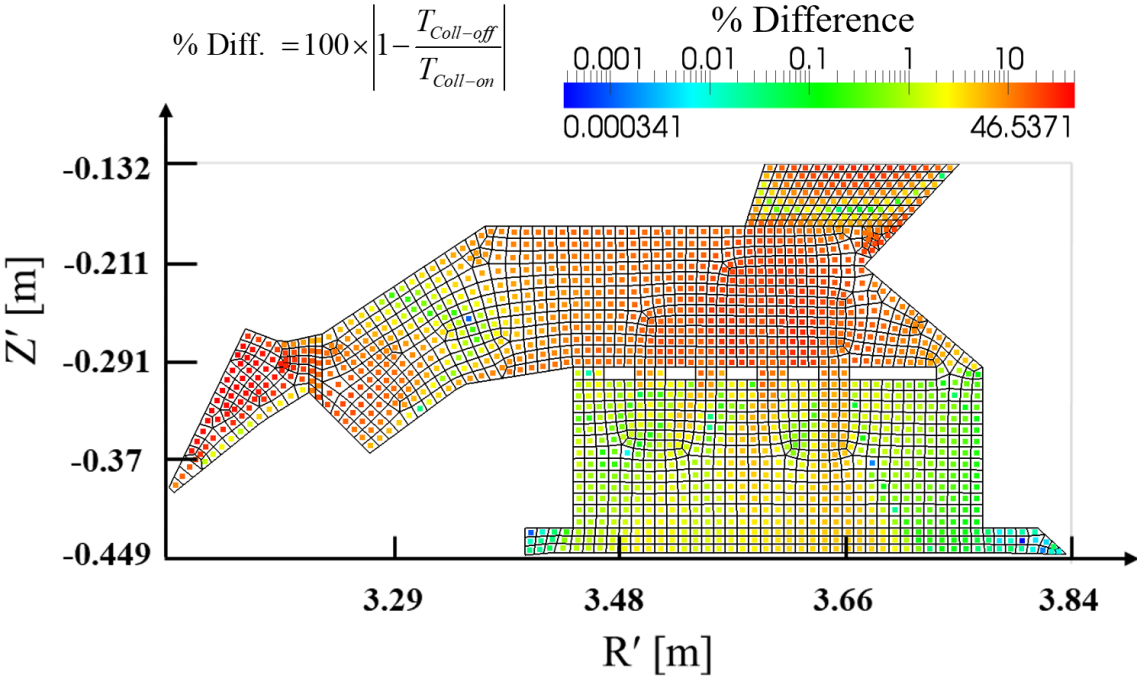

Figure 5.27 The temperatures $T_{Coll\text{-}on}$ and $T_{coll\ off}$ are sampled across the JT-60SA domain and the relative difference (%) between collisionless and collisional DSMC calculations estimated.

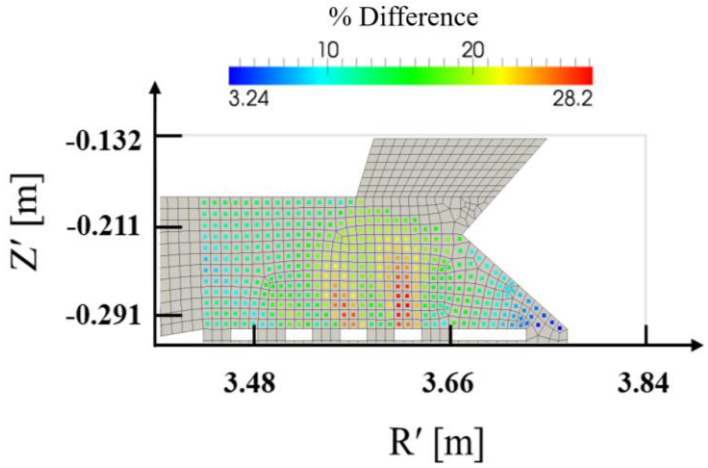

Figure 5.28 The temperatures $T_{coll\ ON}$ and $T_{coll\ OFF}$ are sampled across region II in JT-60SA domain. It can be seen the relative difference (%) of the translational temperature between collisionless and collisional DSMC calculations.

The present analysis demonstrates the capabilities of *dsmcFoam* to handle colisionless and collisional gas flows. The major outcomes of this section are:

- By turning off the collision kernel in DSMC, a comparison between NEUT2D and DSMC is performed. Good agreement between NEUT2D and DSMC regarding flow speed profiles are only found in region II in JT-60SA (node wise). However, in regions I, III and IV only partial agreement is found between approaches.
- NEUT2D calculates a colder gas than DSMC. With the available information it has not been possible to explain the reason of this observation.
- For collisional flows, it has been demonstrated that the collision frequency obtained with DSMC and the theoretical expression are in good agremment since the results differ by less than 1% across the sub-divertor. In this study the VHS binary collision model has been employed.
- As a result of the sensitivity analysis, for regions in the sub-divertor where the conditions $T/T_{ref} > 1$ or $T/T_{ref} \gg 1$ hold, it has been observed that the following relation for the collision frequency between models is true:

  $$\nu_{HS} > \nu_{VHS} > \nu_{Maxwell}$$

  This can be used to estimate the introduced error on the number of collisions by using a particular collision model.
- The effects of collisions in JT-60SA for the so-called Scenario #2 have been studied solely with DSMC. Deviations in the pressure of 20% and 40% between a collisionless and a collisional DSMC are obtained. Temperature deviations of 3% to 46% are also found, with the maximum differences at the inlet and outlet regions.

5.2 Particle exhaust in ITER divertor

Having established confidence in the DSMC solver for calculating collisional and collisionless flows in tokamak divertor and simple geometries, the application of the DSMC method to present fusion devices in operation and reactor-relevant devices currently being built is addressed.

First, the analysis of the neutral gas flow in ITER sub-divertor is introduced. Once again, the investigation is based on a two-dimensional flow of a single gas. The boundary conditions resulted from the a SOLPS analysis for the ITER high-divertor pressure scenario with a total average gas pressure of 9.9 Pa above the dome. The resulting pressure distribution along the divertor cassette facing the plasma SOL and PFR, defines the boundary conditions of the DSMC simulations.

The main aim of this sub-schapter is to quantify the effect of the pumping conditions on ITER sub-divertor flows. This has been done by analyzing the flow field variables as function of the pressure at the entrance of the pumping port. Collisional effects have been observed and correlated to the pumping conditions. Part of the analysis also focuses on the pressure value comparison across the flow domain between the DSMC approach and the ITERVAC code, which is a known tool for calculating vacuum flows.

5.2.1 Gas flow modelling in ITER divertor geometry and boundary conditions

The simulated ITER divertor geometry is based on the 2009 3D-design [41] illustrated in Figure 5.29. The DSMC simulation domain is simplified to a 2D-cut in the sub-divertor region in order to apply the input of the SOLPS, which is also two-dimensional. The DSMC domain is shown in Figure 5.29 (red domain). The pressure is imposed at the five main contributions to the particle exhaust coming from the SOL and private flux region (positions I-V). The pressure at the pumping port is taken as parameter (position VI). The arrows shown in yellow depict the possible flow path directions of the neutral gas. Therefore, the pressure values employed in DSMC shown in Table 5.4, are the output of the plasma calculation defined at the sub-divertor interfaces I-V.

During ITER operation the particles are pumped through the transparencies and slots located between dome (position III), reflectors and small slots near the target corners (positions II and IV). Additionally, two gaps are located at positions I and V, which serve as paths for the gas flow between the sub-divertor region and the main chamber. The pressure at these gaps is typically orders of magnitude lower than the pressure below the dome. The particles that do not follow the path behind the vertical targets move towards the pumping duct (position VI).

Similar to the previous analysis of JT-60SA, in order to obtain the boundary conditions of the DSMC calculation at the locations I to V depicted in Figure 5.29, first a background plasma simulation is performed with the SOLPS code. The SOLPS analysis includes the following species: D_2 molecules, D (representing both hydrogen isotopes D and T), He, C ions and atoms.

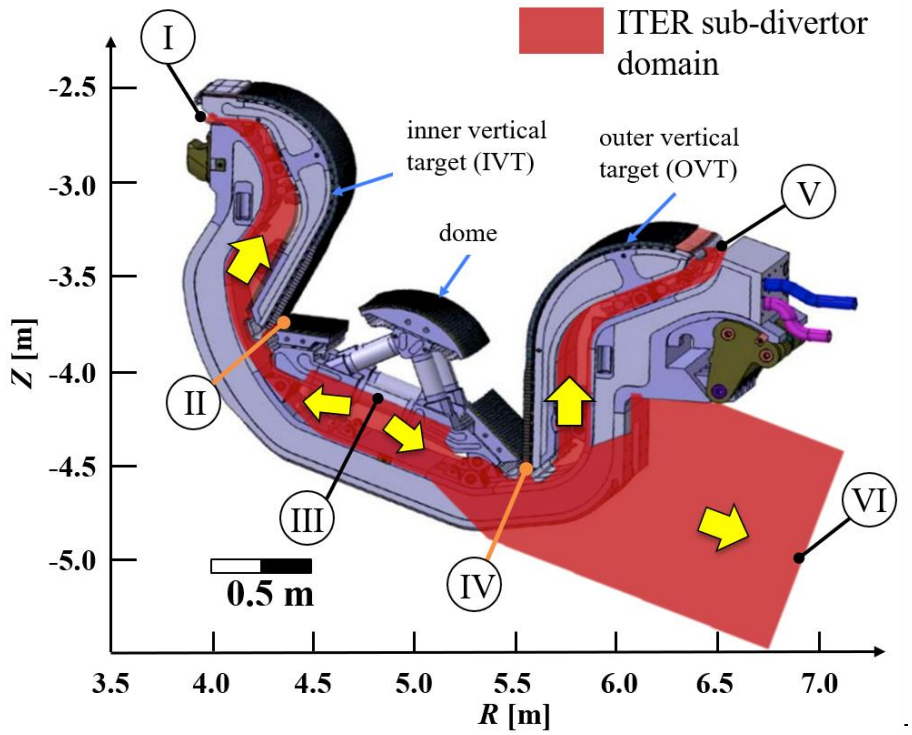

Figure 5.29 Diagram of the ITER divertor geometry [94]. The sub-divertor flow domain (red) is extracted from the 3D CATIA model. For the DSMC calculations an axial cut through an ITER divertor cassette is done. The inlet boundary conditions are imposed at the positions I-V. The exhausted gas flow directions are shown in yellow. Figure taken from [41], [94].

For the DSMC simulations the gas composition is simplified to be only deuterium in molecular form, as this makes up for about 80% of the working gas in the investigated scenario. The ITER high-divertor pressure scenario with a total average gas pressure of 9.9 Pa above the dome (~ 8 Pa D_2 average partial pressure at region III) is selected as the scenario for the DSMC the analysis. Moreover, it is assumed that the neutrals at all inlet locations (I-V) have a reference temperature of 420 K. The same temperature is set in the sub-divertor walls. The temperatures of the neutral particles entering the sub-divertor are typically a factor 3 higher than the ones here applied. However, the value of the temperature is set to 420 K, since ITERVAC analyses are available at this temperature for the same ITER geometry and pressure boundary conditions, allowing a comparison between DSMC and ITERVAC code results, which are shown later in this section.

The present analysis of the neutral flow is conducted by varying the pressure at the pumping port entrance p_{VI} (position VI) maintaining the same divertor conditions. The pressure p_{VI} takes the following values:

- 0 Pa (case #1, referred also as ideal case)
- 10^{-3} Pa (case #2)
- 10^{-2} Pa (case #3)
- 10^{-1} Pa (case #4)
- 1.0 Pa (case #5)

In the present work the DSMC algorithm based on the No-Time Counter (NTC) scheme is implemented for simulating the gas flow. The variable hard-sphere (VHS) model is employed and the time increment is taken as $\Delta t = 1 \times 10^{-6}$ s; other values smaller than the selected are disregarded, as they do not essentially change the results. The computational mesh shown in Figure 5.30 is unstructured with a total number of triangular cells of 4.6 x10^4.

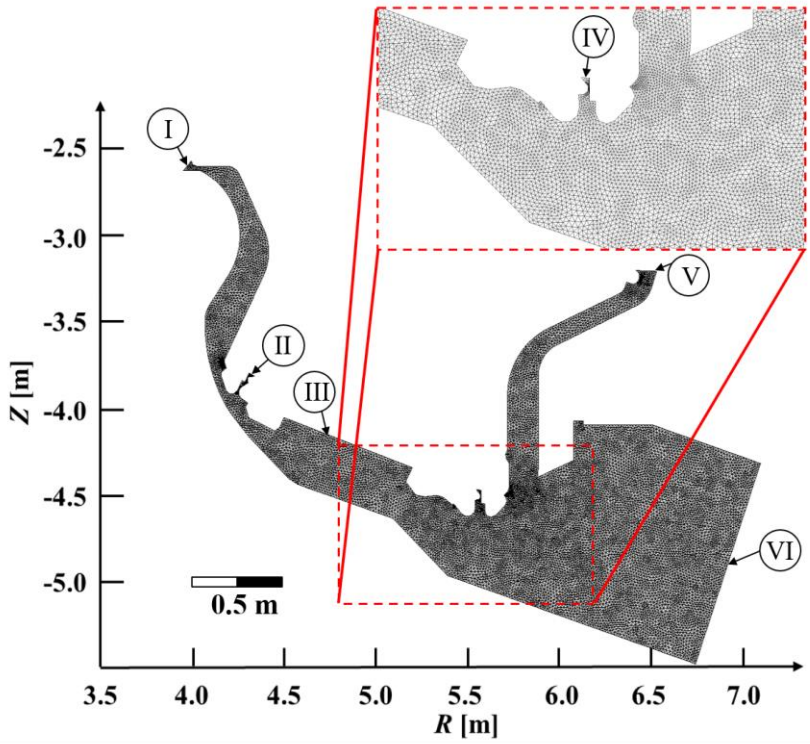

Figure 5.30 A 2D ITER sub-divertor unstructured grid and a close-up to the region near location IV. Particle fluxes enter the sub-divertor at positions I-V, where the pressure boundary conditions are applied. At the pumping duct (VI) the pressure values are varied.

The mesh is chosen as a result of preliminary grid studies with different number of elements. Since the study cases employed the same boundary conditions at locations I-V, the grid employed throughtout the analyses has not been modified. Care has been taken for the region near the pumping port (position VI) where the chosen grid meets the requirement that at least 10-20 DSMC particles are found at each cell for all simulations, as shown in Figure 5.31 for the extreme cases #1 and #5. This assures that for the rest of the cases #2 to #4, the number of DSMC particles per cell lie in between this range.

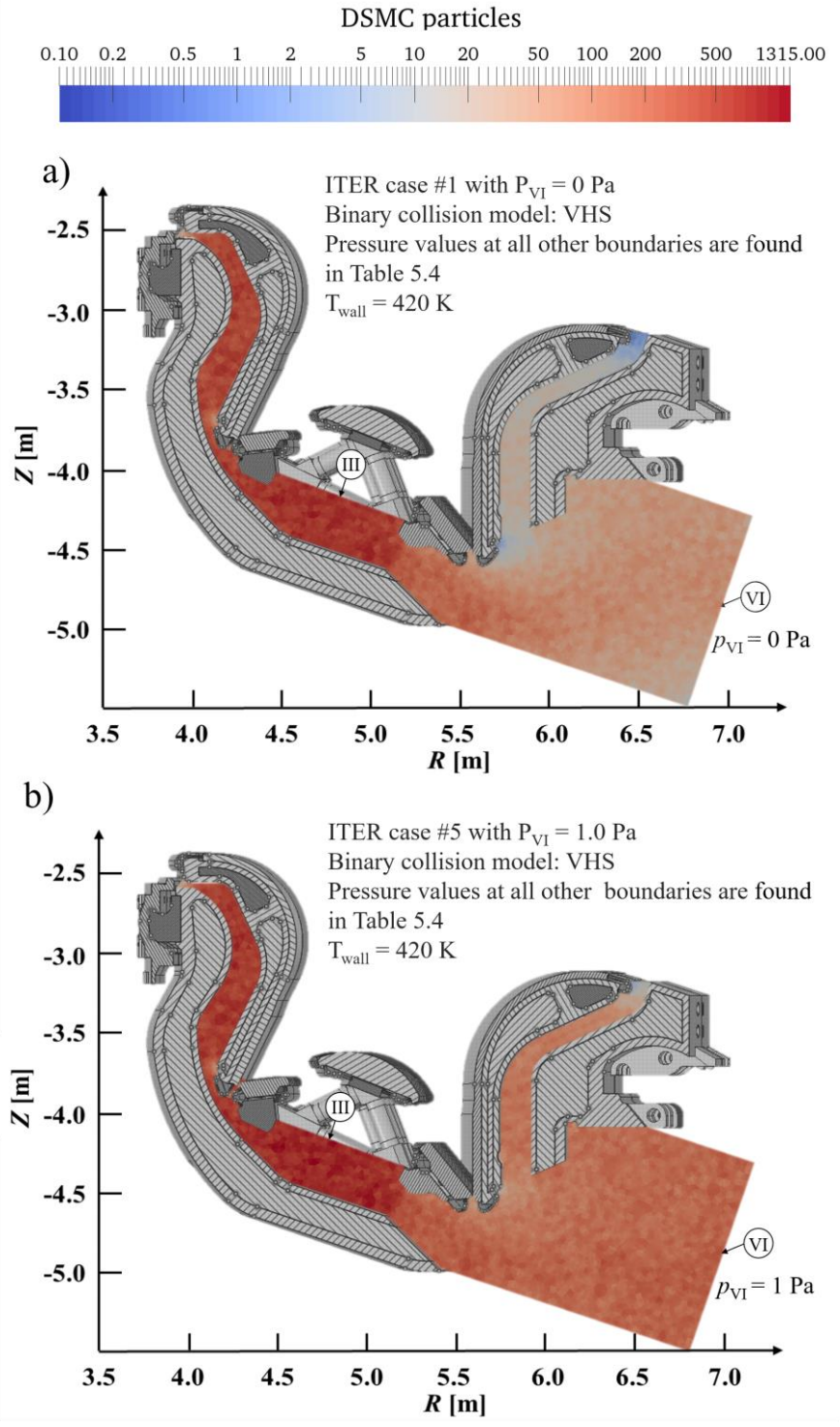

Figure 5.31 Number of DSMC particles in the computational domain for the ITER divertor for divertor pressure of 9.9 Pa (~ 8 Pa D_2 average partial pressure at position III) for two cases: (a) Case #1 with 0 Pa at position VI and (b) case #5 with 1.0 Pa at position VI.

Table 5.4 The summary of the modelling parameters for ITER type divertor

	Type / Parameter	Value	Unit
Boundary name			
I	Pressure type (inlet)		
	Pressure	8.82×10^{-4}	Pa
II	Pressure type (inlet)		
	Pressure	23.6	Pa
III	Pressure type (inlet)		
	Pressure	7.82	Pa
IV	Pressure type (inlet)		
	Pressure	15	Pa
V	Pressure type (inlet)		
	Pressure	8.12×10^{-4}	Pa
VI	Pressure type (outlet)		
	Pressure	$0,10^{-3}, 10^{-2}, 10^{-1}, 1$	Pa
DSMC properties			
Time step	Δt	1×10^{-6}	s
Conversion factor	F_N	$8 \times 10^{12}, 1 \times 10^{13}$	-
Particle-wall interaction	Diffuse reflection		
	Temperature	420	K
Binary collision model	Variable Hard Sphere model		
	Reference temperature	273	K
Particle attributes			
Particle name	Deuterium (D_2)		
mass	m	6.69×10^{-27}	kg
diameter	d	2.92×10^{-10}	m
rotational DoF	Rotational DoF	2	-
viscosity index	ω	0.73	-

5.2.2 Effects of increasing the pressure at the pumping port: velocity and pressure fields

It is intuitive that the particle interaction in terms of collisionality has to increase as the pressure value at the pumping duct is increased. However, the question remains whether the gas flow is sensitive to these changes and if this is the case, which fundamental mechanisms are involved. For the modelled divertor conditions, neutral particle flow towards the plasma vessel is observed to take place via the upper gaps I and V. Figure 5.32 shows a typical neutral gas flow pattern found in ITER sub-divertor.

The net particle flow at the upper gaps I and V is estimated once the steady conditions are reached, i.e. at the point in time where the avering process in the DSMC simulation starts. As before, this state is reached by monitoring the total number of DSMC particles in the system, as shown in Figure 5.33 exemplary for the cases #1 and #4 with a

pressure at location VI of $p_{VI} = 0$ Pa and $p_{VI} = 0.1$ Pa, respectively. Following the criterion defined in Chapter 3.6, in ITER simulations the plateau of the DSMC particles is reached around 200, 000 timesteps and the peak-to-valley is less than 2% during the run.

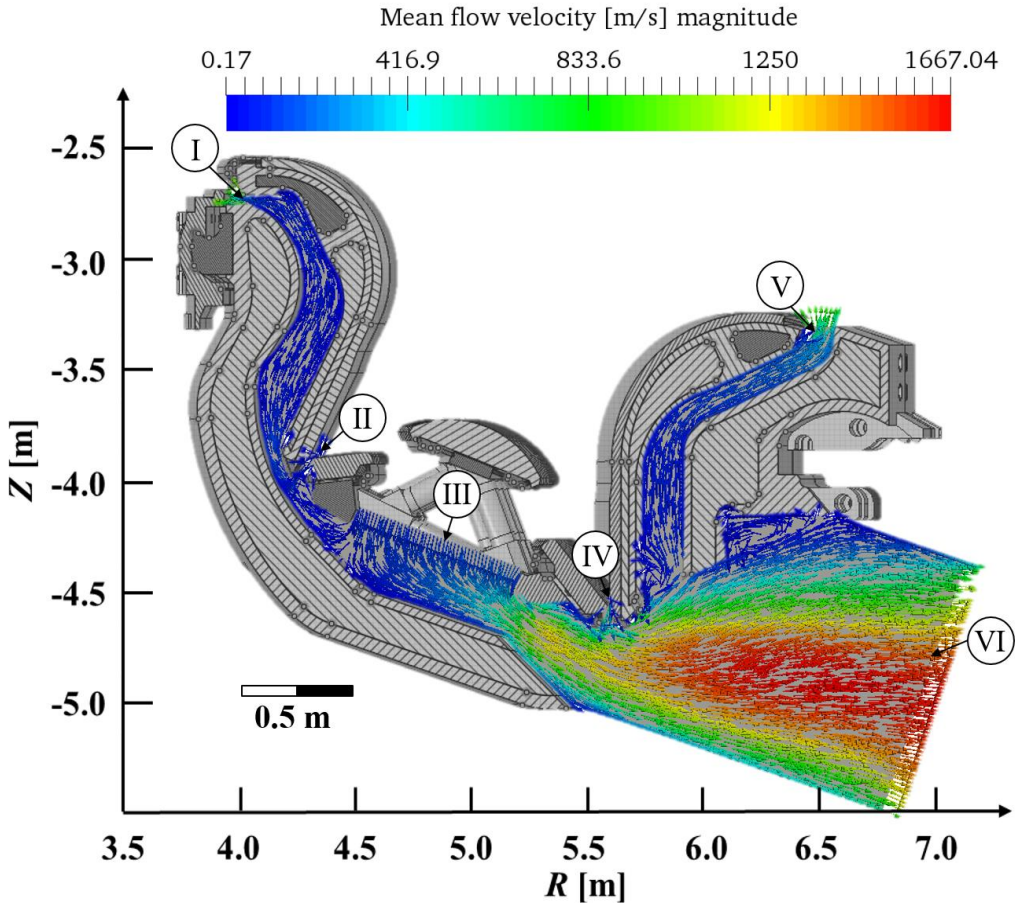

Figure 5.32 Velocity flow field in the ITER sub-divertor domain for the case #1 with a pressure of 0 Pa at location VI (pumping port). The boundary conditions at positions I-VI read $p_I = 8.82 \times 10^{-4}$ Pa, $p_{II} = 23.6$ Pa, $p_{III} = 7.82$ Pa, $p_{IV} = 15$ Pa, $p_V = 8.12 \times 10^{-4}$ Pa and $p_{VI} = 0$ Pa. The wall temperature of the sub-divertor is set to T = 420 K and VHS is the employed binary collision model.

a) ITER case with P_{VI} = 0 Pa: first 1.2x10^6 timesteps
Binary collision model: VHS
Pressure values at all other boundaries are found in Table 5.4
T_{wall} = 420 K

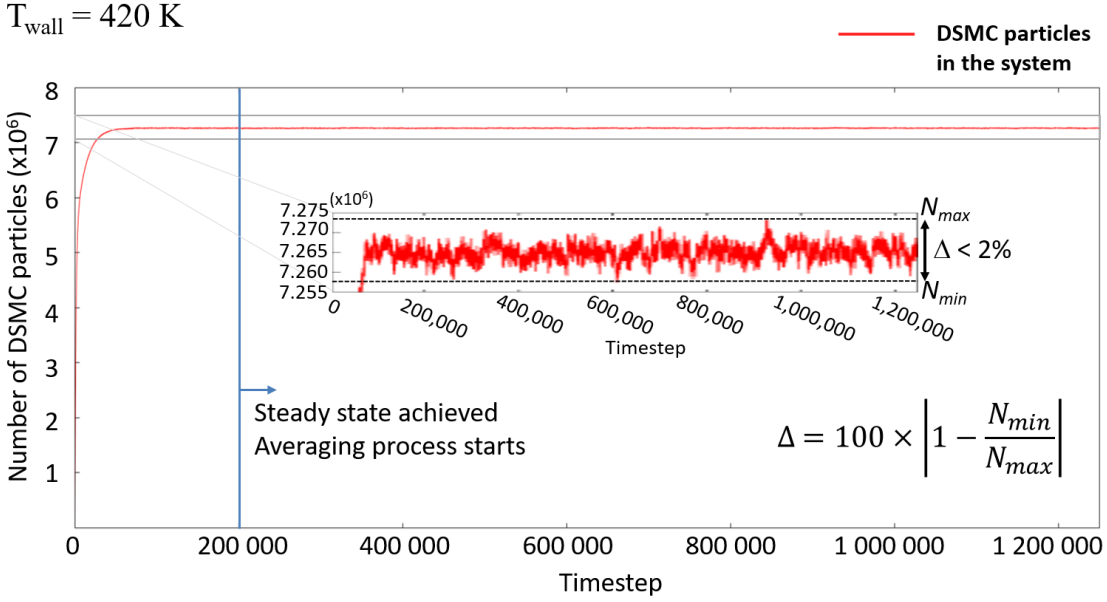

b) ITER case with P_{VI} = 0.1 Pa: last 500,000 timesteps
Binary collision model: VHS
Pressure values at all other boundaries are found in Table 5.4
T_{wall} = 420 K

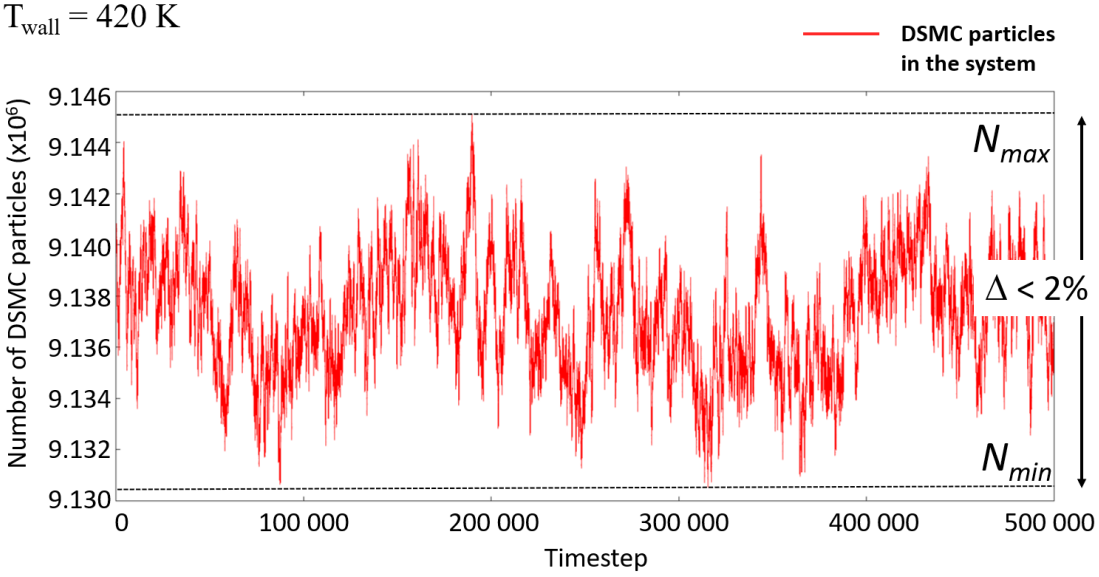

Figure 5.33 Stationary conditions with respect to the total number of particles in a DSMC simulation for ITER. The temporal evolution of the ITER cases is shown for the analysis (a) with a pressure value of 0 Pa at the boundary number VI and (b) with a pressure value of 0.1 Pa at the boundary number VI. The analyses are focused on deuterium gas in its molecular form with VHS as binary collision model. The diffusion-reflection wall with full accommodation is employed as particle-wall interaction in the sub-divertor domain.

In Table 5.5 the net average rates at locations I and V are normalized to those found in the ideal case, $p_{VI} = 0$, namely 4.64×10^{21} D_2 m^{-1}s^{-1} and 2.85×10^{20} D_2 m^{-1}s^{-1} for the inner (I) and outer locations (V), respectively. In Table 5.5, the superscript k denotes the location of interest while the subscript m the study case number. Relative to the case with back pressure $p_{VI} = 0$ Pa, a maximum difference of ~ 3 % (case $p_{VI} = 10^{-2}$ Pa) is found with the net flow at location I, for all the other cases the difference is less than 1 %. The particle flows at positions I and V show an asymmetry as the pressure at the pumping port increases. This observation is discussed below together with the introduction of the pressure distribution in the sub-divertor.

Table 5.5 Average particle fluxes at locations I and V. The results of Cases #2, #3, #4 and #5 are normalized to the respective average fluxes found in the Case #1 with $p_{VI} = 0$ Pa

Ratio of particle flux (case 2, 3, 4, 5) to particle flux of Case #1 $p_{VI} = 0$ Pa at locations I and V				
$\langle D_2\ m^{-1}s^{-1}\rangle_m^k / \langle D_2\ m^{-1}s^{-1}\rangle_{0\ Pa}^k$				
k	m (case #)			
(Location)	Case#2/Case#1	Case#3/Case#1	Case#4/Case#1	Case#5/Case#1
I	1.0003	1.0279	0.9914	0.9959
V	1.0438	1.0689	1.2293	8.3173

To provide a better idea of the impact of the values of Table 5.5, the ratio R_{D2} of the exhausted particles to the particle at positions (sum of I and V) is calculated by $R_{D_2} = \Gamma_{VI}/\Gamma_{I+V}$. This ratio reflects the competition between the gas conductance of both boundary positions of the divertor legs (I+V) and that of the pumping port (VI). The ratio reads for the 0.1 Pa- and 1 Pa-cases 23.04 and 18.18, respectively. The rest of the cases have a maximum of 2 % difference relative to the 0.1 Pa-case. The results tell us that the pumping conditions dominates the flux distribution in the sub-divertor, which can be shown in terms of quantitative numbers by modifying the back pressure at the pumping duct of ITER.

The modelling also shows that for pressures below the 1 Pa the ratio inner-to-outer fluxes between the two outlet boundaries behind the divertor targets ranges $9.2 < \Gamma_I/\Gamma_V < 15.6$. An increase of the pressure to 1 Pa at the pumping port leads to an increase flux only at the outlet boundary V (outer region) with no significant change at location I. In contrast, the fluxes at position V show a rather monotonic increase for all cases with a drastic increase of the particle flux when the pressure is 1 Pa at the pumping port. A value of

8.31 is obtained for the ratio of fluxes between case #5 and case #1 at position V, see Figure 5.34. At this condition, the value of the flux at location V is of particular interest, since it means that by enhancing the back pressure at the pumping port, the number of neutral particles flowing towards the plasma at the low-field side increases, *feeding* the plasma with the same order of magnitude of fluxes as the high-field side (position I).

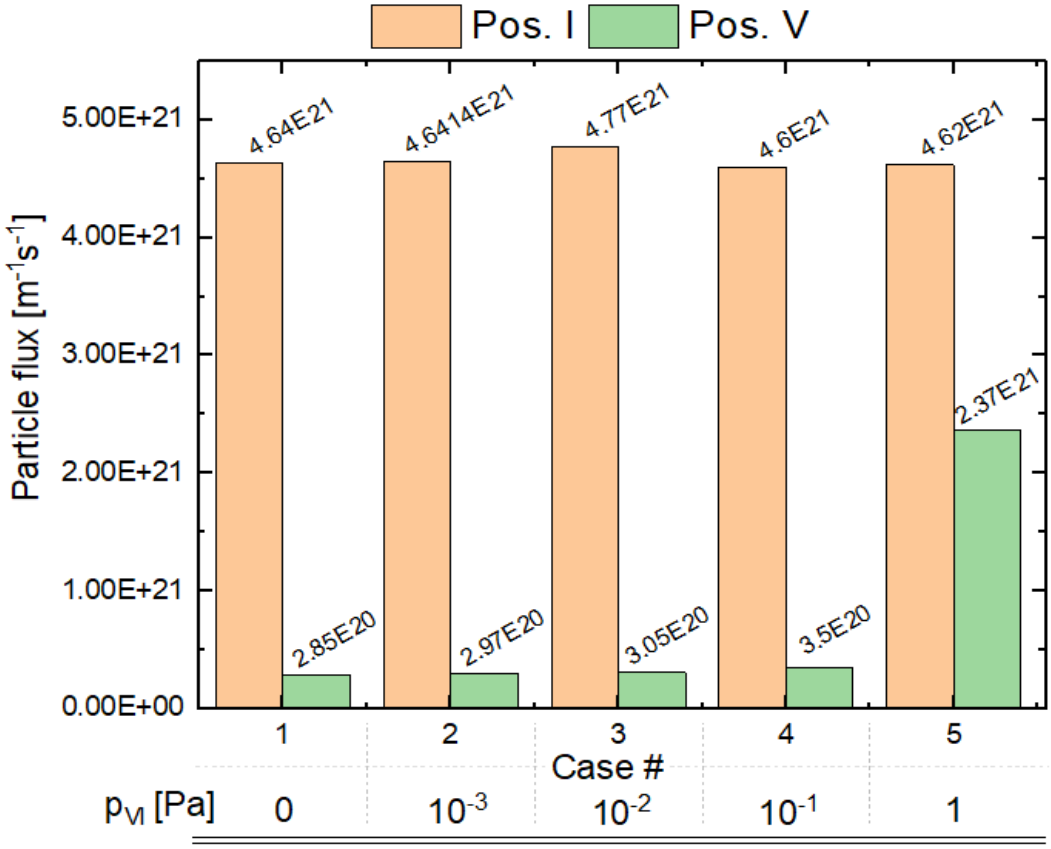

Figure 5.34 Particle fluxes in ITER sub-divertor sampled at the end of the ducts behind the vertical targets (position I and V). The pressure boundary conditions for all cases read $p_{\mathrm{I}} = 8.82 \times 10^{-4}$ Pa, $p_{\mathrm{II}} = 23.6$ Pa, $p_{\mathrm{III}} = 7.82$ Pa, $p_{\mathrm{IV}} = 15$ Pa, $p_{\mathrm{V}} = 8.12 \times 10^{-4}$ Pa. The temperature of the gas at the boundary locations (I-V) and the sub-divertor walls is set to 420 K.

It has been observed that the particle flux at location I and V is altered by increasing the value of the back pressure at position VI. However, there must be a more fundamental mechanism that helps to understand such findings. To answer this, the streamlines of the particle flow are now the subject of our attention. Figure 5.35 depicts the velocity streamlines of two extreme study cases: Case #1 with $p_{\mathrm{VI}} = 0$ Pa and Case #5 with $p_{\mathrm{VI}} = 1.0$ Pa.

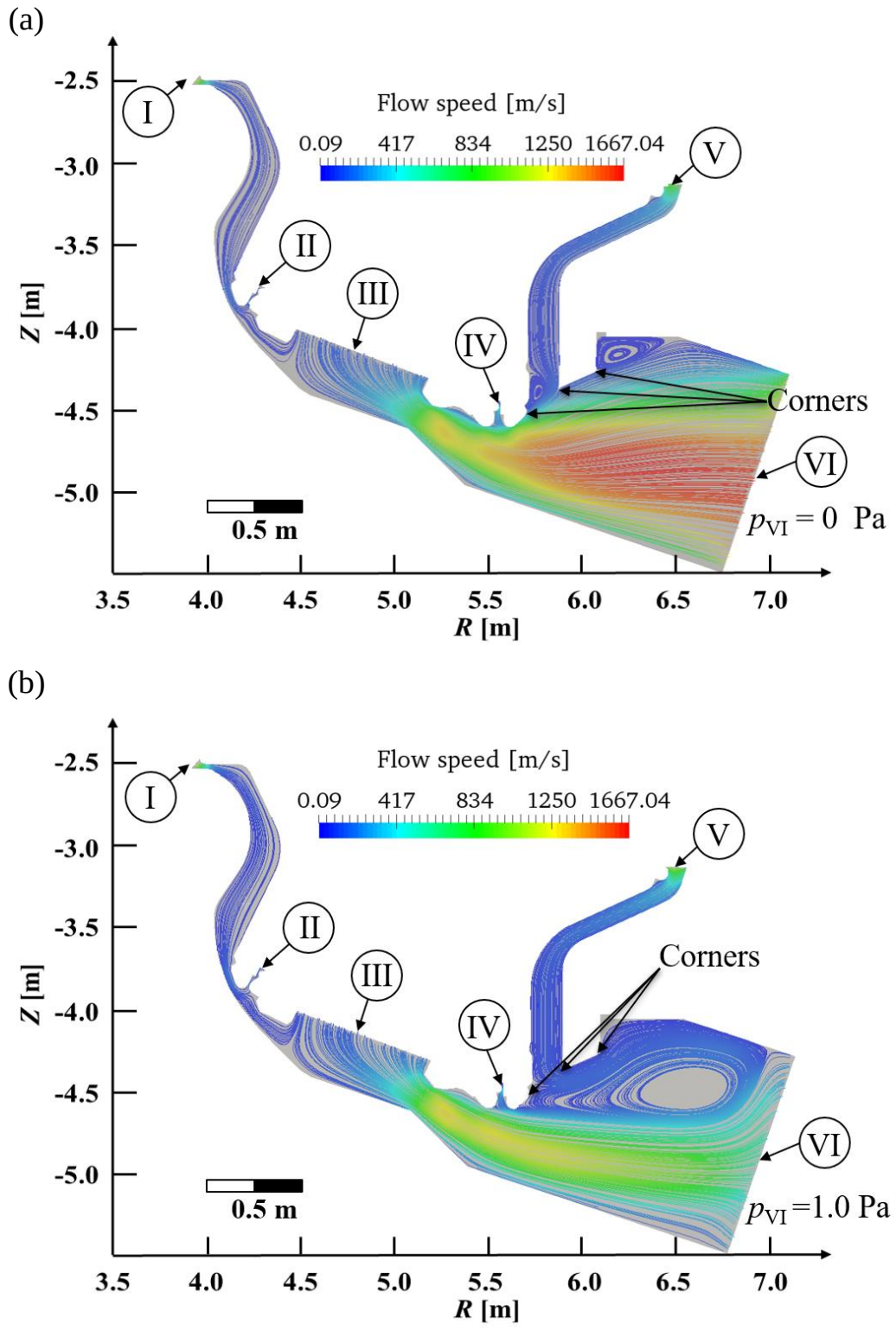

Figure 5.35 (a) Streamlines in ITER sub-divertor, divertor pressure 9.9 Pa and case p_{VI} = 0 Pa. (b) D_2 streamlines in ITER sub-divertor for a high divertor pressure case (9.9 Pa) for the case study with p_{VI} = 1.0 Pa.

A common phenomenon in gas dynamics is the separation of the streamlines due to pressure gradients in the flow field. This effect is typically seen at the so-called boundary

layer. This boundary layer separation is occurring on the rear surface of a streamlined shape where the flow is expanding due to the curvature of the solid surface and the flow velocity increase whereas the pressure decreases in the flow direction. This process sets up a pressure gradient such that each fluid element experiences a force opposing its motion in the direction of the flow as depicted in Figure 5.36 (a). Thus, gas particles close to the solid surface have a low momentum and can be brought to rest or even moved in a counterflow direction by the pressure gradient.

By using the boundary-layer equations, see Chapter 7 in [95], applied to Figure 5.36(a) for a flow in steady state conditions, force-free (external) and with a zero-velocity at the wall located at $y = 0$, it is obtained:

$$\mu\left(\frac{\partial^2 V}{\partial y^2}\right)_{wall} = \left(\frac{dp}{dx}\right)_{wall}, \tag{5.3}$$

where μ is the dynamic viscosity and the derivatives are evaluated at the wall. This relation shows that the velocity profile at the wall is determined by the pressure gradient and that the curvature of the profile is influenced by the sign of the pressure changes. Two particular conditions are relevant for the gas flow at ITER pumping port:

- $dp/dx < 0$ which results in $\partial^2 V/\partial y^2 < 0$ giving a negative curvature of the velocity profile. This means that the slope of the velocity is decreasing for *y*-values towards the wall. In this case, it is said that a favorable pressure gradient acts on the flow.

- $dp/dx > 0$ results in a positive curvature of the velocity profile, thus $\partial^2 V/\partial y^2 > 0$. In this case, a pressure increase or adverse pressure gradient acts on the flow. Additionally, there exists a point inside the boundary layer where the second derivative of the velocity is zero, i.e. an inflection point of the velocity profile exists.

Although the velocity has two components in the present study, the same phyiscal mechanism applies. The velocity flow field and pressure profile are plotted along 5 different straight lines, which are defined along the width of the ITER pumping duct as shown in Figure 5.36 (b). The position of the vertical lines is defined in such a way that it is covered the expansion region of the gas while exiting the sub-divertor domain. Since the study cases #1 to #4 exhibit no practical difference on the values of the fluxes at locations I and V, and thus a comparison between case #1 and case #5 is necessary (extreme cases). Results for the velocity components along the vertical lines for the study case #1 and #5 are shown in Figure 5.37 and Figure 5.39, respectively. Both pressure profiles along the vertical lines are depicted in Figure 5.38 and Figure 5.40.

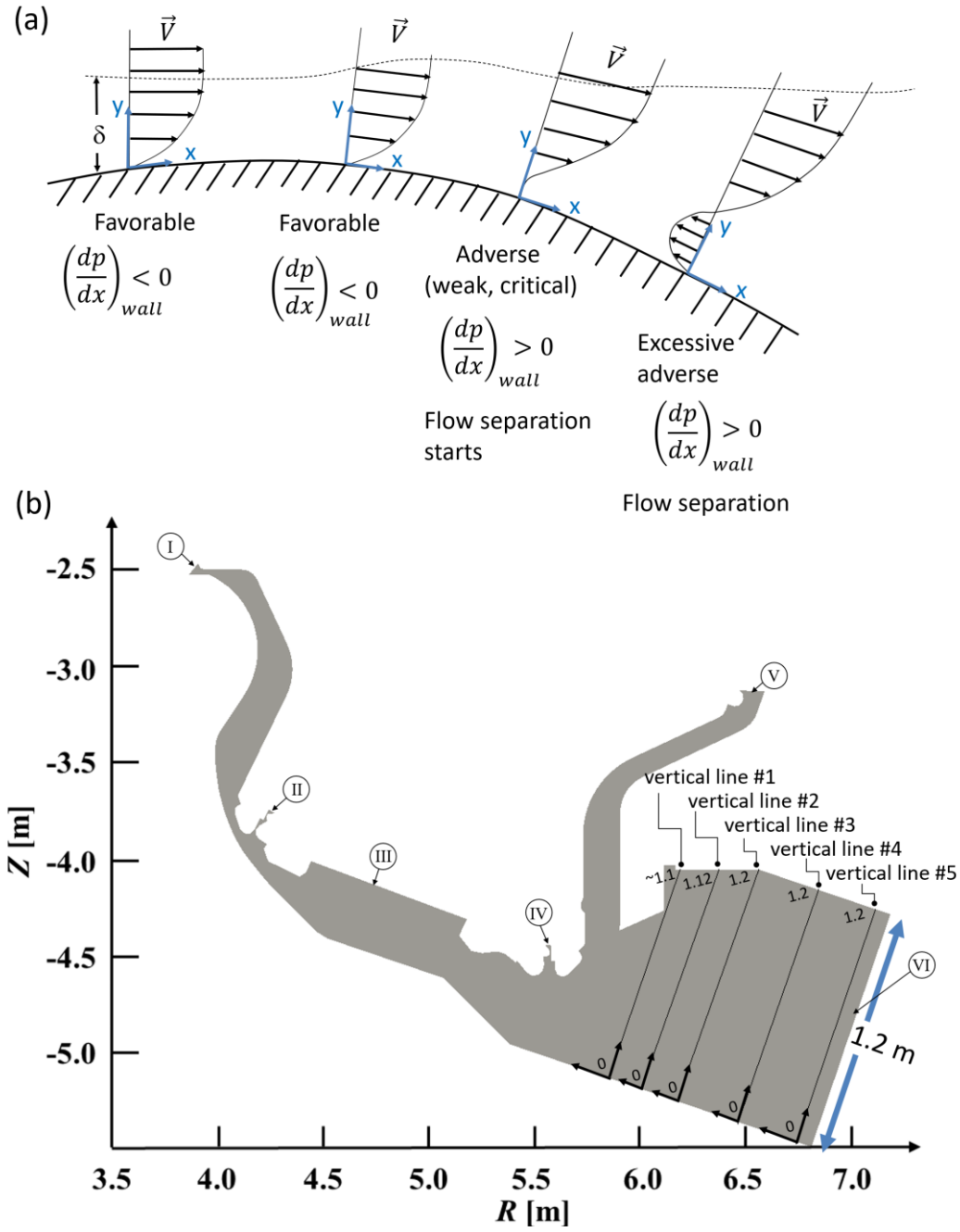

Figure 5.36 (a) Schematic of the flow separation over a curved surface. The flow velocity profile at four different points along the curve is depicted, where a favorable ($dp/dx < 0$) or adverse ($dp/dx > 0$) pressure gradient acts at the point of contact between the fluid and the wall. (b) The flow quantities for ITER Case #1 and Case #5 are plotted along 5 different paths in order to identified the flow separation along the pumping duct of the sub-divertor.

It can be seen in Figure 5.37 that the velocity profile has parabolic-like shape near the exit of the pumping duct, which is consistent with the results shown in Figure 5.34(a) where the streamlines are colored by the magnitude of the flow speed. As the vertical line is moved away from the exit of the duct, the value of the slope of the velocity component V_R decreases along the vertical line. It can also be appreciated by comparing the results

along lines #5, #4 and #3 that both velocity components have a change in their curvature, i.e. an inflection point exists, which is a characteristic of a flow with adverse pressure gradient.

A closer look to the vertical line #3 in Figure 5.37 and Figure 5.38 shows that at the wall (position Z ~ -4.1 m) a zero-slope condition for the velocity and pressure is met, indicating that critical adverse conditions are set for flow separation. The transition of sign change in the velocity is appreciated in the plot of line #2 in Figure 5.37. Here at around the value of the vertical length of 1.0 m or (R, Z) = (6.29, -4.24) the velocity becomes negative, meaning that the fluid moves in the negative R-direction. This can also be observed in Figure 5.35(a), where at a corner the separation of streamlines takes place forming a region of closed lines. In the case of the z-component of the velocity, the change of sign has occurred between line #5 and #4 and its amplitude increases from line #4 to #1.

The results obtained for the ITER case #5 (p_{VI} = 1.0 Pa) seem to offer the best opportunity for the analysis of flow separation conditions. In Figure 5.39 it is seen that the change of sign in the velocity profile in the z-direction occurs already at line #5, next to the outlet of the pumping duct, which can be confirmed by looking also at the stream-lines in Figure 5.35(b). Along line #4, the radial component of the velocity shows flow reversal, accompanied with a positive change of the pressure shown in Figure 5.40 (see lines #3 to #5). The calculated results towards line #2 and line #1 show a decrease in the pressure at the wall and as a consequence the magnitude of the velocity components are also reduced, lowering the momentum of the counterflow (negative R-direction).

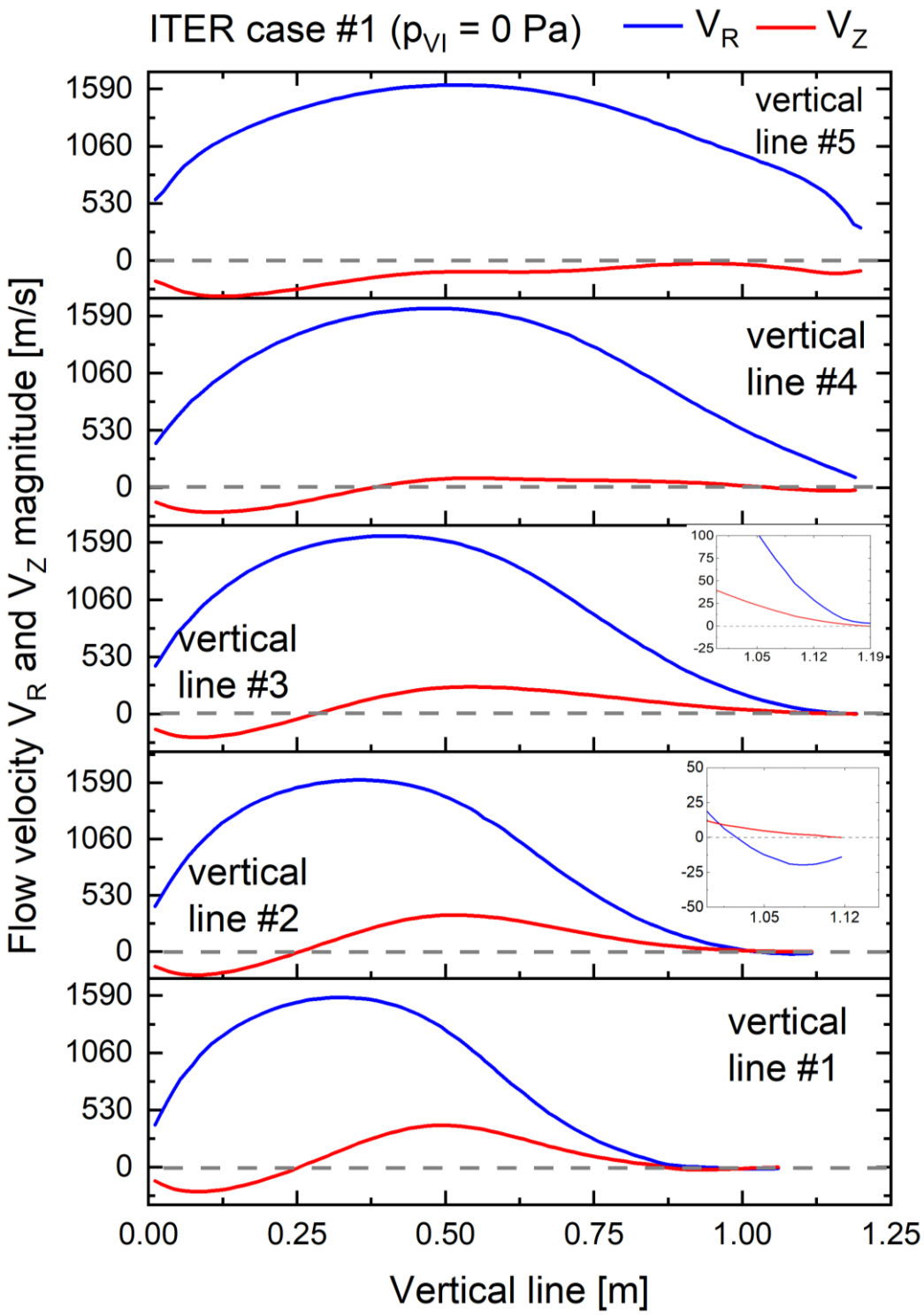

Figure 5.37 Deuterium gas flow velocity distribution (V_R, V_Z) along straight lines located across the pumping duct for the ITER high divertor pressure case (9.9 Pa) and for the case study with p_{VI} = 0 Pa (case #1) at the exit of the pumping duct (close to the vertical line #5).

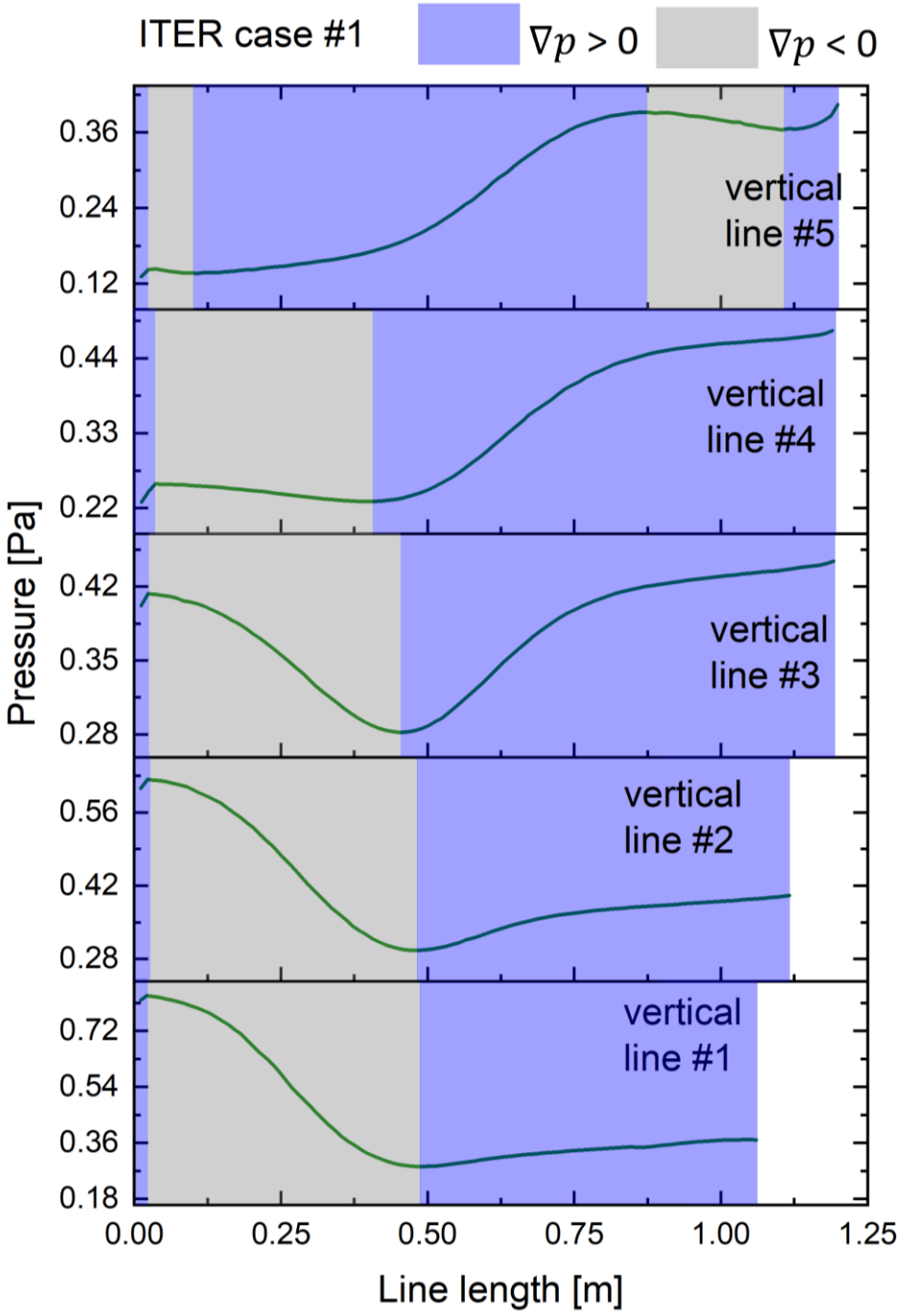

Figure 5.38 Pressure profiles sampled along the vertical lines defined at the pumping duct of ITER sub-divertor. The plots correspond to a high divertor pressure case (9.9 Pa) and for the case study with the ressure at the location VI p_{VI} = 0 Pa (case #1). The boundary conditions at positions I-V read $p_I = 8.82 \times 10^{-4}$ Pa, $p_{II} = 23.6$ Pa, $p_{III} = 7.82$ Pa, $p_{IV} = 15$ Pa and $p_V = 8.12 \times 10^{-4}$ Pa. The wall temperature and the reference temperature of the gas at the inlets is set to T = 420 K and T = 273 K, respectively.

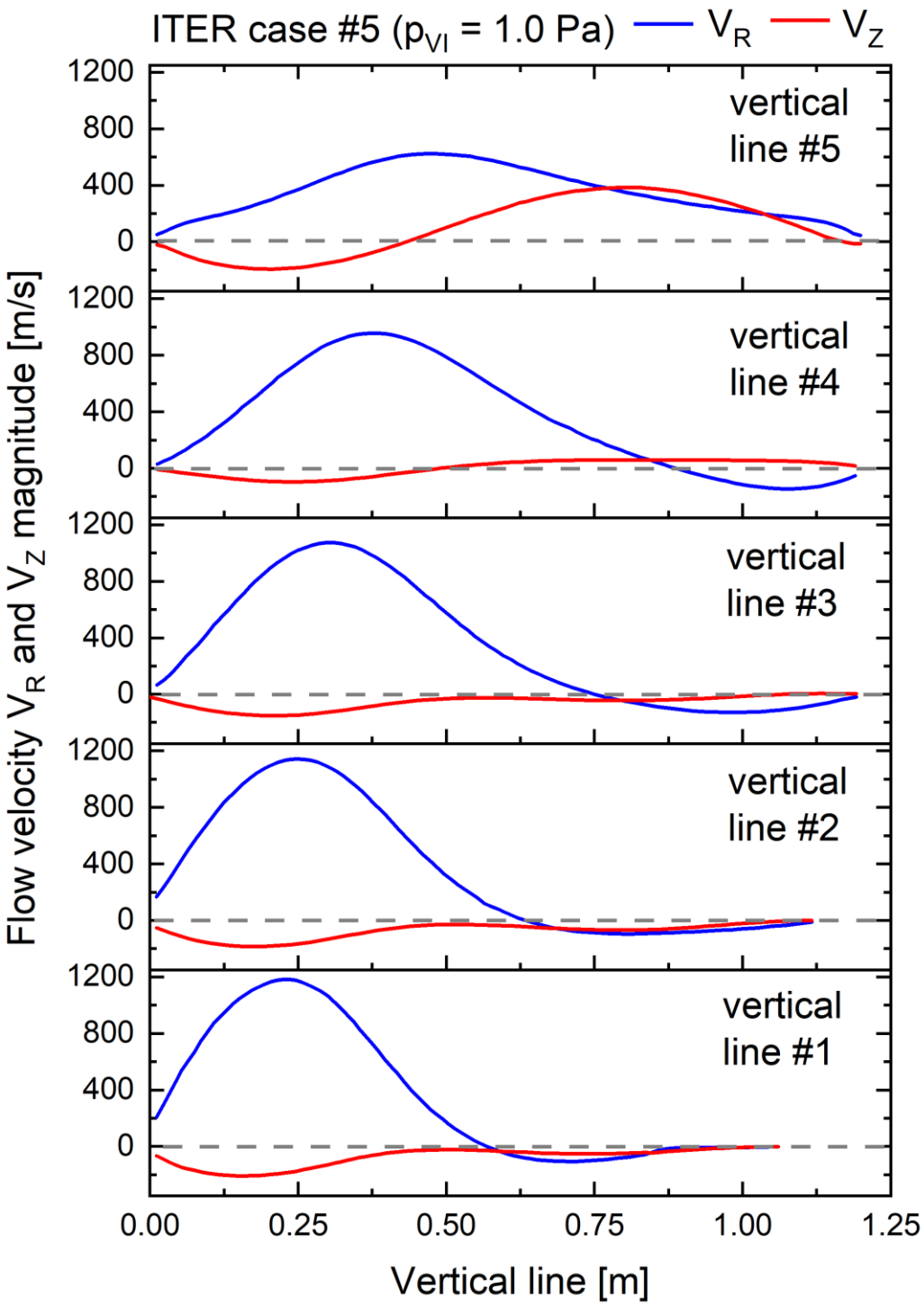

Figure 5.39 Deuterium gas flow velocity distribution (V_R, V_Z) along straight lines located across the pumping duct for the ITER high divertor pressure case (9.9 Pa) and for the case study with p_{VI} = 1.0 Pa (case #5) at the exit of the pumping duct (next to the vertical line #5).

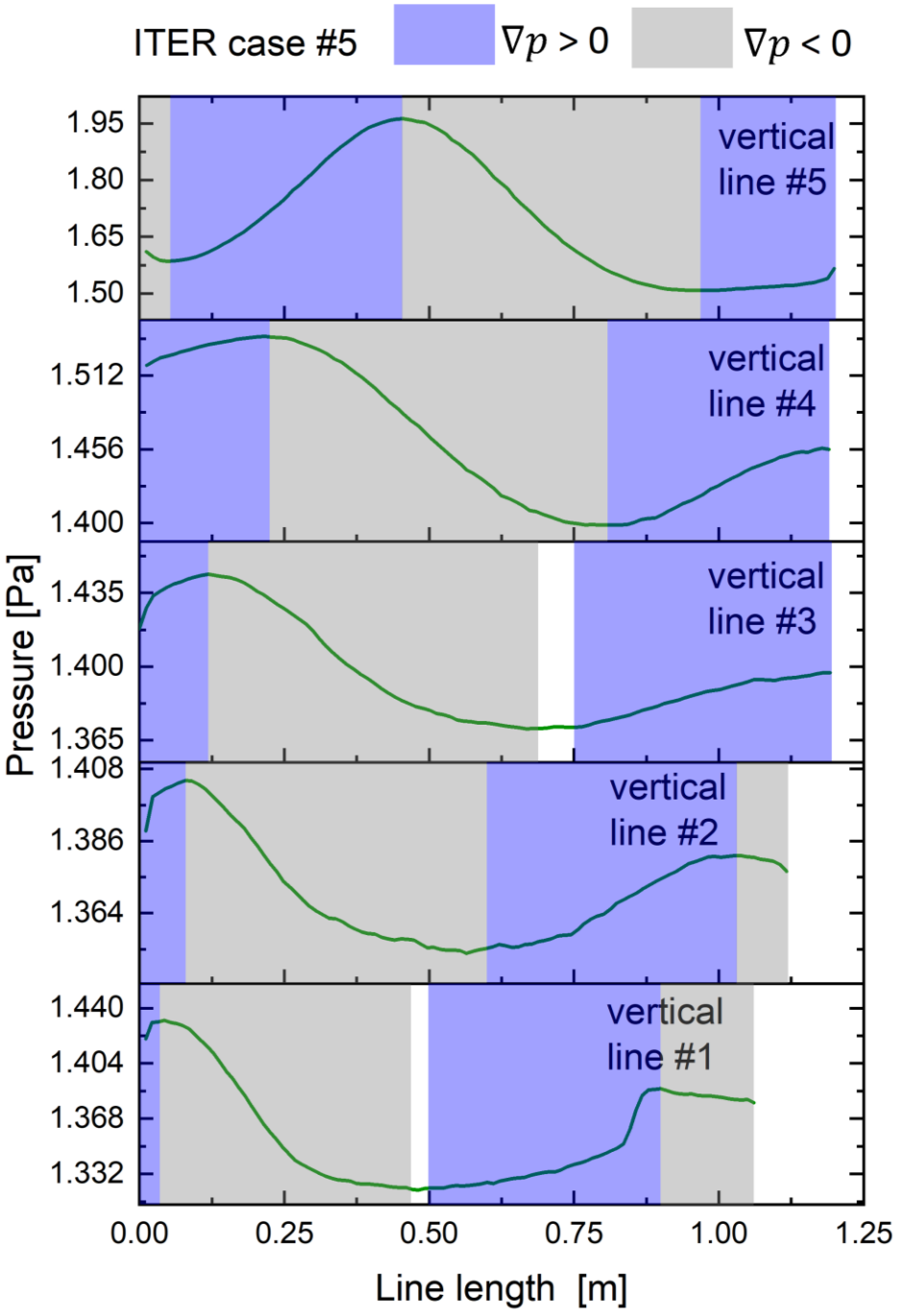

Figure 5.40 Pressure profiles sampled along the vertical lines defined at the pumping duct of ITER sub-divertor. The plots correspond to a high divertor pressure case (9.9 Pa) and for the case study with the pressure at the location VI p_{VI} = 1.0 Pa (case #5). The boundary conditions at positions I-V read $p_I = 8.82 \times 10^{-4}$ Pa, $p_{II} = 23.6$ Pa, $p_{III} = 7.82$ Pa, $p_{IV} = 15$ Pa and $p_V = 8.12 \times 10^{-4}$ Pa. The wall temperature and the reference temperature of the gas at the inlets is set to T = 420 K and T = 273 K, respectively.

Thus, the above results show that the pressure increase at the pumping duct is translated in a reduction of the maximum velocity achievable at the exit of the sub-divertor as well as flow separation. Additional physical mechanisms in the flow that have to do with vorticity in the gas flow is present in the LFS of the sub-divertor (see "corners" in Figure 5.35(a) and (b)). The vorticity involves fluid movement in a domain with bended walls or sharp corners. Moreover, not only the the sharp corners but the density and pressure gradients in the gas flow are generators of vorticity.

In Figure 5.41(a) and Figure 5.42(a), the pressure distribution, the isobars and the pressure gradient (vectors) for the study cases with $p_{\mathrm{VI}} = 0$ Pa and $p_{\mathrm{VI}} = 1.0$ Pa are shown. As the neutral gas expands from "dome" region to the pumping port, a variation of pressure, density and temperature takes place. Analog to the pressure, the density also varies in *Z*- and *R*-directions (distribution not shown). The combination of these forces generates a torque proportional to $\nabla p \times \nabla \rho$ which induces the flow circulation. This occurs if the lines of constant density are not parallel to the lines of constant pressure (baroclinic effect). The situation is depicted in Figure 5.41(b) and Figure 5.42(b) for the study cases with $p_{\mathrm{VI}} = 0$ Pa and $p_{\mathrm{VI}} = 1.0$ Pa. In these figures, it is also appreciated that at the duct sections of HFS (towards boundary I) and LFS (towards boundary V) the baroclinic contribution is negligible since the isolines of pressure and density are parallel to each other.

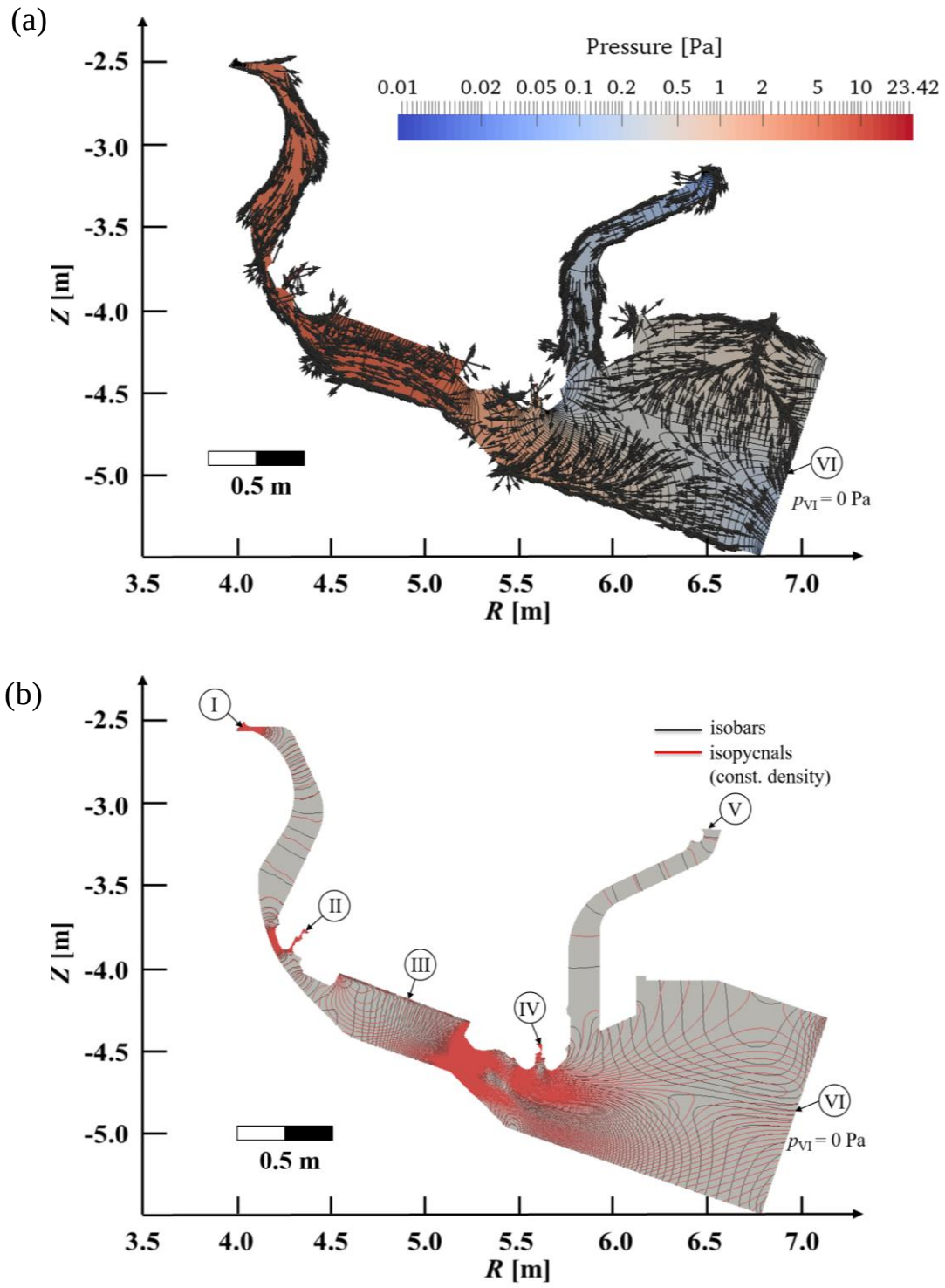

Figure 5.41 (a) Pressure distribution, isobars and pressure gradient direction for the case study #1 with $p_{\mathrm{VI}} = 0$ Pa at the pumping port. (b) Isobars and isopycnals (constant mass density) distribution. The boundary conditions at positions I-VI read $p_{\mathrm{I}} = 8.82 \times 10^{-4}$ Pa, $p_{\mathrm{II}} = 23.6$ Pa, $p_{\mathrm{III}} = 7.82$ Pa, $p_{\mathrm{IV}} = 15$ Pa, $p_{\mathrm{V}} = 8.12 \times 10^{-4}$ Pa and $p_{\mathrm{VI}} = 0$ Pa. The wall temperature of the sub-divertor is set to T = 420 K and VHS is the employed binary collision model.

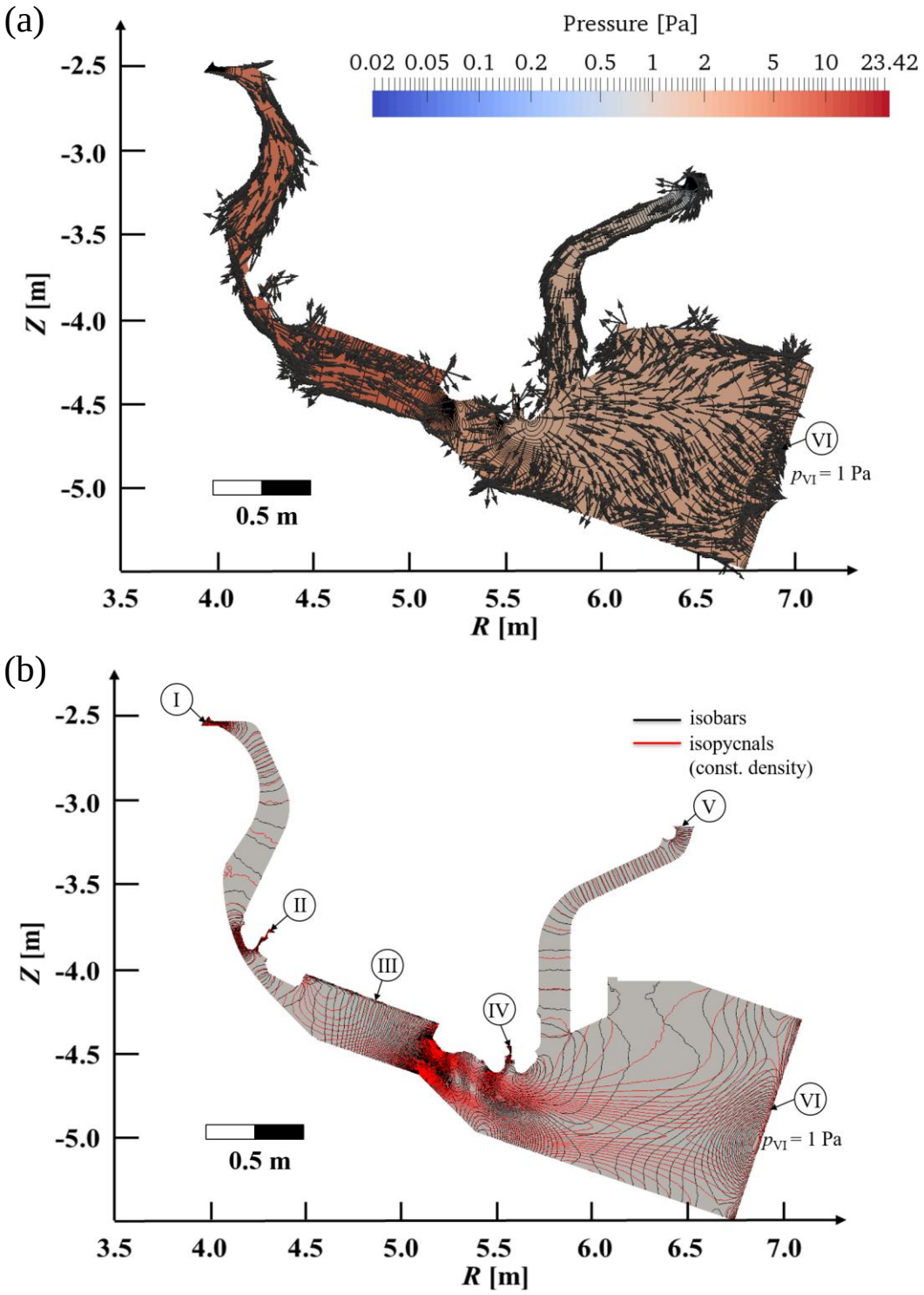

Figure 5.42 (a) Pressure distribution, isobars and pressure gradient direction for the case study #1 with $p_{VI} = 1$ Pa at the pumping port. (b) Isobars and isopycnals (constant mass density) distribution. The boundary conditions at positions I-VI read $p_I = 8.82 \times 10^{-4}$ Pa, $p_{II} = 23.6$ Pa, $p_{III} = 7.82$ Pa, $p_{IV} = 15$ Pa, $p_V = 8.12 \times 10^{-4}$ Pa and $p_{VI} = 1$ Pa. The wall temperature of the sub-divertor is set to T = 420 K and VHS is the employed binary collision model.

In this part of the analysis a comparison between the present DSMC modelling and ITERVAC calculations is performed considering the study of case #1 with $p_{\mathrm{VI}} = 0$ Pa at the pumping port. ITERVAC modelling considers the divertor cassette as a complex network of interconnected channels with a predefined shape and length. Thus, since the network consists of binding nodes and channels, by placing a gas source or sink (pressure or pump boundary) at a node, the mass flow across each channel of the network can be calculated and at the same time the node-wise mass balance is considered, i.e. inflow and outflow. ITERVAC employs an empirical equation with 4 fitting parameters for the calculation of the dimensionless flow rate *F* across the channel [96], which is given by:

$$F = \frac{c_1}{Kn} + c_2 + \frac{c_3 Kn}{c_4 + Kn}, \tag{5.4}$$

where *Kn* is the Knudsen number and the coefficients c_1 represents the limiting value of the expression in the continuum regime ($Kn \to 0$) whereas the sum $c_2 + c_3$ is related to the free molecular limit ($Kn \to \infty$). The coefficient c_3 indicates the beaming effect of the molecular flow across the channel and c_4 represents 50% of the beaming effect contribution of c_3 in the continuum limit. The accuracy of the above expression depends on the flow regime of interest as well as the ratio length-to-diameter (hydraulic diameter) of the channel under consideration. In [96] is mentioned that a 3% of average error is found for viscous flows for long and short channels with circular and triangular cross-sections. Relevant to the present ITER gas flow analysis, the transition regime, the authors in [96] have reported an accuracy of 5%-20% for circular tubes with various length-to-diameter ratios and up to 8%-40% of deviation is reported for thin orifices under different upstream pressures. In the transition regime the deviation is calculated by comparing ITERVAC results to kinetic theory solutions.

In a standard ITERVAC simulations, the ITER calculations are done by considering a 3D domain containing the 54 ITER toroidal divertor cassettes. For the present comparison, ITERVAC analyses have been performed considering only one divertor cassette in its two-dimensional representation, thus a direct comparison with DSMC can be done. Therefore, it is possible to extract the pressure at the inlet and the outlet for every channel of the network. By doing this the DSMC values of the local pressure are extracted at the positions indicated in Figure 5.43(a), and termed as probe locations. Thus, for consistency of the results, the location of the ITERVAC channel outlet coincides with the probe location, ensuring that the spatial location is the same for both numerical approaches. 10 probe locations are distributed along the sub-divertor domain. A pair of probes is located at each divertor leg, one nearby the bottom of each boundary (positions II, IV from Figure 5.43(b)), a pair below the dome and 2 horizontal co-linear probes towards the pumping duct are placed.

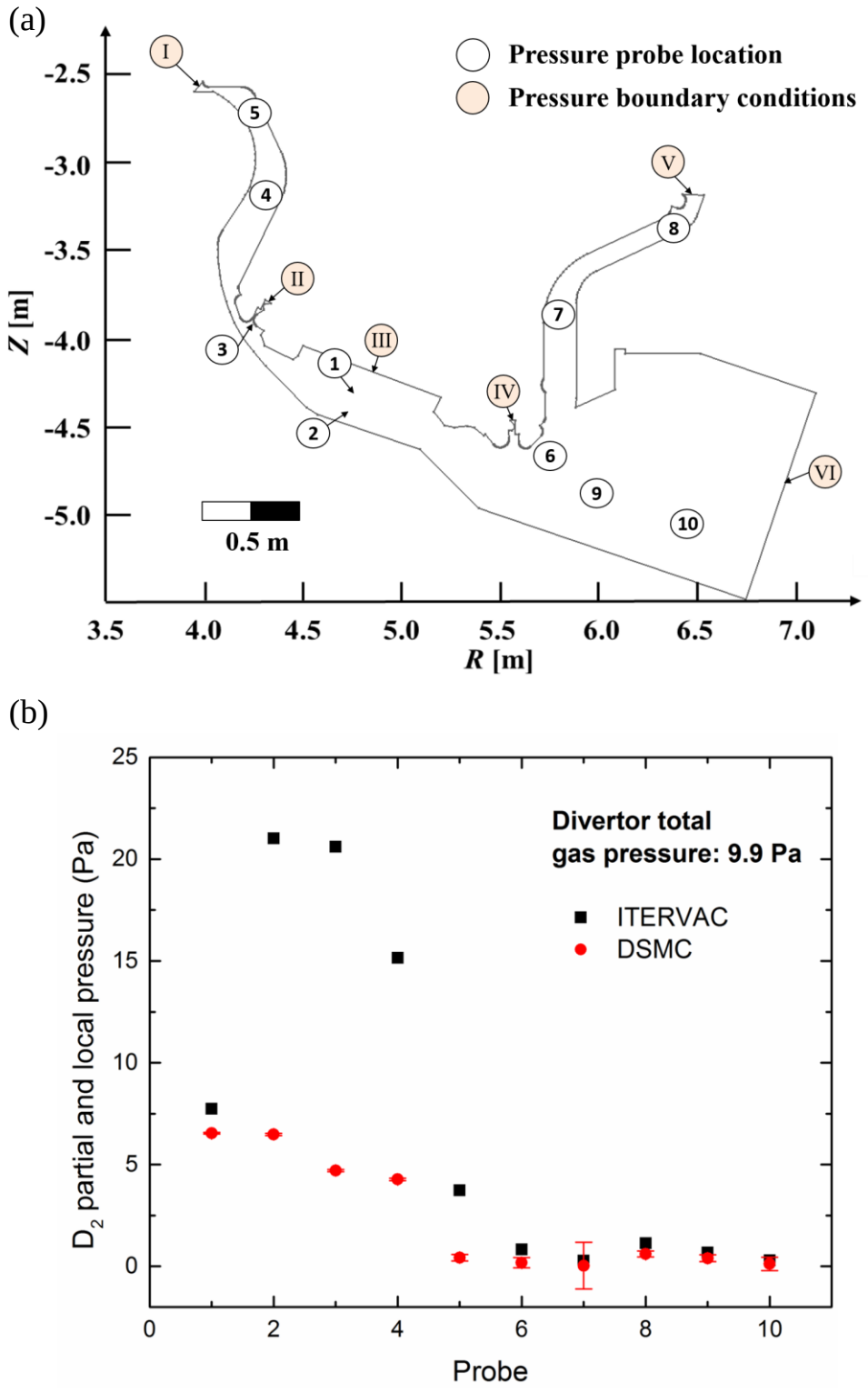

Figure 5.43 (a) Partial and local pressure of deuterium gas is calculated at probes along the sub-divertor geometry. (b) The pressure values are sampled by both DSMC and ITERVAC for the study case #1 with an isothermal gas flow with wall temperature of T = 420 K. The pressure boundary conditions at positions I to VI are: $p_{\mathrm{I}} = 8.82 \times 10^{-4}$ Pa, $p_{\mathrm{II}} = 23.6$ Pa, $p_{\mathrm{III}} = 7.82$ Pa, $p_{\mathrm{IV}} = 15$ Pa, $p_{\mathrm{V}} = 8.12 \times 10^{-4}$ Pa and $p_{\mathrm{VI}} = 0$ Pa.

As seen in Figure 5.43(b), the predictions of the two approaches at the probes 1 and 6-10 are in good agreement with each other to within statistical error bar of DSMC. At probes 2 to 5 the two approaches differ by a factor equal or greater than 2. A closer look to the pressure drop between position II and probe 3 at the HFS, lead us to the following observations. First of all, from the upstream pressure BC of p_{II} ~ 23 Pa the gas pressure is reduced by a factor of ~ 4 in a rather reduced region as depicted in Figure 5.44(a). The gas undergoes an expansion due to a combination of local *converging-diverging-converging-diverging* passages, see Figure 5.44(b). Starting at location II with zero velocity (bulk), the gas accelerates reaching a value of 50 m/s (first passage). Thereafter, as the area increases the gas decelerates reaching the second passage, where the velocity increases as the area of the passage is reduced. At this second passage a maximum velocity of ~193 m/s is reached. Finally, the gas exits this region where it decelerates to ~50 m/s (position of probe 3) and at this point, the gas starts flowing towards location I.

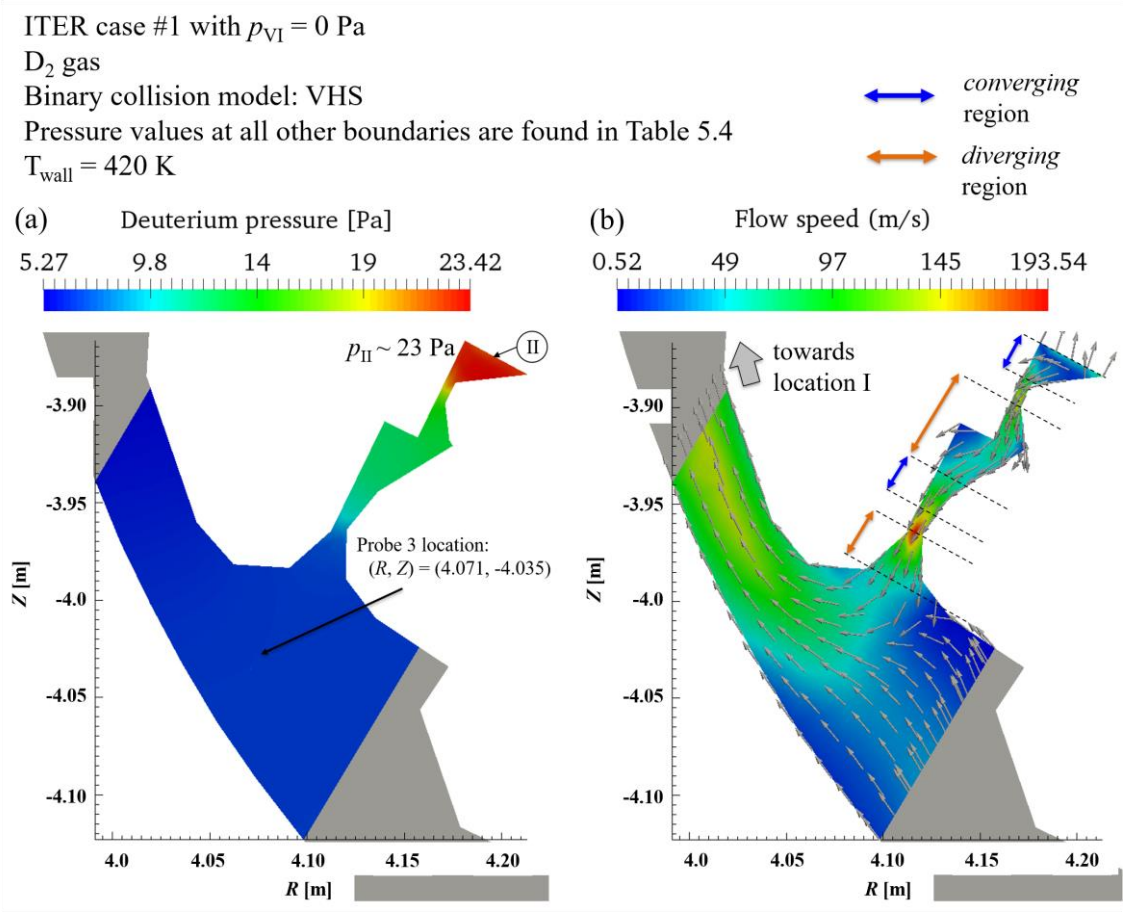

Figure 5.44 (a) Pressure distribution near the inlet boundary location II (~23 Pa). (b) Velocity vector field and velocity distribution of the gas flow. The plots correspond to a high divertor pressure case (dome pressure of 9.9 Pa) and for the case study with the pressure at the location VI of 0 Pa (case #1).

A possible explanation of the differences at probe #3 (factor of aprox. 3) between DSMC and ITERVAC can be related to the uncertainty by modelling thin orifices in

ITERVAC or the mesh strategy employed in DSMC in this region. By taking the worst case reported accuracy of 40% of ITERVAC leads, at probe #3, a value of 12 Pa. This is still twice the value obtained with DSMC. If this region is modelled in ITERVAC with a serie of multiple orifices, each corresponding accuracy to each modelled part contribution will add up to the relative difference. Once the gas travels from location II to the location of probe #3, the neutral particles move towards the upper left outlet boundary (position I) and also towards the region below the dome (position III), where a pressure inlet boundary condition of 7.8 Pa is imposed. Clearly, the values of the pressure near probe 3 cannot exceed this value, making plausible the pressure values at probes 1 and 2 calculated with DSMC (less or equal than 7.8 Pa). However, ITERVAC predicts a pressure of ~ 20 Pa at probe 2, which would translate in a movement of gas particles from the bottom of the sub-divertor towards the dome, i.e a gas flow with a velocity component in the +z-direction, which is not observed in the DSMC analyses.

The collisionality is analyzed in terms of the local Knudsen number $\mathrm{Kn}_{\mathrm{loc}} = \lambda / L_n = \lambda |\nabla n| / n$ is employed. Here λ is the VHS-mean free path [25] and n the deuterium number density. The local Knudsen number is calculated for case #1 ($p_{\mathrm{VI}} = 0$ Pa) and case #5 ($p_{\mathrm{VI}} = 1$ Pa) and its distribution across the domain is shown in Figure 5.45. Over a straight line of 2.37-meter length depicted in Figure 5.46(a), the Knudsen number is estimated for all the case studies. This path is representative for the flow path between the region below the dome and the pumping port in ITER sub-divertor. The previously discussed explanation based on collisionality effects is supported for the cases where the pressure $p_{\mathrm{VI}} > 0.01$ Pa. It is noticed that for the case with $p_{\mathrm{VI}} = 0.1$ Pa the increasingly monotonic slope of $\mathrm{Kn}_{\mathrm{loc}}$ is broken at a same point 20 cm before pumping port entrance, as seen in Figure 5.46(b). This is an indication that the competition between collisions and the magnitude of the local density variation is enhanced by interacting more frequently with the D_2 particles coming from the pump region and thus of reducing the ratio of $\mathrm{Kn}_{\mathrm{loc}}$. It is interesting to note that the $\mathrm{K}n_{loc}$ values of the sub-divertor flow are < 0.03 below the dome and $0.01 < \mathrm{K}n_{loc} < 0.18$ in the region near the pumping port for all the study cases, except for the cases 0.1 Pa- and 1 Pa. Comparison between the 0.1 Pa- and 1 Pa-cases at the port shows a reduction in the $\mathrm{K}n_{loc}$ of factor 4. The reason is that the Knudsen number for each case depends on the combination of the number density and its local gradient at that region.

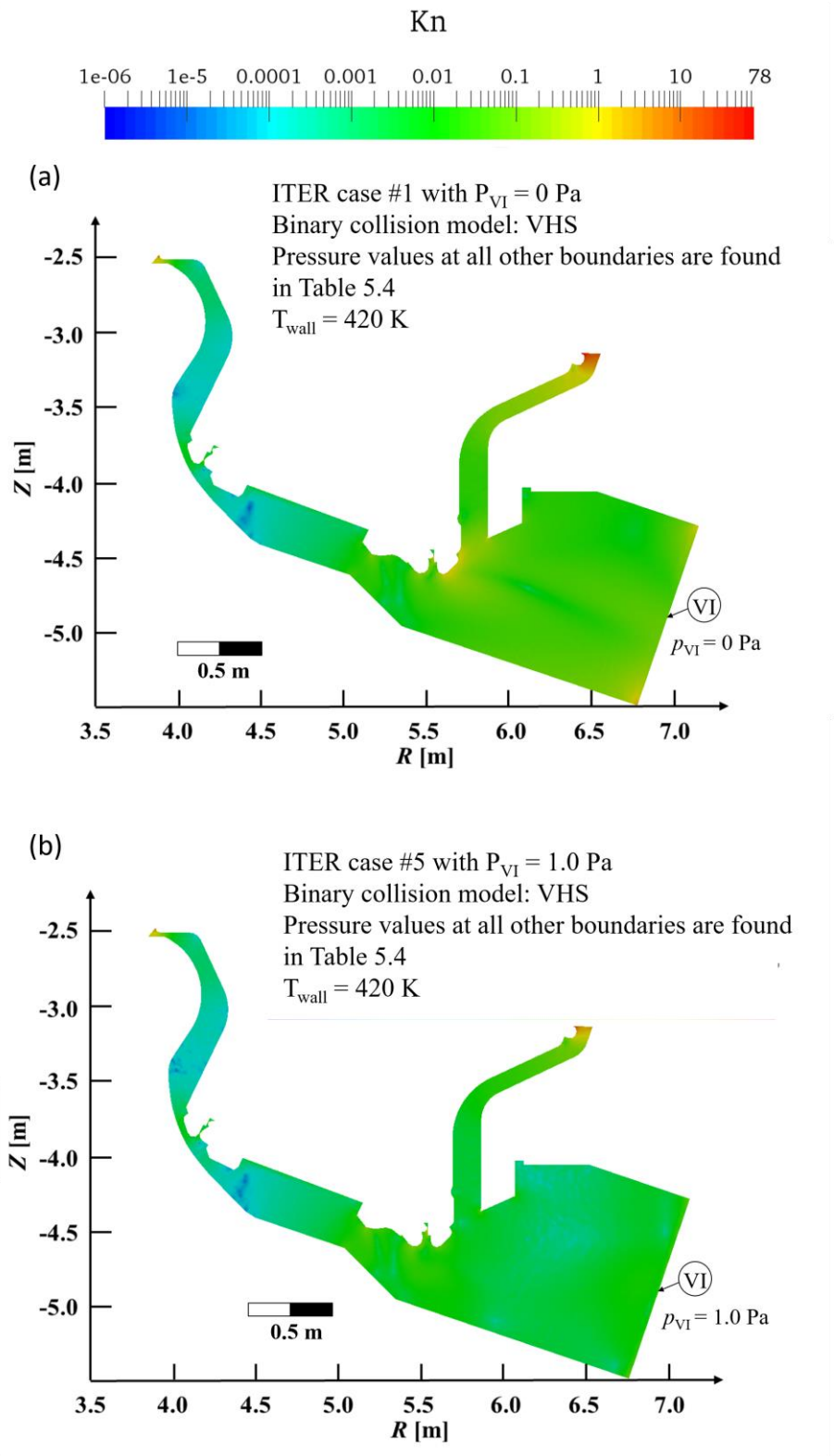

Figure 5.45 Local Knudsen number calculated for cases (a) p_{VI} = 0 Pa- and (b) p_{VI} = 1 Pa. The boundary conditions at positions I-VI read $p_I = 8.82 \times 10^{-4}$ Pa, $p_{II} = 23.6$ Pa, $p_{III} = 7.82$ Pa, $p_{IV} = 15$ Pa, $p_V = 8.12 \times 10^{-4}$ Pa and $p_{VI} = 1$ Pa. The wall temperature of the sub-divertor is set to T = 420 K and VHS is the employed binary collision model.

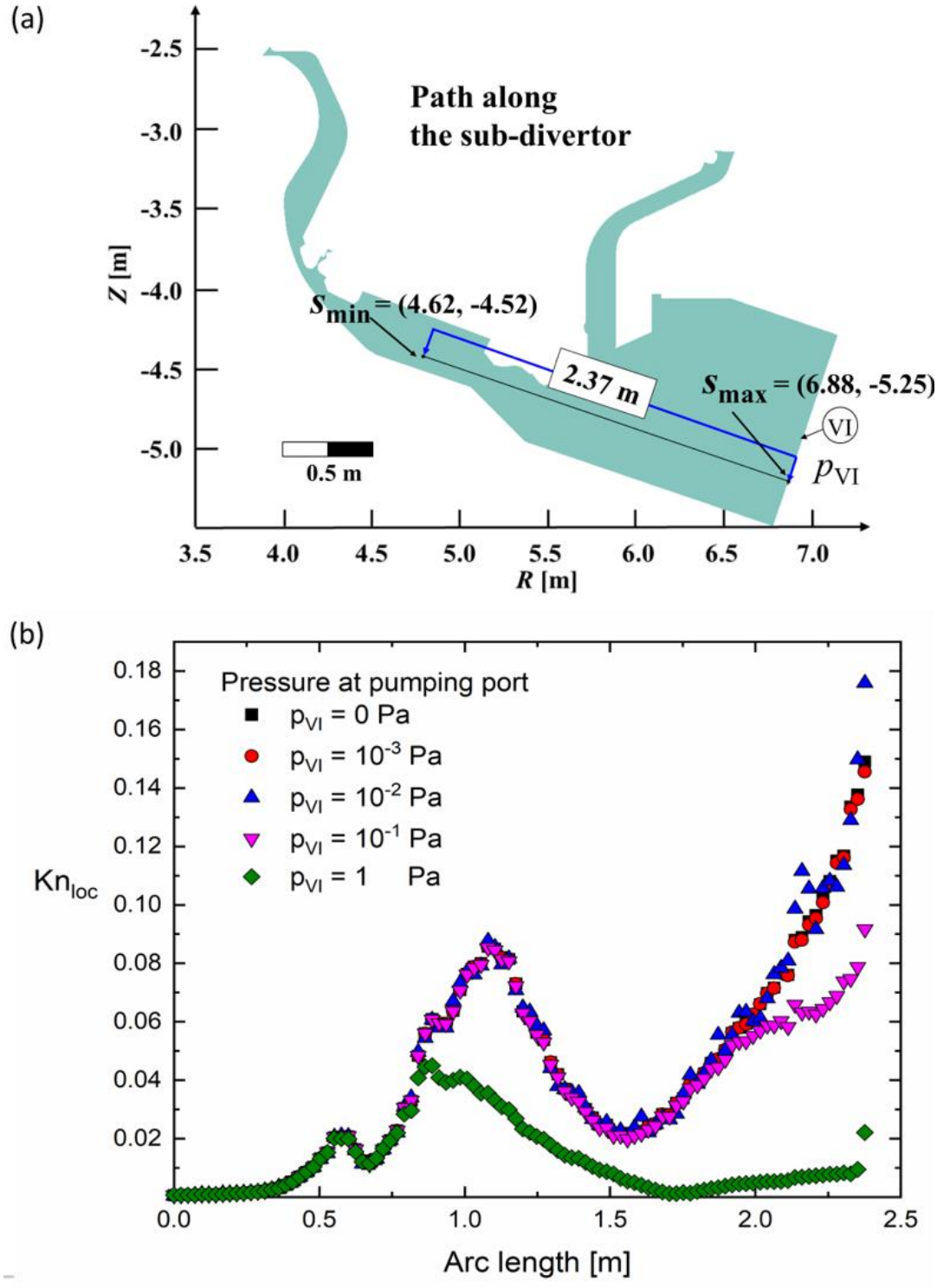

Figure 5.46 (a) Definition of line path across the ITER sub-divertor from point s_{min} to s_{max}. The region covered comprises the zone below the dome (location of region III) until the pumping port (location of region VI). (b) Evolution of the local Knudsen number along the path for all the study cases.

In summary, the DSMC approach is applied to a ITER background plasma calculated by SOLPS for a high-pressure divertor scenario (total pressure 9.9 Pa, 80 % D_2). The DSMC simulations indicate a weak influence on the sub-divertor neutral pressure at the HFS (position I) for the examined values of pressure range at the pumping port (position VI). Between the two extreme ITER cases #1 and #5, a reduction of the peak velocity by a factor of 1.5-2 is found near the pumping port.

The present analysis also demonstrates that a classification of the findings in two groups is possible. The first group involves the conditions with a pressure value up to 10^{-1} Pa at the boundary VI, where no dramatic impact is found on the onset of flow separation neither in the increase of particle flow at location V. This suggests that the study cases #1 to #4 are not sensitive to pressure changes at the pumping duct (location VI).

The second group focuses on conditions as case #5, where the onset of flow separation appear right before the exit of the pumping port and a significant enhancement of the particle flows towards location V occurs (factor of ~8 from case #1 to case#5). Moreover, it was found that the particle flux at the location I (divertor leg inner boundary) is 17 times greater than the flux at the location V (divertor leg outer boundary), but the sum of both I and V is 22 times smaller than the particle flux being pumped out towards the pumps. Additionally, the sub-divertor exhibits a collisional flow regime, where the local Knudsen number varies in the range of $Kn_{loc} = 10^{-3}$ to $Kn_{loc} = 0.18$.

With the present results it is reinforced the idea of considering DSMC as a strong candidate for describing the particle exhaust in future tokamaks. Before ITER starts operations, it is mandatory for any modelling to predict current observations in present fusion devices. An step forward in this direction has been done for a mid-size tokamak, which is the focus of the next section.

5.3 Particle exhaust in the ASDEX Upgrade

The particle exhaust of the H-mode plasma discharge with full cryopump in ASDEX Upgrade (AUG) is modelled. The plasma discharges have been part of an experimental campaign at ASDEX Upgrade with the aim to the study the effect of the neutral particle flow during a discharge by operating the machine with full, 1/3 and no cryogenic pumping (with only turbomolecular pumps active). As a result, the time traces of the neutral particle fluxes with manometers placed at different locations in the vacuum vessel are measured. The experimental data include the pressure measurements at the main chamber and at the sub-divertor region. The plasma discharge setup, diagnostics and experimental results taken from the discharges are found in Appendix D.

From the modelling perspective, pressure measurements are employed as boundary conditions for the DSMC code. The inlet boundary condition is imposed and set to the value of the manometer measurement located below the divertor dome. The outlet boundary conditions are imposed at the cryopump surface, where a sticking probability is employed as done for JT-60SA in section 5.1. The flow field variables are calculated and the fluxes estimated for a direct comparison with the experimental values. The analysis of particle flows in AUG is organized as follows:

1. The sub-divertor domain together with the position of relevant AUG diagnostics for the DSMC modelling are introduced.
2. The numerical domain and the description of the models are presented. The models are described in terms of the effects to be captured.
3. A summary of results is presented followed by a discussion of the numerical analysis.

5.3.1 Modelling of particle exhaust in ASDEX Upgrade

The details of the sub-divertor structure are particularly important for establishing the geometry and mesh of the neutral model since they affect the flow paths and fluxes in ASDEX Upgrade. The topology of the AUG divertor and its dimensions are depicted in Figure 5.47(a). In the figure two images taken by the AUG team during the installation of the divertor III showing the divertor region, divertor dome and targets as well as the vessel structures in the sub-divertor region are shown in Figure 5.47(b)-(c).

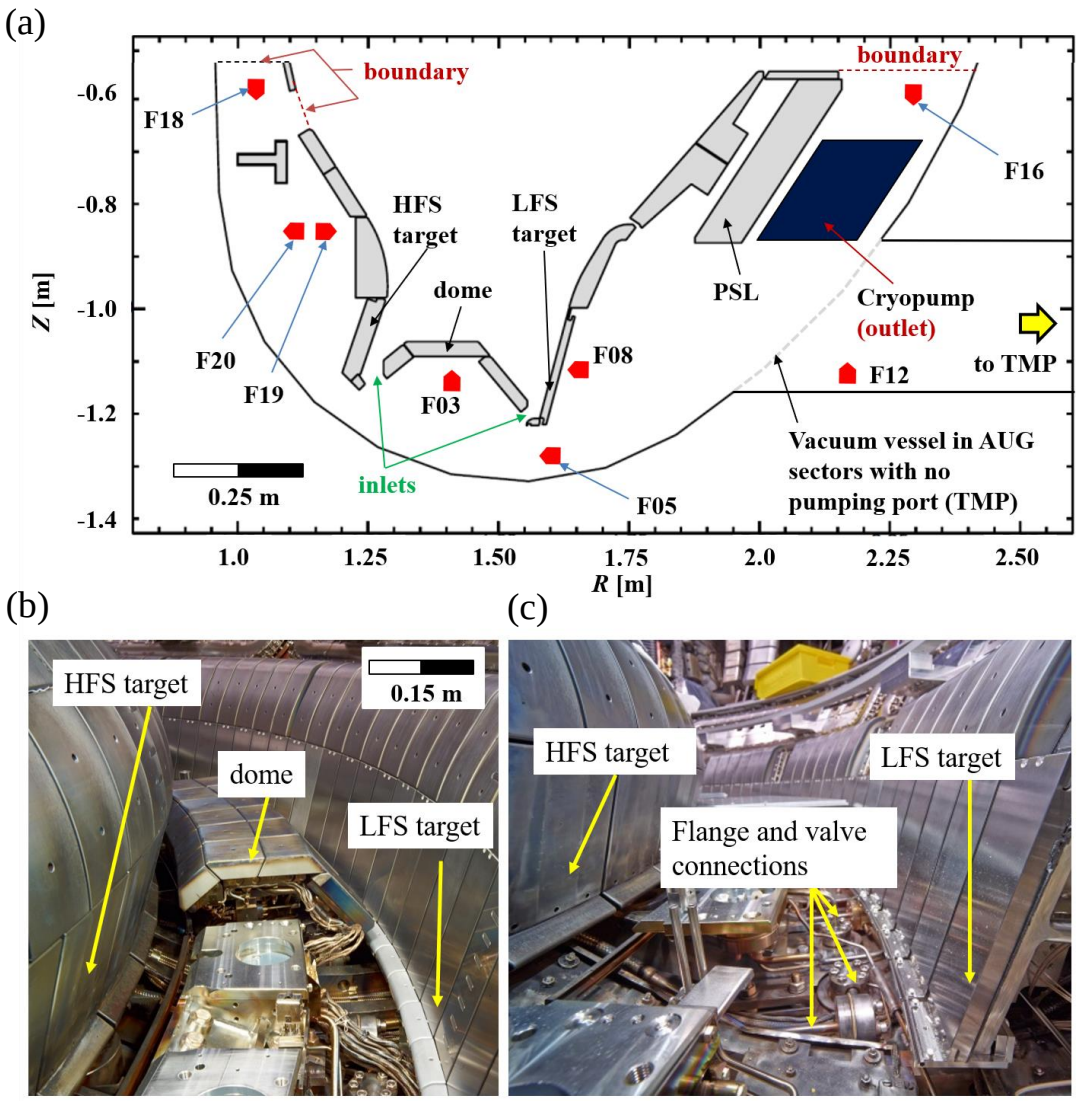

Figure 5.47 (a) ASDEX Upgrade cross-section scheme of the lower-half of the complete vessel. The neutral gas enters the sub-divertor at the inlets, the gas manometer positions are shown in red symbols, the cryopump in blue is the main outlet for the particles. Other boundaries are indicated in red color. In case the AUG sector under consideration is connected to the turbomolecular pump (TMP), then a pumping port is included in the model, otherwise the vacuum vessel is taken as shown (grey dashed line). (b) and (c) Photographs taken of the lower part of AUG vessel, which show the structure below the dome with the different structures along the sub-divertor region. Images courtesy of Volker Rohde (IPP Garching).

The definition of the flow domain is based on the CAD-geometry of AUG, see Figure 5.48(a). The refined geometry in the simulations is obtained after a careful analysis of the CAD model, the previous employed numerical geometries in AUG and the real geometry (direct inspection of the AUG vessel has been possible in the framework of this analysis). The full cryopumping is assumed to be toroidally symmetric and thus a two-dimensional model of the AUG sub-divertor is here implemented. The two-dimensional sub-divertor domain does not include the main chamber (plasma region) and the divertor

tiles facing the plasma as shown in Figure 5.48(b). In Figure 5.48(c) and (d) the two AUG sub-divertor domains for the DSMC analysis are presented. Figure 5.48(c) shows the sub-divertor region of the tokamak, where the pumping occurs solely at the cryopump. The second domain of interest is shown in Figure 5.48(d), where the duct leading to the turbomolecular pump (TMP) is included. In the following, the former geometry is referred as the AUG *closed* domain, whereas the latter as the AUG *open* domain.

For both open and closed sub-divertor domains five common boundaries serve as inlets and outlets, which are illustrated in Figure 5.48(c) and (d). The inlets at the divertor dome, denoted as $F03_{inner}$ and $F03_{outer}$ inject particles to the system. The outlets are located at the boundaries F18, F16 and the cryopump pumping surface. Additionally, for the *open* domain an outlet at the end of the pumping duct is defined as TMP.

Due to the fact that no plasma edge simulation is available for the present plasma discharges, the procedure of elaborating the sub-divertor model with DSMC employs various particle flux measurements done at the sub-divertor. The manometers readings at both HFS and LFS are used in the DSMC model. Here the HFS means high-field side, which refers to positions in the sub-divertor with a radial position $R < 1.25$ m, whereas low-field side or LFS means radial positions greater than $R = 1.25$ m. The particle flux is assumed to be split in equal parts at the divertor inlets, i.e. at the positions referred as $F03_{inner}$ and $F03_{outer}$ in Figure 5.48(c) and (d). The resulting pressure is then imposed at these boundaries in the DSMC model as a gas that enters to the sub-divertor domain with a Maxwellian distribution centered at 300 K. In the simulations it is assumed that the deuterium gas enters the flow domain in its molecular form where no dissociation or recombination processes are considered. Regarding the outlets F18 and F16, the pressure values of the manometer readings are imposed at the respective boundary surfaces.

The gas-surface interaction is modelled as a diffusive wall (full accommodation), in which the deuterium molecules are absorbed and then desorbed from the surface in their ground state, with a desorption velocity sampled from a Maxwellian distribution centered at 300 K. The absence of the exact information of the gas-wall interaction during the experiments in the sub-divertor domain, introduces an uncertainty in the actual modelling of the interaction particle and surfaces.

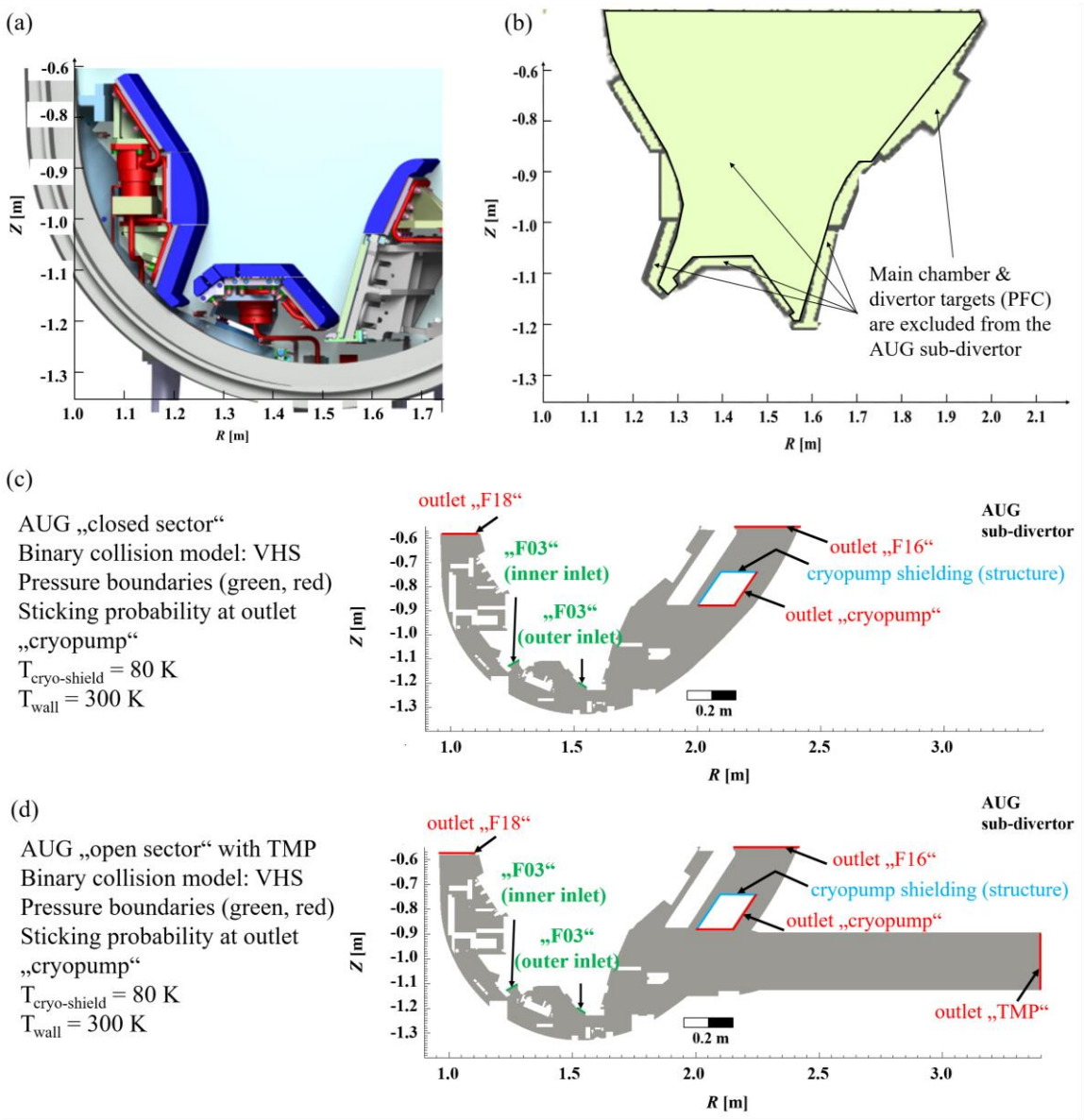

Figure 5.48 (a) AUG divertor CAD-geometry: divertor targets (blue structures), gas valves and their routing (red structures). (b) Main chamber region and plasma facing components (PFC) are excluded from the sub-divertor domain. (c) Sub-divertor region of a sector of AUG with no port leading to the vacuum pump (TMP), here denoted as AUG *closed* sector. (d) An *open* sector of AUG, which includes the pumping port that leads to the location of the turbomolecular pump.

The computational mesh needs to accomplish the DSMC criteria of $\Delta x < \lambda, \Delta t < \tau_{res}$ together with the condition of having at least 20 to 30 DSMC-particles at each cell. The unstructured mesh in the simulations consists of ~ 8 000 and ~ 10 000 cells for the *closed* and *open* AUG sub-divertor domains, respectively. Only 0.4% of the total cells in the computational domain, less than 10 particles per cell are found. This translates in good statistics for the present DSMC calculations since in average 100 particles per cell are found in the present calculations. The real-to-simulated particle ratio F_N of 10^{12} was

employed.

The VHS collision model is employed throughout the studies in the framework of the NTC collision selection scheme. As before, by using the data of [93] it is obtained the viscosity dependence on the temperature (power-law) for deuterium. The resulting value of the exponent is applied in the VHS model as the viscosity index ω, giving a value of 0.73. As a consequence of the high neutral fluxes at the HFS (F18), the estimated mean collision time $\tau_{coll} = \lambda_{\mathrm{VHS}}/v_{mp}$ has a value of 3.98×10^{-6}s in that particular region. This condition constraints the value of the time step Δt to be a fraction of the mean collision time. Hence, Δt is set to 1×10^{-7} s.

Three different models of the AUG divertor are here proposed. Two models address specific effects of the modelling parameters and a third model resembles the experimental conditions in AUG:

1. Model #1 focuses mainly on the effect of the pumping conditions on the gas dynamics by changing the sticking probability at the cryogenic pump surface. Two domains of interest where studied, the AUG divertor with pumping port towards the turbopump (closed sector) and without port (open sector). Three sticking probabilities are applied to the cryopump and also an outlet pressure at the TMP is employed. Here the boundary F16 is considered as wall (structure) reflecting the particles back to the domain.

2. In contrast to model #1, model #2 includes the contribution of the particle flux coming from the boundary surface “F16”, located above the cryopump. In model #2 a sticking coefficient of unity is set at the cryopump surface. Model #2 can be considered as a model #1 with an additional pressure boundary.

3. Model #3 on the other hand, resembles the experimental conditions of the subdivertor for the discharge #31998. The difference between models #2 and #3 is the sticking coefficient of the pump, which is set to a value of 0.17.

A summary of the employed parameters and boundary conditions of the DSMC modelling in AUG is found in Table 5.6.

Table 5.6 The summary of the modelling parameters of gas flow in AUG divertor

	Type / Parameter	Value	Unit
Boundary name			
F03 inlet	Pressure type (inlet)		
	Pressure	1.4	Pa
F18 outlet (model 3)	Pressure type (outlet)		
	Pressure	2.0, open	Pa
F16 outlet	Pressure type (outlet)		
	Pressure	0.197, closed	Pa
TMP outlet	Pressure type (outlet)		
	Pressure	10^{-3}	Pa
Wall sub-divertor	Wall type		
	Temperature	300	K
Cryopump shielding	Wall type		
	Temperature	80	K
Cryopump	Pump type (outlet)		
	Sticking probability	Model #1 = 0.25, 0.5, 1.0 Model #2 = 1.0 Model #3 = 0.17	-
	Velocity (reflected)	(0, 0, 0)	m/s
	Temperature	300	K
DSMC properties			
Time step	Δt	1×10^{-7}	s
Conversion factor	F_N	1×10^{12}	-
Particle-wall interaction	Diffuse reflection (full accommodation)		
	Temperature	300	K
Binary collision model	Variable Hard Sphere model		
	Reference temperature	300	K
Particle attributes			
Particle name	Deuterium (D_2)		
mass	m	6.69×10^{-27}	kg
diameter	d	2.92×10^{-10}	m
rotational DoF	Rotational DoF	2	-
viscosity index	ω	0.73	-

5.3.2 Summary of results

The parametric analysis in model #1 show that the calculated fluxes are barely affected by the modification of the sticking probability ξ, independently of the AUG domain (with and without TMP). For the AUG studies, the simulations underestimate the fluxes by a factor 10 and 8 at the F19 and F20, respectively. Regardless of the BCs at F03 and F18, in all simulations of model #1 a maximum value of the flux at the entrance of the pumping chamber (F05) is obtained, see Figure 5.49.

For the models with sticking coefficient of unity and 0.5, the fluxes at F05 are significally higher than the experimental value. This can be explained by the fact that higher pressure difference exists between inlet region (below the dome) and the cryopump chamber. The results of model #1 suggest that the gas dynamics in the LFS of the sub-divertor (F05, F8, F12, F16) are quite sensitive with the selection of the sticking coefficient in combination with the assumption at the boundary F16.

In model #2 with the combination of $\xi_{\mathrm{cryo}} = 1$ at the cryopump and pressure boundary (F16) can reproduce qualitatively the measured particle fluxes across the sub-divertor. Overall, the fluxes in model #2 are lower than the experimental data in both the HFS and LFS of the sub-divertor. This reflects the fact that the balancing between pumped gas and the rest of the gas is not sufficient to build the locally measured flux. The particle fluxes calculated below the divertor dome and in the HFS have lower values than their respective fluxes in model 1 as a direct consequence of the open boundary at the surface boundary "F18" (sink, all particles impinging the surface are absorbed). Lower number densities are then expected together with the combination of gas thermalization (lower value of the local flow velocity), results in an overall lower neutral flux.

Model #3 is defined by reducing the sticking probability ξ_{cryo} of model #2 by ~80%, namely $\xi_{\mathrm{cryo}} = 0.17$ instead of unity. This value is set by the relation

$$\xi = \frac{A_{pump}}{A_{tot}} = \left(\frac{\dot{N}_{puff}}{\Gamma_{F16}} \right)_{\mathrm{exp}} \frac{1}{A_{tot}} = 0.17\,, \tag{5.5}$$

and thus, all the characteristics of the plasma discharge regarding the neutral influx and pumping are taken into account in the modelling. The first consequence of the usage of the experimental value of ξ_{cryo}, is that the neutral flux below the divertor dome in model #3 is increased by a factor of 5.5 at F03 and ~ 3.5 at F05 and F08 (compared to corresponding values of model #2). Relative to model #2, the net effect of setting ξ_{cryo} to 0.17 is that a higher neutral pressure below the divertor dome is established. The pressure driven flow towards the cryopump occurs as expected, where faster and denser neutrals move towards the pumping chamber, as shown by Figure 5.49. At first sight, the modification of the sticking probability at the cryopump and addition of a neutral source at the

LFS leads to an overall increase of neutral flux at F03 and F05; at these locations the DSMC modelling show good agreement with the experimental fluxes and their values lie well above the other models.

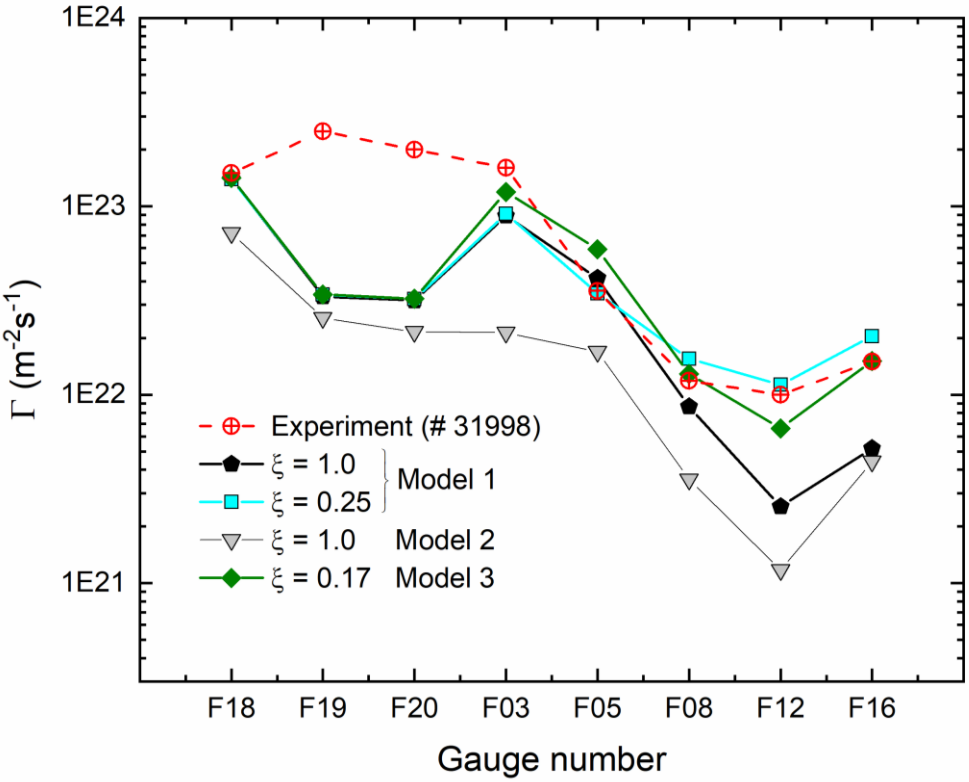

Figure 5.49 ASDEX Upgrade sub-divertor fluxes for model 1, 2 and 3 evaluated at the gauge locations. Experimental data of plasma discharge #31998 is shown in red open circles with a cross in the middle. Filled symbols depict DSMC modelling. Model #1 where the F16 boundary is closed: black pentagon represents the simulation with sticking probability ξ_{cryo}= 1 with no TMP and DSMC simulation with $\xi_{cryo} = 0.25$ is depicted square (cyan). Model #2 and #3 includes the contribution of neutrals at F16 boundary. Model #2 is represented by faced-down triangles (grey) and assumes a sticking probability at the cryopump of unity and no pumping port towards the TMP. Model #3 is depicted by green diamonds, the sticking probability in the cryogenic pump has been set to the experimental value of 0.17 and no TMP is considered. In model #3, pressure boundary conditions at the boundary F18 and F16 are set to the flux measured by the manometers.

A number of interesting observations have been generated in the present AUG flow studies:

Model #1 shows that at the pumping region in the LFS, by *closing* the outlet boundary "F16" and employing a sticking probability less than 0.5 it cannot be effectively model the particle flux close to the manometers F12 and F16. A further decrease of the sticking probability results on a better agreement with experiments.

It is recognized in model #2 that by adding the pressure boundary at the "outlet F16" and by considering a sticking probability of unity at the cryopump, the values

of the fluxes across the sub-divertor are underestimated, worsening the relative difference between experiments and DSMC simulations. Thus, the effect of pumping dominates the effect of placing an extra particle source (pressure boundary) at the LFS.

By employing model #3, the relative difference between experiments and particle fluxes of DSMC are minimized for the values of the particle fluxes calculated around the divertor dome region (F03) and at the LFS. The results suggest that the combination of a pressure boundary and the sticking coefficient has a dramatic effect on the flowfield near the pumping region. The results of model #3 and model #1 with ξ_{cryo}= 0.25 demonstrate this, since two completely different setups lead to comparable results.

The numerical results of all three models showed a deficiency on the modelling of the flowfield at the HFS region behind the targets. At the gauge locations of F19 and F20, a factor of 8-10 between experimental values and simulations is found.

5.3.3 Discussion

The primary reason for undertaking the calculations with maximum pumping conditions (sticking probability of unity at cryopump) and inclusion/exclusion of particle sources such as the outlet "F16" is to provide a sensitivity of the flow field in AUG sub-divertor between different flow conditions.

In the framework of AUG sub-divertor model #1, the impact of the pumping efficiency on the fluxes is observed in the DSMC simulations at the gauges located near the cryogenic pump, i.e. F8, F12 and F16. The experiments exhibit near the cryogenic pump a different particle behavior characterized by a local minimum at F_{12}, see relative position of red lines in Figure 5.50. The simulations of model #1 are able to reproduce qualitatively this observation. However, the results with a sticking coefficient of unity underestimate the experimental values.

By placing the TMP in model #1, the neutral flow splits in two streams, one flowing towards the cryopump and the other one towards the long pumping duct. It is observed that in this model, the concentration of neutrals is decreased by a factor 1.7 since $\Gamma_{\mathrm{F12,closedSector}}/\Gamma_{\mathrm{F12,openSector}} \approx 1.7$. In Figure 5.50 the results obtained with the model $\xi = 0.25$ are also shown. As expected for lower sticking probability, an increase of the flux value at the location of the gauges near the pump is obtained. Nevertheless, at F08 and F16 an overestimation of ~30% is calculated, whereas at F12 the simulation yields a ~13 % higher value than the measurement.

In the set of simulations of model #1 (closed and open sector domain) a maximum

value of the flux at the entrance of the pumping chamber (F05) is obtained, see Figure 5.51. For the models with sticking coefficient of unity and 0.5, the fluxes at F05 are significally higher than the experimental value. This can be explained by the fact that higher pressure difference exists between the region below the dome and the cryopump chamber.

The results of model #1 also suggest that the dynamics in the LFS of the sub-divertor (F05, F08, F12, F16) are quite sensitive with the selection of the sticking coefficient in combination with the assumption at the boundary F16. As mentioned before, at the HFS (manometers F19 and F20) the calculated fluxes are barely affected by the modification of the sticking probability ξ in model #1, independently of the AUG domain (with and without TMP), see Figure 5.51. This reminds us to the ITER gas flow analysis, where only the particle flow near the pumping duct is strongly affected by the pressure conditions at the sink (pumping duct/port). The AUG simulations of model #1 significally underestimate the fluxes by a factor 10 and 8 at the probes F19 and F20, respectively.

Figure 5.50 Comparison between DSMC simulations (bar charts) and experimental data (red line)

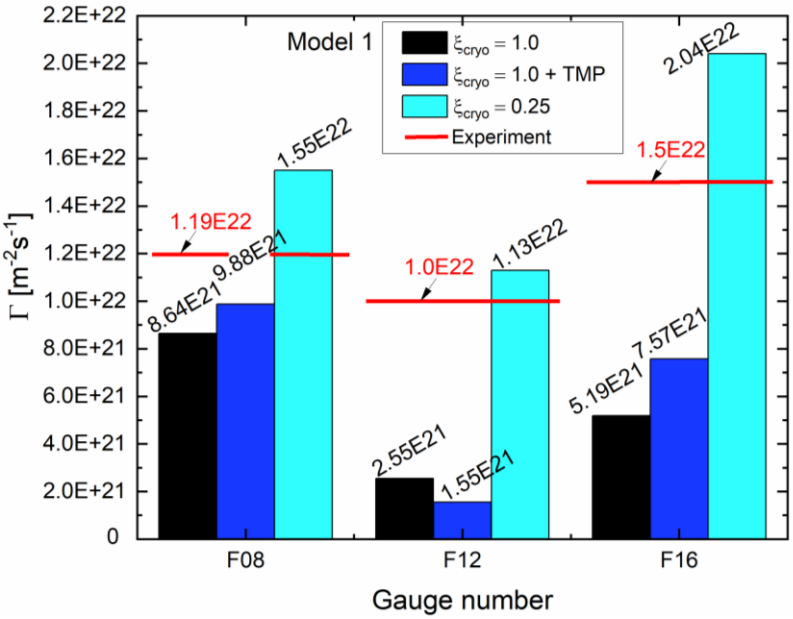

for the AUG sub-divertor model #1: T_{wall} = 300 K, p_{inlet} = 1.4 Pa, p_{F18} = 2.0 Pa. The F16 is taken as a closed boundary (wall) and the sticking coefficients at the cryopump are set to the following values: 1.0, 0.5 and 0.25. Additionally, for the AUG sub-divertor *open* domain, at the end of the pumping duct a value of 10^{-3} Pa is assumed.

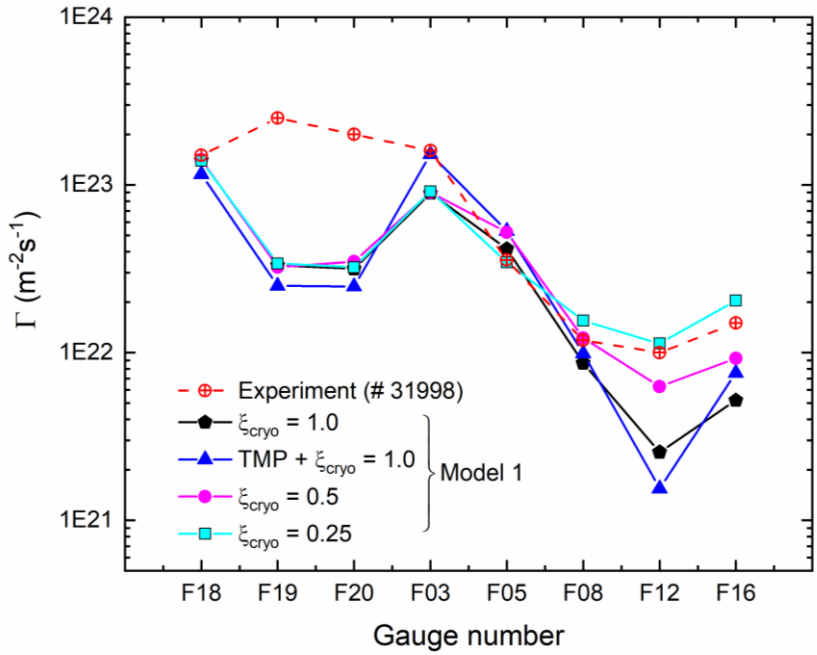

Figure 5.51 AUG sub-divertor fluxes for model #1. Experimental data of plasma discharge #31998 is shown in red open circles with a cross in the middle. Filled symbols depict DSMC modelling black pentagon represents the simulation with sticking probability $\xi_{cryo} = 1.0$ with no TMP, blue triangle has a sticking probability of $\xi_{cryo} = 1.0$ and includes the TMP pump duct. DSMC simulations with $\xi_{cryo} = 0.5$ and $\xi_{cryo} = 0.25$ are depicted in circle (magenta) and square (cyan).

In contrast to model #1, both models #2 and #3 include the contribution of particle flux coming from the boundary surface "outlet F16", located above the cryopump at aprox. the vertical position Z = -0.6 m. The Figure 5.52 show the flow patterns near the position of the F16 manometer for all three models. For model #1 with $\xi_{\mathrm{cryo}} = 0.25$ and model #3 where despite of the different BCs at the LFS and pumping efficiency the ratios of $\Gamma_{model\#1,\xi=0.25}/\Gamma_{exp} = 0.49$ and $\Gamma_{model\#3,\xi=0.17}/\Gamma_{exp} = 0.41$ at location F16 are found. Thus, a higher pumping efficiency and closed outlet F16 at the LFS in model 1 with $\xi_{\mathrm{cryo}} = 0.25$, yields to flux values similar to model #3 in this region. The combination of pumping efficiency and pressure boundary dictates the actual flow pattern near the cryopump which differs entirely between models, see Figure 5.52.

By closing the outlet F16 as in model #1, the gas impinges the wall, being thermalized by it and as the particles are reflected from the wall, a pressure gradient towards the cryopump forces the gas to exit the domain at this surface. For instance, in model #2 the flow at the outlet "F16" and near the gauge position is directed towards the cryogenic pump, i.e. net flow pointing downwards whereas the pressure difference in model 3 sets a flow pattern in the opposite direction. The relation of pumping and sub-divertor conductance provides an idea of the different dynamics that could be found across AUG sub-divertor as a function of the overall conductance in the LFS of the sub-divertor. The

relevance of such flow characteristics has been addressed previously in [97], where a coupling of the recycled neutrals with the plasma edge takes place.

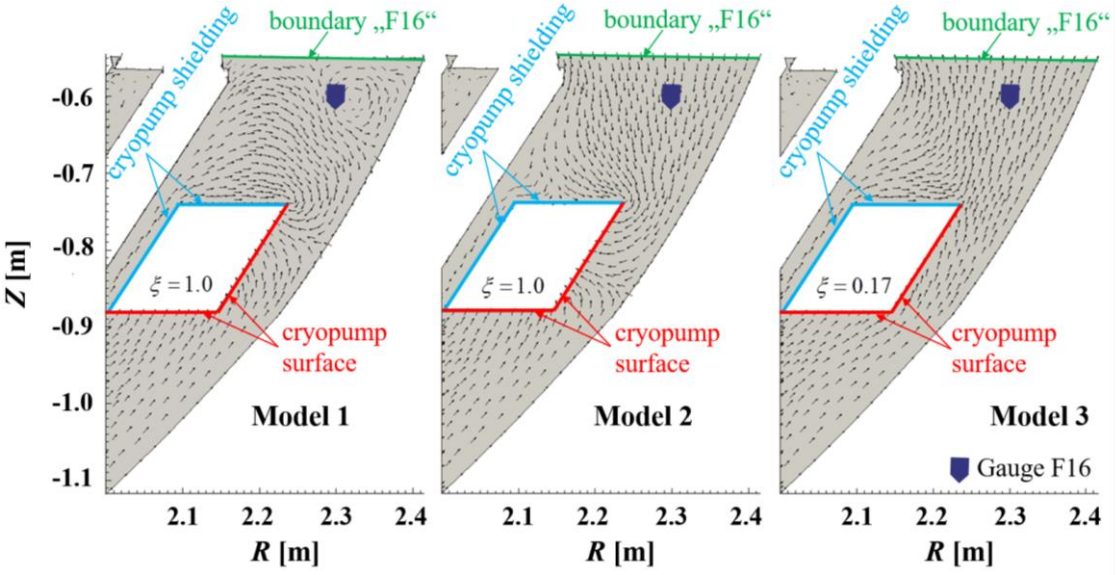

Figure 5.52 ASDEX Upgrade sub-divertor flow patterns for different sub-divertor models. From left to right: Model #1: with ideal pumping at the cryogenic pump and a closed bypass at the LFS (upper surface is a wall). Model #2: the bypass is opened at the LFS and set to the correspondent pressure of the particle flux read by manometer F16 and the pumping efficiency is set to unity. Model #3: LFS bypass is set to the pressure experimental value of F16 and the pumping efficiency is set to $\xi_{\mathrm{cryo}} = 0.17$, which is the value obtained by considering the effective pumping speed for the experiments.

The above-mentioned findings are summarized in Figure 5.53, where the relative fluxes $\Gamma_{\mathrm{DSMC}}/\Gamma_{\mathrm{exp}}$ are plotted at different discrete locations where the manometers are located in AUG. Satisfactory agreement, ratio experimental data to modelling is found particularly below the dome and in the pumping chamber (LFS). This is a significant result because it indicates that the 2D modelling recovers the observed flux at F05 towards the pumping chamber, e.g. relative error of 25% in model 3 found. The agreement between experiment and model in the pumping chamber also means that the total neutral distribution in the present AUG simulations is representative of the experimental conditions behind the outer target and the vicinity of the cryogenic pump. Thus, the main source of neutrals contributing to the pumped flux originates directly from the dome region in combination with the pressure boundary “F16”.

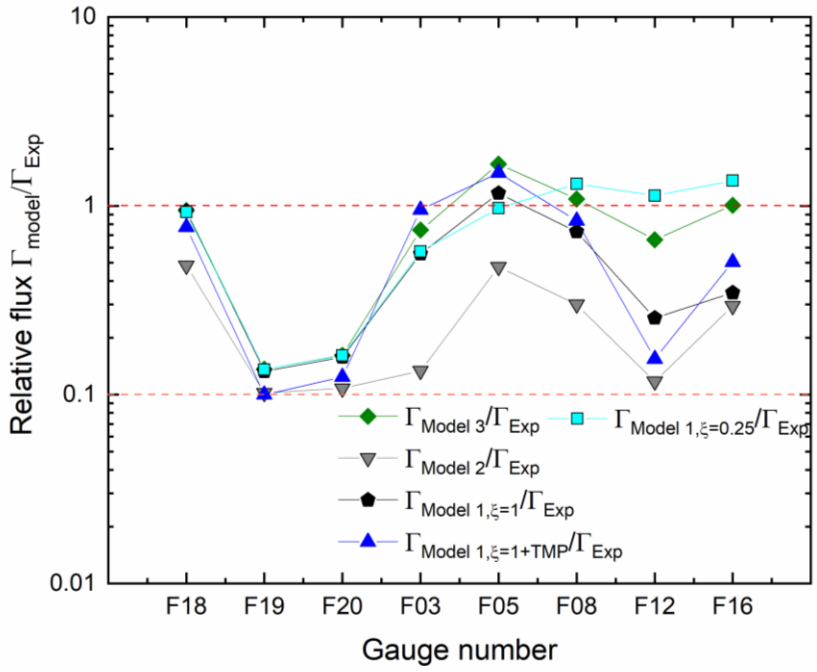

Figure 5.53 ASDEX Upgrade sub-divertor fluxes relative to experimental data # 31998 at t = 3 s. for models 1, 2 and 3. Model #1 with $\xi_{cryo} = 1$ ideal pumping and TMP pump duct is represented by blue triangle facing upwards. Model #1 with ideal pumping conditions and without duct is represented by the black pentagon. Model #2, which differs from model #1 by including a bypass at the LFS, considers ideal pumping conditions and is shown by the grey triangles facing downwards. Data regarding model #3 is depicted by green diamonds, here the sticking probability in the cryogenic pump has the experimental value of 0.17, no TMP duct is considered and HFS as well as LFS bypasses are considered in the simulations.

A common deficiency of the three models is the underestimation of the particle fluxes at the HFS behind the inner target namely at position of manometers F19 and F20. For instance, in model #3, the ratios $\left(\Gamma_{model3}/\Gamma_{exp}\right)_{F19} = 0.14$ and $\left(\Gamma_{model3}/\Gamma_{exp}\right)_{F20} = 0.16$ are found. The present simulations suggest that:

1. At the position of manometers F19 and F20 additional sources of neutrals are found building up the local density. This working hypothesis can be partly confirmed by looking at the experimental results shown in Appendix D (X-point displacement). The time traces of the neutrals show an increase of the F19 signal during the time frame where the strike point of the plasma undergoes an offset in the z-direction. The offset moves the plasma and its strike point towards the position where the manometer F19 is located. Previous studies in AUG [98] have shown a significant particle flux at the inner target plates at different H-mode conditions. The effect is observed as the electron density showed strong correlation with the HFS manometer signals near the inner vertical targets.

This reinforces the need of extending the present modelling by including both regions: sub-divertor and SOL for a complete picture between the physics occurring in the main chamber and sub-divertor.

2. The present assumption of the particle-wall interaction might not be properly modelled at the HFS. A sensitivity study with accommodation coefficients is here suggested. The common feature in the models 1, 2 and 3 where a fully packed physical domain with structures may affect the flow pattern locally at F19 and F20. The use of diffuse-wall reflection with full accommodation model implies that the particle at the HFS *forgets* it previous state as soon as it impinges the wall, this could represent a limitation of the model, with which an unknown error must be associated.

In order to characterized the pressure across AUG sub-divertor, sample points or probes are placed at different points of the flow domain, as shown in Figure 5.54.

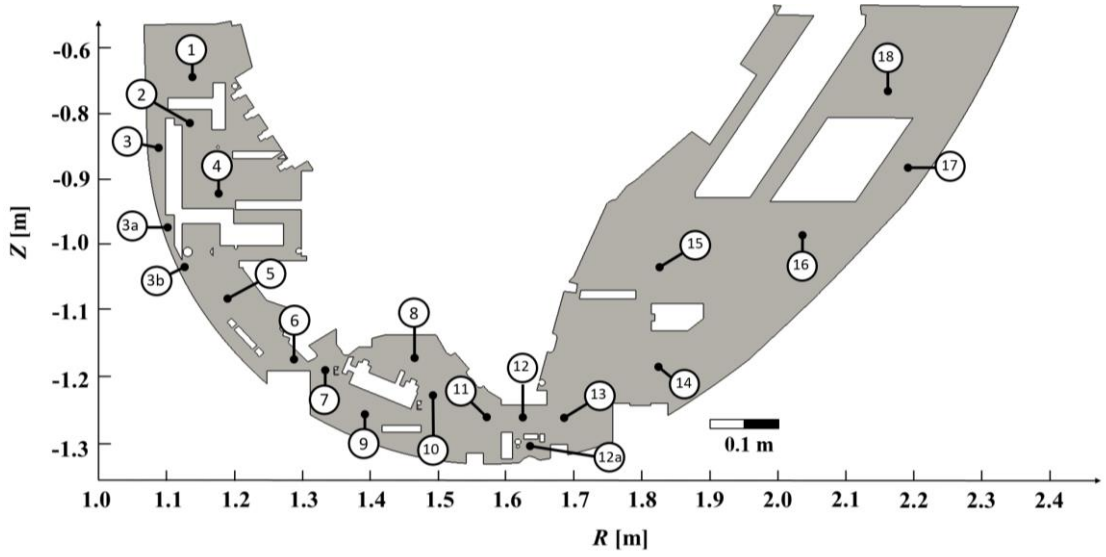

Figure 5.54 Probe locations across AUG sub-divertor placed in the DSMC model to calculate the pressure values.

Simulations show two different aspects characterized by a quasi-homogeneous value of the pressure behind the inner vertical targets (HFS). In this region, a maximum of 10% difference is found between model #1 with ξ_{cryo} = 1 + TMP and all models with no pumping port (model #1, #2 and #3). On the basis of Figure 5.55, where the isobars and normalized pressure field of model #3 are presented, it can be seen that a pressure gradient is established from the HFS to the divertor dome. Therefore, the flow moves towards the region below the dome, where the differences between models are enhanced as the pumping efficiency varies between models. Due to the development of the flow,

high particle flux moves near the structures located below the dome which could explain the higher values of the probes 9 and 10 in relation to the probe 8, which is located below the divertor dome. The pressure drop towards the cryopump is also appreciated in Figure 5.55. Here the pressure ratio at "cryo"-to-"dome" ~ 70% in contrast to ~ 94% for model #1 and ~ 93% for model #2 (not shown). It should be also noted that a ratio of 4.7 at (*R, Z*) = (1.2, -0.9) is needed in order to capture the particle fluxes measured at the gauge F19.

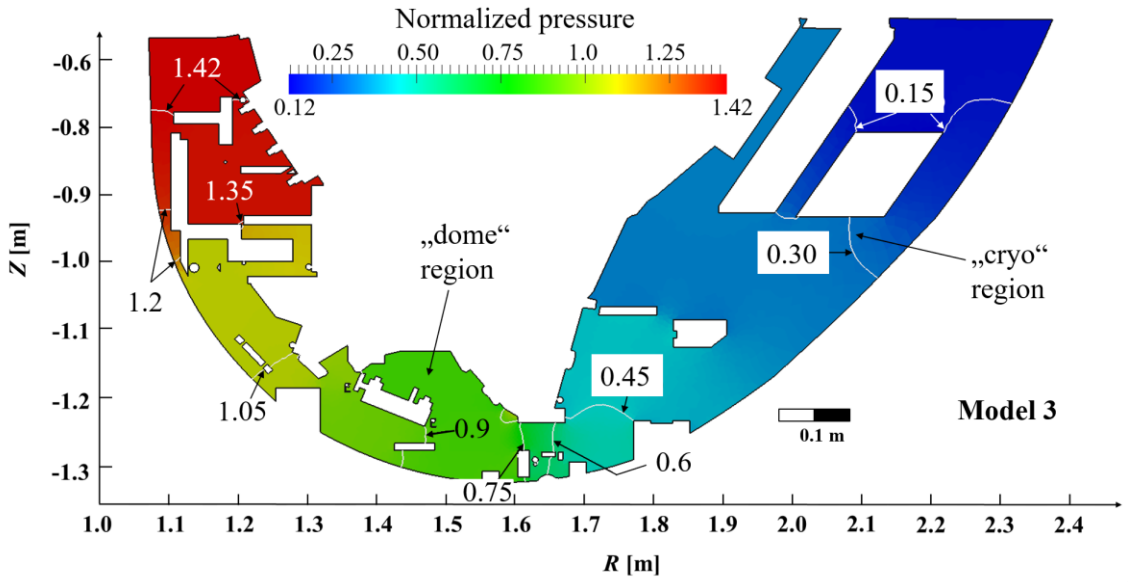

Figure 5.55 Model #3: pressure field and isobars normalized to the value of the pressure at F03 inlet boundary (1.4 Pa).

From the bar plots in Figure 5.56 it is possible to appreciate two main outcomes in the DSMC simulations. By looking at the pressure values of the probes 12 to 18 located at the LFS of AUG, the first outcome shows that the DSMC models with a pumping efficiency different from unity, a pressure difference between probe 11 and 13 between the values of 40%-50% is found. As expected, the pressure profile of model #1 with $\xi_{\mathrm{cryo}} = 0.5$ lies between the profiles of model #3 and model #1 with $\xi_{\mathrm{cryo}} = 1$.

The second outcome focuses on the effect of the sticking coefficient of unity at the cryogenic pump. For instance, in model #1 a decrease of ~57 % in the pressure values is found between probes 11 and 13. The observation is independent of the employment of a sub-divertor domain with or without a pumping port (TMP). This gives an idea that if a section is under the influence of a strong sink (cryopump), the dynamics are mainly dominated by this pump and thus a second sink (TMP in this case) does not strongly affect the neutral flow at the channel. The introduction of the pressure boundary "F16" in model 2 results on a pressure difference of 54 % at the aforementioned probes (11, 13). The

common BC at this surface between model 2 and 3 is appreciated in the value at probe 18, which for both models same order of magnitude is found.

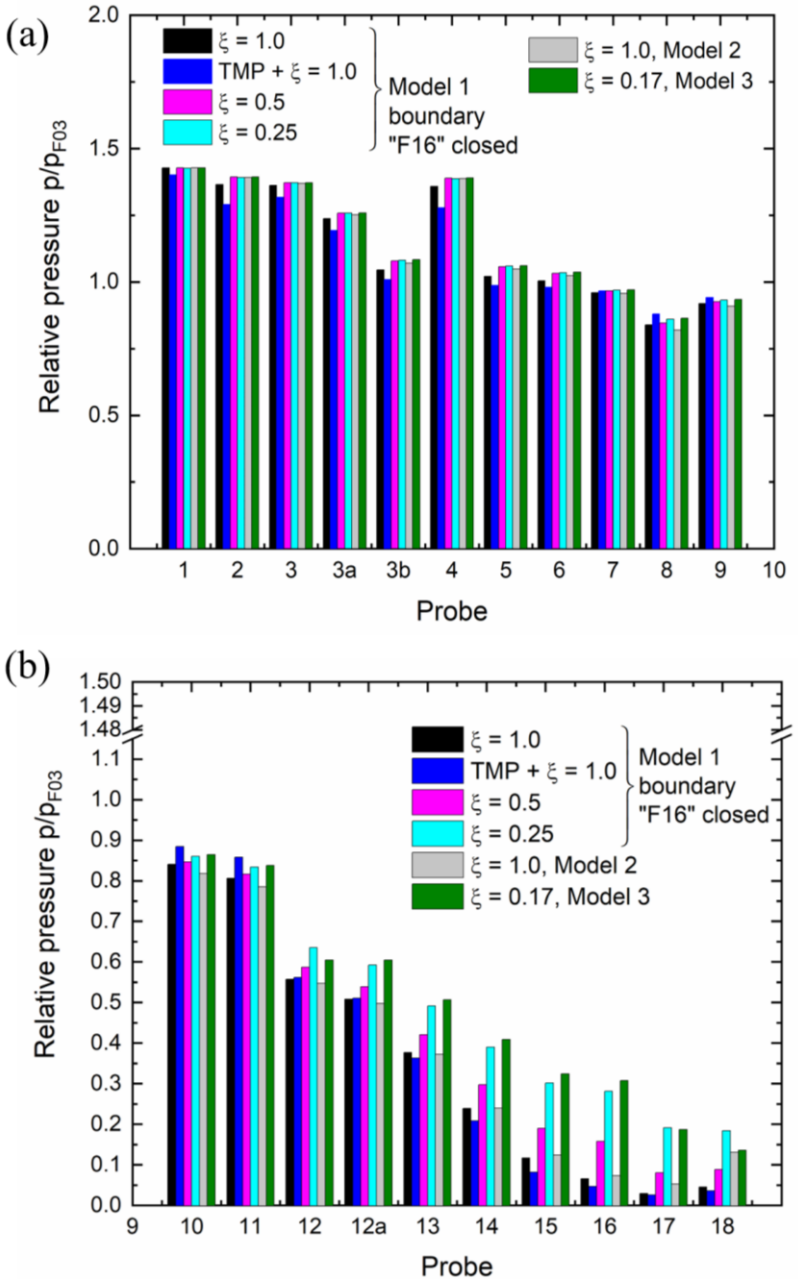

Figure 5.56 Pressure values normalized to the pressure inlets (p_{F03}) at the locations shown in Figure 5.54 (a) Relative pressure sampled at the probes #1 to #10, covering the HFS until the region below the dome. (b) Relative pressure sampled at the probes #11 to #18, spaning the region from the dome to the pumping region in the LFS.

Besides the pressure distribution and particle fluxes across the sub-divertor, a common characterization of a flow can be done through dimensionless quantities like Reynolds number or Mach number. The dependence of the Mach number on the pumping conditions in AUG is shown in Figure 5.57 for model #1 and model #3. Simulations show

that a subsonic flow is found in most regions of the sub-divertor. Only at the vecinity of the cryopump surface in model #1 the gas reaches the value of Ma = 1. A further interesting conclusion is that the flow velocity (and thus the Ma number) at the HFS is unaffected by sticking coefficient variation. In the HFS region the models predict Mach numbers close to zero, hence the gas is at rest. In general, the open boundaries in the sub-divertor do affect the overall behavior of the particle exhaust during a discharge since the particles exchange between the sub-divertor and the plasma edge in the main chamber takes place. Unfortunately, the lack of symmetry at the mid-plane in AUG does not allow the usage of a two-dimensional model of the upper part of the tokamak in order to study the overall conductance of the machine, which is beyond the scope of the present disseration. One open question is the establishment of the non-symmetric neutral flux at the mid-plane in AUG, when the plasma discharge is under the operation of one-third of the nominal pumping speed of the cryogenic pump.

Finally, the collisionality of the flow in AUG is calculated in terms of the Knudsen number. One option is to defined the Knudsen number as the ratio λ/L with a global characteristic length in the sub-divertor of ASDEX Upgrade. However, one faces the problem that every region in the sub-divertor domain has its own *fingerprint*. For instance, the HFS and LFS have their own structures and diagnostics, thus a common characteristic length might not properly describe both regions simultaneously. Hence, here the local flow properties and gradient-length approach has been used for the definition of the Knudsen number. The candidate for the flow property is either the pressure or the particle number density, since the temperature of the flow is almost constant in the whole domain except in the surroundings of the cryopump where the cryoshield is placed. Thus, the approach $\lambda|\nabla\varphi|/\varphi$ is adopted here and the Knudsen number is calculated as

$$Kn = \frac{\lambda}{p}\|\nabla p\|, \tag{5.6}$$

where λ is the mean free path (VHS), p pressure value and $\|\nabla p\|$ the magnitude of the pressure gradient.

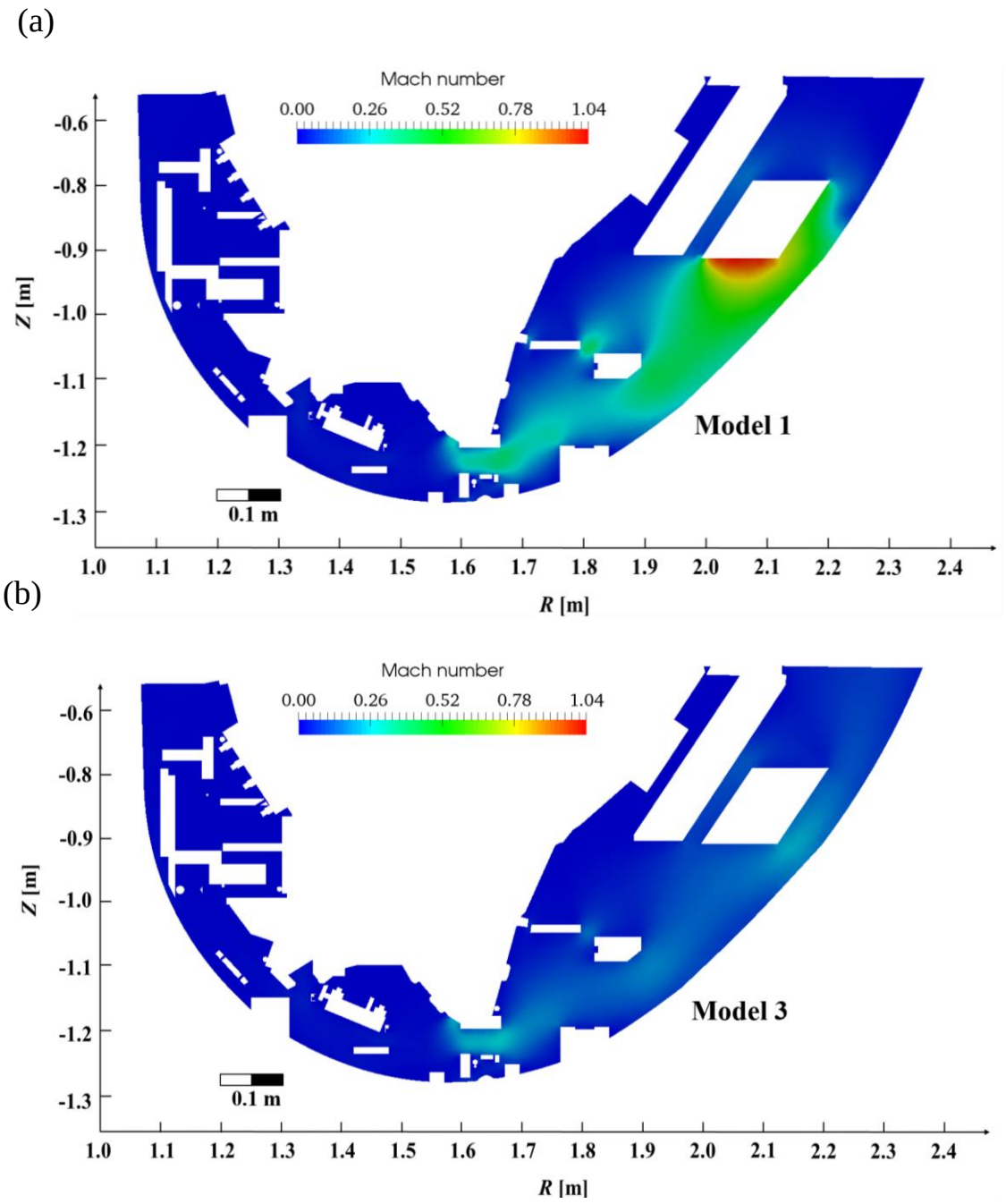

Figure 5.57 (a) Mach number across AUG sub-divertor for model #1 with ξ=1.0 at the cryopump. (b) Calculated Mach number for model #3 with ξ_{cryo}=0.17 at the cryopump. The boundary conditions for both models read p_{F18} = 2 Pa, whereas p_{F16} is a closed surface (model #1) and p_{F16} = 0.197 Pa (model #3). The temperature at the sub-divertor wall and cryopump shielding is set to 300 K and 80 K, respectively.

For the three models, the Knudsen number is calculated and plotted in Figure 5.58. The neutral pressure distribution is quite similar at the HFS in all models and since it has been previously shown that the pumping has a negligible effect on the gas flow in this region. Similar values are found between models at the inner sub-divertor. Such low

Knudsen numbers behind the inner target, where the manometer F19 and F20 are located, and below the structures at the HFS indicates a region of high collisionality. The observation is supported by the found pressure profile. It is worth noting that two different locations within the same region, e.g. Kn $< 10^{-3}$, can actually differ and to illustrate that in model #3, a relative difference of 10% is found between the location of F20 and near the location of the virtual probe 3b, which is located at the HFS near the point (*R, Z*) = (1.12, -1.05). At the HFS region, the flow conditions in narrow and long sections, depicted in green color in Figure 5.58(a) and (b), yield to a decrease on the Knudsen number by one order of magnitude.

Below the divertor dome a high collisionality region Kn < 10^{-3} is found and differs to its surroundings, i.e. at the inner divertor slot and at the divertor volume below the structures where values of the Knudsen number between 10^{-3} and 10^{-2} are found. The Knudsen number profile is common in all models at the HFS and below the dome, which coincides with the pressure and fluxes values previously reported. However, remarkable differences are found as the flow continues its trajectory to the pump chamber in the LFS. The first observation is that for all models with sticking probability $\xi_{cryo} = 1$ the value *Kn* lies slightly below 0.1 at the channel region, just below the outer divertor target leg.

The *Kn* values for model #3 lie below the values of model #1 and #2 in all the pumping chamber area. This is a direct consequence of the lower pumping (sticking probability) in model #3 relative to model #1 and #2 ($\xi_{\text{Model\#3}} \sim 0.2\ \xi_{\text{Model\#1}}$). At the *channel* passage below the LFS divertor target (outer, at ~ *R* = 1.65 m), a transition in the Knudsen number profile from its highest values in both models 1 and 2 to model 3 is found via the models 1 with $\xi_{cryo} = 0.5$ and $\xi_{cryo} = 0.25$ (not shown). Thereafter the gas flow expands into the pump chamber towards the cryopump and thus zones with different Knudsen number can be clearly identified.

Two extreme situations are depicted in Figure 5.58(a), where different regions are shown for models 1 and 3. In model #1, the LFS is characterized by its 3 zones where the Knudsen number ranges between the values of 10^{-2} and 10. These conditions correspond to the slip and transitional collisionality regime. The distribution of the Knudsen number is dictated by the pressure distribution in these regions subjected to the rather high-value of pumping conditions. In the case of model #3, the lower pumping efficiency and the increase of neutral flux at the LFS-boundary "F16" define flow conditions favorable to a higher collisionality regime, as seen in the green and bright yellow areas, namely $10^{-3} < \text{Kn}_{green} \leq 10^{-2}$ and $10^{-2} < \text{Kn}_{br.yellow} \leq 10^{-1}$ respectively. Nevertheless, in model #3 the Knudsen number variation is bounded between 10^{-2} and 10^{-1} with a *Kn* mean value of 0.03 at the LFS and with a maximum variation between probes of 10 (ratio of probe 17 to probe 15). The above findings suggest that the overall conditions in the sub-divertor for the shot #31998 are more likely to be in a collisional flow regime.

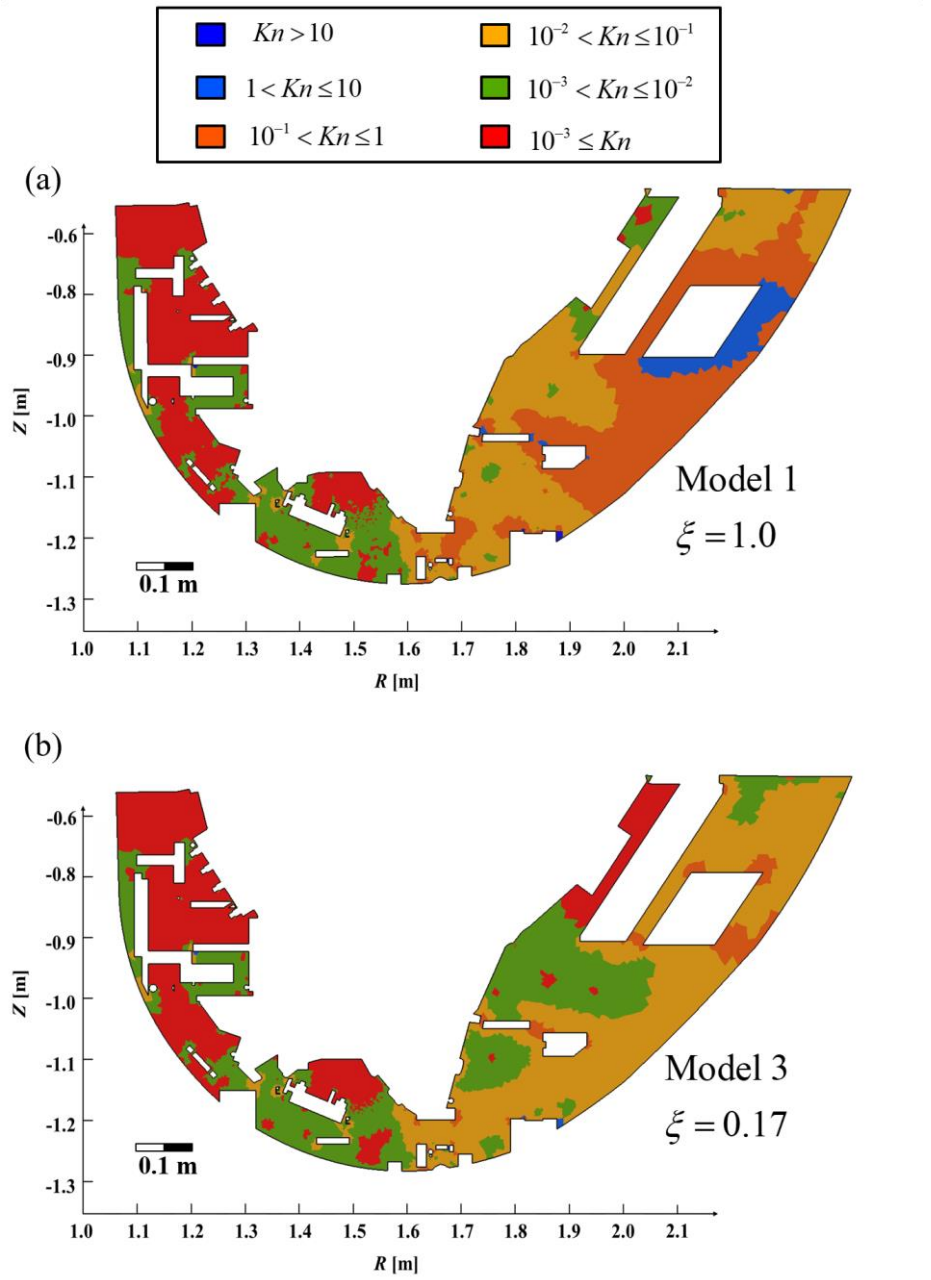

Figure 5.58 (a) Knudsen number *Kn* for ASDEX Upgrade for the sub-divertor models #1 and #3. (b) Following the location of the virtual probes in figure 5.24, the Knudsen number is calculated for all the 3 models. Briefly, in model #1 it is considered and sticking coefficient of unity with a closed surface at the LFS structure (boundary "F16"). The inclusion of the particle flux at the LFS surface "F16" is performed in model #2 and #3. In model #2 the ideal cryopumping is assumed in order to assess the effect of the boundary with a defined pressure value in the collisionality regime with an overestimation of the pumping. Next, model #3 includes the sticking probability ξ in the actual pumping in ASDEX Upgrade.

Additionally, it has been observed that in the area below the PSL and nearby the cryopump two regions coexist, each with a different collisionality regime (order of magnitude) and the observation is independent of the employed sub-divertor model. Thus, the

flow pattern is established in a way that the regions between the plasma chamber in the sub-divertor and PSL are filled out with particles and those remain in this region. The flow that still moves from the divertor dome towards the pump chamber cannot reach this region anymore due to the high population of neutrals which increases the particle interaction and thus a high-collision region below the PSL is formed. The particles which are can cross a certain threshold at $(R,Z)=(R_{thr},Z_{thr})$ are pumped out with a higher probability.

6 Conclusions

6.1 Summary

To achieve an optimum particle balance and plasma density in tokamaks usually one combines fueling and exhaust of particles. During tokamak operation, the particle flow in the divertor region influences the divertor dome pressure [12] and the gas throughput to the torus pumps [11]. This is why predictive modelling of the neutral particle phenomena occurring in the particle exhaust at the divertor is crucial for understanding and optimizing the operation of present and future vacuum systems in fusion devices.

In the present work, the neutral gas flow of the particle exhaust in different tokamak divertors is modelled and simulated by means of the Direct Simulation Monte Carlo (DSMC) method. The DSMC method allows to treat the particle transport of mass, momentum and energy by including neutral–neutral interactions providing an accurate description of the flow field of the neutral gas. In the context of employing a tool that describes the neutral gas flow in tokamak sub-divertors, a step-wise approach is implemented in this dissertation:

1. Verification and validation of the DSMC code by applying it to a gas flow in a simple geometry.
2. Benchmark DSMC code against a neutral code for a collisionless flow in JT-60SA sub-divertor.
3. Comparison of collisional and collisionless flow with DSMC: quantification of the collisional effects in the macroscopic variables of the gas flow in JT-60SA sub-divertor.
4. Application of DSMC method to study the gas flow in ITER sub-divertor as a function of the backpressure of the pumping duct.
5. DSMC modelling of gas flow in ASDEX Upgrade: comparison and model validation against experimental measurements in the sub-divertor region.

In chapter 4 the validation and verification process of the DSMC code have been performed by studying rarefied gas flow through a channel of finite length L. The results with *dsmcFoam* have been compared to analytical solutions [88] and to independent DSMC results in the literature [24]. Simulations show that the pressure has maximum difference between *dsmcFoam* and theory at the channel entrance. This difference is reduced towards the channel outlet. The relative percentage difference lies in the range of (0.01, 41) and (0.06, 25) for high- and mid-collisionality regimes, respectively. In all flow regimes, the difference between theory and *dsmcFoam* is less than 10% for positions in the channel greater than $x = 0.3L$. The calculated reduced flow rate for the lowest collisionality regime yields a difference of 10% (coarse mesh) and 2% (fine mesh) between the present results and the DSMC calculations in the literature. Thus, the present mesh

strategy needs a refinement optimization loop in order to achieve comparable results with respect to the simulations obtained with weighted-zone mesh employed in literature [24]. Regarding the flow in free-molecular regime it has been observed that the time step variation has the most drastical effect on other macroscopic flow variables. By increasing the time step by two orders of magnitude, both the axial velocity and the translational temperature show significant deviations from their expected monotonic behavior, which is as a direct consequence of violating the condition for decoupling the moving (free-flight) and collision step in the DSMC method.

The *dsmcFoam* code has been extended to include the sticking coefficient boundary condition (BC), which can be applied in pumping surfaces located in the sub-divertor of fusion devices. With the new BC and the capability of *dsmcFoam* to switch on and off its collision kernel, new insights of the gas flow in JT-60SA sub-divertor are here reported for the first time.

In the first part of Chapter 5.1 a detailed comparison of the DSMC simulations with the NEUT2D code has been carried out for collisionless flow conditions in JT-60SA sub-divertor. The velocity profiles of both codes show good agreement (relative difference less than 5%) in the region II below the dome and partial agreement near the pumping region (difference less than 5% up to 50%). However, at the high-field side (HFS) near Gate 2 discrepancies in the temperature are found between codes. NEUT2D calculates a colder gas at Gate 2 by a factor of 3 with respect to DSMC, which cannot be justified since neutrals enter the domain at Gate 2 with a certain thermal velocity and the pressure difference between gates induces a force to the gas, accelerating the gas until Gate 1 is reached, where a free-expansion takes place (and thus a cooling process, but in Gate 2). The change of velocity and the expected behaviour of a temperature decrease have been captured by DSMC. Moreover, DSMC results show a certain degree of non-equilibirum of the flow field by looking at the values of the translational and rotational temperatures. Although in the expansion region near Gate 1 in the low-field side (LFS), the temperature profiles differ in shape, a relative difference of ~1% up to 35% between NEUT2D and DSMC is found.

The analyses in JT-60SA confirm that the inclusion of collisions plays a significant role for the transport mechanism and the flow development in the sub-divertor. First, a sensitivity study is performed by only changing the inlet pressure at Gate 2. The main goal was to compare the analytical expression of the collisional frequency with the DSMC analyses. A relative difference between the analytical expression and DSMC of less than 1% is found across the domain. The sensitivity analysis closes with the comparison between binary collision models. A major outcome has to do with the fact that for regions in the sub-divertor with values of $T/T_{ref} > 1$ and $T/T_{ref} \gg 1$ the hard sphere modelling overestimates the number of collisions relative to the VHS model, whereas the Maxwell model understimates the collision frequency relative to VHS.

By means of DSMC simulations, deviations in the pressure of 20% and 40% between a collisionless and a collisional conditions are obtained for the Scenario #2 [91]. Moreover, the temperature flow field also is affected by the inclusion of collisions, particularly near both inlets of the sub-divertor where a relative difference between 3% and ~46% is found. In the region near the pumping surface the difference between collisional and collisionless DSMC is found to be less than 5%. The results are first-of-its-kind and are of great value for further design works and contribute to the understanding of the sub-divertor particle flow during JT-60SA operation.

Chapter 5.2 presents the neutral gas dynamics as a function of the pressure at the entrance of the pumping port in the 2009-design ITER divertor cassette. The level of detail of the physical domain together with the modelling with neutral-neutral interactions represent a novelty in the field. The pressure increase at the pumping port translates in an increase of the gas circulation Γ_{circ} flowing from the sub-divertor region to the main chamber. The gas moves towards the main chamber through two passages located in the sub-divertor behind the divertor targets and ending at the boundaries number I (inner region, HFS) and V (outer region, LFS). The modelling shows that for pressures below 1 Pa at the pumping port, the ratio inner-to-outer fluxes between the two outlet boundaries behind the divertor targets ranges $9.2 < \Gamma_I/\Gamma_V < 15.6$.

At a pressure value of 1 Pa at ITER pumping port is observed that an increase of particle flux only at the outlet boundary V (LFS) with no significant change at boundary I (HFS). As a consequence, the ratio between these fluxes is reduced to 1.95. The increase of flux at the LFS boundary V has been also explained in terms of flow separation. For all studied cases an adverse pressure exists along of the pumping port near the wall, establishing a region with flow reversal. The simulations indicate that the localization of flow separation setpoint increases radially towards the pumping port as the pressure at the pumping port increases.

Chapter 5 finalizes with the modelling of experiments of particle exhaust in ASDEX Upgrade (AUG). In contrast to JT-60SA and ITER analyses, here experimental data has been employed as boundary conditions for the DSMC modelling. The BCs of interest are based on the plasma discharge #31998 and its corresponding particle exhaust measurements and parameters. Three models have been proposed to describe the gas flow in AUG: model #1 and #2 address specific aspects of the modelling parameters whereas model #3 resembles the experimental conditions in AUG.

For instance, one major outcome of the AUG gas flow modelling concerns the validation of the sticking probability BC developed for *dsmcFoam*. This BC has been employed in the DSMC model #3 with astonishing good results by obtaining the mea-sured value of the particle flux (manometer) near the cryogenic pump. Moreover, the analysis of the flow collisionality shows that the distribution of the Knudsen number at the LFS is strongly affected by the different pumping conditions. Model #3 shows that a wide range

of collisionality regimes across the pump chamber is found, the Knudsen number at the pump chamber has mainly 2 different Kn-regions covering the interval 10^{-3} to 1, i.e. slip-flow and transition collisional regimes coexist at the LFS.

The addressed sensitivities in model #1 and #2 of AUG have shed light onto dependencies among sub-divertor parameters, which are known to be of relevance in divertor operation control [99]. As second major outcome of the AUG analysis regards the modification of the sticking probability value at the cryopump. The sensitivity analysis on the sticking probability shows that its value mainly affects the particle fluxes and pressure distribution around the pump chamber (LFS) and it barely influences the flow field at the HFS region. This effect has been observed in the ITER analyses as well. Model #1 shows that the pressure distribution around the cryopump results from a combination of sticking probability and gas particles coming from the LFS.

A key message of the present dissertation has been to demonstrate the ability of the DSMC method to describe neutral gas transport in tokamak sub-divertors. Most of the objectives presented in Chapter 1.3 have been addressed with a certain level of success. However, there are still discrepancies in the modelling, which suggests that important aspects are missing in the current assumptions or refinements of the existing models are needed. These open issues and further improvements on the present approach are the subject of the next section.

6.2 Outlook

Discrepancies in the flow speed and temperature profiles between DSMC and NEUT2D in collisionless flow conditions are observed in the present work. To tackle this, modification of the cell distribution across the pumping region shall be performed. This can be done by employing a mesh strategy that is based on the profile of the velocity flow field. The focus should be given at the region where the maximum of the profiles is found. The cold region near Gate 2 shall be explained in terms of the verification of the boundary conditions. As second option, further simplifications on the model can be done by restricting the degrees of freedom (DoF) to translational modes in DSMC in order to ease the comparison. Since the rotational DoF become more relevance for high temperatures or expansions at the entrance/outlet regions, as second step, a direct comparison between approaches including both translational and rotational modes.

Independent of the employed model in ASDEX Upgrade (AUG), the particle fluxes at AUG's HFS calculated with DSMC, namely at F19 and F20, show a clear discrepancy: factor of 10 lower than the experimental observations. As possible routes to fix this, the following actions are proposed:

i. **Particle-wall interaction model in AUG**. Assuming that the employed pressure boundary condition at the HFS holds and no extra particle sources are placed, a

first path involves the exploration of the role of the particle temperature after reflection.

- Since the diffuse-reflection depends solely on the wall temperature as parameter, it is suggested a sensitivity analysis based on the variation of the reflected temperature of the neutrals. Typically, the temperature of the neutrals is not measured in the sub-divertor during experiments and therefore, data is scarce in the literature in order to validate this hypothesis. However, a correlation can be developed for the particular experiment of interest.

A second possible path to follow is to select an alternative gas-surface interaction to the diffuse reflection with full accommodation employed throughout this dissertation. A working hypothesis may also rely on the fact that:

- The particles are allowed to have two accomodation coefficients after reflection, i.e. a normal and a tangential to the wall-surface. In this case, the CLL model, introduced in section 3.4 of chapter 3, can be applied. From the implementation perspective, *dsmcFoam* code release, such as the one presented in [100], includes already this interaction model. Adjustments of the model can be based on experimental observations [74].
- Alternatively, the particles can be reflected from the walls as function of their incident energy before colliding with the wall. This involves previous knowledge of both the particle incident velocity (via experimental data or with an ansatz) and a model involving the gas-surface interaction database as a function of such incident energy. Scattering models presented in [101] are compared to experiments of monoenergetic beams of atoms scattering from clean surfaces. The *energy accommodation coefficients boundary condition* can be implemented in *dsmcFoam* as part of the gas-surface interactions library based on the relations between selected working gases and surfaces reported in [101] and the references therein.

ii. **Interpretation of the fluxes relate to neutrals at SOL and not only the sub-divertor for AUG.** Flow paths between the divertor cassettes and between target slits, allow particle flow between main chamber and sub-divertor, resulting in additional particle sources in the sub-divertor at that particular point. The experimental observations of a vertical offset of the x-point suggests that particles near the strike point in the main chamber interact with the manometers.

Futher improvements. The following points have not been addressed in the present work and are necessary to enrich the physics of the neutral transport modelling in fusion sub-divertors with DSMC:

1. Multi-species analysis with reaction physics.
2. Coupling with a plasma solver.
3. Extension to 3D-geometries to address asymmetrical conditions in the sub-divertor.

The nature of the divertor dynamics involves not only one type of particle as main component of the gas flow, but many. Thus, the inclusion of other species in the simulations will enrich the physics in the modelling. In this context, recent work on describing the JET sub-divertor flow by considering a binary mixture has been performed [102]. Upon available information of molar concentrations, the use of multi-species in the DSMC should be considered as a standard way of modelling sub-divertor flows.

On the other hand, interactions such as dissociation and recombination between species as well as particle-surface chemistry should be included in the modelling. The former is a module in *dsmcFoam* that has been developed for applications to external and hypersonic flows [103]. The module activation is straightforward and only the desired interactions should be declared as an input in the DSMC simulation. The module plays a key role in the description of the gas in the dome region at the sub-divertor inlets, since for high-energetic particles (> 1000 K) one needs to include, additionally to the translational mode, also the vibrational and rotational modes in the particle collisions.

The workflow presented here has served as the foundation for establishing, in a self-consistent manner, the simulation of the particle exhaust by manually coupling a DSMC solver and the SOLPS plasma edge code [104] until convergence was achieved. The self-consistent coupling is of course highly desirable in order to update the sub-divertor input at each time step. Further work regarding automation is needed as well as code development focusing on the data transfer between domains DSMC and the plasma solver at each time step.

The extension of the present workflow from a two- to a three-dimensional flow domain should be done. This is due to the 3D nature of the particle exhaust in fusion devices. To apply the DSMC criteria: $\Delta x < \lambda$ and $\Delta t < \tau_{\mathrm{coll}}$ is not the problem, but to define a strategy to wisely choose those parameters. One option is to employ Adaptive Mesh Refinement strategies [105]. This allows to optimize the computational grid (iterative process during running time) by finding the max. and min. of the mean-free path and adjusting the mesh size accordingly. The use of clusters and super computers could overcome the computational efforts, but still the DSMC simulations should be planned with double care in order to optimize the simulation time.

More detailed analysis of the interaction between the sub-divertor flows and the SOL should be performed. For instance, this could have a great impact in the understanding of ASDEX Upgrade observations presented in this work. The inter-cassette gaps as well as the different inlet and outlet boundaries (HFS, LFS), such as bypasses or slots,

seem to play a crucial role in the development of the neutral particle dynamics. Particularly at the HFS, DSMC simulations suggest that the difference between simulations and experiment to do with a possible extra source of neutrals in this region (recirculation of neutrals through toroidal slits). The complexity of the modelling is of course increased since one needs to make use of the 3-dimensional calculation and a coupling with a 2D/3D plasma edge code.

7 Bibliography

[1] D. J. Griffiths, Introduction to Quantum Mechanics, 2nd ed. New Jersey: Prentice Hall, 1995, ISBN 0-13-124405-1.

[2] S. Atzeni and J. Meyer-ter-Vehn, The Physics of Inertial Fusion: Beam Plasma Interaction, Hydrodynamics, Hot Dense Matter, 1st ed. Oxford: Oxford University Press, 2004, ISBN 978-0198562641.

[3] D. D. Clayton, Principles of Stellar Evolution and Nucleosynthesis, 1st ed. Chicago and London: The University of Chicago Press, 1983, ISBN 0-226-10952-6.

[4] W. M. Nevins, A Review of Confinement Requirements for Advanced Fuels, *Journal of Fusion Energy*, 17 1 . 1998 doi: 10.1023/A:1022513215080.

[5] J.-L. Basdevant, J. Rich, and M. Spiro, Fundamentals in Nuclear Physics, 1st ed. New York: Springer, 2005, ISBN 978-0-387-01672-6.

[6] U. Stroth, Plasmaphysik: Phänomene, Grundlagen, Anwendungen, 1st ed. Wiesbaden: Vieweg+Teubner, 2011, ISBN 978-3-8348-1615-3.

[7] ITER Organisation, ITER - What is a tokamak? https://www.iter.org/mach/Tokamak. [Accessed: 22 Nov. 2020].

[8] ITER physics expert group on confinement, Transport, ITER physics expert group on confinement modelling, and ITER physics basis editors, Chapter 2: Plasma confinement and transport, *Nuclear Fusion* 47 12 (2002) 2275–2249. doi: 10.1088/0029-5515/39/12/302.

[9] ITER Physics Expert Group on Divertor and ITER Physics Expert Group on Divert Database and ITER, Chapter 4: Power and particle control, *Nuclear Fusion* 39 12 (1999) 2391–2469. doi: 10.1088/0029-5515/39/12/304.

[10] C. Day, D. Murdoch, and R. Pearce, The vacuum systems of ITER, *Vacuum* 83 4 (2008) 773–778. doi: 10.1016/j.vacuum.2008.05.010.

[11] A. S. Kukushkin et al., Physics requirements on fuel throughput in ITER, *Journal of Nuclear Materials* 415 1 (2011) S497–S500. doi: 10.1016/j.jnucmat.2010.08.050.

[12] C. Day et al., Towards a physics-integrated view on divertor pumping, *Fusion Engineering and Design* 89 7–8 (2014) 1505–1509. doi: 10.1016/j.fusengdes.2014.04.077.

[13] ITER Organisation, ITER Divertor. https://www.iter.org/mach/Divertor. [Accessed: 30 Aug. 2020].

[14] J. Wesson, Tokamaks, 3rd ed. Oxford: Oxford University Press, 2004, ISBN 0198509227.

[15] NIST, Cross-section: Planned ITER Fusion Reaction Vessel. https://www.nist.gov/image/nistlightsourceilluminatesfusionpowerdiagnosticsjpg. [Accessed: 06 Sep. 2020].

[16] P. C. Stangeby, The Plasma Boundary of Magnetic Fusion Devices, 1st ed. London: IoP Publishing LTD, 2000, ISBN 978-0750305594.

[17] V. Hauer et al., Design of the ITER torus prototype cryopump, *Fusion Engineering and Design* 82 15–24 (2007) 2113–2119. doi: 10.1016/j.fusengdes.2007.07.039.

[18] C. Day et al., Design progress for the ITER torus and neutral beam cryopumps, *Fusion Engineering and Design* 86 9–11 (2011) 2188–2191. doi: 10.1016/j.fusengdes.2010.11.023.

[19] C. Day and T. Giegerich, Development of Advanced Exhaust Pumping Technology for a DT Fusion Power Plant, *IEEE Transactions on Plasma Science* 42 4 (2014) 1058–1071. doi: 10.1109/TPS.2014.2307435.

[20] R. A. Pitts et al., Physics basis for the first ITER tungsten divertor, *Nuclear Materials and Energy* 20 July (2019) 100696. doi: 10.1016/j.nme.2019.100696.

[21] S. Wiesen et al., Plasma edge and plasma-wall interaction modelling: Lessons learned from metallic devices, *Nuclear Materials and Energy* 12 (2017) 3–17. doi: 10.1016/j.nme.2017.03.033.

[22] S. Varoutis, F. Bonelli, C. Day, and Y. Igitkhanov, Optimization of pumping efficiency and divertor operation in DEMO, *Nuclear Materials and Energy* 12 (2017) 668–673. doi: 10.1016/j.nme.2017.04.001.

[23] S. Varoutis, D. Valougeorgis, O. Sazhin, and F. Sharipov, Rarefied gas flow through short tubes into vacuum, *Journal of Vacuum Science & Technology A* 26 2 (2008) 228–238. doi: 10.1116/1.2830639.

[24] S. Varoutis, C. Day, and F. Sharipov, Rarefied gas flow through channels of finite length at various pressure ratios, *Vacuum* 86 12 (2012) 1952–1959. doi: 10.1016/j.vacuum.2012.04.032.

[25] G. A. Bird, Molecular Gas Dynamics and the Direct Simulation of Gas Flows, 2nd ed. Oxford: Oxford University Press, 1994, ISBN 978-0198561958.

[26] R. K. Agarwal, K. Yun, and R. Balakrishnan, Beyond Navier-Stokes : Burnett equations for flows in the continuum-transition regime, *Physics of Fluids* 13 10 (2001) 3061–3085. doi: 10.1063/1.1397256.

[27] S. Chapman and T. G. Cowling, The Mathematical Theory of Non-uniform Gases: An Account of the Kinetic Theory of Viscosity, Thermal Conduction and Diffusion in Gases, 3rd ed. Cambridge: Cambridge University Press, 1991, ISBN 978-0521408448.

[28] L. C. Woods, An Introduction to the Kinetic Theory of Gases and Magnetoplasmas. Oxford: Oxford University Press, 1993, ISBN 978-0198563938.

[29] B. J. Alder and T. E. Wainwright, Phase Transition for a Hard Sphere System, *Journal of Chemical Physics* 27 1957 (1957) 1208–1209. doi: 10.1063/1.1743957.

[30] M. P. Allen and D. J. Tildesley, Computer Simulation of Liquids, 1st ed. Oxford: Claredon Press, 1989, ISBN 978-0198556459.

[31] D. C. Rapaport, The Art of Molecular Dynamics Simulation, 2nd ed. Cambridge: Cambridge University Press, 2004, ISBN 0521825687.

[32] L. Boltzmann, Kinetische Theorie II: Irreversible Prozesse Einführung und Originaltexte. Wiesbaden: Vieweg+Teubner, 1970, ISBN 978-3-322-84986-1.

[33] P. L. Bhatnagar, E. P. Gross, and M. Krook, A Model for Collision Processes in Gases. I. Small Amplitude Processes in Charged and Neutral One-Component Systems, *Physical Review* 94 3 (1954) 511–525. doi: 10.1103/PhysRev.94.511.

[34] N. G. Hadjiconstantinou, The limits of Navier-Stokes theory and kinetic extensions for describing small-scale gaseous hydrodynamics, *Physics of Fluids* 18 11 (2006) 111301(1–19). doi: 10.1063/1.2393436.

[35] C. Cercignani, Rarefied Gas Dynamics: From Basic Concepts to Actual Calculations. Cambridge:

Cambridge University Press, 2000, ISBN 978-0521659925.

[36] D. Reiter, (2019), The EIRENE Code User Manual Version: September 13, 2019. http://www.eirene.de/html/manual.html. [Accessed: 24 Feb. 2022].

[37] R. Schneider et al., Analysis of cold divertor concepts for ITER, *Journal of Nuclear Materials* 220–222 (1995) 1076–1080. doi: 10.1016/0022-3115(94)00477-3.

[38] D. Reiter, M. Baelmans, and P. Börner, The EIRENE and B2-EIRENE Codes, *Fusion Science and Technology* 47 2 (2005) 172–186. doi: 10.13182/FST47-172.

[39] V. Kotov, D. Reiter, and A. S. Kukushkin, (2007), Numerical study of the ITER divertor plasma with the B2-EIRENE code package. http://www.eirene.de/kotov_solps42_report.pdf. [Accessed: 24 Feb. 2022].

[40] R. A. Pitts et al., A full tungsten divertor for ITER: Physics issues and design status, *Journal of Nuclear Materials* 438 Supplement (2013) S48–S56. doi: 10.1016/j.jnucmat.2013.01.008.

[41] R. A. Pitts et al., Status and physics basis of the ITER divertor, *Physica Scripta* T138 (2009) 014001. doi: 10.1088/0031-8949/2009/T138/014001.

[42] R. A. Pitts, (2007), Tokamak edge physics and plasma-surface interactions. https://crppwww.epfl.ch/~pitts/pitts/pitts_hppw2008_26_03_2008_vg_final.pdf. [Accessed: 24 Feb. 2022].

[43] A. S. Kukushkin et al., Finalizing the ITER divertor design: The key role of SOLPS modeling, *Fusion Engineering and Design* 86 12 (2011) 2865–2873. http://dx.doi.org/10.1016/j.fusengdes.2011.06.009.

[44] V. Hauer and C. Day, Conductance modelling of ITER vacuum systems, *Fusion Engineering and Design* 84 2–6 (2009) 903–907. doi: 10.1016/j.fusengdes.2008.12.115.

[45] V. Hauer and C. Day, ITER divertor gas flow modelling, *Fusion Engineering and Design* 98–99 (2015) 1775–1778. doi: 10.1016/j.fusengdes.2015.04.012.

[46] H. Kawashima et al., Development of Integrated SOL/Divertor Code and Simulation Study in JAEA, *Plasma and Fusion Research* 1 (2006) 031–031. doi: 10.1585/pfr.1.031.

[47] H. Kawashima et al., Simulation of divertor pumping in JT-60U with SOLDOR/NEUT2D code, *Journal of Nuclear Materials* 363–365 1–3 (2007) 786–790. doi: 10.1016/j.jnucmat.2007.01.127.

[48] D. Stotler and C. Karney, Neutral Gas Transport Modeling with DEGAS 2, *Contributions to Plasma Physics* 34 (1994) 392–397.

[49] D. Stotler and C. Karney, (2013), User's Guide for DEGAS 2. https://w3.pppl.gov/degas2/Doc/degas2_all.html. [Accessed: 24 Feb. 2022].

[50] A. L. Garcia and W. Wagner, Time step truncation error in direct simulation Monte Carlo, *Physics of Fluids* 12 10 (2000) 1–27. doi: 10.1063/1.1289691.

[51] W. H. Press, S. A. Teukolsky, W. T. Vetterling, and B. P. Flannery, Numerical Recipes in C: The art of scientific computing, 2nd ed. Cambridge: Cambridge University Press, 2002, ISBN 978-0521431088.

[52] E. Meiburg, Comparison of the molecular dynamics method and the direct simulation Monte Carlo technique for flows around simple geometries, *The Physics of Fluids* 29 10 (1986) 3107–3113. doi: 10.1063/1.865961.

[53] G. A. Bird, Direct simulation of high-vorticity gas flows, *The Physics of Fluids* 30 2 (1987) 364–

366. doi: 10.1063/1.866386.

[54] F. J. Alexander, A. L. Garcia, and B. J. Alder, Cell size dependence of transport coefficients in stochastic particle algorithms, *Physics of Fluids* 10 6 (1998) 1540–1542. doi: 10.1063/1.869674.

[55] W. G. Vincenti and C. H. Krüger Jr., Introduction to Physical Gas Dynamics, 1st ed. New York: John Wiley & Sons, 1986, ISBN 978-0882753096.

[56] J. Lutisan, The Treatment of Molecular Collisions in DSMC Methods, *Molecular Simulation* 14 3 (1995) 189–206. doi: 10.1080/08927029508022016.

[57] L. D. Landau and E. M. Lifshitz, Statistical Physics Part I, 3rd ed. Oxford: Pergamon Press Ltd., 1980, ISBN 978-0080230382.

[58] C. Shen, Rarefied Gas Dynamics: Fundamentals, Simulations and Micro Flows. Berlin: Springer, 2005, ISBN 978-3-540-23926-0.

[59] G. A. Bird, The DSMC Method, 1st ed. CreateSpace Independent Publishing Platform, 2013, ISBN 978-1492112907.

[60] G. A. Bird, Perception of numerical methods in rarefied gas dynamics, *Progress in Astronautics and Aeronautics* (1989) 211–226. doi: https://doi.org/10.2514/5.9781600865923.0211.0226.

[61] K. Koura, A sensitive test for accuracy in evaluation of molecular collision number in the direct-simulation Monte Carlo method, *Physics of Fluids A: Fluid Dynamics* 2 7 (1990) 1287–1289. doi: 10.1063/1.857577.

[62] K. Koura, Improved null-collision technique in the direct simulation Monte Carlo method: Application to vibrational relaxation of nitrogen, *Computers & Mathematics with Applications* 35 1–2 (1998) 139–154. doi: 10.1016/s0898-1221(97)00264-2.

[63] T. Abe, Generalized scheme of the no-time-counter scheme for the DSMC in rarefied gas flow analysis, *Computers & Fluids* 22 2–3 (1993) 253–257. doi: 10.1016/0045-7930(93)90057-G.

[64] A. L. Garcia and W. Wagner, Generation of the Maxwellian inflow distribution, *Journal of Computational Physics* 217 2 (2006) 693–708. doi: 10.1016/j.jcp.2006.01.025.

[65] G. S. Fishman, Monte Carlo: Concepts, Algorithms, and Applications, 1st ed. New York: Springer, 1996, ISBN 978-0387945279.

[66] B. A. Berg, Markov Chain Monte Carlo Simulations and Their Statistical Analysis, 1st ed. World Scientific, 2004, ISBN 978-9812389350.

[67] J. N. Moss, G. A. Bird, and G. N. Markelov, DSMC Simulations of Hypersonic Flows and Comparison With Experiments, *AIP Conference Proceedings* 762 1 (2005) 547–552. doi: 10.1063/1.1941593.

[68] J. C. Maxwell, The Scientific Papers of James Clerk Maxwell. Cambridge: Cambridge University Press, 2011, ISBN 978-0511710377.

[69] C. Cercignani and A. Frezzotti, Numerical Simulation of Supersonic Rarefied Gas Flows Past a Flat Plate: Effects of the Gas-Surface Interaction Model on the Flowfield, Rarefied Gas Dynamics: Theoretical and Computational Techniques, American Institute of Aeronautics and Astronautics, 1989, 552–566.

[70] F. C. Hurlbut and F. S. Sherman, Application of the Nocilla Wall Reflection Model to Free-Molecule Kinetic Theory, *The Physics of Fluids* 11 3 (1968) 486–496. doi: 10.1063/1.1691943.

[71] M. Becker, F. Robben, and R. Cattolica, Velocity Distribution Functions Near the Leading Edge of

a Flat Plate, *AIAA Journal* 12 9 (1974) 1247–1253. doi: 10.2514/3.49461.

[72] C. Cercignani and M. Lampis, Kinetic models for gas-surface interactions, *Transport Theory and Statistical Physics* 1 2 (1971) 101–114. doi: 10.1080/00411457108231440.

[73] R. G. Lord, Application of the Cercignani-Lampis Scattering Kernel to the Direct Simulation Monte Carlo Calculations, *Rarefied Gas Dynamics: Proceedings of the 17th International Symposium on Rarefied Gas Dynamics, Aachen 1990* (1991).

[74] M. S. Woronowicz and D. F. G. Rault, Cercignani-Lampis-Lord gas surface interaction model - Comparisons between theory and simulation, *Journal of Spacecraft and Rockets* 31 3 (1994) 532–534. doi: 10.2514/3.26474.

[75] N. G. Hadjiconstantinou and A. L. Garcia, Statistical Error in Particle Simulations of Low Mach Number Flows, First MIT Conference on computational fluid and solid mechanics, 2000, 1–10. https://digital.library.unt.edu/ark:/67531/metadc1405358/.

[76] G. Chen and I. D. Boyd, Statistical Error Analysis for the Direct Simulation Monte Carlo Technique, *Journal of Computational Physics* 126 2 (1996) 434–448. doi: 10.1006/jcph.1996.0148.

[77] M. Fallavollita, D. Baganoff, and J. McDonald, Reduction of simulation cost and error for particle simulations of rarefied flows, *Journal of Computational Physics* 109 1 (1993) 30–36. doi: 10.1006/jcph.1993.1196.

[78] F. Reif, Fundamentals of Statistical and Thermal Physics, 1st ed. McGraw-Hill, 1965, ISBN 978-0070518001.

[79] N. G. Hadjiconstantinou, A. L. Garcia, M. Z. Bazant, and G. He, Statistical error in particle simulations of hydrodynamic phenomena, *Journal of Computational Physics* 187 1 (2003) 274–297. doi: 10.1016/S0021-9991(03)00099-8.

[80] A. L. Garcia, Estimating hydrodynamic quantities in the presence of microscopic fluctuations, *Communications in Applied Mathematics and Computational Science* 1 1 (2006) 53–78. doi: 10.2140/camcos.2006.1.53.

[81] H. G. Weller, G. Tabor, H. Jasak, and C. Fureby, A tensorial approach to computational continuum mechanics using object-oriented techniques, *Computers in Physics* 12 6 (1998) 620–631. doi: 10.1063/1.168744.

[82] CFD Direct LTD, OpenFOAM Foundation Documentation. https://cfd.direct/openfoam/documentation/. [Accessed: 22 Nov. 2020].

[83] C. Geuzaine and J. F. Remacle, Gmsh: A 3-D finite element mesh generator with built-in pre- and post-processing facilities, *International Journal for Numerical Methods in Engineering* 79 11 (2009) 1309–1331. doi: 10.1002/nme.2579.

[84] Open Cascade SAS, (2020), Salome Platform Documentation. https://docs.salome-platform.org/7/gui/SMESH/index.html. [Accessed: 22 Nov. 2020].

[85] ANSYS Inc., (2017), ANSYS 18.2 release notes. https://storage.ansys.com/doc_assets/ril_docs/RIL_182.pdf. [Accessed: 22 Nov. 2020].

[86] C. White, M. K. Borg, T. J. Scanlon, and J. M. Reese, A DSMC investigation of gas flows in micro-channels with bends, *Computers & Fluids* 71 (2013) 261–271. doi: 10.1016/j.compfluid.2012.10.023.

[87] F. Sharipov, Benchmark problems in rarefied gas dynamics, *Vacuum* 86 11 (2012) 1697–1700. doi: 10.1016/j.vacuum.2012.02.048.

[88] M. A. Gallis and J. R. Torczynski, Steady Isothermal Gas Mass Flow Rate in a Microscale Tube from Continuum to Free-Molecular Conditions, 41st AIAA Fluid Dynamics Conference and Exhibit, 2011, 1–18. doi: 10.2514/6.2011-3994.

[89] T. Ewart, P. Perrier, I. A. Graur, and J. G. Méolans, Mass flow rate measurements in a microchannel, from hydrodynamic to near free molecular regimes, *Journal of Fluid Mechanics* 584 (2007) 337–356. doi: 10.1017/S0022112007006374.

[90] M. Gad-el-Hak, The MEMS Handbook, 2nd ed. CRC Press, 2002, ISBN 978-0849300776.

[91] JT-60SA Research Unit, (2018), JT-60SA Research Plan Version 4.0. http://www.jt60sa.org/b/index_nav_3.htm?n3/operation.htm. [Accessed: 23 Nov. 2020].

[92] Y. Kamada et al., Plasma regimes and research goals of JT-60SA towards ITER and DEMO, *Nuclear Fusion* 51 7 (2011) doi: 10.1088/0029-5515/51/7/073011.

[93] M. J. Assael and S. Mixafendi, The Viscosity of Normal Deuterium in the Limit of Zero Density, *Journal of Physical and Chemical Reference Data* 16 2 (1987) 189–192. doi: 10.1063/1.555778.

[94] R. J. Hawryluk et al., Principal physics developments evaluated in the ITER design review, *Nuclear Fusion* 49 6 (2009) doi: 10.1088/0029-5515/49/6/065012.

[95] H. Schlichting and K. Gersten, Boundary-Layer Theory, 9th ed. Berlin Heidelberg: Springer, 2017, ISBN 978-3662529171.

[96] C. Day et al., Development of a simulation code for ITER vacuum flows, Proceedings 21st IAEA Fusion Energy Conference, 2006, 1–8. https://www-pub.iaea.org/MTCD/Meetings/FEC2006/it_p2-12.pdf.

[97] A. Kallenbach, R. Dux, J. Gafert, and G. Haas, Edge transport and its interconnection with main chamber recycling in ASDEX Upgrade, *Nuclear Fusion* 43 7 (2003) 573–578. doi: 10.1088/0029-5515/43/7/310.

[98] K. McCormick, R. Dux, R. Fischer, and A. Scarabosio, Main chamber high recycling on ASDEX upgrade, *Journal of Nuclear Materials* 390–391 (2009) 465–469. doi: 10.1016/j.jnucmat.2009.01.145.

[99] A. S. Kukushkin and H. D. Pacher, Neutral recirculation—the key to control of divertor operation, *Nuclear Fusion* 56 12 (2016) doi: 10.1088/0029-5515/56/12/126012.

[100] C. White et al., dsmcFoam+: An OpenFOAM based direct simulation Monte Carlo solver, *Computer Physics Communications* 224 October (2018) 22–43. doi: 10.1016/j.cpc.2017.09.030.

[101] A. Muis and J. R. Manson, Calculations of the energy accommodation coefficient using classical scattering theory, *Surface Science* 486 1–2 (2001) 82–94. doi: 10.1016/S0039-6028(01)01034-2.

[102] S. Varoutis et al., Simulation of neutral gas flow in the JET sub-divertor, *Fusion Engineering and Design* 121 (2017) 13–21. doi: https://doi.org/10.1016/j.fusengdes.2017.05.108.

[103] T. J. Scanlon et al., Open-Source Direct Simulation Monte Carlo Chemistry Modeling for Hypersonic Flows, *AIAA Journal* 53 6 (2015) 1670–1680. doi: 10.2514/1.J053370.

[104] F. Bonelli et al., Self-consistent coupling of DSMC method and SOLPS code for modeling tokamak particle exhaust, *Nuclear Fusion* 57 6 (2017) doi: 10.1088/1741-4326/aa686f.

[105] A. L. Garcia, J. B. Bell, W. Y. Crutchfield, and B. J. Alder, Adaptive Mesh and Algorithm Refinement Using Direct Simulation Monte Carlo, *Journal of Computational Physics* 155 1 (1999) 134–155. doi: 10.1006/jcph.1999.6305.

[106] D. Neuwirth, V. Rohde, and T. Schwarz-Selinger, Formation of ammonia during nitrogen-seeded discharges at ASDEX Upgrade, *Plasma Physics and Controlled Fusion* 54 8 (2012) 085008. doi: 10.1088/0741-3335/54/8/085008.

[107] B. Streibl et al., Chapter 2: Machine Design, Fueling, and Heating in ASDEX Upgrade, *Fusion Science and Technology* 44 3 (2003) 578–592. doi: https://doi.org/10.13182/FST03-A400.

[108] V. Rohde et al., Dynamic and static deuterium inventory in ASDEX Upgrade with tungsten first wall, *Nuclear Fusion* 49 8 (2009) doi: 10.1088/0029-5515/49/8/085031.

[109] A. Herrmann et al., Design and concept validation of the new solid tungsten divertor for ASDEX Upgrade, *Fusion Engineering and Design* 88 6–8 (2013) 577–580. doi: 10.1016/j.fusengdes.2013.03.007.

[110] A. Herrmann et al., Solid tungsten Divertor-III for ASDEX Upgrade and contributions to ITER, *Nuclear Fusion* 55 6 (2015) doi: 10.1088/0029-5515/55/6/063015.

[111] H. S. Bosch et al., Particle exhaust studies in ASDEX Upgrade, *Plasma Physics and Controlled Fusion* 39 11 (1997) 1771–1792. doi: 10.1088/0741-3335/39/11/002.

[112] ASDEX Upgrade Team, (2016), ASDEX Upgrade TPS Website. ASDEX Upgrade Database. [Accessed: 01 Sep. 2016].

[113] G. Haas et al., Pressure Gauges and Neutral Pressure Measurement in ITER, Diagnositics for Experimental Thermonuclear Fusion Reactors 2, P. E. Stott, G. Gorini, P. Prandoni, and E. Sindoni, Eds. Boston: Springer, 1998, 559–568.

[114] A. Scarabosio and G. Haas, Behaviour of the ASDEX pressure gauge at high neutral gas pressure and applications for ITER, *AIP Conference Proceedings* 988 2008 (2008) 238–242. doi: 10.1063/1.2905075.

[115] H.-S. Bosch, G. Haas, and M. Lörcher, Helium and hydrogen atom detection in the recycling gas using optical measurements on an ASDEX pressure gauge, *Journal of Nuclear Materials* 196–198 (1992) 1074–1077. doi: 10.1016/S0022-3115(06)80198-4.

[116] F. Reimold et al., Divertor studies in nitrogen induced completely detached H-modes in full tungsten ASDEX Upgrade, *Nuclear Fusion* 55 3 (2015) doi: 10.1088/0029-5515/55/3/033004.

[117] S. Potzel et al., Electron density measurements in detached divertor plasmas of ASDEX Upgrade via Stark broadening of the Balmer lines, *Plasma Physics and Controlled Fusion* 56 2 (2011) doi: 10.1088/0741-3335/56/2/025010.

[118] S. Potzel, Experimental classification of divertor detachment, Ph.D. dissertation, University of Bayreuth, 2012 https://epub.uni-bayreuth.de/210/.

[119] S. Potzel et al., Formation of the high density front in the inner far SOL at ASDEX Upgrade and JET, *Journal of Nuclear Materials* 463 (2015) 541–545. doi: 10.1016/j.jnucmat.2014.12.008.

8 Appendix

Appendix A Survey of gas kinetic theory

Consider a system consisting of neutral gas with different species. In the kinetic approach, all the necessary information is contained in the so-called distribution function $f_\alpha(\mathbf{r}, \mathbf{v}, t)$ of neutrals ($\alpha = 1,2, \ldots, n$) where

$$f_\alpha(\mathbf{r}, \mathbf{v}, t)\, d^3r d^3v = \text{number of particles in } d^3r d^3v \text{ at time } t \tag{A.1}$$

The goal of this survey is to find the expression that describes dynamics of the particles and the rationale of its construction.

First, since the distribution function depends on the spatial coordinates, velocity and time, the total change in time of the distribution function of a particle of type α reads:

$$\begin{aligned} \frac{df_\alpha}{dt} &= \frac{\partial f_\alpha}{\partial t} + \frac{\partial f_\alpha}{\partial \mathbf{r}} \frac{\mathrm{d}\mathbf{r}}{dt} + \frac{\partial f_\alpha}{\partial \mathbf{v}} \frac{\mathrm{d}\mathbf{v}}{dt} \\ &= \frac{\partial f_\alpha}{\partial t} + \mathbf{v} \cdot \nabla f_\alpha + \left(\frac{1}{m_\alpha} \sum \mathbf{F} \right) \cdot \nabla_{\mathbf{v}} f_\alpha . \end{aligned} \tag{A.2}$$

The change of the vector position **r** respect to time is the velocity **v** and the acceleration in the third term is replaced by the sum of all forces acting on the particle α of interest using the equation of motion of Newtons law. The following notation is also employed for the spatial derivative $\partial/\partial\mathbf{r} \equiv \nabla = (\partial/\partial x, \partial/\partial y, \partial/\partial z)$, which acts in the real space (x, y, z), whereas the velocity derivate $\partial/\partial\mathbf{v} \equiv \nabla_{\mathbf{v}} = \left(\partial/\partial \mathrm{v}_x, \partial/\partial \mathrm{v}_y, \partial/\partial \mathrm{v}_z\right)$ operates in the velocity space (v_x, v_y, v_z).

The time evolution of the distribution function of a single particle is also affected by the collisions occurring in the volume d^3r of the particle α with other partiles in the system and thus Eq. (A.2) reads:

$$\frac{\partial f_\alpha}{\partial t} + \mathbf{v} \cdot \nabla f_\alpha + \left(\frac{1}{m_\alpha} \sum \mathbf{F} \right) \cdot \nabla_{\mathbf{v}} f_\alpha = \left(\frac{\partial f_\alpha}{\partial t} \right)_{coll} . \tag{A.3}$$

The term on the right-hand side of the equation is called the collision term or operator and has two main contributions, the *gain* term, which corresponds to the particles that enter the volume element d^3r after a collision and the *loss* term describing the particles that are scattered away from the same 3-dimensional volume:

$$\left(\frac{\partial f_\alpha}{\partial t}\right)_{coll} = \left(\frac{\partial f_\alpha}{\partial t}\right)_{gain} - \left(\frac{\partial f_\alpha}{\partial t}\right)_{loss}, \tag{A.4}$$

Before introducing the gain and loss terms, a few useful results are presented. First, the integration of Eq. (A.1) over the velocity leads us to the following result:

$$n_\alpha(\mathbf{r},t) \equiv \iiint_v f_\alpha(\mathbf{r},\mathbf{v},t)\, d^3v, \tag{A.5}$$

which tells us the number of particles of specie α per unit volume.

By multiplying the distribution function with the velocity **v** of a particle, one obtains the average velocity of particle α

$$\mathbf{V}_\alpha = \langle \mathbf{v}_\alpha(\mathbf{r},t) \rangle = \iiint_v \mathbf{v}\, f_\alpha(\mathbf{r},\mathbf{v},t)\, d^3v. \tag{A.6}$$

Regarding the gain and loss terms:

- The collision takes place between particle α and particle *i*.
- Particle α changes its velocity after collision from **v** to $\mathbf{v}'$
- Particle *i* changes its velocity from $\mathbf{v_i}$ to $\mathbf{v_i}'$
- Assume that the initial velocities of both particles are uncorrelated before they encounter each other:

$$f_\alpha(\mathbf{r},\mathbf{v},t)\, d^3v\, f(\mathbf{r},\mathbf{v_i},t)\, d^3v_i. \tag{A.7}$$

- The scattering process is described by the product of the cross-section and the corresponding change of velocity d^3v: $\sigma'(v, v_i \to v', v_i) d^3v d^3v_i'$
- The total contribution after collision is obtained by looking at the product of the above scattering probability with the relative flux of particle α, i.e. $|v - v_i| f(r,v,t) d^3v$ and the particle-*i* that produce that scattering $f(r, v_i, t) d^3r d^3v_i$
- At the end, one needs to sum over all possible initial velocities v_i of particle-*i* which particle α can collide and also an additional sum over all possible final velocities $\mathbf{v}'$ and $\mathbf{v_i}'$, which yields to:

$$\left(\frac{\partial f_\alpha}{\partial t}\right)_{gain} = \tag{A.8}$$

$$\iiint_{v_i'}\iiint_{v'}\iiint_{v_i}\left[|\mathbf{v}-\mathbf{v}_i| f_\alpha(\mathbf{r},\mathbf{v},t)d^3v\right]\left[f_i(\mathbf{r},\mathbf{v}_i,t)d^3rd^3v\right]\times \left[\sigma'(\mathbf{v},\mathbf{v}_i\rightarrow\mathbf{v}',\mathbf{v}_i')d^3v'd^3v_i'\right].$$

- For the loss term, one uses the concept of inverse collisions resulting from the invariance of the equation of motion under the transformations $t \rightarrow -t$ and $r \rightarrow -r$, thus one has:
  - Now the particle α is approaching the particle *i*.
  - The initial and final states are exchanged, which means that the particles collide initially with $\mathbf{v}'$ and $\mathbf{v_i}'$ and emerge from the collision with velocities $\mathbf{v}$ and $\mathbf{v_i}$.
  - Repeat procedure as before with the cross-section and the product with the relative flux.
  - After summing over all initial velocities previous to the collision and the sum over all possible post-collision velocities

$$\left(\frac{\partial f_\alpha}{\partial t}\right)_{loss} = \tag{A.9}$$

$$\iiint_{v_i}\iiint_{v_i'}\iiint_{v'}\left[|\mathbf{v}'-\mathbf{v}_i'| f_\alpha(\mathbf{r},\mathbf{v}',t)d^3v'\right]\left[f_i(\mathbf{r},\mathbf{v}_i',t)d^3rd^3v_i'\right]\times \left[\sigma'(\mathbf{v}',\mathbf{v}_i'\rightarrow\mathbf{v},\mathbf{v}_i)d^3vd^3v_i\right].$$

By substracting Eq (A.9) from Eq. (A.8), introducing the inverse collision concept in the loss term as $\sigma'(\mathbf{v}',\mathbf{v_i}' \rightarrow \mathbf{v},\mathbf{v_i}) = \sigma'(\mathbf{v},\mathbf{v_i}\rightarrow\mathbf{v}',\mathbf{v_i}')$, defining $\mathbf{v_{rel}} = \mathbf{v}-\mathbf{v_i}$ and $\mathbf{v_{rel}}' = \mathbf{v}'-\mathbf{v_i}'$, it is obtained

$$\left(\frac{\partial f_\alpha}{\partial t}\right)_{coll} = \iiint_{v_i'}\iiint_{v'}\iiint_{v_i}\left[f_\alpha' f_i' - f_\alpha f_i\right]|\mathbf{v}_{rel}|\sigma'(\mathbf{v},\mathbf{v}_i\rightarrow\mathbf{v}',\mathbf{v}_i')d^3v_id^3v'd^3v_i', \tag{A.10}$$

where the terms inside the square brackets are defined as

$$
\begin{aligned}
f_\alpha &\equiv f_\alpha(\mathbf{r},\mathbf{v},t) \\
f_i &\equiv f_i(\mathbf{r},\mathbf{v_i},t) \\
f_\alpha' &\equiv f_\alpha(\mathbf{r},\mathbf{v}',t) \\
f_i' &\equiv f_i(\mathbf{r},\mathbf{v_i}',t),
\end{aligned}
\tag{A.11}
$$

i.e. pre- and post-collision distribution functions of particles of type α and type *i*.

The Boltzmann equation can be written as

$$
\frac{\partial f_\alpha}{\partial t} + \mathbf{v}\cdot\nabla f_\alpha + \left(\frac{1}{m_\alpha}\sum \mathbf{F}\right)\cdot\nabla_{\mathbf{v}} f_\alpha = \left(\frac{\partial f_\alpha}{\partial t}\right)_{coll}
\tag{A.1}
$$

$$
= \iiint_{v_i'}\iiint_{v'}\iiint_{v_i}\left[f_\alpha' f_i' - f_\alpha f_i\right]\times
$$

$$
\left|\mathbf{v}_{rel}\right|\sigma'\left(\mathbf{v},\mathbf{v}_i \to \mathbf{v}',\mathbf{v}_i'\right) d^3v_i d^3v' d^3v_i'.
$$

Appendix B Maxwellian distribution

Here the deduction of the mean, most probable and root mean squared (rms) velocity of a particle in equilibrium is presented. The mean value of a variable or observable *A*, reads to:

$$
\begin{aligned}
\left\langle A(\mathbf{r},t)\right\rangle &= C\iiint_{v} A\, f_{eq}(\mathbf{r},\mathbf{v},t)\, d^3v, \\
&= \left(\frac{m\beta}{2\pi}\right)^{3/2}\int_0^\infty v^2 dv \int_0^\pi \sin\theta d\theta \int_0^{2\pi} d\varphi A\, e^{-\beta\frac{mv^2}{2}}.
\end{aligned}
\tag{B.1}
$$

Here, f_{eq} is the Maxwell-Boltzmann distribution function and *C* the normalization constant. Also, it has been introduced the variable $\beta = 1/k_B T$. The mean velocity of a particle is then obtained by substituting in the above equation the velocity *v* instead of *A*, yielding:

$$\begin{aligned}\langle v\rangle &= \left(\frac{m\beta}{2\pi}\right)^{3/2}\int_0^{\infty} v^2 dv \int_0^{\pi}\sin\theta d\theta \int_0^{2\pi} d\varphi v\, e^{-\beta\frac{mv^2}{2}}, \\ &= 4\pi\left(\frac{m\beta}{2\pi}\right)^{3/2}\int_0^{\infty} v^3 e^{-\beta\frac{mv^2}{2}} dv = 4\pi\left(\frac{m\beta}{2\pi}\right)^{3/2}\int_0^{\infty} v\left(-\frac{2}{m}\right)\frac{\partial}{\partial\beta}\left(e^{-\beta\frac{mv^2}{2}}\right) dv, \\ &= 4\pi\left(\frac{m\beta}{2\pi}\right)^{3/2}\left(-\frac{2}{m}\right)\frac{\partial}{\partial\beta}\int_0^{\infty} v e^{-\beta\frac{mv^2}{2}} dv, \\ &= \left(-\frac{8\pi}{m}\right)\left(\frac{m\beta}{2\pi}\right)^{3/2}\frac{\partial}{\partial\beta}\int_0^{\infty} v e^{-\beta\frac{mv^2}{2}} dv.\end{aligned} \tag{B.2}$$

By introducing the variable $x = \beta\, mv^2/2$ and its differential $dx = \beta mv\, dv$, the mean velocity is obtained:

$$\begin{aligned}\langle v\rangle &= \left(-\frac{8\pi}{m}\right)\left(\frac{m\beta}{2\pi}\right)^{3/2}\frac{\partial}{\partial\beta}\int_0^{\infty}\frac{e^{-x}}{\beta m} dx, \\ &= \left(-\frac{8\pi}{m}\right)\left(\frac{m\beta}{2\pi}\right)^{3/2}\frac{\partial}{\partial\beta}\left[\frac{1}{\beta m}\left(-e^{-x}\right)\Big|_0^{\infty}\right] = \left(-\frac{8\pi}{m^2}\right)\left(\frac{m\beta}{2\pi}\right)^{3/2}\frac{\partial}{\partial\beta}\left[\frac{1}{\beta}\right], \\ &= \left(-\frac{8\pi}{m^2}\right)\left(\frac{m\beta}{2\pi}\right)^{3/2}\left[-\frac{1}{\beta^2}\right] = \frac{2^{3/2}}{m^{1/2}\beta^{1/2}\pi^{1/2}}, \\ &= \sqrt{\frac{8}{\pi m\beta}} = \sqrt{\frac{8k_B T}{\pi m}}.\end{aligned} \tag{B.3}$$

The most probable velocity is defined as the maximum of the probability density function (Maxwell-Boltzmann):

$$\begin{aligned}v_{mp} &= \frac{\partial}{\partial v}\left[\left(\frac{m\beta}{2\pi}\right)^{3/2} v^2 e^{-\beta\frac{mv^2}{2}}\right] = 0, \\ &= \left[2ve^{-\beta\frac{mv^2}{2}} + v^2\left(-\beta mv\right)e^{-\beta\frac{mv^2}{2}}\right] = 0,\end{aligned} \tag{B.4}$$

by rearranging the terms inside the bracket, the expression reads,

$$v_{mp} = 2ve^{-\beta\frac{mv^2}{2}}\left[1-\frac{\beta mv^2}{2}\right]=0, \tag{B.5}$$

$$\Rightarrow$$

$$v_{mp} = \sqrt{\frac{2}{m\beta}} = \sqrt{\frac{2k_BT}{m}}.$$

The root mean square expression of the velocity is found by calculating:

$$v_{rms} = \sqrt{\langle v^2 \rangle} = \sqrt{\left(\frac{m\beta}{2\pi}\right)^{3/2}\int_0^\infty v^2 dv \int_0^\pi \sin\theta d\theta \int_0^{2\pi} d\varphi v^2 e^{-\beta\frac{mv^2}{2}}}, \tag{B.6}$$

$$= \left[4\pi\left(\frac{m\beta}{2\pi}\right)^{3/2}\int_0^\infty v^4 e^{-\beta\frac{mv^2}{2}}dv\right]^{1/2} = \left[4\pi\left(\frac{m\beta}{2\pi}\right)^{3/2}\int_0^\infty\left(-\frac{2}{m}\right)\frac{\partial}{\partial\beta}\left(v^2e^{-\beta\frac{mv^2}{2}}\right)dv\right]^{1/2},$$

$$= \left[4\pi\left(\frac{m\beta}{2\pi}\right)^{3/2}\left(-\frac{2}{m}\right)\frac{\partial}{\partial\beta}\int_0^\infty\left(-\frac{2}{m}\right)\frac{\partial}{\partial\beta}\left(e^{-\beta\frac{mv^2}{2}}\right)dv\right]^{1/2},$$

$$= \left[4\pi\left(\frac{m\beta}{2\pi}\right)^{3/2}\left(-\frac{2}{m}\right)\frac{\partial}{\partial\beta}\int_0^\infty v^2e^{-\beta\frac{mv^2}{2}}dv\right]^{1/2},$$

$$= \left[4\pi\left(\frac{m\beta}{2\pi}\right)^{3/2}\left(\frac{4}{m^2}\right)\frac{\partial^2}{\partial\beta^2}\int_0^\infty e^{-\beta\frac{mv^2}{2}}dv\right]^{1/2}.$$

The integral can be obtained by recalling that

$$I(x) = \int_0^\infty e^{-ax^2}dx = \frac{1}{2}\sqrt{\frac{\pi}{a}}\,. \tag{B.7}$$

Therefore,

$$
\begin{aligned}
v_{rms} &= \left[4\pi \left(\frac{m\beta}{2\pi} \right)^{3/2} \left(\frac{4}{m^2} \right) \frac{\partial^2}{\partial \beta^2} \frac{1}{2} \sqrt{\frac{\pi}{\beta \frac{m}{2}}} \right]^{1/2}, \\
&= \left[4\pi \left(\frac{m\beta}{2\pi} \right)^{3/2} \left(\frac{4}{m^2} \right) \frac{1}{2} \frac{\sqrt{2\pi}}{\sqrt{m}} \frac{\partial^2}{\partial \beta^2} \left(\frac{1}{\sqrt{\beta}} \right) \right]^{1/2}, \\
&= \left[m^{3/2} \beta^{3/2} \left(\frac{4}{m^{5/2}} \right) \frac{\partial}{\partial \beta} \left(-\frac{1}{2} \right) \beta^{-3/2} \right]^{1/2}, \\
&= \left[\beta^{3/2} \left(\frac{4}{m} \right) \left(-\frac{1}{2} \right) \left(-\frac{3}{2} \right) \beta^{-5/2} \right]^{1/2}, \\
&= \left[3 \left(\frac{1}{m} \right) \left(\frac{1}{\beta} \right) \right]^{1/2}, \\
&\Rightarrow \\
v_{rms} &= \sqrt{\frac{3}{m\beta}} = \sqrt{\frac{3k_B T}{m}}.
\end{aligned}
\tag{B.8}
$$

Appendix C NEUT2D and DSMC node sub-indexing

This appendix presents additional material regarding the benchmark between NEUT2D and *dsmcFoam*. In chapter 5.1.2 the velocity profiles in region II have been presented, where only sampled points of region below the JT-60SA divertor dome (near Gate 1 at the low-field side) were shown. In this section, the velocity profiles across the domain are reported. At the beginning of chapter 5.1.2 four regions of the sub-divertor domain of JT-60SA are defined, where a sub-indexing is established in order to ease the comparison between both codes.

The following dummy variables, which are employed during post-processing, are here recalled: (i, j) in region I, region II (k, l), region III (q, r) and finally in region IV (k, l). Only the regions and their corresponding sub-indexes, which have not been presented in chapter 5.1.2, are here shown. Region I is defined along the domain at the high-field side of the sub-divertor where Gate 2 is located, see Figure 8.1(a) and (b). In Figure 8.2 the node indexing of region II is presented.

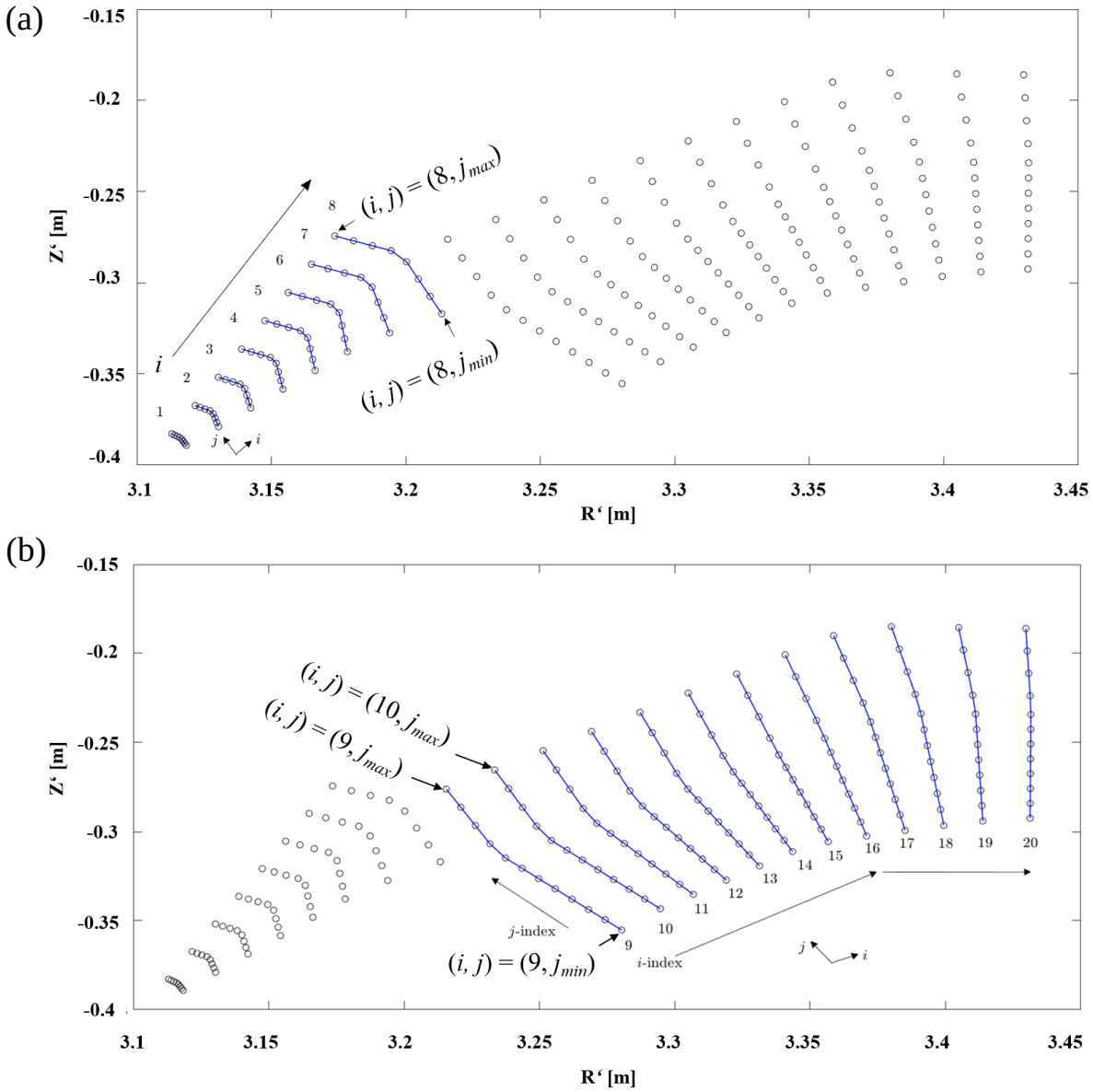

Figure 8.1 (a) and (b): Region I of the sub-divertor JT-60SA. Here the nodes are given a sub-indexing (*i*, *j*). The sub-index *i* can take values from 1 to 20, whereas the *j*-index takes the values between 1 and 10.

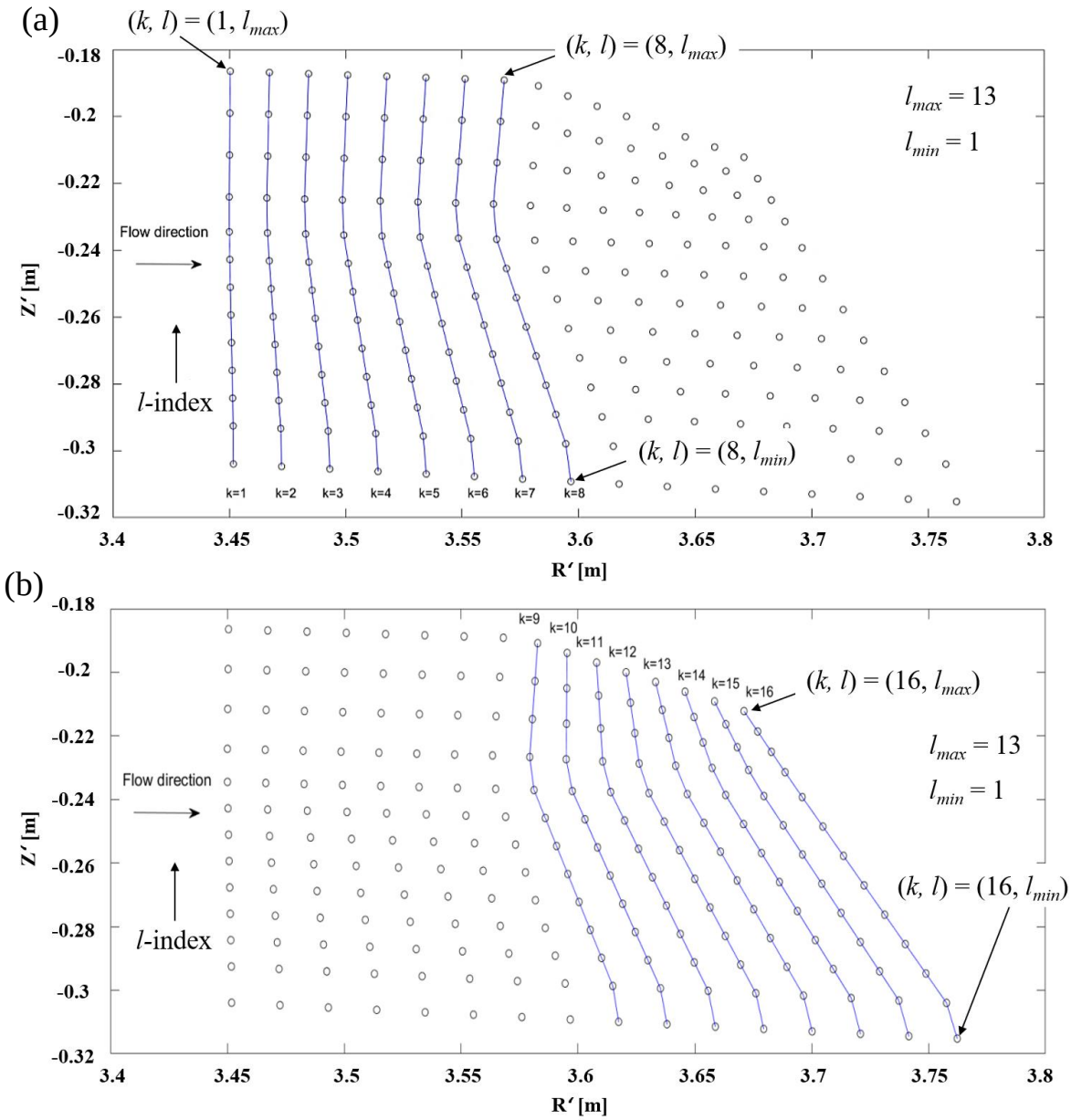

Figure 8.2 Region II of the sub-divertor JT-60SA. Here the nodes are given a sub-indexing (*k*, *l*). (a) For the first part of the domain, the sub-index *k* takes the values from 1 to 8, whereas in (b) the *k* takes the values from 9 to 16. In region II the *l*-index takes the values between 1 and 13.

Complementary results of the benchmark between DSMC and NEUT2D

The DSMC simulations show that the gas flow speed in region I (for *i*-index > 9) has a maximum close to *Z'* = -0.3 m with a parabolic-like narrow shape, see top-right and bottom-left plots of Figure 8.3(b). As the gas moves towards region II, the velocity profile flattens out and thus widening its parabolic shape as depicted in the bottom-right plot of Figure 8.3(b).

On the other hand, in region I NEUT2D calculates velocity profiles which are similar to DSMC, i.e. monotonic increase of the velocity until a maximum value is reached. However, systematically DSMC predicts higher values of the flow speed in most of the points in region I. The differences between approaches increases with the *i*-index until the threshold to region II, at this point and across region II both codes predict quantitively the same flow speed. The good agreement can be observed in Figure 8.4 and Figure 8.5, where the flow speed profile is evaluated at each node (*k, l*) at constant *k*-value in region II.

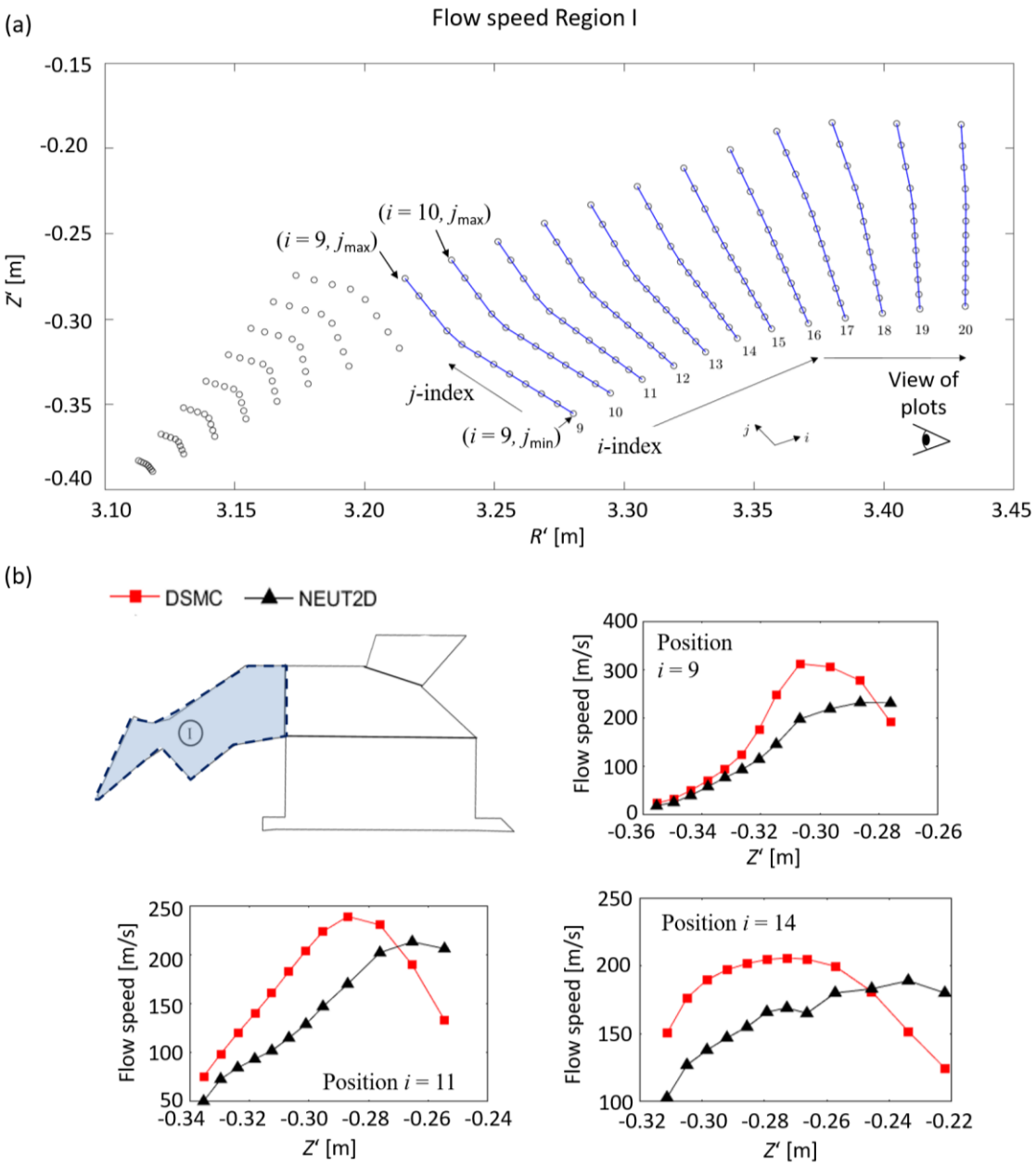

Figure 8.3 Results of the comparison between flow speeds calculated with NEUT2D and DSMC (without collisions). (a) Flow speed profile evaluated at each node (*i*, *j*). (b) Region I of the sub-divertor JT-60SA. Here the nodes are given a sub-indexing (*i*, *j*). The sub-index *i* can take values from 9 to 20, whereas the *j*-index takes the values between 1 and 12.

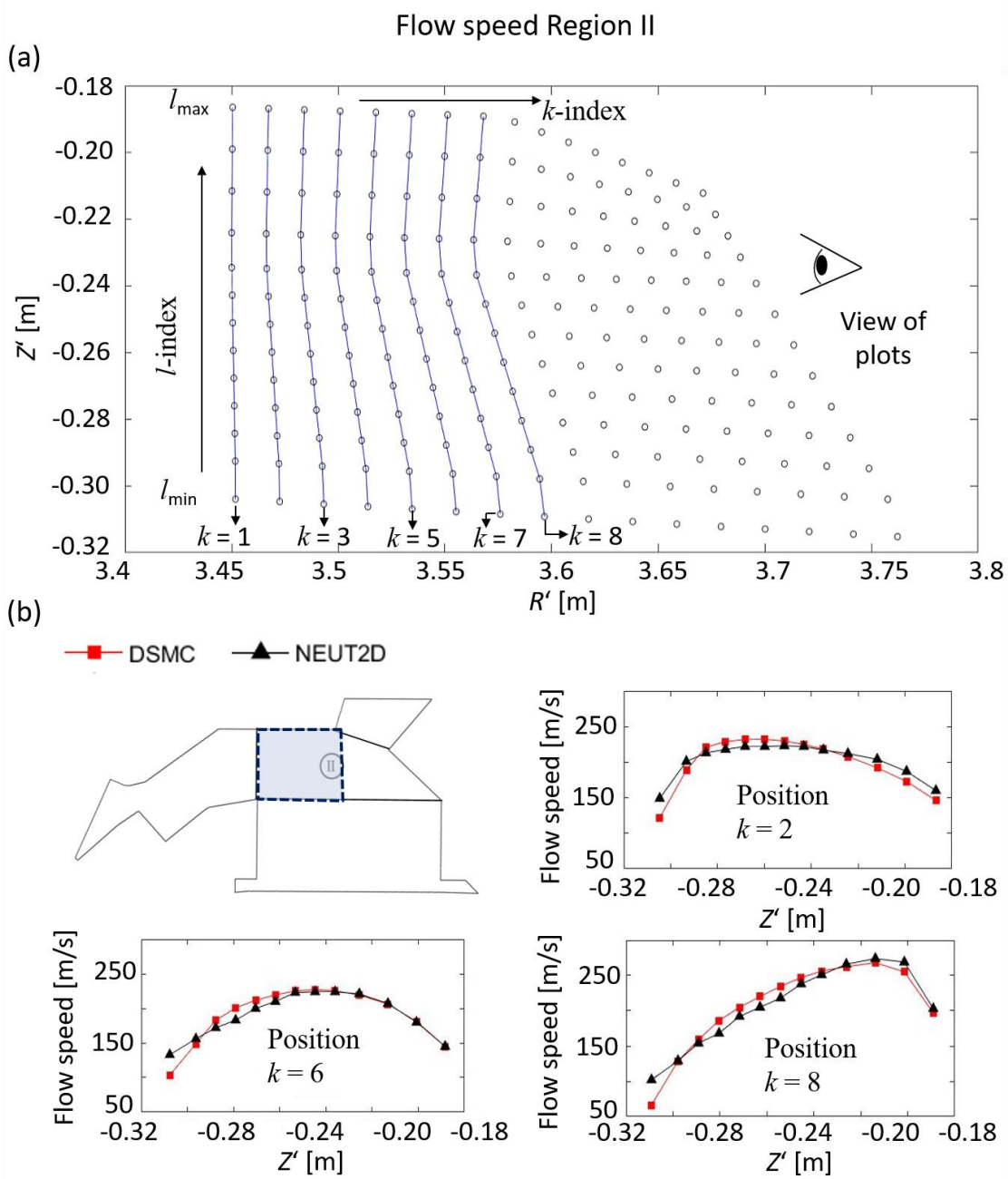

Figure 8.4 Results of the comparison between flow speeds calculated with NEUT2D and DSMC (without collisions). (a) Flow speed profile evaluated at each node (k, l) at constant k-value in region II. (b) Region II of the sub-divertor JT-60SA. Here the nodes are given a sub-indexing (k, l). The sub-index k can take values from 1 to 16, whereas the l-index takes the values between 1 and 13.

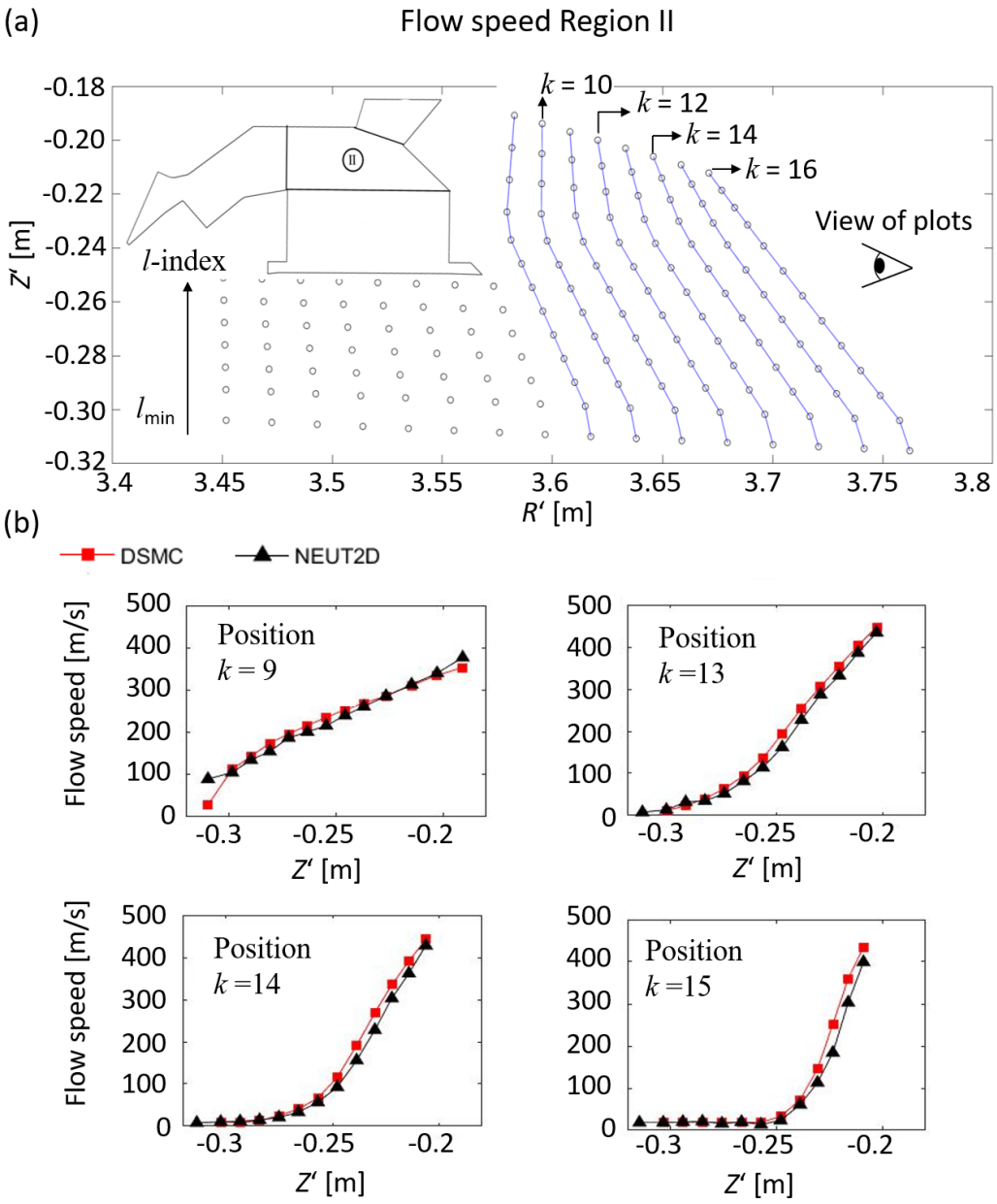

Figure 8.5 Results of the comparison between flow speeds calculated with NEUT2D and DSMC (without collisions). (a) Flow speed profile evaluated at each node (*k*, *l*) at constant *k*-value in region II. (b) Region II of the sub-divertor JT-60SA. Here the nodes are given a sub-indexing (*k*, *l*). The sub-index *k* can take values from 1 to 16, whereas the *l*-index takes the values between 1 and 13. Here the pairs (*k*, *l*) are shown for values of *l* between 9 and 16.

Appendix D ASDEX Upgrade experimental results: different cryopump operational modes

In Figure 8.6 it is shown a poloidal cross section of an AUG section where the port that connects the main vessel with the turbomolecular pumps (TMP) is included. The main operational AUG parameters are also given in Figure 8.6. The machine status here referred is the one of 2015-2016.

ASDEX Upgrade tokamak	
Major radius R	1.65 m
Minor radius a	0.5 m
Plasma volume V_p	14 m^3
Plasma current I_p	0.4-1.6 MA
Ohmic Heating Power	~ 1 MW
NBI Heating Power	20 MW at 60 and 100 keV
ICR Heating Power	6 MW at 30-40 Hz
ECR Heating Power	4 MW @ 105-140 Hz
Pulse length t_l	< 10 s

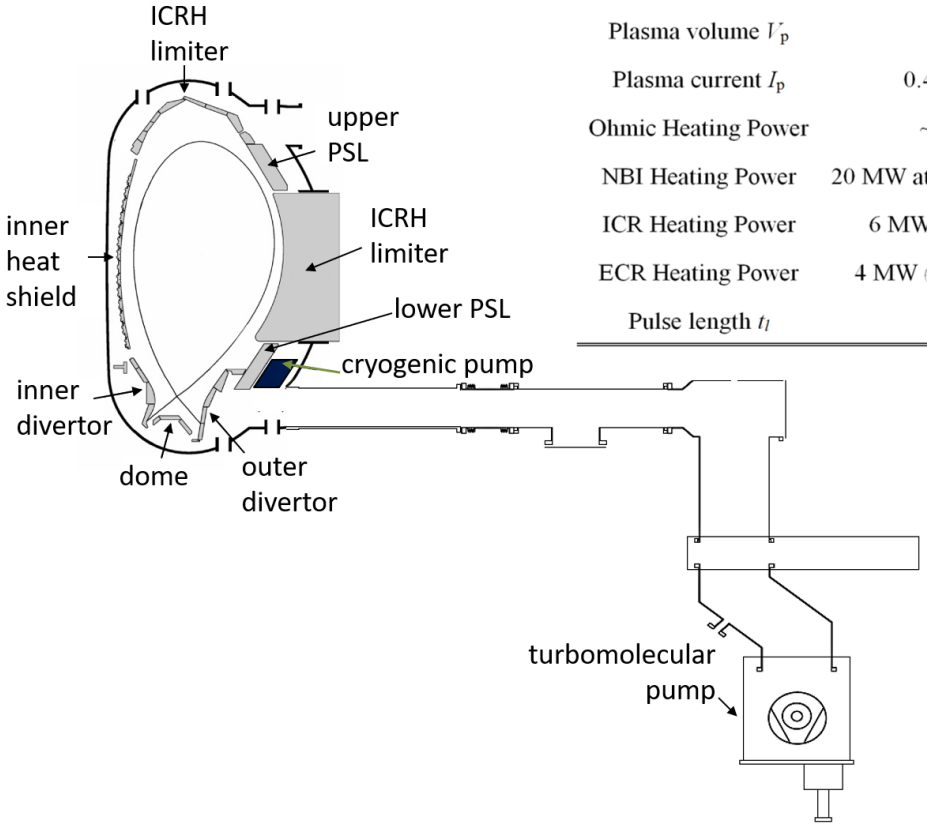

Figure 8.6 Poloidal cross section of the ASDEX-Upgrade tokamak as for the experimental campaign 2014-2016. The vacuum vessel is a torus and extends toroidally into and out of the page. A Single Null (SN) magnetic configuration (X-point at the lower divertor) is shown. Upper and lower passive stability loop (PSL) elements are indicated and serve for MHD control (resistive modes stabilization). The full tungsten divertor and the dome are indicated. The area/volume below the divertor structures will be here referred as sub-divertor. The region near the cryogenic pump (blue rhomboid) is referred as the pumping chamber. Image adapted from [106] and table from [107].

ASDEX Upgrade is a medium size tokamak located at the Max Planck Institute for

Plasma Physics (IPP) in Garching near Munich, Germany. AUG plays a crucial role in understanding plasma and machine performance towards ITER and DEMO devices since AUG has ITER-like machine conditions with a full tungsten wall [108], divertor [109] as well as its unique pumping speed control, heating and fueling systems. The exploitation of these unique characteristics in AUG allow the investigation of relevant questions for future divertor tokamak scenarios with focus in design and optimization [110].

In the following sections an overview is given of the experiments performed in ASDEX Upgrade (AUG) in the framework of the experimental campaign coordinated by the author in 2015. First a description of the vacuum, fueling and heating systems is presented. An introduction to the relevant diagnostics employed in the experimental setup as well as the experimental setup of the plasma discharges and key results are here presented.

ASDEX Upgrade fuelling, heating & pumping systems

For future long-pulse reactor operation the pumping of neutral gas is an essential feature that any fusion device should handle. Additional to the pumping, the fueling and heating systems in AUG provide the necessary gas injection and power to sustain and control tokamak conditions for standard L-mode operation and to achieve the so-called H-mode regime. The latter present better plasma confinement and thus, it is suitable regime for reactor scenarios. Moreover, AUG is equipped with a vast set of diagnostics for further research on edge, SOL, core and divertor physics.

Vacuum and pumping systems. ASDEX Upgrade is equipped with 11 TMPs connected to the divertor chamber nearly equally distributed along the 16 sectors of AUG. Each TMP has a nominal pumping speed of 3.5 m^3s^{-1} [111], however due to the length of the pumping port the effective pumping speed in the vessel can be reduced to 1 m^3s^{-1}. The overall deuterium pumping speed of the TMPs is $S_{\mathrm{TMP}} = 13\ \mathrm{m^3 s^{-1}}$ [107]. In addition to this, a toroidally symmetric cryogenic pump with a total deuterium pumping speed of $S_{\mathrm{cryo}} = 100\ \mathrm{m^3 s^{-1}}$ is placed in the pump chamber below the outer divertor target (below the lower PSL). The functional dependence of the pumping speed of the cryopump and TMPs with the pressure has been determined experimentally and a linear and quadratic dependences have been found, respectively [108]. The outer area of the cryopump, which faces the lower PSL and the ICRH limiter as depicted in Figure 8.6, is cooled with liquid nitrogen and is kept to 80 K through the discharges. A chevron baffle is the permeable part of the cryogenic pump and serves as shielding of the inner part of the pump from high energetic plasma particles. As mentioned before, not only the tokamak pumping refers to a solely technical issue but also links the particle transport in the SOL and divertor plasma. In this framework, ASDEX Upgrade offers the possibility to establish plasma discharges with cryogenic pump under full pumping capabilities, one third or completely switched off cryopump (acting only the 11 TMPs as pumping actuator). For the full and one-third of pumping capabilities the 11 TMPs are always working.

Fuelling and heating systems. Neutral gas fuelling in ASDEX Upgrade is performed via fast-response piezo electric valves. The valves are connected to a gas matrix which allows the injection in different toroidal and poloidal locations as shown in Figure 8.7.

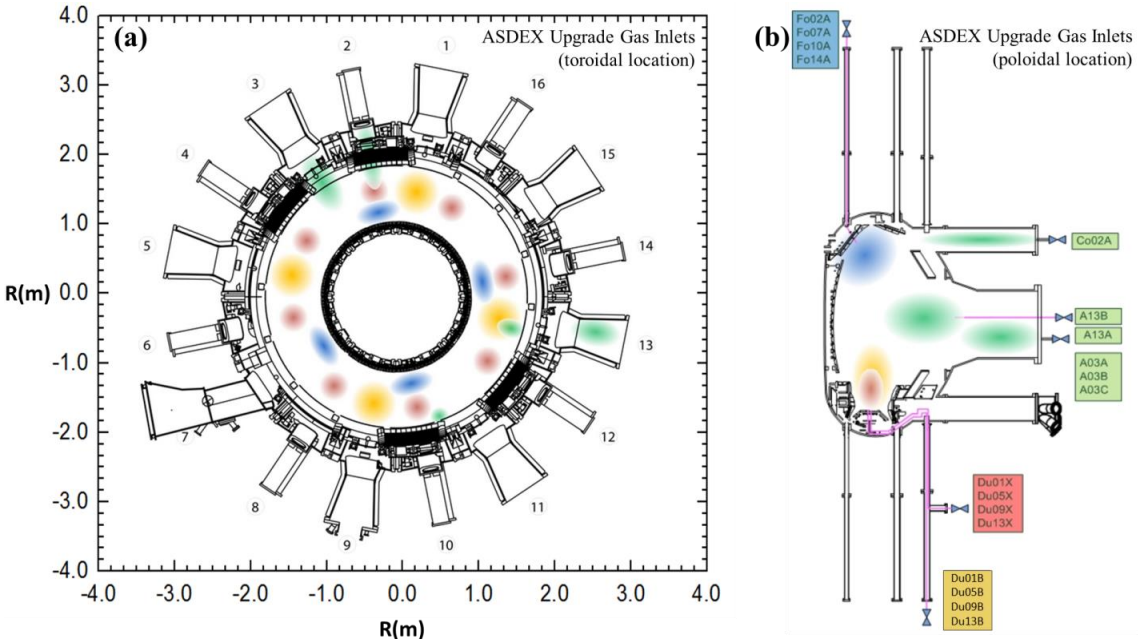

Figure 8.7 Gas inlet system. Fast response system of piezo electric valves located (a) toroidally and (b) poloidally is connected to a gas matrix. Additionally, in (a) the top-down view from AUG with the AUG sector numbers is indicated. In this work, mainly the sub-divertor inlets and the valves at the A port (mid plane) were employed for the gas injection during the plasma discharges. Images adapted from [112].

Different gas circuits in the matrix allow the injection of light and noble gases such as H_2/D_2, He, Ne, N_2 and Kr where the mass flow through the valves is controlled via a feedback-control loop. Figure 8.7(b) shows the different gas valves distributed poloidally in AUG that will be referred later on in this chapter in the experimental setup description. The gas flux can either be programmed in a feed-forward mode with a prescribed wave-form, or can be feedback-controlled on other plasma parameters, i.e. the line averaged density or the divertor neutral gas pressure.

ASDEX Upgrade heating systems include the ohmic and the external heatings: NBI, ICRH and ECRH systems. The ohmic heating is intrinsic in a tokamak due to the plasma current whereas the latter systems provide energy power to the plasma externally. For instance, a total of eight sources (each with a power of 2.5 MW at 95 kV[1]) make the NBI system. The sources are assembled in two boxes which are located diametrically opposite (mid-plane in sectors 7 and 15, see Figure 8.7(a) and Figure 8.8. Furthermore,

[1] This number corresponds to the acceleration voltage in the NBI. The voltage can be varied (reduced) in order to achieve different power.

in order to specifically provide energy to the ions and electrons, ICR and ECR heating systems are also available in AUG. The ICRH antennas shown in Figure 8.8 are available with a total power up to 6 MW with a wave frequency in the resonant range for $\omega_{c,i}$ = 30–40 MHz. Last but not least, eight gyrotrons make up the ECRH system in AUG and they deposit their power (ca. 500 kW each) to the electrons in the plasma by coupling the emitted microwave of the gyrotron with the electrons at a frequency of 140 GHz or 105 GHz.

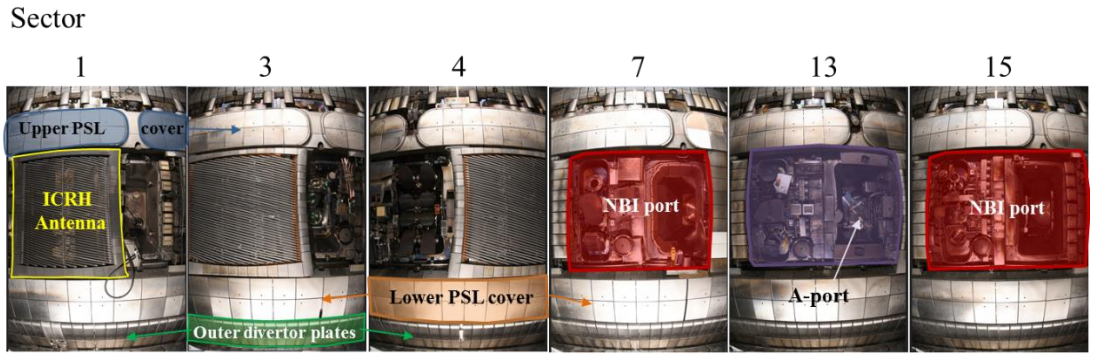

Figure 8.8 ASDEX Upgrade external heating systems: Neutral Beam Injection (NBI; NBI-port shown in red), ion cyclotron resonant heating (ICRH; antenna is shown in yellow) and electron cyclotron resonant heating (ECRH). Additionally, the outer divertor plates (green), upper and lower PSL covers (blue & orange) and the A-port are indicated. The importance of the A-port relies on the gas injection at the mid-plane during discharges.

ASDEX Upgrade diagnostics

The precise characterization of the core and boundary plasma in AUG is the result of huge experimental efforts throughout the machine operation since the past 25 years. Here for modelling purposes, only the most relevant diagnostics employed in the plasma discharges, namely the neutral gas manometer. The divertor spectroscopy diagnostics are also described for completness.

Ionization Gauges. Neutral gas measurements are performed in ASDEX Upgrade by ionization gauges [113], [114] shown in Figure 8.9. The ionization gauges are distributed along the torus in the main chamber, in the sub-divertor region below the dome, upper part of the vessel, behind lower and upper PSL, in the pump chamber as well as in the so-called high field side (HFS) behind the inner divertor plates. Neutral gas flow enters the gauges through an entrance slit, then it is ionized by electron impact and the induced ion current is then measured [115]. From the signals the neutral gas flux is obtained being a measurement absolutely calibrated to atomic deuterium flux.

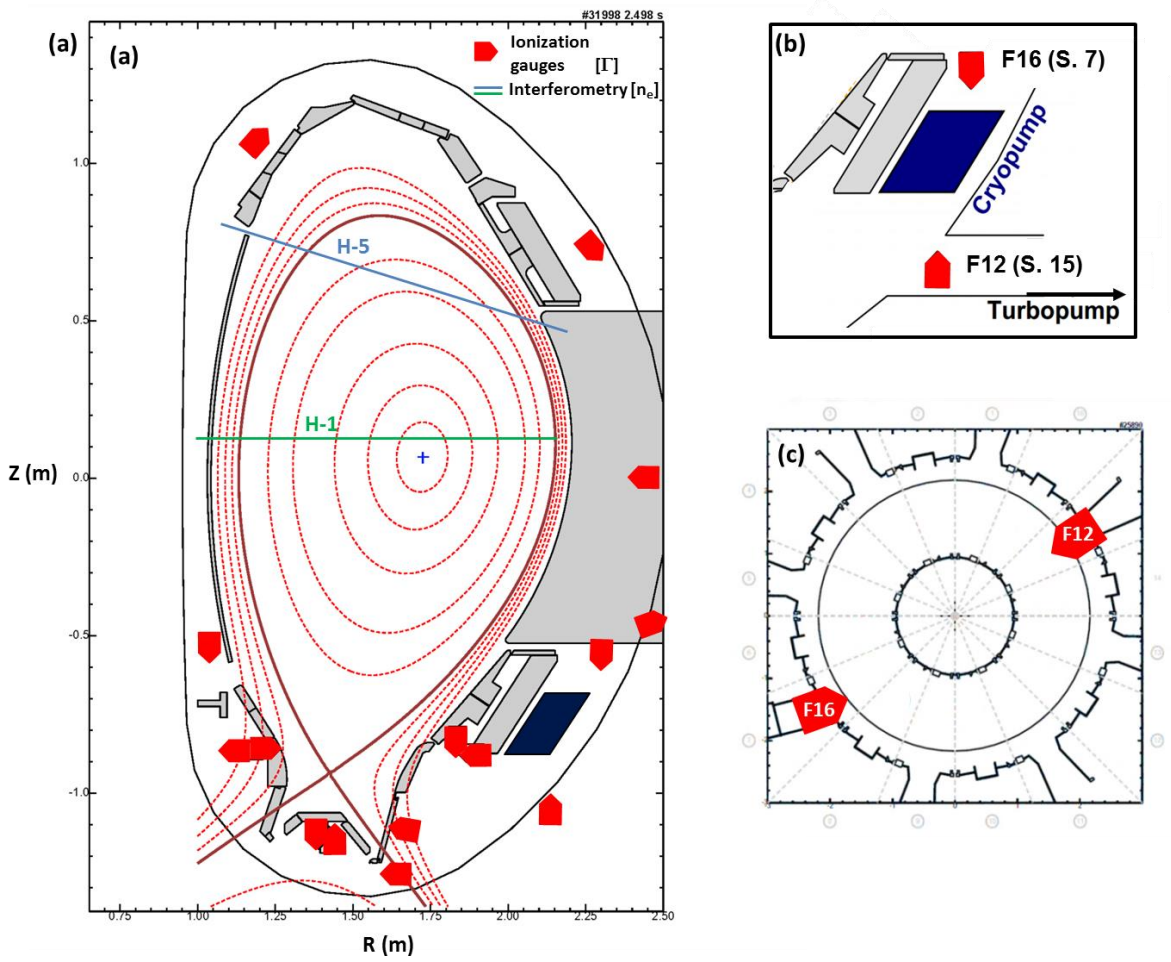

Figure 8.9 Ionization gauges locations in ASDEX Upgrade. (a) Poloidal locations of the gauges (red): The pin of the symbols indicates the orientation of the gauge entrance (pinhole) where the neutral gas flux Γ is able to pass in order to perform the measurement. Additionally, the interferometer chords H-1 and H-5 that measure the integrated line electron density n_e are depicted in green and blue lines, respectively. (b)-(c) Pump chamber ionization gauges located in two opposite locations in the torus. Image in (b) is adapted from [116].

For thermalized deuterium atoms in the sub-divertor region, equilibrium conditions are met and thus equations (3.38) and (3.39) can be utilized in order to relate the particle flux Γ with the neutral density and the average molecular velocity of the gas, i.e. $\Gamma_{D_2} = 0.5\frac{1}{4} n\sqrt{\frac{8k_B T}{\pi m}}$. Here the prefactor 0.5 takes into account the conversion of atomic (calibrated measurement) to molecular flux (main component of the sub-divertor gas specie). Nevertheless, the temperature is not a parameter that is usually known, making a bit problematic the conversion into pressure or density from the value of the particle flux. The ionization gauges have been tested under strong magnetic fields showing good performance up to values of 6 T and pressures below 15 Pa [113], where saturation is reached. In this work, the term manometer, pressure or ionization gauge are used indistinctively, unless otherwise stated.

Divertor spectroscopy. As mentioned before coexistence of neutral particles, ions and electrons in the plasma periphery in a tokamak takes place and via spectroscopic methods relevant quantities of interest of SOL dynamics can be measured. For instance, the Stark Broadening Diagnostic (SBD) can measure the electron density in the divertor volume via the Stark broadening of the Balmer lines [117].

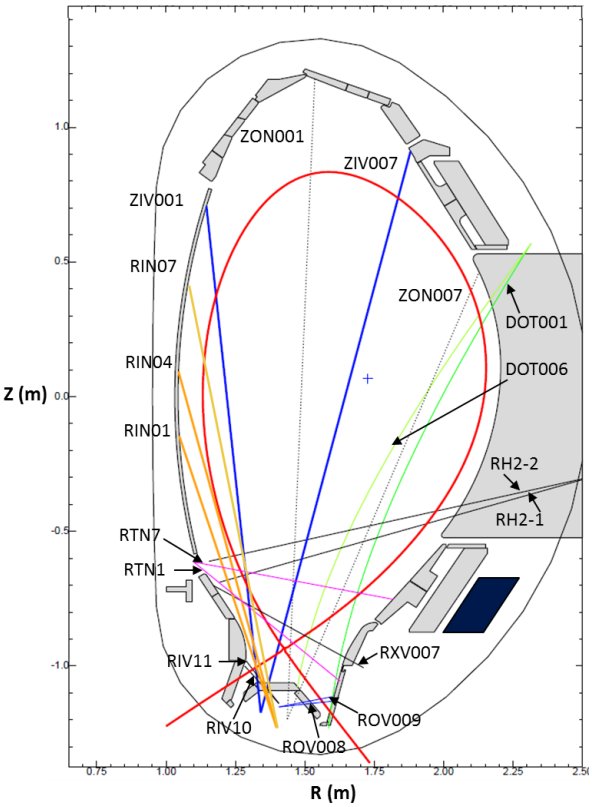

Figure 8.10 Divertor spectroscopy line of sight (LOS) employed in ASDEX Upgrade for the Stark Broadening Diagnostic.

In order to see the splitting of the atomic spectral lines of an atom, under the action of external electric fields, the atom should be first polarized. Then, the interaction of the resulting dipole moment with the external electric field will split the energy levels, this is known as the linear Stark effect. The allowed transitions of energy levels are described by the Balmer line series (mathematical relation between frequencies and main quantum numbers resulting from the solution of the Schrödinger equation) which constrains the frequencies (wavelengths) that can be measured in an spectrometer. However, the Stark effect of an emitter (atom) is also influenced by the surrounding particles (atoms, ions, electrons). The structure of the spectral lines is affected by collisional effects that changes the life-time of transitions and a broadening occurs by the thermal motion of the particles adding a Doppler effect. Thus, the broadening of an spectral line is a consequence of different physical mechanisms and the combination of both leads to the Stark broadening. This has been taken into account in the spectroscopic measurement of the SBD in ASDEX Upgrade. The reader is referred to [118] for a complete description of the diagnostic, theoretical background, development and benchmark with other diagnostics, such as the aforementioned ionization gauges. The different line of sight (SOL) of the spectroscopic measurements are shown in Figure 8.10. The spectral information in the plasma periphery has provided further inside of different plasma states in the so-called attach or detach plasma conditions in various tokamaks like AUG and JET [116], [119].

Experiments on particle exhaust in ASDEX Upgrade

The following results are part of the experimental campaign performed in ASDEX Upgrade (AUG), where the author of this dissertation has actively participated as experiment coordinator. Regarding the experiments in AUG:

- The machine operation during the plasma discharges has been performed by Prof. Dr. Arne Kallenbach. This includes the L- and H-modes with different pumping schemes.
- The vacuum systems operation and wall conditioning have been performed by Dr. Volker Rohde.
- The manometers and spectroscopic measurements have been performed and post-processed before storing them in AUG database by Dr. Andreas Scarabosio and Dr. Stefen Potzel, respectively.

The author of this dissertation has participated directly with the AUG team during the plasma discharge planning including the definition of the pumping schemes. During the experiments and as part of the experiment coordination, the author has accessed the AUG experimental data of the manometers in order to extract the corresponding boundary conditions for the DSMC modelling. The time traces of the plasma discharge are also here shown, since the particle pumping shall be put in context of the main plasma parameters.

Discharges setup

The strategy on defining the present plasma discharges is based on developing a series of simple L- and H-mode scenarios in attached conditions. The parameter in the plasma scenarios is defined via the variable pumping capabilities in ASDEX Upgrade, namely that the cryogenic pumping of the vessel is run in its full, one-third and zero cryogenic pumping speed.

Table 8.1 summarizes the characteristics of the present discharges. All the H-mode discharges are characterized by a single null divertor configuration (SN) with a lower triangularity of $\delta = 0.47$, a plasma current of $I_p = 0.8$ MA and a toroidal magnetic field of $B_t = -2.5$ T set a safety factor at the 95% of the flux surfaces of $q_{95} = 5.18$. A rather big clearance between the plasma and the upper part of the vessel is needed for a X-point displacement. This fact will be used to displace the X-point in order to see an effect on the sub-divertor flows. In all the set of discharges the electron density in the core is maintained to $n_e = 7 \times 10^{19}\,\mathrm{m}^{-3}$ with a total external heating power of 7.6 MW, leading to a Greenwald limit of $n / n_{\mathrm{GW}} \sim 0.6$[2]. The deuterium gas puffing is done via the divertor

[2] Magnetic confinement experiments cannot operate over an arbitrary range of plasma densities. Together with the MHD limitations, by exceeding this limit in tokamaks the discharge can terminate in a disruption. The Greenwald line average density reads $n_{GW} = I_p / \pi a^2$ in units of 10^{20} m^{-3}, the plasma current I_p in MA and the minor radius a in m.

valves DuB (see Fig. 8.11) in order to achieve an homogeneous puffing distribution along the torus flows.

Table 8.1 Shot number parameters corresponding to the series of pumping studies.

Shot #	Behavior	Plasma	Pumping scheme
31991			0
31993	L	D	1/3
31995			full
31992			0
31994	H	D	1/3
31998			full

For steady state conditions, for times $t > 2$ s, the condition where the gas puffed into the chamber equals the pumped-out gas is achieved. In the case of the L-mode series, they were performed in lower SN divertor configuration with a lower triangularity of 0.41, a plasma current of $I_p = 0.8$ MA, a toroidal magnetic field of $B_t = -2.5$ T and a safety factor of $q_{95} = 4.92$. The plasma density and total heating power were $n_e = 5.67 \times 10^{19}\,\mathrm{m}^{-3}$ and 0.569 MW, respectively.

The time traces of the plasma discharge H-mode with full cryogenic pumping are shown in Figure 8.11. The puffing flat top was reached at 1.7 s for the full-cryo case, whereas in the 1/3 and 0-cases the flat top is reached at ~ 2.5 s. This is important in order to determine the values to be use in the DSMC simulations.

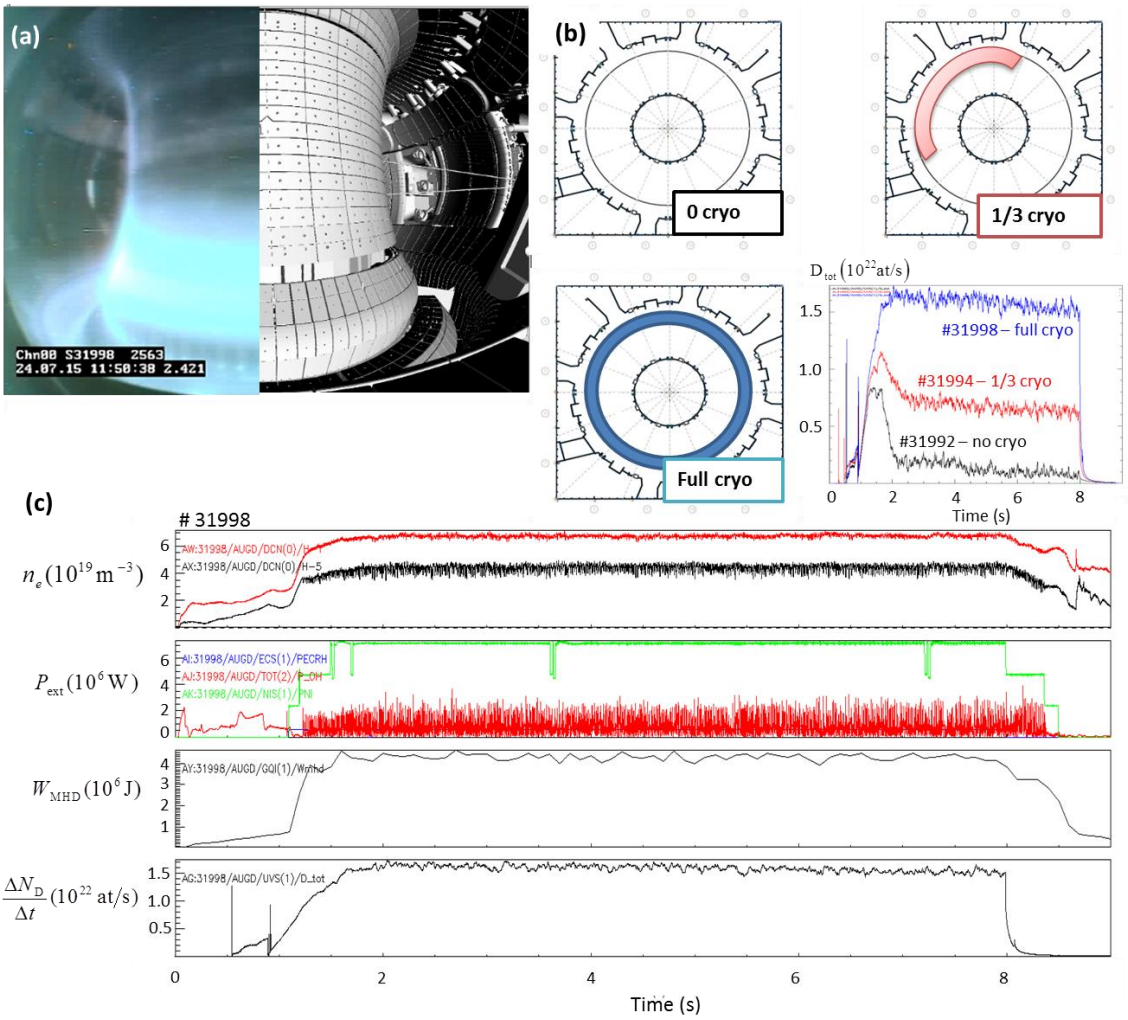

Figure 8.11 Predictive particle exhaust experiments in AUG. (a) Superimposed to the CAD model of AUG vessel a camera image from the discharge 31998 is shown. (b) The pumping setup for the set of H-modes discharges: full-, 1/3- and no-cryopumping is depicted (top-down view). Additionally, the corresponding gas puffing to maintain the same density in the plasma for the H-mode discharges is also presented. (c) Time traces of the H-mode with full cryogenic pumping are shown.

During the flat top phase of the discharges the X-point height was increased by $\Delta z = +1$ cm for $\Delta t = 1$ s from $t_0 = 4$ s to $t_f = 5$ s and then brought the X-point again to its initial position for the rest of the discharge. The change of the vertical position of the X-point can be observed in Figure 8.12. This allowed the measurement of the sub-divertor flow changes behind the targets in the divertor, pump as well as in the main chamber.

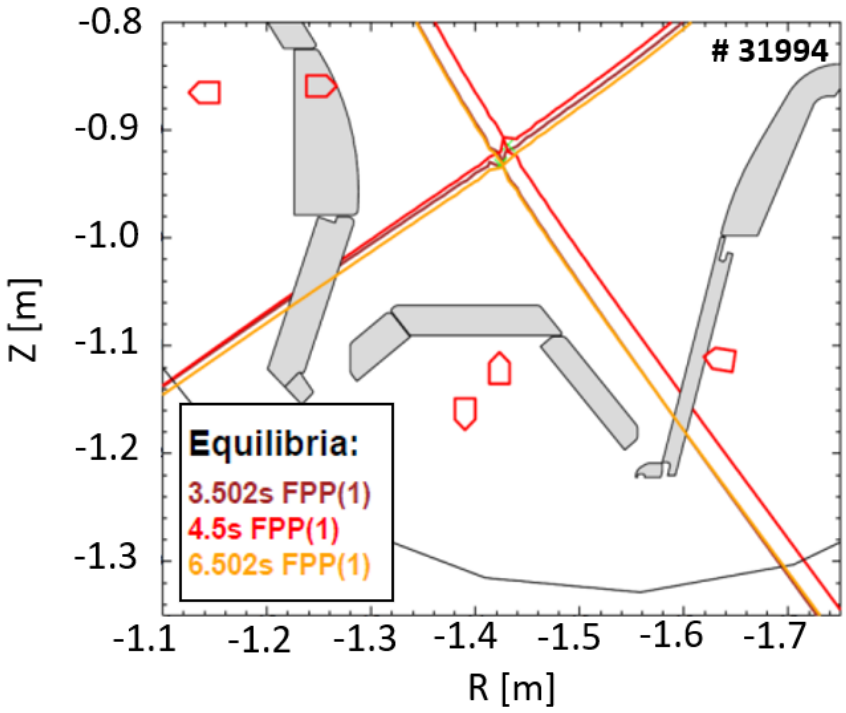

Figure 8.12 In this plot the magnetic equilibrium of the plasma discharge #31994 is shown. A displacement of +1 cm in the vertical direction is pre-programmed during the discharge at t = 4 s, lasting 1 second, before the X-point is brought back to its initial position.

Summary

Sub-divertor flows have been subject of study in ASDEX Upgrade for a set of L- and H-mode discharges. For each set of discharges, the pumping scheme has been varied by operating the machine with full, 1/3 and no cryogenic pumping (only turbomolecular pump active). The experiments for L- and H-mode show:

- Neutral fluxes in the main chamber and pump chamber are correlated to the local pumping. In the framework of the machine operation with 1/3-cryopump the symmetry in the main chamber fluxes is broken. As a result, it is observed that in the sectors where the cryopump was not active, the fluxes behave as the case of no-cryopump configuration. On the other hand, in sectors where the 1/3 cryopump was active, the time traces of the fluxes in the main chamber near the pump show no differences with the fluxes at same location in main chamber with full cryopumping. This is an unexpected result.

- The above described is independent of the confinement mode, i.e. the observations hold for L and H confinement mode. The asymmetry in the main chamber in non-

symmetric pumping configurations will lead to different compression ratio $\Gamma_{div}/\Gamma_{main}$, thus care must be taken when estimating this figure of merit of any tokamak divertor. Symmetrical pumping configurations lead to no substantial variations in the sub-divertor fluxes.

- Assuming steady state conditions, i.e. the puffed gas is pumped out, the particle rate at the pump was expressed by an effective pumping area A_{pump} and thus, the actual reduction of pumping speed could be estimated (relative to the full cryopump scenario). For the L-mode with 1/ 3-cryo actually a reduction of 50% relative to the full cryopump scenario was estimated whereas in the H-mode discharges, a ratio of 0.33 is found between the full and 1/3-cryopumping scenarios.

- During the flattop phase of the discharges, the X-point was shifted upwards by + 1 cm. The effect of X-point displacement is depicted in Figure 8.12 (observation holds for the 3 different pumping schemes and confinement mode).

- The neutral particle fluxes in the divertor below the dome remained constant during the X-point movement. The local recycling on both targets on the other hand, reacts with an increase on the fluxes of a factor of ~ 1.2 and ~ 2.5 on the inner and outer targets, respectively. The fluxes in the pump chamber barely react to the X-point location, thus the dynamics are strongly dominated by the pumping in that region. However, the manometers at pointing towards the divertor tiles, F08 (LFS) and F10 (HFS) do show a variation of the signal during the X-point displacemtent, this can be observed in time traces of neutral fluxes in Figure 8.13.

- The neutral gas flow below the dome in the divertor, main chamber and pumping chamber in sectors 13 and 15 shares a common neutral behavior although a different pumping is taking place. This finding gives us an idea on how the sectors are interconnected to each other and provides a better idea of the neutral distribution in the sub-divertor domain and the main chamber.

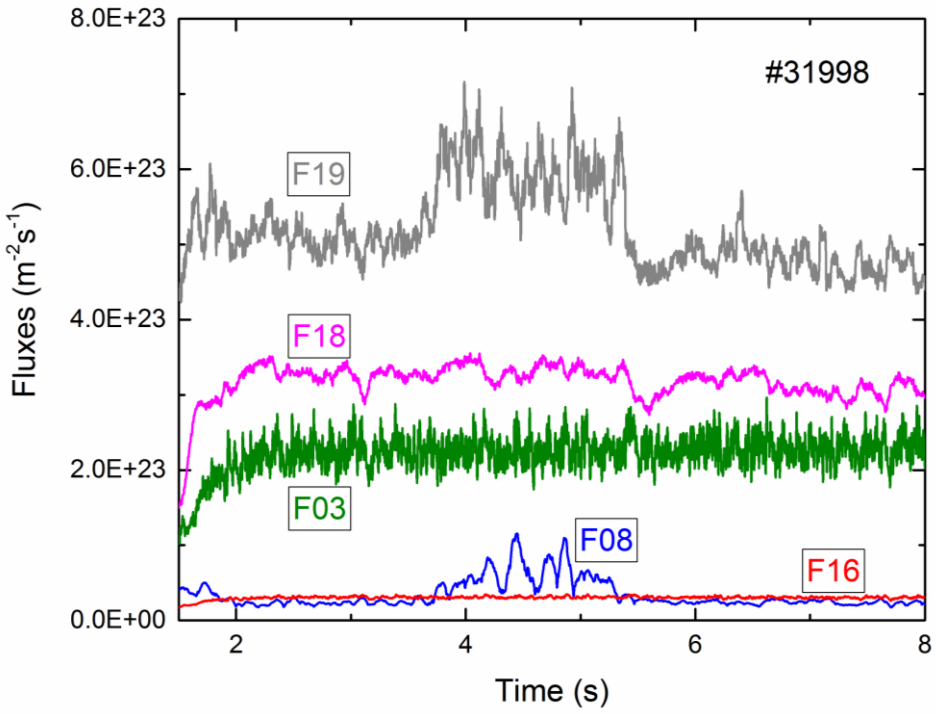

Figure 8.13 Time traces of neutral fluxes in HFS gauges (F18, F19), divertor dome (F03), LFS (F08) and pump chamber (F16). The manometer measurements were kindly provided by Dr. Andreas Scarabosio.